THE UNIVERSITY *of* EDINBURGH

Microscopic studies of surface growing bacterial populations

Diarmuid Padraig Lloyd

Doctor of Philosophy
The University of Edinburgh
2014

Abstract

In this thesis, I present three microscopy studies of surface growing *Escherichia coli* (*E. coli*) microcolonies. All experiments were carried out by growing microcolonies on agarose pads, and imaging their growth using phase contrast, fluorescence and confocal microscopy.

In the first project, the importance of spatial structure and growth strategies between competing populations of *E. coli* was studied. An agarose pad was seeded with bacterial cells and their colonisation success tracked. Cell lag-times and local cell density were found to play important roles in determining the eventual success of a colony. Arrangements of neighbouring cells were found to be partially responsible at high cell densities. These results were reproduced using a simple simulation, which also highlighted the importance of exponential expansion in determining colonisation success.

The second project investigates the effect of confinement on growing microcolonies restricted to one plane (2d growth). Colonies were grown in agarose micro-channels with different aspect ratios, and in unconfined environments. In particular internal physical colony structure and genealogical structure was studied by using single-cell tracking. Results showed that relatedness between cells was directionally biased (cells tended to be more closely related to cells at their poles, than to their side) regardless of the amount of spatial restriction. Furthermore, confinement caused cells to align with each other more, and induced high cell velocities at the colony edges driven by cell expansion.

In the final project, growth of secondary layers in growing colonies of *E. coli* was studied. Cells initially grew as a monolayer, before invading the agarose bulk, producing a secondary layer. By analysing time-lapse movies, this layer was found to initially expand rapidly well in excess of cell growth rates and initial colony

expansion rates, before slowing down. The initial secondary growth rate likely depends on the colony area at agarose invasion. Furthermore, the colony area when colonies invaded the agarose depended on their rate of growth, suggesting a complex interplay between forces exerted by the agarose, and by the colony.

Lay Summary

This thesis describes experiments which investigate surface growing populations of the bacterium *Escherichia coli* (*E.coli*). A useful feature of some bacteria is how quickly they grow: in the right conditions, a single *E. coli* cell resting on a surface can grow into a microcolony comprising tens of thousands of cells within several hours. This rapid growth is exploited in this thesis, where we watch the development of microcolonies under a microscope to investigate some of their interesting features, and attempt to extrapolate the results to other types of general situations in the wider world.

First, the factors which influence the probability one microcolony will outcompete a neighbouring colony for space is studied. This is important in the context of ecological theory, which states organisms can compete for local space via a number of different expansion mechanisms. Using a simple laboratory model, the importance of these mechanisms was explored by imaging a surface which had been completely colonised by *E. coli* cells. By using labelled cells, we were able to tell which colonies succeeded in capturing more space than others. From these observations, it was found that two competing factors (initial times to divide, and cell density) were the driving contributors to the eventual success of a colony.

Second, the effect of confinement on colonies was investigated. This is important because colonies often grow in restricted environments in the real world. Furthermore, cooperation between cells has been shown to occur between cells which are related to each other (kin-selection), and so we investigated how confinement influenced the 'relatedness' of neighbouring cells. A complete family-tree of the cells within the colony was built using time-lapse movies where individual cells could be seen. Results showed that relatedness between cells was

directionally biased (cells tended to be more closely related to cells at their poles, than to their side) regardless of the amount of restriction, and that confinement caused cells to align with each other more, allowing higher cell velocities at the colony edges driven by cell expansion.

Third, the development of early 3d colony structure was studied. In the experiments, single cells are sandwiched between a soft gel, and a glass surface. Early colonies therefore grow in a single layer . Eventually however, they invade the soft gel. This is similar to the way bacteria cause urinary tract infections, where cells are trapped between the hard surface of a catheter and soft tissue. Using time-lapse movies, the secondary layer was found to rapidly expand at a rate that depended on the stiffness of the soft, gel surface, which could be controlled in experiments. Furthermore, the point at which cells invaded the gel depended on their growth rate, suggesting frictional forces play an important role in the invasion event.

Declaration

I declare that this thesis was composed by myself, that the work contained herein is my own except where explicitly stated otherwise in the text, and that this work has not been submitted for any other degree or professional qualification except as specified.

(*Diarmuid Padraig Lloyd, March 2015*)

Acknowledgements

There are too many people to whom I owe a great deal of thanks for their support and encouragement throughout this Ph.D. to fit on this page - I hope they all know who they are. First, my grateful thanks to my supervisor Rosalind Allen for agreeing to take me on as a student, and whose guidance, patience, objective insight and enthusiasm was utterly invaluable. I'd also like to thank Angela Dawson for all her help (and considerable patience!) in the laboratory, and Jane Patterson, the former Graduate School Secretary, for her support.

I would also like to thank and acknowledge Dario Dell'Arciprete and Bartek Waclaw for helping with the design and construction of PDMS structures, and to Andrew Garrie in the construction of the perspex frames used in this thesis. Also, EPSRC, who funded my Ph.D., and whose financial support allowed me to travel to conferences, attend courses and engage with other researchers.

Thank you to the lovely people in rooms 1511, 2510, 2509, and 1505 for all their helpful discussions. In particular, Siobhan, who had to endure my countless questions for almost four years, and to Dario and Alex, for their helpful chats and shared pain in bacteria time-lapse experiments. Thank you to my fellow lab-mates for their endurance of my bacteria-related questions, Anne for image analysis chat, Kym for anything coding related and Zach for the coffee breaks. Outside of the JCMB, thank you to friends for keeping me sane, particularly those at the EU Shukokai Karate Club, past and current members alike.

For their unwavering love and support, my thanks to my parents Greg and Siobhan, their partners Deborah and Maggy, and to my brother Eamon. You all might have some idea of how much you helped me, but I can assure you it's at least an order of magnitude greater than you think.

Finally, to Clare, who is my greatest support, and somehow kept a brave face even when I submitted this thesis three days before our wedding day: none of this would have been possible without you. Thank you.

Contents

Abstract i

Lay Summary iii

Declaration v

Acknowledgements vi

Contents vii

List of Figures xiv

List of Tables xx

1 Introduction 1

2 Surface growing colonies 3

2.1 Introduction 3

2.2 Early microcolony organisation 4

2.2.1 Surface adherence 4

2.2.2 Initial cell colony development 5

2.3 Confined colony growth 6

2.3.1 Internal structure 6

2.3.2 Cell growth and mobility 8

2.4 Self-organisation in bacterial structures 9

2.4.1 Cooperativity 9

2.4.2 Pattern formation 11

3 Materials and Methods 13

3.1 Bacterial strains 13

3.2 Culturing and Storing Bacteria 14

3.2.1 Growth media 14

3.2.2 Growing cultures 15

3.2.3 Long-term storage 17

3.2.4 Growth curves 18

3.2.5 Antibiotic resistance 18

3.3 Agarose Pads 19

3.3.1 Thin pads 20

3.3.2 Thick pads 21

4 Microscopy Background 23

4.1 Introduction 23

4.1.1 Microscopy principles 24

4.1.2 Illumination Plane 27

4.1.3 Resolution limits 28

4.1.4 Phase-contrast 30

4.1.5 Fluorescence 31

4.1.6 Confocal 33

4.2 Time-lapse microscopy 34

4.3 Single Cell Tracking 35

4.3.1 Schnitzcells 35

4.3.2 Workflow 35

5 Competition for space during bacterial colonisation of a surface 39

5.1 Introduction 39

5.1.1 Ecological implications of spatial structure 39

5.1.2 Bacteria as models in ecology 40

5.1.3 Colonisation by scattered populations 42

5.1.4 The microbial model system 43

5.2 Experimental Results 44

5.2.1 Overview of a typical competition experiment 44

5.2.2 Quantifying colonisation success 45

5.2.3 Do winner and losers have different colony shapes? 47

5.2.4 Fourier descriptors 48

5.2.5 Cell-lagtimes and expansion competition 51

5.2.6 Boundary competition at high cell density 56

5.2.7 Does Voronoi patch shape influence success? A more detailed analysis 58

5.3 Discussion 64

5.3.1 Voronoi-colony shape correlation 65

5.3.2 Why do smaller colonies show higher WI values? 66

5.3.3 Expansion competition versus boundary competition 66
5.4 Conclusion 67
5.5 Future Work 67
5.6 Expanded methods 69
5.6.1 Microbial competition protocols 69
5.6.2 Lag-time protocols 72
5.6.3 Multi-linear regressions 74

6 Simulating microbial competition 76

6.1 Introduction 76
6.2 Simulation method 77
6.2.1 Simulation setup 78
6.2.2 Growth rules 79
6.2.3 The effects of 'pushing parameter' η 82
6.2.4 Analysis 84
6.3 Expansion competition: lag-time, growth regimes and density 84
6.3.1 WI distributions with no lagtimes 85
6.3.2 WI distributions with lag-times 85
6.3.3 Does lag-time or colony area play a dominant role? 88
6.3.4 Summary 89
6.4 Boundary effects: Voronoi polygon morphologies 91
6.4.1 Does the number of neighbours affect WI? 91
6.4.2 Predicting WI based on morphology 92

6.4.3 Similarities between Voronoi polygon Fourier spectra 94
6.5 Discussion 96
6.5.1 Removing lag-times 96
6.5.2 Lag-times are more important than density 97
6.5.3 Voronoi morphology 97
6.6 Conclusion 98
6.7 Future work 99

7 Confined microcolony growth 100

7.1 Introduction 100
7.1.1 Physical structure of the confined colony 101
7.1.2 Relatedness and cooperation 102
7.1.3 Ageing in colonies 104
7.2 Method for constructing patterned agarose structures 105
7.2.1 PDMS masks 106
7.2.2 Agarose channels 106
7.3 Charactering the physical structure of confined microcolonies 109
7.3.1 Microchannel growth 109
7.3.2 Microchannel colony morphology 110
7.3.3 Cell morphology 111
7.3.4 Cell orientational order 112
7.3.5 Density and cell size 114
7.3.6 Cell velocities 116

7.3.7 Summary 120

7.4 Genetic structure in confined colonies 121

7.4.1 Common ancestor interfaces 122

7.4.2 Calculating genetic distances 123

7.4.3 Genetic distance distributions 125

7.4.4 Genetic distance dynamics in growing colonies 126

7.4.5 Summary 133

7.5 Age distribution of old poles in confined colonies 133

7.5.1 Quantifying pole ages 136

7.5.2 Old pole positions 138

7.6 Discussion 140

7.7 Conclusions 142

7.8 Future Work 143

8 Microcolony growth in three dimensions 144

8.1 Introduction 144

8.2 Methods 147

8.2.1 Sample preparation 147

8.2.2 Microscopy set-up 147

8.2.3 Image analysis 148

8.3 Results 148

8.3.1 Transition from 2d to 3d growth 148

8.3.2 Growth of a second layer of cells after agarose invasion 150

8.3.3 Expansion dynamics of the primary and secondary layers.... 153
8.3.4 Invasion occurs at multiple locations 157
8.3.5 3d structure of colonies 158
8.3.6 Agarose invasion area dependency on cell growth rate 160
8.4 Discussion 165
8.4.1 Transition from 2d to 3d 165
8.4.2 Secondary layer dynamics 168
8.5 Conclusion 170
8.6 Future work 170

9 Conclusions 172

A Schnitzcells workflow 175

B Isolating secondary layers in growing colonies 177
B.1 Tracking layer dynamics 177

C Supplementary information to microchannel colonies 180
C.1 Malformed channels 180

Bibliography 182

List of Figures

(2.1) A scanning electron microscopy image of *E. coli* K-12 cells and their fimbrae. 5

(2.2) Examples of *E. coli* colonies growing in microfluidic chemostats. . 7

(2.3) Examples of different types of spatial structure in surface growing bacterial colonies. 10

(3.1) Illustration of agar plate preparation steps 16

(3.2) Growth curves for RJA002 and RJA003 growing in M9-glucose + CAA 19

(3.3) Comparison of final optical density measurements for strains grown in different concentrations of a variety of antibiotics. 20

(3.4) Types of agarose pads used to grow bacteria on for the purposes of microscopic studies. 21

(4.1) Schematic of a basic microscope system, exploiting 'infinity-optics'. 25

(4.2) Ray diagram of illumination and imaging planes for a properly set-up microscope 26

(4.4) Schematic illustrating an objective's numerical aperture. 29

(4.5) Illustration of a phase-plate's effect on background light 31

(4.6) Schematic of a dichroic mirror used in fluorecence microscopy studies 32

(4.7) The workflow and GUI of the *Schnitcells* single - cell segmentation software 36

(4.8) Snapshots of problems associated with the Schnitzcells software package. 38

(5.1) Examples of segregation of two fluorescent strains of *E.coli* and the yeast *Saccharomyces cerevisiae*. 40

(5.2) Illustration of surface competing organisms. 41

(5.3) A montage of the bacterial landscape, constructed from 286 individual snapshots. 44

(5.4) Experimental Voronoi tessellations and resulting colony after surface growth. 45

(5.5) Comparison of the Voronoi polygon area distributions for 'high' and 'low' density experiments. 46

(5.6) Histograms of the WI for exponentially growing cells, with two different Voronoi polygon area distributions. 47

(5.7) Voronoi areas versus winner indices for high and low density experiments. 48

(5.8) Fourier descriptor spectra for idealised shapes. 50

(5.9) Pearson correlation coefficients between Voronoi and colony Fourier descriptor magnitudes. 52

(5.10) Combined histogram of lag-times (t_{lag}) for both RJA002 and RJA003, seeded on agarose when in the exponential phase of growth and heat-shocked from stationary phase. 53

(5.11) Comparison of WI distributions between cells which have been heatshocked, and those not. 55

(5.12) An example of colony success by boundary competition. 56

(5.13) Median WI versus Voronoi face numbers for low and high Voronoi area distributions 57

(5.14) Median WI values against binned Fourier descriptor magnitudes for low density experiment 59

(5.15) Median WI values against binned Fourier descriptor magnitudes for high density experiment 60

(5.16) Plots of similarities between Fourier descriptor spectra of Voronoi polygons, and with ideal shapes. 62

(5.17) Illustrations and experimental Voronoi tessellations. 71

(5.18) Phase contrast images of cells on the verge of dividing. 73

(6.1) A snapshot of an example simulation showing 'colonies' competing for space. 77

(6.2) Illustration demonstrating the growth methods for simulated colonies. 79

(6.3) Flowchart of main steps taken in bacterial growth simulation. . . 80

(6.4) Montage showing the effect of varying the η parameter on growth rates and colony morphologies. 81

(6.5) Voronoi diagram showing which polygons were kept for analysis. . 83

(6.6) WI distributions for simulated bacterial landscapes with different numbers of initial cell densities to cover 'low' and 'high' Voronoi area distributions. 86

(6.7) Bar plots showing the increase in dispersion in WI distributions as lagtimes are introduced 87

(6.8) Interpolated surface plots showing the relationship between Voronoi polygon area, lag-time, and WI. 90

(6.10) Multidimensional scaling plots of Euclidean distances betweeen Fourier spectra of the top and bottom 10 % of WI Vorono-colony pairs from simulations. 95

(7.1) Adapted plots of others showing buckling instabilities and streaming patters in colonies grown in microfluidic devices. 102

(7.2) Illustration demonstrating how genetic distance is calculated in microcolonies. 103

(7.3) Snapshots of a growing microcolony, linking the old poles between frames. 104

(7.4) Cartoon of agarose casting process while building agarose microchannels 107

(7.5) Fluorescenent images of colonies growing in microchannels, and a normal surface growing colony. 108

(7.6) Comparisons of colony growth metrics for microchannel grown and standard growing colonies. 109

(7.7) Effect of agarose microchannels on colony morphology 110

(7.8) Development of spurs on bacterial cell for growth in microchannels 111

(7.9) Cell angles as a function of colony population for normal and microchannel grown cells. 113

(7.10) Cell orientation order parameter for cells growing in channels and normal growing colonies. 115

(7.11) Global colony cell density, maximum colony cell density and average cell division lengths as a function of colony cell population. 116

(7.12) Comparison of instantaneous cell velocities for colonies growing in different growth geometries. 117

(7.13) Surface maps of instantaneous cell velocities for a microcolony with 61 cells and 624 cells 118

(7.14) Maximum cell velocities for microchannel grown colonies and predicted maximum velocities based on a simple cell expansion model. 119

(7.15) Representative cell masks in colonies growing in different microchannels, coloured by their common ancestor. 122

(7.16) Reprint of Fig.7.2. 123

(7.17) Schematic illustrating how neighbour cells are divided into two class types 124

(7.18) Histograms of genetic distances to nearest neighbours in microchannels and normal growing colony at $N = 61$ cells. 127

(7.19) Variation in the probability that a cell's neighbour is its 'sister' as a function of colony population. 128

(7.20) Distributions of final sister-cell distances before each lineage terminates. 129

(7.21) Distributions of final relative sister-cell positions before each lineage terminates. 130

(7.22) Interpolated maps showing the degree of distance between neighbouring cells in colonies grown in and out of channels (120 cells) . 132

(7.23) P(D=d) as a function of colony population, for $3 \leq d \leq 12$. . . . 134

(7.24) P(D=d) as a function of colony population, for longitudinal and latitudinal cells. $3 \leq d \leq 12$. 135

(7.25) Interpolated maps of mean local genetic distances for a normal growing colony at various points of colony development. 136

(7.26) Illustration demonstrating how pole age is quantified. 137

(7.27) Trace plots showing the path taken by an old pole in each colony type. 137

(7.28) Distances of cells carrying the older poles from the colony centre of mass. 139

(8.1) Idealised illustration of the experimental system, showing bulk layer development. 146

(8.2) $x - z$ slice of a confocal image with fluorescent bacteria embedded in fluorescent stained agarose. 148

(8.3) Phase-contrast micrographs showing a colony transitioning from 2d growth to 3d growth. 149

(8.4) Colony buckle area as a function of agarose concentration. 150

(8.5) Area expansion curves for primary and secondary layers for colonies grown on 3 % agarose. 152

(8.6) Micrographs showing the fixed width difference between layer fronts for a colony growing on 4 % agarose. 154

(8.7) Evolution of the distance d between the primary and secondary layer fronts. 155

(8.8) Detail of a phase contrast micrograph highlighting the apparently tiered structure of the microcolony. 156

(8.9) Illustration of the two proposed ways cells can migrate from the primary to the secondary layer. 157

(8.10) Initial invasion locations and micrographs of a growing *E. coli* colony exhibiting invasion regions in the primary layer not yet covered by the secondary layer. 159

(8.11) Collection of deconvolved confocal microscopy z-stack slices of a developed colony and maximal colony depths as a function of agarose concentration. 161

(8.12) Comparison of colony area doubling times on difference agarose concentrations while still growing in 2d. 162

(8.13) Comparison of colony area doubling times using M9-glucose-CAA and M9-glucose on different agarose concentrations. 164

(8.14) Illustration showing how the monolayer width d might determine where cells invade the agarose. 169

(B.1) Montage of image processing steps for isolating the 2d projection of the bulk layer. 179

(C.1) Phase contrast images of the PDMS moulds made in this study. . 181

List of Tables

(3.1) Summary of strains referred to in the thesis. 13

(4.1) Summary of the objectives used in this thesis 23

(4.2) Summary of the microscope, stages and cameras used in this thesis 24

(5.1) Predictor values for Fourier descriptors from a linear, stepwise multilinear regression model. 61

(6.1) A summary of the different simulation parameters presented in this chapter, and the number of repeats for each. 84

(6.2) Coefficients for Fourier descriptors from a stepwise multilinear regression model. 94

(7.1) Summary of agarose microchannel dimensions 106

(A.1)Summary of key functions written to exploit Schnitzcells datasets. 176

Chapter 1

Introduction

Bacteria comprise one of the three main domains which make up the phylogenetic tree of life. They are found in abundance across the planet, and play their part in a host of vital processes in the natural environment, from aiding digestion in the mammalian gut, to recycling nutrients as part of the global biogeochemical cycle. However, pathogenic variants of bacteria are also the source of many diseases, such as tuberculous, cystic fibrosis and cholera, for example. Their global ubiquity reflects their remarkable adaptability, and despite their relative simplicity as unicellular microorganisms, they can display a plethora of complex behaviours that belies their small size.

While many bacterial species are motile, and can be found in the natural world suspended in aqueous environments, for the most part, bacteria grow on surfaces to form multicellular assemblages. Invariably, this results in heterogeneous populations, and far from simply being sessile aggregates of individual cells, they can exhibit complex behaviour, such as quorum sensing, biofilm production and other collective behaviours. Understanding how these structures develop, proliferate, and ultimately interact with their surroundings is therefore vital within the wider context of surface growing communities.

In this thesis, I present three studies on surface growing colonies of *Escherichia coli* (*E. coli*), a model organism which is commonly used in microbiology studies, and has well characterised properties. As such, it is a powerful tool which can be exploited to answer wider, more general questions beyond the specific organism

itself. In the first study, I address what factors influence the likelihood that some surface growing colonies of bacteria will out-compete their neighbours for space, a question that has ecological implications, using both experiments and simulations. In the second study, because many colonies in the natural world grow in small cavities, I investigate the effect of confinement on single cells in growing microcolonies. In the third and final study, I investigate the invasive transition of microcolony growth into agarose, and perform observational studies on the initial growth of these 'bulk' bacterial layers.

The thesis is structured as follows:

Chapter 2 provides a general introduction on surface growing bacteria to familiarise the reader.

Chapter 3 covers laboratory protocols used in this thesis necessary for the culturing of bacteria.

Chapter 4 details the microscopy methods.

Chapter 5 is an experimental study on what factors influence the likelihood that surface growing bacteria can out-compete their neighbours for local space. I show that both cell lag-times and cell densities are important.

Chapter 6 details simulations which reproduce the key findings in the previous chapter, but also shows the importance of exponential expansion

In **Chapter 7**, I present an experimental study on the effect of confinement on small microcolonies, and how it relates to the distributions of 'relatedness' within small colonies. I show that confinement has a strong effect on internal colony physical structure, and to some degree, local bacterial relatedness.

In **Chapter 8** I cover aspects of 3d microcolony growth. Using experiments, I show that agarose concentrations have an effect on the structure of bulk layers of bacterial growth in agarose.

Finally, in **Chapter 9**, the results for the whole thesis are summarised.

Chapter 2

Surface growing colonies

2.1 Introduction

In 1683 a Dutch fabric tradesman, Antonie van Leeuwenhoek, wrote to the Royal Society describing how after examining dental plaque under his homemade microscope, he found:

> *"an unbelievably great company of living animalcules, a-swimming more nim-bly than any I had ever seen up to this time...Moreover, the other animalcules were in such enormous numbers, that all the water...seemed to be alive. "*

This was the first observation of bacteria (a type of prokaryote), a very large group of single-celled microorganisms whose prevalence we now know extends into almost every habitat on the planet. Globally, the total prokaryote population has been estimated at 6×10^{30} individual cells, of which $\approx 94\,\%$ reside in the soil subsurface [1]; in other words, the vast majority of cells grow on surfaces and in small interstices [2]. Given the ubiquity of bacteria, and the significant effects they have on the natural world, an understanding of surface growing bacterial populations is very important.

Surface growth can afford bacteria a number of immediate advantages over planktonic cells. First, cells in nutrient poor environments are better served

growing on a surface. For example, cells which drop out of liquid environments and adhere to a surface can seek out local concentrations of nutrients arising from sedimentation of organic material in the surrounding liquid [3]. Sometimes the surface is a source of necessary nutrients and metabolites, as in the case of *Sewanella*, a genus of bacteria which grow on metals to use them as terminal electron acceptors as part of their respiration cycle [4]. Surface attachment can also result in the eventual formation of large, but highly structured, spatial structures which provide the cells within protection from environmental effects.

This thesis contains three studies, all which investigate surface growing colonies of *E.coli*. This particular species was chosen since it is commonly used as a model organism within biological research, due to its relative genetic simplicity compared to other species, and its rapid growth rate in simple nutritional conditions. This makes it straightforward to culture and conduct experiments, and as a result, there is more known about *E. coli*'s genetic structure than any other organism. Phenotypically, *E. coli* does not behave in a 'standard' way however, as bacteria are a spectacularly diverse domain - for example, it is not a biofilm former, whereas other species, such as *Pseudomonas aeruginosa*, readily form biofilms. But the the fact it is well characterised makes it an attractive choice as a model bacterium for studies of the early stages of surface growth. Within each chapter, I focus on the literature relevant to the project. In this chapter, I provide a general introduction to surface growing populations to familiarise the reader with important aspects of this type of bacterial growth.

2.2 Early microcolony organisation

2.2.1 Surface adherence

In the very early stages of surface colonisation, a single bacterium first has to adhere to a surface. This is achieved through a two step process, where bacteria first rely on non-biological, physiochemical effects to provide a temporary fixture [5]. The second part, which occurs over a longer time-scale (hours, versus minutes) is irreversible, and involves van der Waal forces, but in the case of *E. coli*, surface polymers and hair like appendages known as *fimbria* which stick out of the cell membrane, can speed this process up [6]; Fig.2.1 shows these

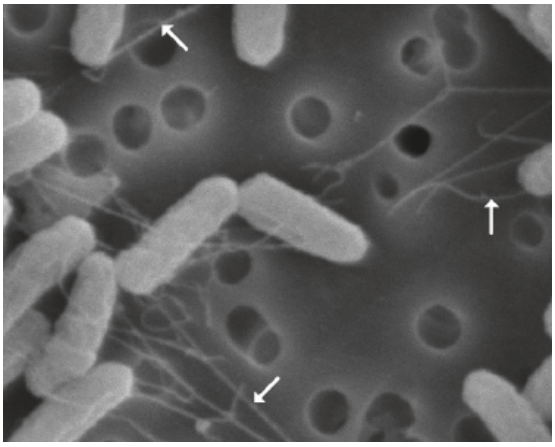

Figure 2.1 A scanning electron microscopy image of *E. coli* K-12 with associated fimbrae marked by the white arrows. Adapted from [6].

features. This process normally inhibits motility through the down regulation of *flagella* production, the locomotive organelle used to propel bacteria through liquid environments [7]. Such behaviour is seen in the strains used in this thesis, which are motile in liquid culture, but motionless when imaged by microscopy on agarose.

2.2.2 Initial cell colony development

Under the right conditions, the cell lengthens and divides in a process called *binary fission*. For non-motile cells growing on agarose, the cells are able to pass over the surface, and after a few rounds of this process, the resulting aggregate of cells has formed a *microcolony*, a small collection of individual cells.

Early studies of *E. coli* colony development on agar were motivated by an interest in the membrane that surrounded cells, and how it developed during the cell division process. Donachie and Begg [8] found that for a single *E. coli* cell growing on an agar bed, there was a common pattern in the new born cells' position after the mother cell divided, namely that after two division cycles, a 2x2 cell array would form. This was attributed to the fact that cells apprarently only grew from the cell pole that had formed as a result of division.

However Shapiro and Hsu [9] found that increasing the local cell density on the agar resulted in a departure from this simple arrangement. Instead, dividing cells would preferentially point themselves in the direction of neighbouring cells -

a result that was interpreted by the authors as cooperative behaviour, since the cells preferred not to remain isolated (which would mean fewer competitors for nutrients). Moreover, larger neighbour microcolonies were observed 'puckering' towards each other, indicating preferential growth on bigger scale. Removing chemotactic sensing in the bacteria still resulted in directional growth between colonies, removing the possibility that colonies were competing for a shared resource [10]. *E. coli* was therefore suited to growing in 'crowded' surface environments. However, when the 4 cell array pattern was observed, it occurred regardless of the different mutants tested, but once colonies reached population sizes approaching a few hundred cells, the colonies took on remarkably different morphologies that did depend on the strain used.

Su *et al.* [11] found in a similar study that mutant *E.coli* cells which lacked lipopolysaccharide production capabilities often formed linear strings of cells, rather than the familiar array. Non-mutant cells (K-12) growing on a substrate which made adherence difficult also resulted in linear strings. This implicated interactions between cell and substrate in the spatial arrangement of cells on surfaces, too.

Collectively, these studies show that even at very early stages of microcolony development, the interaction between cells themselves and with the substrate is very important in determining the initial cell arrangements. As these colonies continue to grow however, cell-cell interactions would be expected to become very important - indeed, colony structure at high cell numbers depended on strain specific qualities. Given many bacteria in the natural environment grow in small spaces, and have been shown to cooperatively seek confined colonies to colonise [12], interest in this particular area of surface colony growth has burgeoned.

2.3 Confined colony growth

2.3.1 Internal structure

To properly study the effect of cell-cell interactions in close confinement, the use of quasi-two dimensional microfluidic devices, which operate as a chemostat to support a colony to high population levels without nutrient limitation, is very

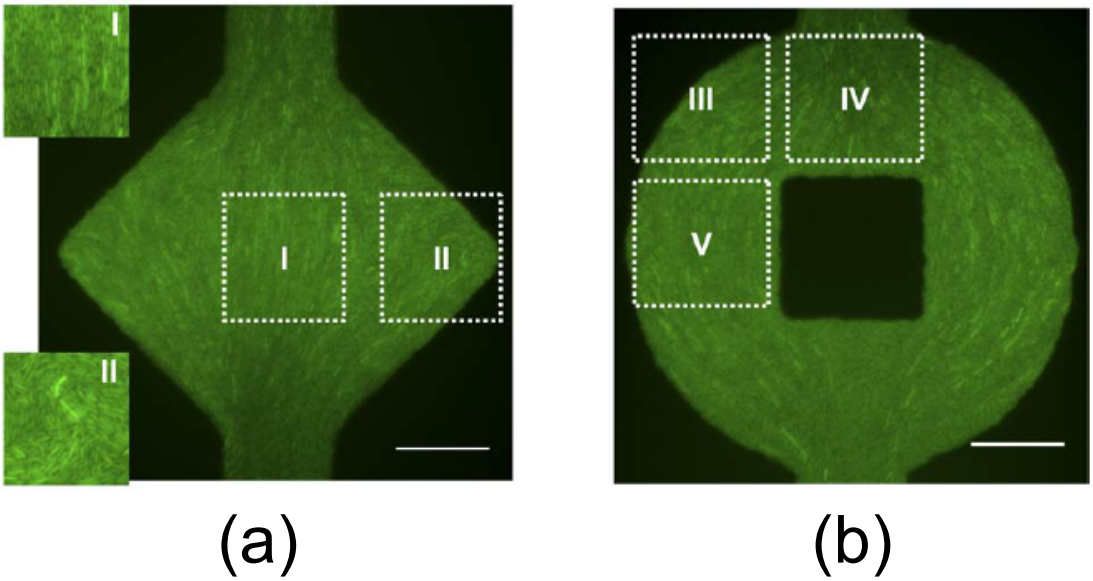

Figure 2.2 *E. coli* colonies growing in (a) rhombus and (b) circle shaped microfluidic chemostats. The dashed boxes refer to field of view details in the original paper (panels I and II are shown in this figure, however). Scale bar 50 µm. Adapted from [13].

powerful. Combining this with microscopy has allowed unparalleled population studies of internal colony structure in these type of environments, and has shown that cells can exhibit orientational ordering at long length scales.

Volfson *et al* [14] was among the first to study these colony features, where they showed that expansion flow arising from cell elongation and division could produce structural changes within the colony. They grew non-motile E. coli cells in an open ended, quasi 2d microfluidic chemostat, and monitored the cell's structural rearrangements as the cells became increasingly packed due to the population expansion. Before space became scarce, cells were shown to have no orientational order: that is, they had an isotropic phase. When cell proliferation resulted in close packing however, cells began to escape at the exits, triggering an internal structural transition, whereby cells aligned along the resulting outgoing cell-flow vectors. At this point, the cell population existed within an imperfect nematically ordered phase.

In a similar piece of research published at the same time, Cho *et al.* [13] monitored the alignment of cells growing in microfluidic devices, but with different geometries than those used by Volfson *et al.* (Fig.2.2). Similarly, they found that orientational ordering was directed along the flow field pointed towards

the chamber exits, and that it extended over many cell lengths. Interestingly, through agent-based models, this research also suggested that the average *E. coli* cell dimensions were at the lower end of the range which would actually allow cell ordering, a possible example of natural selection at play.

2.3.2 Cell growth and mobility

The important role of cell aspect ratio in confined geometries was further shown by Boyer *et al.* [15], who used larger 2d traps, but with one or more exit points, to show why cells never reached perfect nematic ordering. As the cells grew and became ordered, pressure in the regions of the traps where cells were furtherest from the exits grew, which eventually triggered a *buckling instability*: cells would 'pop' out of alignment. Cells now possessed imperfect nematic ordering, similar to that shown by Volfson *et al.* [14]. Significantly, cell aspect ratios were shown to affect the likelihood of the instability occurring: cells near trap exits tended to be larger through better access to nutrients, and did not buckle. As such, the range of nematic ordering lengthened the closer to the trap exits.

However, large cells at trap exits were shown to potentially hinder overall colony function by Mather *et al.* [16] which would temper the potential advantages of cell order, however. Here, rectangular traps were constructed with either one, or both ends open to allow cell escape. They showed that larger cells at the trap exits (which were benefiting from better nutrient access) suffered from drag-induced stagnation, effectively blocking the trap exits to comparatively starved cells flowing from the centre of the colony, deeper within the trap. Complex flow patterns of the smaller cells were also observed as they negotiated their way from the trap around the blockages, showing the non-trivial behaviour within even small micro-colonies.

These studies demonstrated the complex behaviour and structural properties within confined colonies that arose purely from bio-mechanical interactions. What are the benefits of this behaviour? Cell alignment could possibly allow relaxation of internal stresses, allowing better flow of nutrients into the centre of the colony. Furthermore, waste products are able to flow from deep with the colony. In Chapter 7, I explore some effects confinement can have on both the physical structure, and relatedness within the colony, which has potential

implications on the cooperation between cells. Indeed, cooperation in general is a very important aspect of spatial structure in surface growing colonies. I introduce these concepts in the next section.

2.4 Self-organisation in bacterial structures

2.4.1 Cooperativity

It wasn't until Shapiro's seminal review in 1988 [17], that the entrenched view that cells were sessile, individual units that were driven by their own needs, such as competing for local resources, was challenged. Cooperation between cells is now considered to be a common behaviour in bacteria, and one of its key effects is the development of spatial structure in multicellular structures, such as complex swarming (a type of motility observed on semi-solid agar surfaces) patterns in *Paenibacillus vortex* [18] , and stratification of *Escherichia coli* colonies [17] (Fig.2.3). However, spatial structure in growing colonies is not seen just in the laboratory.

Generally, bacterial cells in the natural environment are almost always found as part of large spatial structures called biofilms. These are matrix enclosed, 3d bacterial populations which adhere to a variety of surfaces [2, 22]. The biofilm structure is maintained by an *extra polymeric substance* (EPS), and they are prevalent in many environments: For example, chronic blood infections have been traced to biofilms adhering to pacemakers. The biofilm also affords cells within a degree of protection from antibiotics and heat [22]. Confocal microscopy has shown the EPS structure which surrounds cells is 'open', to allow the flow of nutrients and waste products [23], and could even allow for the diffusion of molecules involved in the spatial positioning of the cells. In Chapter 8, we look at the very early stages of 3d colony development, but consider it from a purely mechanical point of view.

Within these structure, cells can be can be spatially differentiated by their gene expression, or even their cell type. For example, in biofilms of *Bacillus subtilis*, inner, older regions of the structure have been shown to express different genes to identical cells in the newer, outer regions [24]. Furthermore, wild-type variants

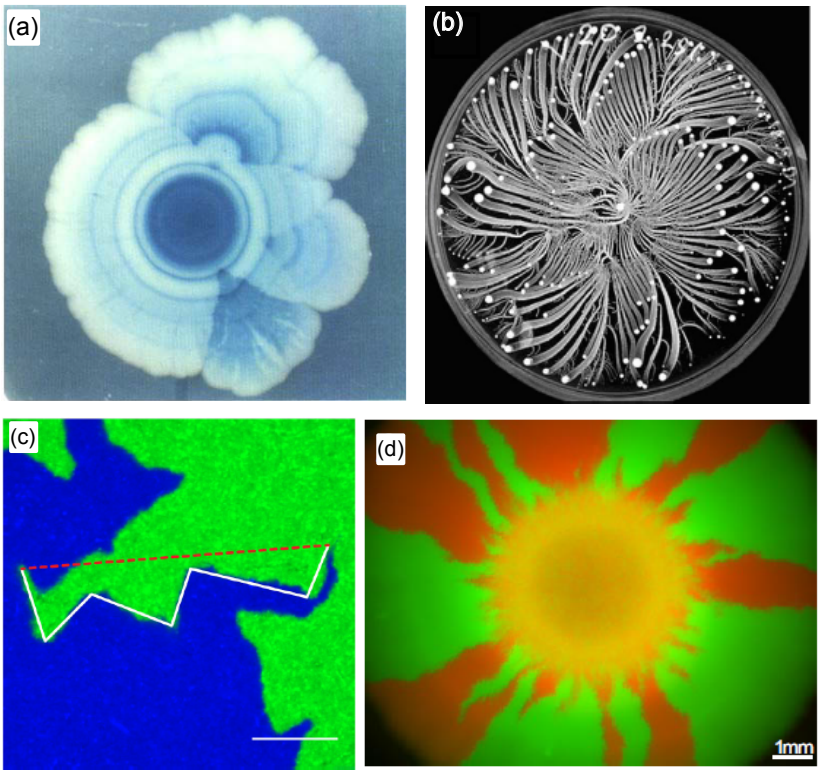

Figure 2.3 Examples of different types of spatial structure in surface growing bacterial colonies. (a) Stratification in a growing colony of *E.coli*. (b) Swarming patterns in *Paenibacillus vortex*. (c) Fractal boundaries arising from collisions between *E. coli* domains (scale bar 30 µm). (d) Genetic domains emerging from random fluctuations in the growth rate of *E.coli* cells at the edge of the colony, which express different fluorescent proteins. Adapted from [19],[18], [20] and [21].

of *Bacillus subtilis* biofilms have distinct regions where cells will sporulate [25].

Regulation of further biofilm development (and the trigger for its onset) is often facilitated by quorum sensing. Here, signal molecules are produced by the bacterial cells, which once they reach a critical concentration, trigger a response in nearby cells [26]. Effectively, it is a means of communication between cells, and has been shown to be essential in the construction of 'effective' biofilms. For example, biofilms produced by deleterious mutants of *Pseudomonas aeruginosa*, which lacked a key quorum sensing gene produced smaller and less complex spatial structures compared to the non-mutant cells [27]. This cooperative process has been shown to confer bacteria which exploit it an advantage, and it is therefore favoured by natural selection [28].

2.4.2 Pattern formation

The distinct, spatially structured 'domains' of cells within these structures will grow and proliferate through cell growth and division. This can lead to interesting spatial patterns that arise from purely mechanical interactions. Moreover, geometry of the interacting cells can affect the emergent spatial patterning.

Rudge *et al.* [20], for example, recently showed in the laboratory environment how cell division and growth alone will produce fractal patterns between colliding colonies of bacteria (Fig.2.3(c)). By using differently labelled fluorescent strains of *E. coli*, they tracked bacterial domains as they grew, which allowed the collision interface to be resolved. These fractal patterns were believed to arise from instabilities caused by the rod-shaped cells: using sphere-shaped mutants produced smoother interfaces.

Hallatschek *et al.* [21] have similarly shown fractal patterns emerging from the collision interfaces of genetically segregated domains by using fluorescent labelled cells. Strikingly however, colony expansion resulted in the segregation of the fluorescent domains (Fig.2.3(d)) which arose from fluctuations in the growth rates of cells at the edge boundaries.

Thus, even in the instances where interactions are purely physical, self-organisation can emerge at the population level in growing bacterial populations. In Chapter 5, I use a similar approach to segregate spatial domains of growing colonies to

study competition between growing colonies.

Chapter 3

Materials and Methods

In this chapter, I describe general microbiology protocols which are relevant to all the projects contained in this thesis. Any amendments to these protocols, or methods specific to an individual experiment will be addressed in the relevant results chapter.

3.1 Bacterial strains

Mutants of *Escherichia coli* K12 expressing fluorescent proteins were used in these projects. The background strain was *E. coli* MG1655, an *E. coli* K12 derivative often considered as "wild-type" (Table 3.1).

Previous to this project, strain RJA002, containing genes for YFP integrated on its chromosome in the loci *intC*, and strain RJA003, containing genes for CFP integrated on its chromosome in the loci *galK* were created by P1 transduction from a strain, MRR, suppled by the Elowitz lab [29]. These strains were also

Strain	Background	Genotype	λ_{ex} / λ_{em} (nm)	Fluoresence
MG1655	-	F- λ- *ilvG*- *rfb*-50 *rph*-1	-	-
RJA002	MG1655		514/527	YFP
RJA003			436/477	CFP

Table 3.1 The bacterial strains used in this thesis, along with their respective antibiotic resistances, and fluorescence properties, if applicable.

conferred antibiotic resistance to chloramphenicol and ampicillin respectively.

3.2 Culturing and Storing Bacteria

This section details the basic types of media used, and growth protocols for preparing bacteria for experiments. Reagents were from Fisher Scientific, Sigma-Aldrich and Oxoid Microbiology Products.

3.2.1 Growth media

The liquid media types used in these experiments can be classified as either 'rich' or 'minimal'. The former supports rapid and reliable growth, since nutrients are in excess, and is useful for generating stock supplies of bacteria. However, minimal media is generally the preferred media type for quantitative experiments because despite the relative scarcity of nutrients leading to slower rates of growth, the constituent ingredients are well controlled, leading to more reproducible growth behaviour. Furthermore, they typically exhibit lower levels of auto-fluorescence, which is important when conducting fluorescence microscopy studies. The two main media types used in this thesis are lysogeny broth (LB) and M9-glucose.

LB

A rich media type [30]. To prepare a final volume of 1 l , measure 10 g tryptone, 5 g yeast extract and 10 g NaCl, and add ≈750 ml distilled water (dH_2O). Mix using a magnetic stir-bar until the solution is free from precipitate, before topping up to 1 l with dH_2O. LB media was used in all overnight cultures, and freezer stocks. Reagents were from Oxoid Microbiology Products.

M9-glucose

A minimal media supplemented with glucose, with very low levels of autofluorescence. The basic media detailed below can be supplemented with additional nutrient sources in order to tune the growth rate. A concentrated stock solution

of salts consisted of 30 g Na_2HPO_4, 15 g KH_2PO_4, 2.5 g NaCl and 5 g NH_4Cl to $\approx$ 750 ml dH_2O. The pH was adjusted to 7.4 using 10 mol NaOH, before topping the solution up to a final volume of 1 l, and autoclaved. For a final volume of 100 ml of 'basic' working media, 25 ml of the sterile concentrate stock solution was mixed with 70 ml dH_2O. Next, 2 ml of 20 % glucose was added, followed by 200 µl 1 mol $MgSO_4$ and 10 µl 1 mol $CaCl_2$; the latter two stock solutions were first sterilised through a 0.22 µm filter. The media was swirled until the $CaCl_2$ precipitate had dissolved, before the solution was topped up to a final volume of 100 ml. Reagents were variously from Fisher Scientific and Sigma-Aldrich.

3.2.2 Growing cultures

In this thesis we use several basic methods for growing bacteria.

Agar plates

Agar plates provide a convenient way to keep an readily available isogenic stock of bacteria. They consist of a shallow petri dish (diameter = 90 mm, height = 15.9 mm) filled with agar, supplemented with growth medium, on which individual bacterial cells grow into macroscopic colonies containing cell clones of the original progenitor bacterium. Supplementary ingredients, such as antibiotics, are often added to selectively grow microorganisms.

Agar plates were prepared by mixing 15 g of agar (Oxoid No.3) per 1 l media (typically LB), autoclaving, mixing while hot, and pouring 25 ml into a petri dish. Alternatively, premixed LB-agar was acquired from Biology store staff (made to the same recipe), and microwaved until molten. Each plate was left to cool until the agar solidified and then placed inverted in an oven for 30 min, allowing a small gap in the lid to allow moisture to escape. Spare plates were sealed and kept at 4 °C for up to 4 weeks.

A small amount of *E. coli* was then scraped from a freezer stock and transferred directly into 5 ml LB, and incubated for $\approx$ 16 h overnight in a shaking incubator (37 °C, 200 rpm). The culture, now in stationary-phase, was streaked onto an LB agar plate (1.5 %) as shown in Fig3.1, sealed with plastic paraffin film (or placed in an airtight container) and incubated inverted in a static incubator at

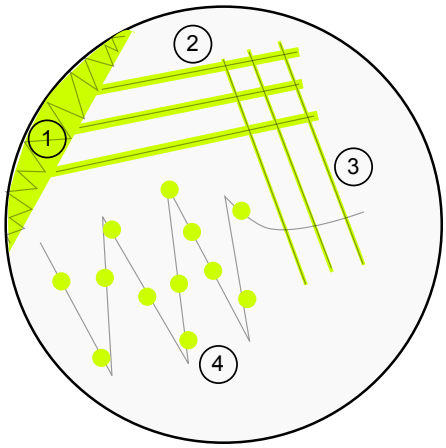

Figure 3.1 Illustration showing the steps in streaking an agar plate (black lines) to obtain small (diameter $\approx$ 2 mm) isogenic starter colonies, as described in [31]. Step 1: using an sterile inoculation loop, scrape a small amount of freezer stock and wipe into a corner of the agar plate. Flame the loop to sterilise. Step 2: Streak three parallel line starting from the reservoir created in step 1. Flame the loop. Step 3: Streak another three lines, this time at 90°, and making sure the loop passes through each of the previous three lines. Flame the loop. Step 4: Streak one line through the three made in step 3, again at 90°, before creating a zig-zag pattern. Green lines show confluent bacterial growth, and green circles the individual colonies expected after incubation.

37 °C for 24 h. The following day, the agar plate was studied for growth and single colonies. If colonies were visible, the plate was stored inverted at 4 °C for up to one week, whereupon a fresh plate was made. This precautionary measure minimised the risk of spontaneous mutants emerging and introducing systematic uncertainty into expected cell behaviour.

Starter Cultures

In order to generate bacterial cells for our experiments we used the following protocol. A small, single colony (as shown in Fig. 3.1, step 4) was picked from an agar plate, and used to inoculate 5 ml of media contained in a plastic falcon tube; the type of media chosen depended on the experiment to be performed. The sample was incubated with shaking (37 °C, 200 rpm) for 16 h overnight. The next day, a 1/1000 dilution was performed, typically by inoculating 10 ml of fresh media with 10 µl of overnight culture in a 100 ml capacity glass conical flask. Generally, final batch volumes were $1/10^{\text{th}}$ the maximum volume of the flask, so if larger volumes were required, a 250 ml flask was used, and the respective liquid volumes scaled appropriately. The diluted culture was incubated until the appropriate *optical density* (OD_{600}), a measure of concentration of bacteria in a suspension, was reached for the experiment, typically in the $OD_{600} = 0.1-0.3$ range, where the cells were in the exponential phase of growth. This was achieved by pipetting 1 ml of liquid culture into a plastic cuvette and using a spectrophotometer (Hach Lange DR5000) to measure the amount of incident light ($\lambda = 600$ nm which was absorbed by the planktonic cells; before each measurement, the spectrophotometer was also calibrated by 'zeroing' the readings with a sample of pure media.

3.2.3 Long-term storage

For experiments with bacteria, it is essential to be able to maintain reliable *freezer stocks* of strains, small volumes of concentrate bacterial culture which can be stored for years at −80 °C without degradation, and from which we sample from to start experiments. However, repeated freeze-thaw cycles reduces cell viability, so fresh 'working' freezer stocks were made annually from a further master freezer stock for each strain. Freezer stocks were created from overnight cultures of LB. A falcon tube containing the culture was spun in a centrifuge (3500rpm for

5 min), and the supernatant discarded, leaving a pellet of cells at the bottom of the container. The cells were re-suspended in 1 ml LB-glycerol to prevent the damage of cell membranes by ice crystals (final glycerol composition 30 %), before pipetted into a 1.5 ml freezer tube and stored at −80 °C.

3.2.4 Growth curves

Bacteria growing in fresh batch liquid culture move through three primary phases of growth: the lag phase, the exponential phase, and finally, stationary phase. Cells in each of the three phases can express different genes, and therefore behave differently. The most consistent and rapid growth phase in terms of cell behaviour is the exponential phase, and so almost all experiments were performed on cells in this phase. Here, cells can be thought in the loosest sense as more active compared to the other two phases. Some also distinguish between early, mid and late exponential phases, which highlights the importance of consistency in the OD used between experiments. For example, in *E. coli*, genes which are regulated by Fis (a protein) have been shown to have different expression patterns at early, mid and late regions of the exponential phase [32].

To check the fluorescent strains used in this thesis were not conferred a relative disadvantage by expressing a different fluorescent protein, optical densities of liquid cultures were measured in time using a plate reader. From these, it was found the growth rates during the exponential phase for each strain were the same regardless of the media type used - a representative growth curve for each strain in M9 + glucose + CAA is shown in Fig.3.2. From this, we conclude the expression of either YFP or CFP in our strains did not confer a disadvantage over the other.

3.2.5 Antibiotic resistance

Strains were tested for their antibiotic resistances to check viability, and to investigate their minimum inhibitory concentrations (MIC). Starter cultures for each strain were grown in LB overnight without antibiotic. Each culture was inoculated into a 96-well plate, where each well held a different antibiotic type and concentration, and grown for 20 h at 37 °C with shaking (200rpm), whereupon

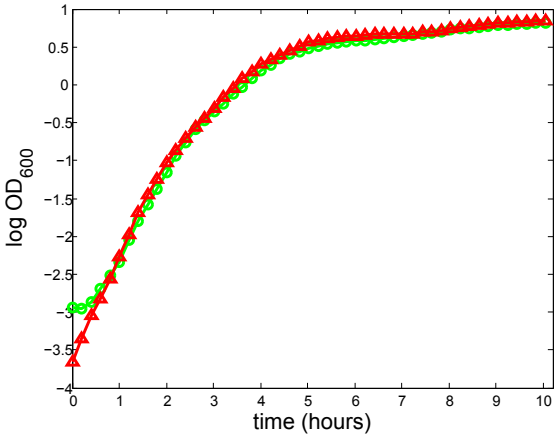

Figure 3.2 Growth curves for RJA002 and RJA003 growing in M9-glucose + CAA. Doubling times (g) during the exponential phase were measured from linear least square fits as $g_{\mathrm{RJA002}} = 40\,\mathrm{min}$ and $g_{\mathrm{RJA003}} = 38\,\mathrm{min}$.

final optical density measurements were made at 600 nm (OD_{600}).

Fig.3.3 shows the final OD_{600} for each antibiotic-strain-concentration combination. The wild-type (MG1655) showed low resistance to each of the three antibiotics tested, with an MIC $\approx 2\,\mu\mathrm{g\,ml^{-1}}$. RJA002, which carried the chloramphenicol resistance gene, showed resistance up to a maximum concentration $\approx 125\,\mu\mathrm{g\,ml^{-1}}$, and low resistance to each of the other two antibiotics (MIC $\approx 2\,\mu\mathrm{g\,ml^{-1}}$). RJA003, which carried the ampicillin resistance gene, was tolerant to high ampicillin concentrations, although returned lower yields around $500\,\mu\mathrm{g\,ml^{-1}}$, suggesting the maximum concentration was being approached. A low MIC of $\approx 2\,\mu\mathrm{g\,ml^{-1}}$ was measured for both chloramphenicol and streptomycin, however. These results showed the strains all behaved as expected, with RJA003 apparently better able to cope at the higher end of its resistance type.

3.3 Agarose Pads

In order to image growing bacterial colonies under a microscope, cells needed to be mounted. Therefore, agarose was used to create small surfaces on which individual bacterial cells were seeded, and allowed to grow into colonies.

Two methods for preparing agarose pads (Fig.3.4) were used, depending on the

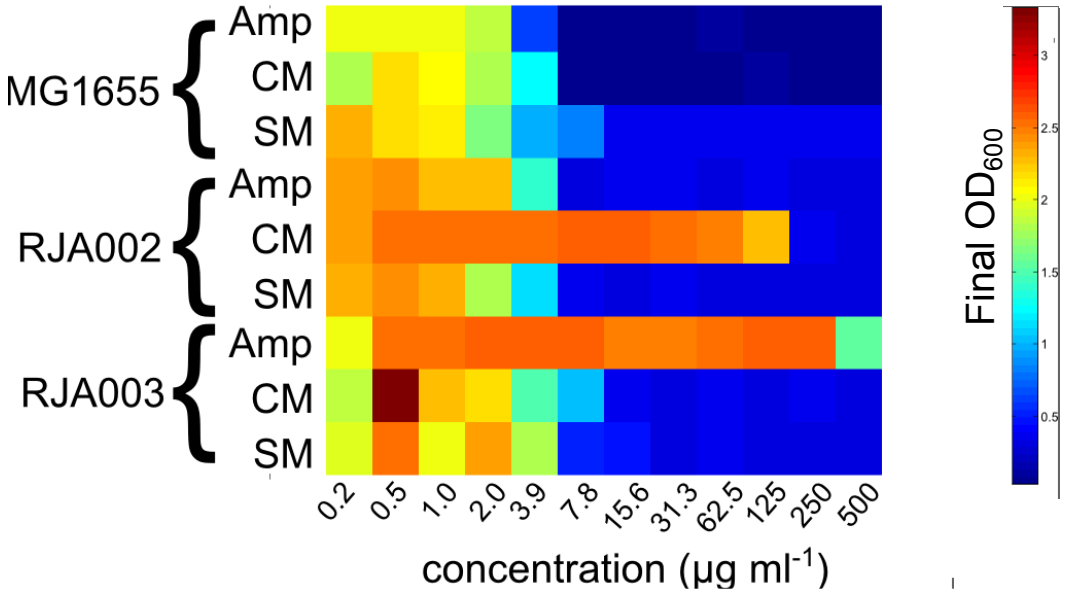

Figure 3.3 Variation of final optical density measurements of cultures of different strains growing in different antibiotic environments, providing suggestions for the respective MICs. Each strain was grown overnight at 37 °C in each of the concentrations and a final OD measured. Amp = ampicillin, CM = chloramphenicol, SM = streptomycin.

experiment performed. The fundamental difference was scale: for longer term growth with relatively low densities of cells, a thicker pad of agarose was used. For short term, or high cell density experiments, a thinner pad was used. Where possible, a thinner pad was preferred because it produced samples which were more robust. Furthermore, they were quicker to prepare, which meant more samples could be constructed when working to tight schedules in the lab.

3.3.1 Thin pads

Thin pads (Fig.3.4(a)) were typically 5 mm in width, 17 mm in length and 0.25 mm thick. To prepare them, the appropriate mass of agarose powder was weighed out and added to a falcon tube; *e.g.* for 3 % (w/v) agarose, 0.3 g agarose was measured). 10 ml media was added, and briefly vortex-mixed to break up large clumps of powder. The falcon tube lid was loosened, and the tube microwaved on the lowest power setting for 20 s bursts. In between each cycle, the powder-liquid mixture was gently swirled to ensure everything was evenly heated.

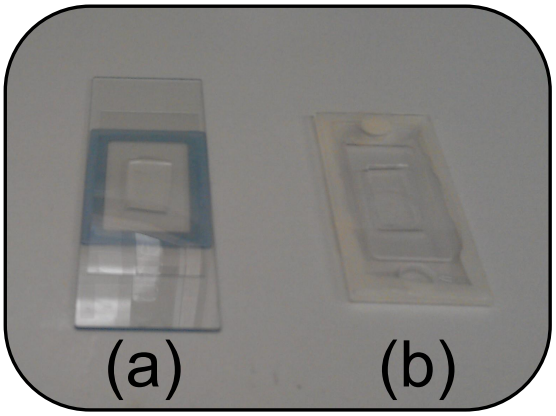

Figure 3.4 Examples of the set-up for thin and thicker agarose pads. (a) A thin slab sitting in the centre of a geneframe attached to a glass slide. (b) A thick slab, showing a perspex frame attached to a slide and sealed with VALAP (the opaque substance).

Once the mixture was clear to the eye and there were no unmelted pieces, the falcon tube was placed in an 80 °C water bath for up to 1 h so any bubbles from the heating process could disperse.

Next, a "Gene Frame" (Thermo-Scientific [1]) was applied in reverse to a standard glass microscope, creating a very shallow cavity approximately 250 µm deep.

The molten agarose was gently mixed using a sterile pipette tip to ensure a homogeneous solution, and a small amount poured into the cavity. A pre-cleaned microscope slide was quickly placed over the molten agarose to flatten it and left to cool, creating a 125 µl slab. After 5 min, the slide was carefully slid off, the agarose trimmed to the required dimensions and allowed to air dry for a further few minutes. A Petri dish cover was used to shelter the agarose from dust or other contaminants. Typically, three separate pads could be fit onto one slide.

3.3.2 Thick pads

Thicker pads (Fig.3.4(b)) were used for experiments requiring bacterial growth longer than 8 h, or if a high cell yield for low inital cell denisty was needed. This was so enough nutrients were present in the medium to ensure near-steady-

[1] Designed for in-situ PCR analysis, these double-sided adhesive consumables function as excellent structures for creating a very shallow cavity: http://www.thermoscientificbio.com/plastic-consumables/gene-frame/

state growth, and pilot experiments showed they tended to survive longer periods in incubation chambers. The approach was conceptually similar to the method described in §3.3.1.

To create the pads, a small rectanglular frame was drilled out a thin perspex block (outer dimensions, 55 mm x 25 mm x 2.4 mm; inner dimensions, 33 mm x 10 mm x 2.4 mm). The frames were soaked in disinfectant (Virkon) and kept in an airtight container until use.

Before an experiment, the frame was sterilised again by rubbing the surface with ethanol. The frame was then lightly secured to a microscope slide by first applying a thin layer of petroleum jelly to one side of the frame, and firmly sticking it down. Next, molten agarose (prepared as described in §3.3.1) was poured in and a clean microscope slide placed over the top to create a flat surface. After 10 min, the slide was gently slid off, and the agarose surface allowed to dry for a further 5 min. If agarose strips were required, they were cut to shape using a sterile scalpel.

After the inoculum was applied and allowed to dry under a petri dish, a glass coverslip was gently placed over the top. Air bubbles would often appear in the centre of the pad if the coverslips were not cleaned beforehand, so it was very important to ensure one side of the coverslip was always pointing down to reduce the risk of contaminants. If air bubbles did appear, the slide was discarded and another attempt made until a satisfactory result achieved.

Normally, petroleum jelly or nail varnish would be used to seal the coverslip. However, the former was found not to be robust enough to withstand long incubation periods, while the latter often proved toxic to the growing cells. Therefore, VALAP [33] was applied instead using a cotton bud to the glass coverlsip edges and where the frame met the micrscope slide. It was made by mixing equal proportions of petroleum jelly, paraffin wax, and lanolin. The advantages of VALAP were that it solidified on contact with the glass, and is biologically inert. Care was taken not to expose it to temperatures greater than 40 °C, beyond which it melted and could vaporise, leading to wide spread contamination of delicate glassware. Despite this, it proved a very convenient means of creating a sealed small scale incubation chamber for the surface growing cells, that could withstand periods in dry incubation environments in excess of the times used in this thesis (*i.e.* over 16 h).

Chapter 4

Microscopy Background

4.1 Introduction

Microscopy was used extensively in these projects. Three different microscopy techniques were employed: phase contrast, fluoresence and confocal microscopy. In conjunction with these, we used high precision raster scanning and time-lapse imaging.

The microscopes used in these projects were a Nikon Ti epi-fluorescent inverted microscope, Nikon E800 epi-fluorescent upright microscope, and a Zeiss Observer.Z1 inverted microscope (plus Zeiss LSM 700 scanning system). The Nikons had custom made incubation chambers (Solent Scientific) in order to grow bacteria at well-controlled temperatures, and so these were used for growth experiments. The confocal microscope was used for detailed, but time-static,

Brand	Magnification	Type	Corrections	Immersion	NA
Nikon	$100x$	Ph3	Plan-fluor	oil	1.3
	$100x$	Ph3	Plan-fluor	oil	1.4
	$20x$	Ph2	Plan-fluor	dry	0.5
	$20x$	DIC	Plan-apo	dry	0.75
Zeiss	$63x$	Ph2	Plan-apo	oil	1.4
	$63x$	Ph2	Plan-fluor	dry	0.75
	$40x$	Ph2	Plan-fluor	dry	0.6

Table 4.1 The objectives used in this thesis.

Microscope model (type)	Camera (manufacturer)	Pixels	Pixel size (µm × µm)
Nikon Ti (inverted)	CoolSNAP HQ2 (Photometrics)	1392 × 1040	6.45 × 6.45
Nikon E800 (upright)	Retiga-2000R (QImaging)	1600 × 1200	7.4 × 7.4

xy - stage	z-control
Prior H117	Physik Instrumente (PI) PIFOC Nanopositioner
Prior H101	H122 fine focus motor (Prior ProScanII)

Table 4.2 Summary of the stages and cameras used in this thesis.

3d imaging at room temperature, since it did not have incubation facilities. The microscope objectives used in these projects are summarised in Tab.4.1 - complete enclosure of the microscope by the incubation chambers meant that objectives and immersion oil (where used) were the same temperature as the sample and other optical components. Either MetaMorph, or MicroManager were used to control the microscope components. The CCD cameras used were a CoolSNAP HQ2, and QImaging Retiga-2000R (Table 4.2).

For fluorescence studies using the YFP and CFP expressing strains RJA002 and RJA003, the relevant excitation light wavelengths were provided by a broad spectrum Mercury lamp in conjunction with Chroma EYFP (part 49003, λ_{ex}=500 nm, λ_{em}=535 nm) and ECFP (part 49001, λ_{ex}=436 nm, λ_{em}=480 nm) filter sets respectively. Motorised Prior Scientific xy stages were also used, with linear encoders to compensate for mechanical backlash; this facilitated a high degree of scanning precision. Time-lapse experiments were automated by using the motorised stage and software auto-focus routines (in the case of MicroManager, the 'Oughta-Focus' algorithm; MetaMorph had a single auto-focus function), and z-movements by either piezo-actuated z-scanners, or motor driven fine-focus control (Table 4.2). For raster scanning of agarose surfaces, auto-focus was often not feasible, so stage movements between coordinates were manually selected and z-positions manually focused.

4.1.1 Microscopy principles

Fundamentally, a microscope is used to obtain images that are too small to see with the naked eye. To achieve this, it is necessary to resolve points which are close together and avoid optical distortions. These requirements are satisfied

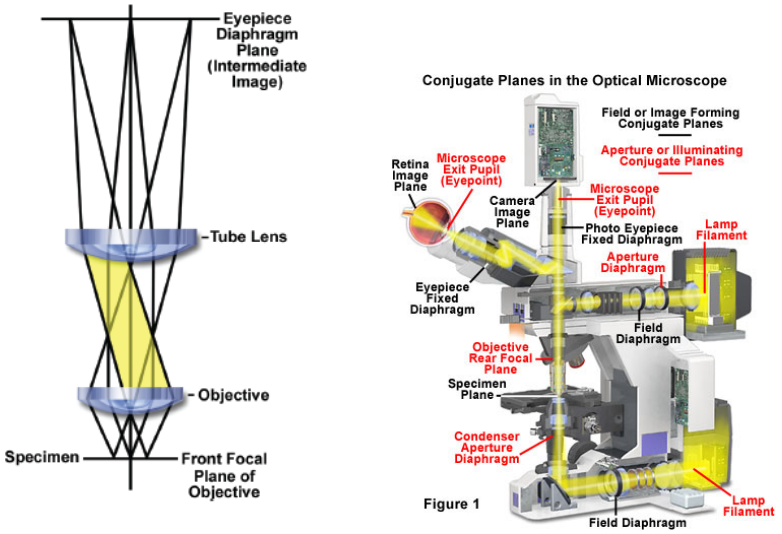

(a) **(b)**

Figure 4.1 Schematic of a basic microscope system which exploits infinity optics. Light emerges from the condenser lens (not shown) and passes through the sample. Light is collected by the objective, where the outgoing light rays are now parallel (*i.e.* focused at infinity). These are converged onto the intermediate imaging plane by the tube lens. (b) Cartoon of a Nikon E600 upright microscope (conceptually similar to the Nikon E800 used in this thesis), showing the various light paths and position of components. Both taken from [34].

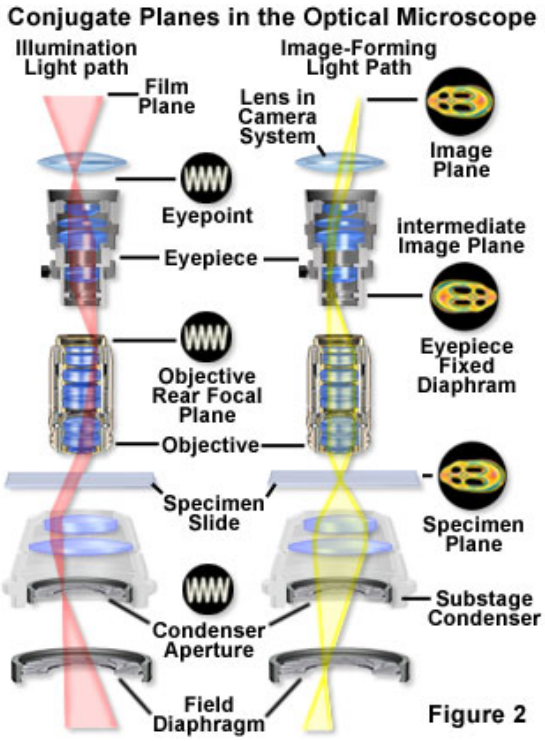

Figure 4.2 A ray diagram in an upright microscope which has been Köeler-ed, showing the illumination planes (left) and imaging planes (right) are conjugate to each other; that is, when one is in focus, the other is out of focus; *e.g.* consider the ray at the condenser aperture and specimen slide positions above. Taken from [34].

using a series of lenses (condenser lens, objective, and tube lens), through which the light path travels through the sample and to the eye piece. The basic steps are thus: light passes through a condenser lens below the specimen, before passing through the specimen itself. The light is collected by the objective, and after passing through the tube lens, is focused at the diaphragm plane (Fig. 4.1(a)). Collectively, this is an example of an infinity-optics system, since the flux of rays leaving the objective are parallel, and would focus at infinity were it not for the tube lens. Doing so allows the distance between the objective and object to vary without changing the distance from detector to objective [35].

Microcopes fall into two main structural classes: up-right and inverted; an example of an upright microscope is shown in Fig. 4.1(b). Both types were used in experiments presented in this thesis, with the main distinguishing feature between them that samples on the inverted microscope are placed "upside-down" compared to those on an upright microscope.

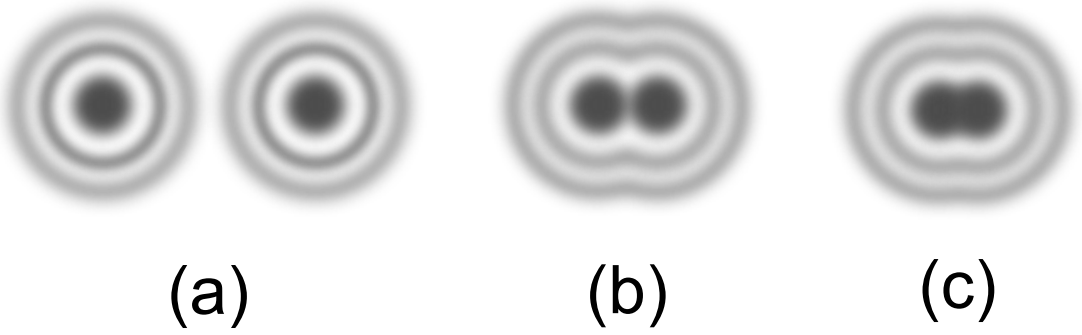

Figure 4.3 Illustration showing the importance of resolution when distinguishing between two objects. Point sources of light manifest as diffraction patterns (known as Airy disks) at the intermediate image plane, resulting in the point source spreading out over multiple fringes. In this example, two adjacent Airy disks are shown to be (a) resolved, (b) at the resolution limit, and (c) unresolved.

The objective lens is one of the most important components of a microscope. Different objectives are required to achieve different levels of magnification, but it is important to consider that different objectives are subject to distortions. Corrective optics within the objective mitigate many of these aberrations, but often at the expense of light flux. Therefore, careful consideration is given to each objective used.

4.1.2 Illumination Plane

To fully understand how a microscope works, we must address the imaging and illumination planes, which must be conjugate to one another (*i.e.* one must be maximally unfocused when the other is focused, and *vice versa*) at specific points along the light path if a high quality image, with uniform illumination, is to be formed.

Consider a light filament which illuminates the sample: it has discrete regions of higher and lower intensity arising from its coil structure, which can lead to artefacts (darker or brighter regions) in the final image. By ensuring the lamp filament is maximally out of focus at the specimen location on the light path (achieved by adjusting the positing of the condenser lens), the discrete variations in the light filament are smoothed out, uniformly illuminating the sample (Fig. 4.2) [35].

Doing so means that any variations in the intensity of the image can be associated with the object (real information), and not systematic uncertainties introduced by the light source [35]. Not only are artefacts reduced, conjugate planes allow a degree of control of resolution and contrast via the field and condenser diaphragms [34, 35]. The process by which the differences between imaging and illumination planes are emphasized was developed by August Köelher [34], and to this day, a user is said to 'Köeler' the microscope before imaging. A detailed step by step process to Köeler-ing can be found in [35].

4.1.3 Resolution limits

Resolution in an optical microscope is arguably the most important feature to consider when imaging a sample. Essentially, resolution is the shortest distance between two points which can be distinguished from each other, which is clearly very important when imaging objects at the micrometre scale, such as bacteria. The limiting factor is driven by diffraction: light passing through a sample will form a diffraction pattern at the intermediate image plane, spreading the information about the object out over multiple orders, making it unsharp.

The simplest example of this phenomenon is a single ray of light broadcast from a point source and passing through a pinhole, where the resulting diffraction pattern of concentric rings is known as an Airy disk (Fig.4.3)(a)). As the distance between the two point sources is reduced, we begin to approach the resolution limit, until we can no longer tell one point source from another (Fig.4.3).

To improve image resolution, an objective must capture as many of these diffraction fringes as possible. In practice, this means maximising the width of the cone of light which is carried to the lens from the sample. Fig 4.4 shows this is achieved by increasing the *numerical aperture* (NA) of the objective, a dimensionless number which characterises the width of the cone of light collected from the object. In turn, there is a dependence on the refractive index n of the medium residing in the gap between glass coverslip and objective, which taken together, we can say:

$$\text{N.A.} = nsin\theta \tag{4.1}$$

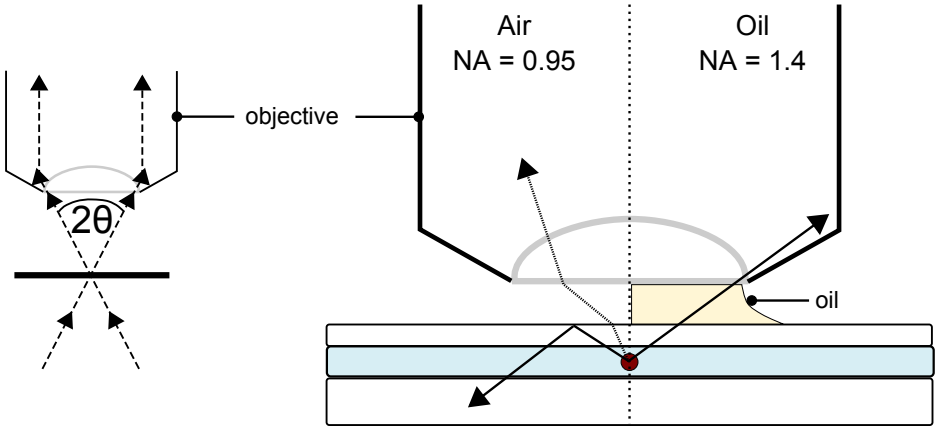

Figure 4.4 Schematic illustrating the effect of using an oil immersion objective on an objective's maximum light cone width (2θ). Total internal reflections limit the width of the available light cone, but index-matching the air gap with the glass coverslip and lens with immersion media means wider cones of light are possible, thus increasing the objective's NA.

where θ is the maximum angle of the incident light ray into the objective, measured with respect to the normal. Fig.4.4 shows that θ also depends on the distance of the objective to the sample, as well as the objective lens' diameter.

The resolution is given by:

$$r = \frac{0.61\lambda}{N.A.} \tag{4.2}$$

where λ is the illumination wavelength, and from which we can determine the resolution limit for a conventional microscope is $\approx$ 200-300 nm, considering the range of λ for visible light (λ =380 nm-750 nm) .

For 'dry' objectives, an air gap exists between the sample and objective's front lens. This limits the maximum NA which can achieved, since the change in refractive index leads to refraction of the light ray (Fig 4.4) as it exits the glass coverslip. The ray will tend away from the normal, and so only a small range of light cone widths are possible before light can no longer enter the objective (Fig.4.4). However, by introducing a medium into the air gap which is index matched with the glass coverslip ($n_{\text{oil}} = 1.515$) means refraction can be minimised (Fig 4.4). For a dry objective, $\text{NA}_{\text{max}} \approx 0.95$, while for an oil-immersion, $\text{NA}_{\text{max}} \approx$ 1.4. Using an oil-immersion objective therefore allows larger NAs, and from Eqn.

4.2, better resolution. Not all objectives are suitable for oil-immersion, however. Some require larger gaps between it and the coverslip (particularly lower powered objectives), and so it is impractical to introduce fluid into the air gap, since it relies on capillary forces to hold it in place. Furthermore, some samples are sensitive to the immersion media, so a dry objective is preferred, despite the drop in image quality.

4.1.4 Phase-contrast

The simplest microscopy technique (brightfield) relies on different amounts of light absorption in different parts of the sample in order to provide contrast so it can be distinguished from the background light. Bacteria however are transparent, which means alternative microscopy methods, such as phase contrast, must be used to heighten contrast between cells and the background.

Phase contrast microscopy is a non-destructive imaging technique developed by Frits Zernike in the 1930s [35]. It allows transparent specimens (such as bacteria), which would otherwise be near invisible in conventional bright field microscopy, to be seen clearly by translating phase shifts in the light passing though the specimen into variations in light intensity. In the case of *positive* phase contrast microscopy as described and used here, this results in *E. coli* cells (which have a higher refractive index than the surrounding media) appearing as lower regions of intensity (*i.e.* dark) against a bright background.

The underlying principle in phase-contrast is to separate the light which is scattered by the object from the non-scattered background light by exploiting phase shifts and path length differences of the light rays by inserting a 'phase-plate' into the objective (Fig.4.5). First, the phase of scattered light is naturally retarded by $\lambda/4$ through its interaction with the object, leading to an overall phase difference between scattered and non-scattered light. The phase plate then advances the background light phase by $\lambda/4$, increasing the overall path length difference to $\lambda/2$. Finally, when the two types of light interfere with each other at the image plane, the object being imaged is manifested as regions of low intensity. To improve contrast, the amplitude of background light is also reduced by $\approx 70\%$ to ensure better destructive interference using a gray filter ring [35].

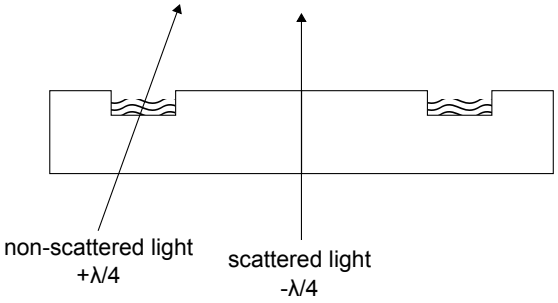

Figure 4.5 Illustration of a phase plate acting on incoming background ('non-scattered') and object light ('scattered'). The background light ray's phase is advanced $\lambda/4$ relative to the scattered light (which has already been retarded by $\lambda/4$ during its interaction with the object) by a ring etched into the phase plate. The ring also reduces the intensity of the background light, furthering increasing the contrast between the two types of light. Illustration based on [35].

4.1.5 Fluorescence

In contrast to bright-field and phase contrast microscopy which rely on sample-specific absorptions of light and path length differences, fluorescence microscopy is a conceptually more straightforward process. Here, excitatory light impinges on the sample, and specific molecules present in the sample react by emitting light at a different wavelength in a process known as fluorescence. Briefly, in this process, electrons in the fluorescent molecules are excited to higher energy levels by the incident light, but rapidly collapse back to their original ground state. In doing so, they emit a photon which has a longer wavelength than the excitation photon, by a process known as Stokes shift. This light is then filtered out from the high intensity incoming light, resulting in an image where the object imaged is highly contrasted with respect to the background.

Fig 4.6 depicts the key component used in a fluorescent microscope: the filter cube. First, excitation light from a spectrally broad arc-discharge Mercury lamp is passed through a filter to select the excitation wavelength of choice. The light is guided towards the sample via a dichroic mirror and the microscope objective (which effectively acts like a condenser lens), and onto the sample. Most of this light passes straight through, but any emitted fluorescence, and reflected excitation light, travels back up the objective. The dichroic mirror directs the majority of reflected excitatory light back to the light source, and the fluorescence light is allowed to pass. A final filter allows this light to pass, and to screen out

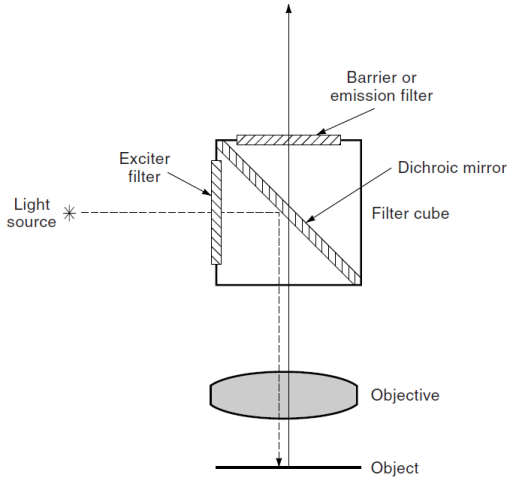

Figure 4.6 Schematic of a dichroic mirror used in fluorecence microscopy studies

any last excitatory light that still exists. Such an arrangement, where the light source and objective are on the same side of the sample, is referred to as an *epi-illuminator*, and microscopes which exploit it as 'epi-fluorescent'.

The main advantage of fluorescence microscopy exploited in these experiments are the low noise, high contrast images which are obtained. For image analysis purposes, they are generally superior to phase contrast images. However, fluorescence molecules are sensitive to prolonged exposure or high intensity light, which can destroy them in process called photo bleaching, meaning that fluorescence imaging over long periods may be impossible. Furthermore, repeated exposure of cells to excitation light can induce harmful chemical reactions which damage the cell (phototoxicity). These constraints can be mitigated by, for example: increasing camera pixel bin counts, testing minimum exposure times, and restricting the irradiated area to the field of view. Light source choice is important too: Mercury lamps, can suffer from day to day variations in power (necessitating controls between experiments), which is problematic for quantitative fluorescence studies, while LEDs or lasers are more consistent (but are more expensive). Finally, many compounds naturally fluoresce (auto-fluorescence), and so the media used to image bacteria in should be carefully chosen to limit background fluorescence as far as possible. An example is LB, which is a poor choice of media for fluorescence imaging.

4.1.6 Confocal

As detailed in the previous section, fluorescence microscopy can produce highly contrasted images. However, these images contain fluorescent light from other focal planes being imaged. Consequently, the fluorescent image can suffer from high background levels, or image distortion. The thicker the sample being imaged, the more light which leaks in from other focal planes, resulting in a noisy image.

Confocal microscopy is a imaging technique which addresses this problem of stray light. The key component is a pinhole situated at the image plane: an opaque piece of material with a small hole cut out of it which blocks the out of focus light diffusing from other focal planes, but allows light in from the image plane. By reducing the extent to which out of plane light reaches the detector, image fidelity is improved.

The basic steps are as follows. Most confocal systems operate in an epi-illumination set-up, as explained in the previous section. Excitation light is provided by diode lasers, which is guided through the objective and onto the sample as a very intense, diffraction limited spot [35]; the spot is traced along the field of view using a galvanometer mirror in a raster pattern. Returning fluorescence light passes back through the objective, and focuses at the image plane consummate with the pinhole diameter (so out of focus light is blocked). The light travels to a photo multiplier tube (PMT), which based on the photon flux, returns different voltages to the computer, which in turn digitises the signal and builds an image. Depending on the image being sampled, the user can vary aspects such as pixel dwell time, scanning speed, image size, and PMT voltage gains, to produce the best possible image.

The main advantage of a confocal image is the high resolution and high contrast image. Also, because individual planes can be clearly imaged, a 3d reconstruction of the object is possible, adding a new dimension to image analysis. However, the time needed to image one plane is much longer compared to a conventional fluorescent microscope. The intensity of the illumination laser beam also leads to rapid photobleaching; moreover, because the illumination beam passes through the entire sample, sections of the sample not currently being imaged will suffer photobleaching. The issue of long exposure times is compounded by the fact the pinhole blocks much of the light, but while expanding the pinhole will reduce

exposure times, it is at the expense of resolution.

4.2 Time-lapse microscopy

Time-lapse microscopy is a powerful method for longer term observations of bacterial growth, and following the appropriate image analysis steps, yields information about the growth dynamics of early and late colony development. Time-lapse movies were made of colonies at a variety of scales, from tracking single cell growth in colonies consisting of less than 700 cells, and lower resolution movies of colonies approaching 100 µm in diameter, containing tens of thousands of cells. Any differences between the two will be addressed in the relevant chapter. Here, I will detail the general steps required in both instances - a useful guide can also be found in [36].

All time lapse experiments were performed on epi-fluorescent microscopes using a combination of phase contrast and fluorescence microscopy. Prior to imaging, the incubation chamber were brought to temperature at least 4 h prior to the experiment; in most cases, they were preheated the night before. In addition, if fluorescence microscopy was used, the Hg lamps were ignited at least 30 min before the experiment. If oil immersion objectives were used, the immersion media was also preheated at least 4 h in advance.

Samples were prepared as described in §3.3 and placed on the microscope stage. Cells were located in phase contrast by first identifying coverglass defects or dust. The objective was gradually stepped in until the agarose surface came into focus; from here cells were located. The microscope was next Köeler-ed as described in §4.1.2. After 15 min, cell positions were saved into the acquisition software - the delay was necessary to ensure the sample temperature had matched the incubation chamber's temperature since during this period, the sample was found to undergo significant drift.

Next, exposure times and wavelengths were set. Fluorescence exposure times were determined by trialling a sensible range on an test area of the sample until a low noise, high contrast image was obtained. If multiple fluorescence wavelengths were used, the longer wavelengths were obtained first. Time intervals for each frame depended on the experiment, but upper limits on temporal resolution were

determined by photo-bleaching, and the number of locations to be imaged: for example, for 10 locations, and a total acquisition time of 5 s (including stage travel) limited resolution to one frame a minute before photobleaching effects were considered.

Autofocus, when used, were software controlled in all experiments. z-steps were driven by either a piezo collar mounted on the objective carousel (Nikon Ti), or a motor driven fine focus control (Nikon E800). The latter set-up was more reliable, and the software (Micromanager) allowed more control options. For reliable auto-focus experiments, the auto-focus field of view (AF-FOV) was always restricted to the sub-area of interest to avoid defects elsewhere causing the software confusion. Edge-detection algorithms were generally appropriate for phase contrast images, while maximum intensity options were used for fluorescence (albeit rarely). As the experiment progressed, the AF-FOV was increased as appropriate to ensure the edge of the object were always passed to the AF programme.

4.3 Single Cell Tracking

4.3.1 Schnitzcells

In order to quantitatively analyse time lapse movies of growing colonies at the single cell scale, MATLAB software written by the Elowitz lab (Caltech) [29, 36] was used extensively. The '*Schnitzcells*' software extracts morphological information on each cell segmented (such as its length, angle or position within the colony), as well as quantifying the level of fluorescence expressed. While the process is largely automatic, the user is given the capability to manually correct the tracking process at various points in the workflow (Fig. 4.7).

4.3.2 Workflow

Process

Cells are segmented using a combination of edge detection, thresholding and watershedding to identify single cells, and discriminate between cells which have

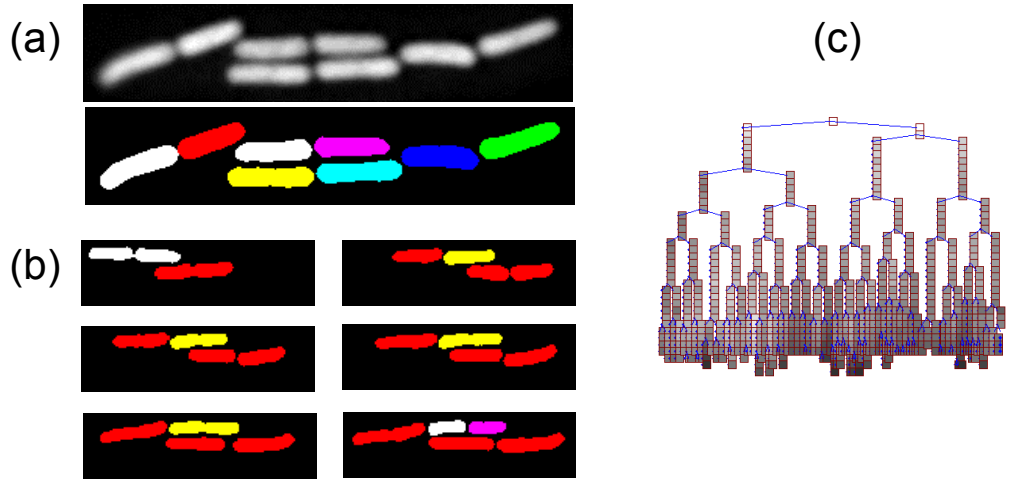

Figure 4.7 (a) A fluorescent image of *E. coli* cells and its corresponding mask, following cell segmentation. The different colours denote different cells. (b) A time-lapse cell lineage tracked across several frames, from birth (white cell) to division (white and pink cells), with the relevant cell highlighted yellow in intermediary frames. (c) A genealogy tree of a microcolony which grew from a single cell to 86 cells in ≈ 240 min. Each of the 185 lineages have been linked to form a complete structure of any given cell's ancestors or descendants.

recently divided or are in the process of doing so. A mask of the original image is then created, and artefacts filtered out using certain segmentation parameters (such as mass thresholds) (Fig. 4.7(a)), the choice of which depend on the type of organism imaged, and the individual experimental conditions at the time. As each cell is assigned its own binary mask, the software performs backbone-fitting, which provides a reasonable estimate of cell width and length, and its orientation within the colony.

The masks are then passed to Schnitzcells' tracking algorithms, which attempt to minimise the distance between cell centre of masses in successive frames. Individual lineages are created by identifying the frame where a cell was born, and following it until it divides; at this point, the cell lineage has ended (Fig. 4.7(b)). The final data output consists of a collection of lineages which describe the colony in its entirety from birth to final frame. Pointers within each lineage link 'daughters' to their 'mother' cells, which allow the complete genealogy of any cell in the time-lapse movie to be explored (Fig. 4.7 (c)). A summary of the functions written to exploit these features for the purposes of this thesis are presented in Appendix A (p.175).

Implementation

Fig.4.8 demonstrates some of the advantages of the software, as well as the drawbacks and other idiosyncrasies. For example, Schnitzcells was consistent at low cell densities in determining when a cell divided, but as the colony grew to above 100 cells, divisions were either missed, or pre-empted at high frequency, necessitating manual corrections. However, the built in manual correction GUIs made correction processes straightforward, if time consuming. Furthermore, because average cell sizes tended to get smaller as a colony reached high population levels, fewer pixels described each cell. This meant the error associated with the length, width, and other quantitative measures associated with a cell mask increased. Therefore, the higher image quality, the better.

Schnitzcells had the flexibility to segment either phase contrasts or fluorescent images. The former, as a non destructive imaging method, was the initially preferred option. However, fluorescent movies were almost always exclusively used as the input images because fluorescent segmentation routines were found to have a much higher success rate at correctly identifying cells. While this meant time resolution, movie length and camera bin settings could be curtailed, this was mitigated by quicker image processing times. Phase contrast images were adequately segmented until cells within the colony began to be harder to resolve due to crowding, or when halo artefacts surrounding the cells became too numerous to correct.

Images almost always required pre-processing before being handed to Schnitzcells. Generally, this involved background subtraction, Gaussian smoothing, or applying unsharp masks.

Overall Schnitzcells proved to be a powerful tool in extracting cell information from time-lapse movies. However, additional functions were written in Matlab in order to obtain the data used in this thesis. These included functions to re-order data into a frame-by-frame format, rather than lineage format, recursive functions to link any two cells in the genealogical tree, and error checking functions to identify orphaned or barren cells which could be corrected. A summary of the functions written, and the order they were implemented as part of typical workflow are found in Appendix A.

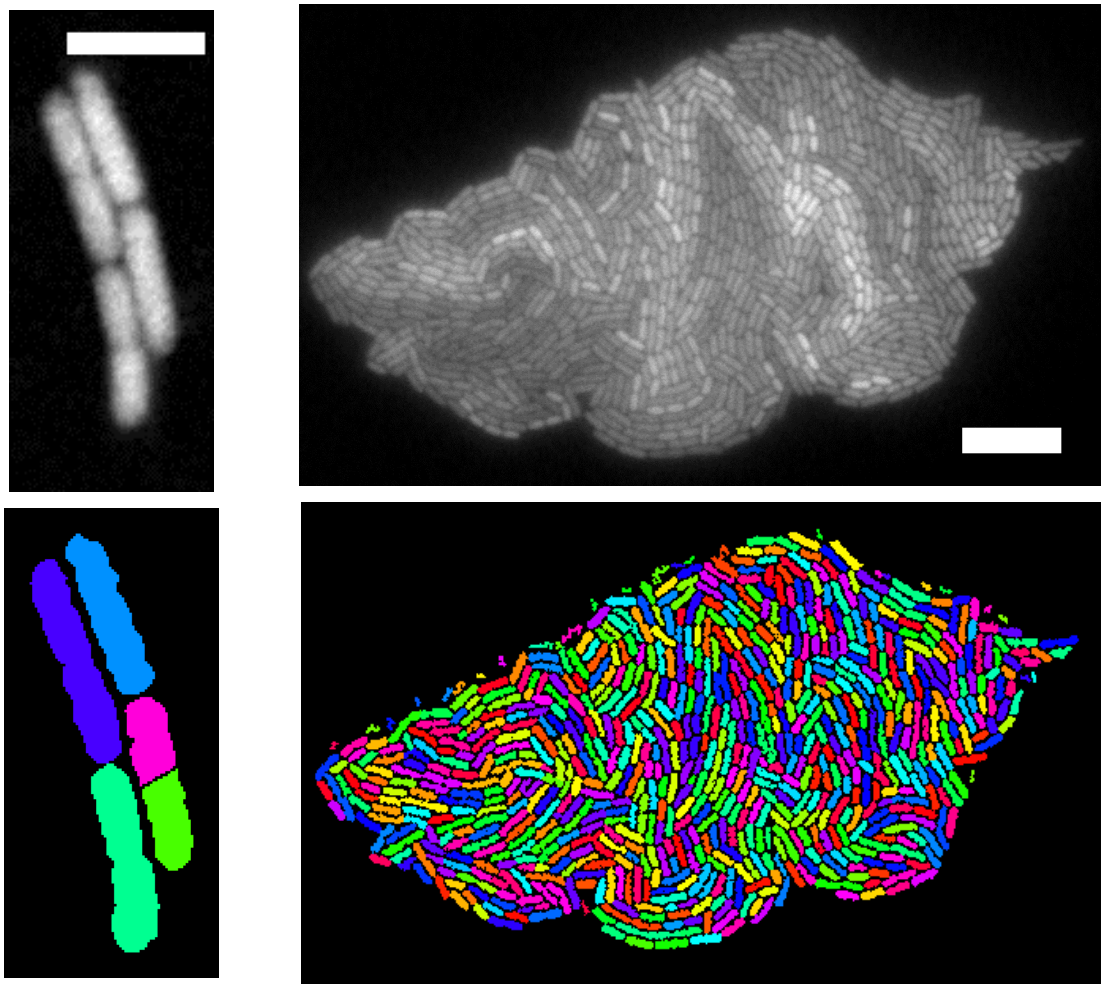

Figure 4.8 Fluorescent microscopy images of colonies and their respective cell masks, illustrating problems associated with the Schnitzcells software package. (a) Cells could often be mis-cut when Schnitzcells incorrectly interpreted one cell as two. This happened more often at high population levels; for clarity, a small colony has been shown here. However, generally, cell masks matched cell morphologies at lower cell populations. Scale bar = 4 µm. (b) Fringing on the outside of colonies resulted in artefacts which were often interpreted by Schnitzcells as bacteria. These could be deleted manually, but one frame could hold hundereds if the image quality was not up to standard. Furthermore, fewer pixels were used to describe cells at high population levels, resulting in higher uncertainty and more manual error checking to ensure cell masks were representative of the cell. In this example, many cells in the colony interior have been mis-cut, or not all. prompting manual editing from the user. Scale bar = 10 µm.

Chapter 5

Competition for space during bacterial colonisation of a surface

5.1 Introduction

This chapter presents an experimental study of a system in which differently labelled populations of *E.coli* bacteria compete to colonise an agarose surface. We use this as a model to investigate the importance of spatial structure and growth strategies between competing organisms.

5.1.1 Ecological implications of spatial structure

In general ecological terms, the spatial structure of an organism's growth environment (a *habitat*) has important effects on population dynamics, population composition and species diversity for a range of organisms, from plants to bacteria [37]. Historically, ecological models have tended to assume that organisms are well-mixed [37], but in reality, habitats are complex, with spatially dependent environmental conditions. This can affect ecological outcomes: for example, the spread of invasive pathogens in woodland has been shown to be dependent on environmental heterogeneity [37–39]. Even in habitats where the environment is homogeneous, interesting spatial effects can arise, such as travelling waves of species coexistence [40, 41] or community self-organisation [42]. The need to

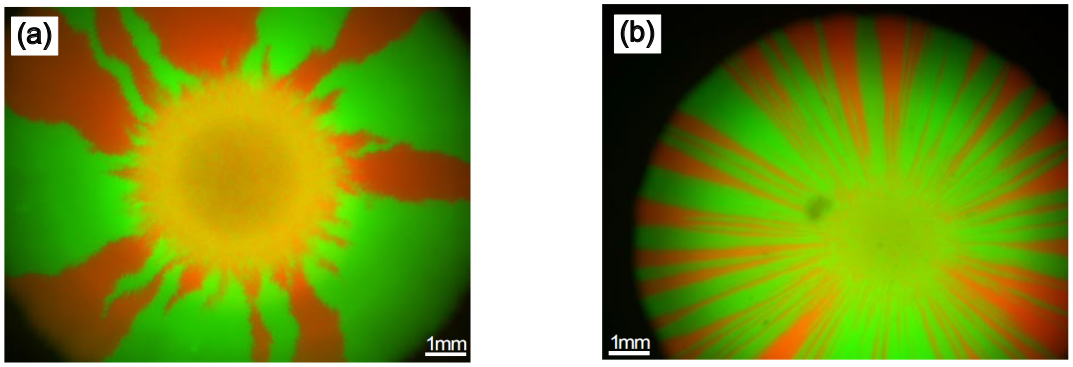

Figure 5.1 Segregation of two fluorescent strains of (a) *E.coli* and (b) the yeast *Saccharomyces cerevisiae*. Random fluctuations in the band of cells at the colony front produce the sectors. Taken from [21]

include spatial effects in ecological models has now become widely recognised, but relatively few experimental systems exist in which their predictions can be tested.

5.1.2 Bacteria as models in ecology

Designing and carrying out reproducible experiments to investigate spatially structured habitats of plants and animals is difficult however, due to the time taken to collect data in the field, and the difficulty in achieving controlled perturbations of large habitats [43]. Bacterial systems provide a potential solution since they can be studied and manipulated under well-controlled conditions in the lab, and they reproduce much faster than plants or animals. Indeed, bacteria have been used in a variety of contexts to test the predictions of ecological and evolutionary theory. For example, using novel growth chambers, the evolution of antibiotic resistance in bacterial communities were tracked and observed to arise very rapidly in the presence of antibiotic gradients in short spaces of time (10 h) [44]. The complex interplay between migratory behaviour and extinction has also been explored using experimental microbial models [45]. These studies provide examples of how bacterial experiments can shed light on larger-scale ecological and evolutionary phenomena.

Recently, an influential set of studies has been carried out in which bacteria are used to model range expansions - the spreading of a population into a previously

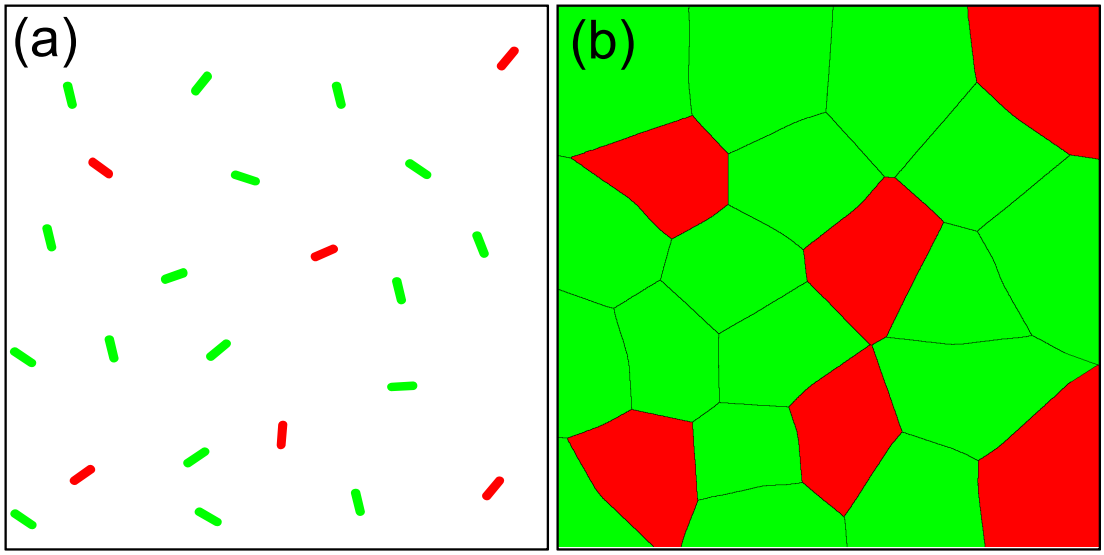

Figure 5.2 A simple illustration of surface competing organisms, as explored in this chapter. (a) There is an initial seeding of the surface by some organisms, and descendants (b) of the these progenitors race via dispersal for the available space.

empty habitat. These studies have been used to shed light on how mutations can arise and become fixed at the edges of an expanding population. Using fluorescent strains of bacteria and yeast, Hallatschek *et al.* [21] inoculated an agar plate with a mixture of two different colours of bacteria (or yeast) and tracked the expansion of the populations outward from the initial 'homeland'. Strikingly, they observed the formation of genetically segregated sectors containing bacteria of all one colour (Fig.5.1). These sectors form because the effective population size at the expanding colony front is small, amplifying the stochasticity of random birth events. From measurements of the wandering interfaces between different genetic domains of the expanding colony front, it was shown that neutral fluctuations at the edges of expanding population fronts could strongly affect the spatial structure and genetic mixing of the population. This is important, because it shows how larger-scale migratory histories might be recorded in the genetics of populations left in the wake of the expansion more generally [21, 46, 47]. These experiments demonstrate the power of experimental microbial systems in general in explaining large-scale ecological and evolutionary behaviour.

5.1.3 Colonisation by scattered populations

In this chapter we describe a set of experiments which are similar in style to those of Hallatschek *et al.*, in that they use two different coloured fluorescent bacterial strains. However, here we study a different case in which an empty habitat is seeded by a scattered population of sessile individuals, which then proliferate in patches and compete for space at collision boundaries (Fig.5.2). In the natural world, this type of proliferation is seen in a multitude of situations. Examples include: proliferation of lichen on rock surfaces [48], 'encrusting' tide pool algae [49], liverwort on bark surfaces [50], and plant populations striving to maximise solar exposure [51].

Ecological theory points to three primary mechanisms whereby neighbouring individuals may compete for space in this scenario. The first is *expansion competition*, which can be summarised as the race to colonise empty space not already occupied by neighbouring organisms [52, 53]. Colonisation in this context could mean the contiguous growth of organic tissue (such as lichen growth), or the placement of off-spring (such as asexual bacterial reproduction) [52]. For organisms undergoing expansion competition, two competing trade-offs contribute to the overall likelihood of success. The first, an 'expansion-survival' trade-off, describes the balance between fecundity (loosely, the organism's reproductive rate) and mortality rate: the expansion rate and death rate of an organism tend to be positively correlated [50, 54]. This operates in balance with the second trade-off: 'accumulation-export', or in other words, the need for individuals to take advantage of local resources and reproduce, while balancing this against dispersing offspring as widely as possible to colonise new ground [53].

The second ecological mechanism which is expected to be at play in the scenarios in Fig.5.2 is *lottery competition*. This refers to colonisation of space which was previously occupied by another organism, but which through the original coloniser's mortality, is now free for colonisation. In this situation, only the neighbouring organisms (or their off-spring) are in a position to colonise the newly freed space, hence an effective lottery decides which will prevail [53, 55].

The third ecological mechanism predicted to be at play involves *boundary interactions* at the patch edges within the habitat, which is referred to as 'overgrowth' [53] or 'dominance control' [56]. These interactions can occur in

a number of different ways, including physically growing over a neighbour, or speeding expansion to undercut the competitor, but the fundamental principle is that they involve gaining control of space from a neighbouring competitor at the patch interface.

The aim of the work described in this chapter is to investigate the relative roles of these ecological mechanisms, for a simple microbial system.

5.1.4 The microbial model system

Following the work of Hallatschek *et al.* [21, 46, 47], we use mixed populations of two fluorescently labelled strains of *Escherichia coli* to investigate competition between physiologically identical, but genetically distinct populations. In contrast to the work of Hallatschek *et al.*, rather than study range expansion, we specifically address the 'homeland', which consists of a scattered population of cells which must compete for local space (patches). In our experimental system, cells are not motile, and dispersal of descendants is purely driven by cell division, and the resultant pushing forces between colony fronts which eventually collide, producing a 'landscape' colonised by contiguous patches of fluorescent bacteria (Fig. 5.3). It is also important to note that cells do not die on the time-scale of our experiments. As a result, this system allows us to probe the relative importance of two competitive ecological strategies previously discussed in scattered populations, namely expansion competition, and boundary competition (we do not observe lottery competition due to the lack of cell death).

The structure of the chapter is as follows. Before each result is introduced, a brief summary of the relevant experimental details are described. The results are then discussed together, along with concluding remarks. Finally, a detailed expansion of the methods and protocols mentioned throughout the results are presented at the end of the chapter.

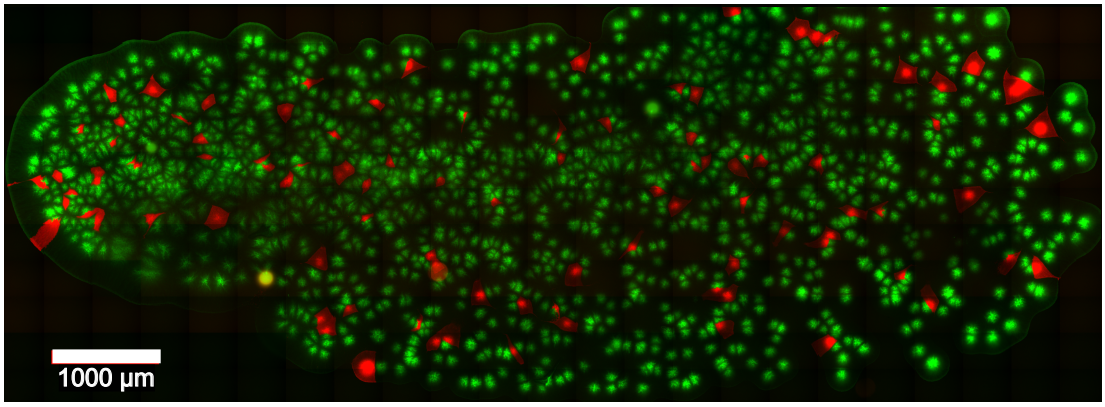

Figure 5.3 A fluorescence montage image of a colonised slab of agarose, constructed from 286 individual snapshots. In order to resolve the shapes of individual colonies, 95% of the seed cells expressed yellow fluorescent protein (shown here as green), and the remaining 5% expressed cyan fluorescent protein (shown as red). The darker green regions are a result of decreased fluorescence levels often observed in the YFP strain (RJA002) after prolonged growth periods. For this reason, RJA003, which produced a strong CFP signal was used for quantitative analysis. Regions within the colony which appear black are actually green regions, but due to contrast issues in a montage image, the signal appears weaker than it actually is.

5.2 Experimental Results

5.2.1 Overview of a typical competition experiment

In a typical experiment, a population of *E.coli* cells was distributed across an agarose surface, of which 95 % expressed YFP, and 5 % expressed CFP, and sealed with a glass coverslip. The single cells would grow and form microcolonies, which collided with neighbouring colonies as they proliferated. This process would continue until all available space had been occupied (Fig.5.3). By using fluorescent microscopy immediately after cells were distributed across the agarose, and after they had colonised the surface, we were able to link individual progenitor CFP cells to their resulting colony, since the surrounding YFP light could be filtered out. A full description of the methods and image analysis techniques are found in §5.6.1 (p.69). However, to probe the role of competitive strategies within the growing population, we required a way of quantifying success.

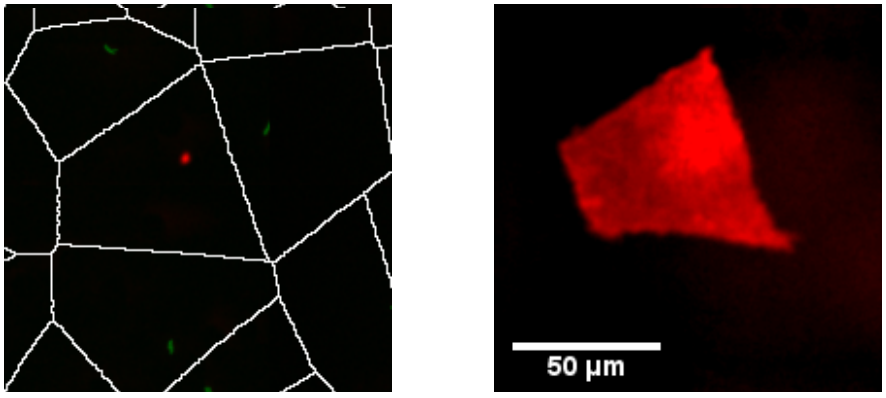

Figure 5.4 (a)Fluorescent image showing seed cells (red and green) shortly after being distributed on the agarose surface, and the Voronoi diagram (white lines) generated from their positions. (b) The resulting shape of the colony descended from the red progenitor cell in the previous frame after ≈16 h incubation.

5.2.2 Quantifying colonisation success

Using a mixture of fluorescent strains allowed the patch originating from a given cell to be separated from the surrounding mat of cells. This allowed us to directly measure the success of a given cell by the patch area: larger patches implied the cell had more descendants, and had successfully colonised more space than a smaller patch. However, to account for the fact some cells might have differing arrangements of competing neighbours than others, we also took into account the amount of space which each cell could colonise without competing with neighbouring cells.

A Voronoi tesselation was used to demarcate space 'belonging' to each founder cell seeded on the agarose surface. Fig.5.4(a) illustrates this procedure for a small collection of cells. Two Voronoi area distributions are shown in Fig.5.5 as a result of using inoculates with different optical densities. For the low density experiments, the median cell density was $\rho_{\text{low}} = 1.5 \times 10^{-4}\,\text{cell}/\mu\text{m}^2$, while for high density experiments, the median cell density was $\rho_{\text{high}} = 7.2 \times 10^{-3}\,\text{cell}/\mu\text{m}^2$. Fig.5.5 shows that in each case, this density could vary within the 'landscape', but on average, there was an order of magnitude difference between cell density in the two experiments.

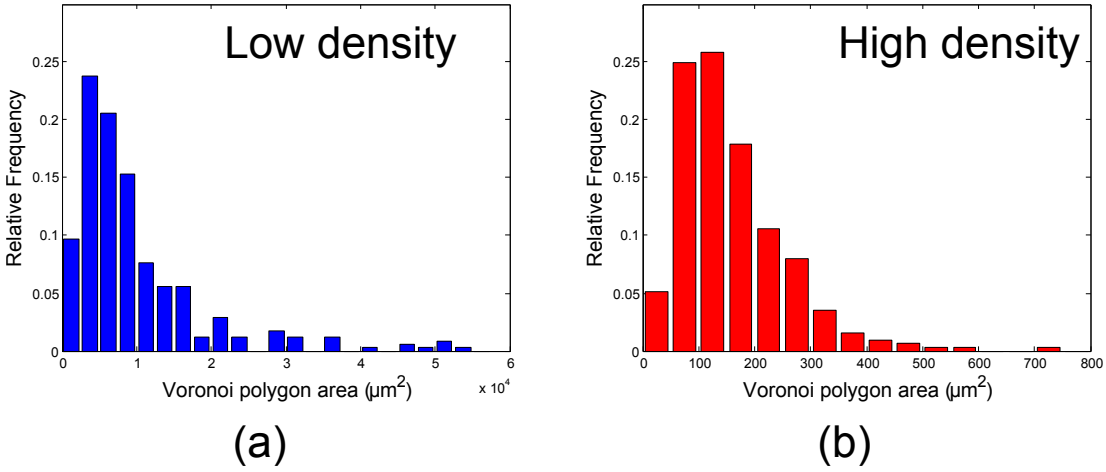

Figure 5.5 Comparison of the Voronoi polygon area distributions for 'low' and 'high' density experiments, with median Voronoi polygon areas and initial cell density. (a) Low density experiment, $\mathrm{med}(A_\mathrm{v})$ $=6.7 \times 10^4\,\mu\mathrm{m}^2$, ρ_low $=1.5 \times 10^{-4}\,\mathrm{cell}/\mu\mathrm{m}^2$, (b) High density experiment, $\mathrm{med}(A_\mathrm{v})$ $=1.4 \times 10^2\,\mu\mathrm{m}^2$, ρ_high $=7.2 \times 10^{-3}\,\mathrm{cell}/\mu\mathrm{m}^2$.

From this, a simple measure of relative success was defined, based on the area of each Voronoi polygon[1] (A_v), and the final colony area (A_c) after cells had colonised their local patches:

$$WI = \frac{A_\mathrm{c}}{A_\mathrm{v}}\,. \tag{5.1}$$

Using this definition, a value of $WI < 1$ would describe the case where a colony had colonised less space than predicted by the Voronoi tessellation, and be considered a 'loser'. Comparatively, a colony which exceeded the area predicted by the tessellation would have $WI > 1$, and therefore would be described as a 'winner'. In the case of Fig.5.4(b), the resulting colony descended from the red cell in Fig.5.4(a) shows good agreement with the predicted Voronoi area and shape.

Using this definition, the distributions of WI for two different experiments were analysed, where each experiment had a different initial seed cell density

[1]The usual nomenclature is 'Voronoi cell'; however, in this chapter I have used the phrase 'Voronoi polygon' or 'Voronoi patch' in order to avoid potential confusion with bacterial cells, which are often just referred to as 'cells'.

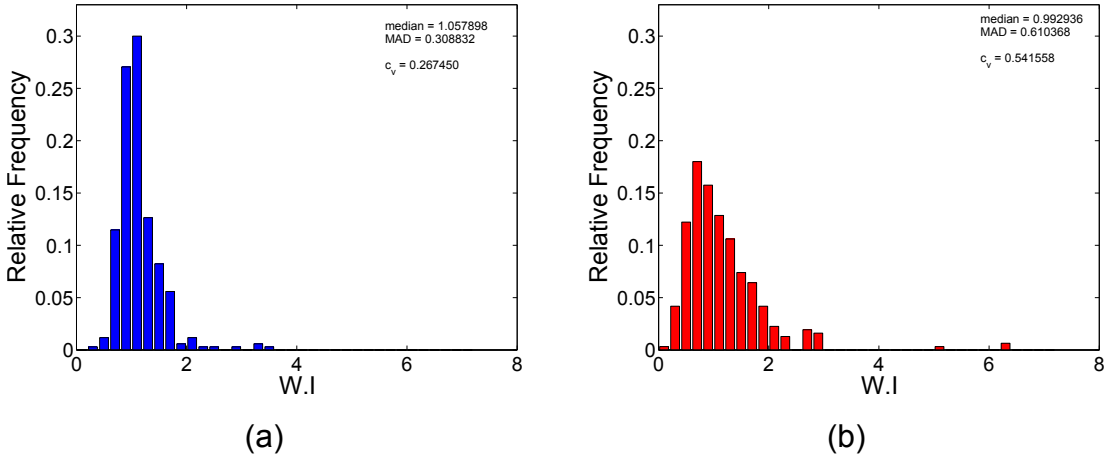

Figure 5.6 Histograms of the WI for exponentially growing cells, with two different Voronoi polygon area distributions, with distribution statistics shown in each, where c_v is the log-normal coefficient of variation, and MAD the median absolute deviation. (a) Low density, 340 colony-Voronoi pairs measured (b) High density, 313 colon-Voronoi pairs measured.

(Fig.5.6). In both instances, cells were seeded on the agarose surface during their exponential phase. Interestingly, we see a clear effect of cell density: while both experiments had peaks around WI=1 (med(WI_{high})= 0.99), med(WI_{low})= 1.05)), the higher density experiment resulted in a wider distribution of WI values. For higher densities, 34% of colonies had a WI < 0.8, and 37% had WI > 1.2. In the case of lower density experiments, the proportions were 13% and 37% respectively. We can see from Fig.5.7 that the source of the winners tended to be colonies with associated smaller Voronoi areas, while those with larger Voronoi areas, tended to be close to $WI = 1$. This suggests density plays a role in likelihood to succeed, and is addressed later in this chapter.

5.2.3 Do winner and losers have different colony shapes?

The WI distributions showed that there were both winners and losers, *i.e.* some seed cells produced colonies which colonised more space than predicted, and some colonised less space than predicted. The Voronoi model used to define success also provides information on the shape of space which 'belonged' to each progenitor cell. We therefore wondered if this was reflected in the colony shape: to what extent did winners and losers preserve their predicted shape?

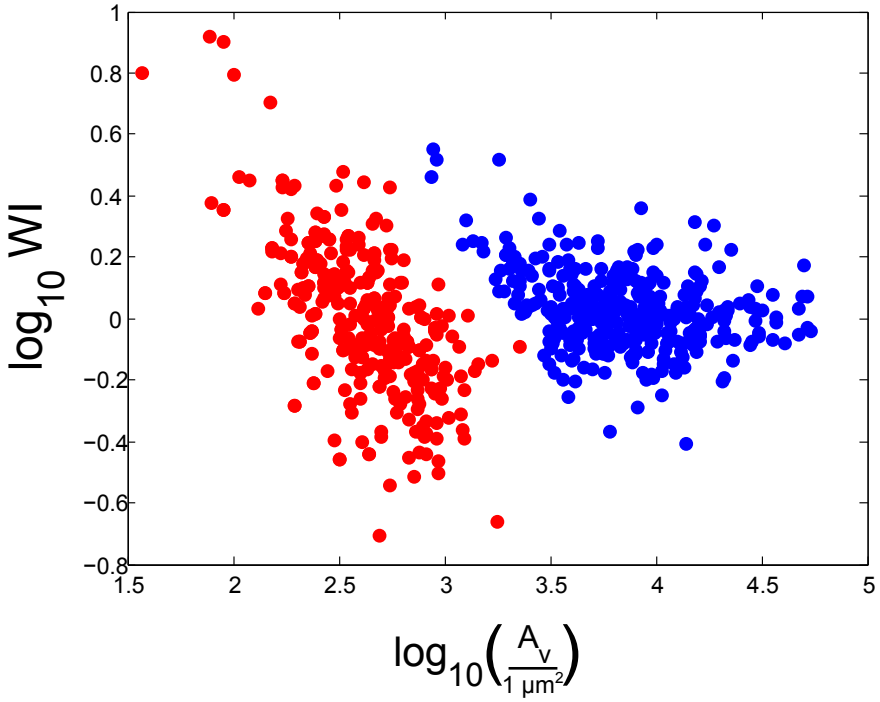

Figure 5.7 $log_{10}WI$ versus $log_{10}A_{\mathrm{v}}$ for low (•) and high (•) density experiments. For low density colonies, large areas tend to be closer to WI

Our expectation was that for $WI = 1$, the resulting colonies would match the associated Voronoi polygons, but that for WI values deviating from unity, there would be less agreement between the expected and final colony shapes. To measure this, we used the Fourier descriptor method to quantify the shapes of both Voronoi polygons and final colonies, and compared the two measurements. I first briefly outline this method, and then present the results.

5.2.4 Fourier descriptors

We chose to use a method in the class of *boundary morphometrics*, where the coordinates of the shape boundary are analysed. Specifically, we used Fourier descriptor analysis which has been successfully used in a number of physical and biological studies studying object morphology [57–59]. The method has a number of advantages, such as being invariant to rotational, scale, and translation transformations, and is suited to analysing complex shapes. In brief, we apply a Fourier transformation to a function describing the shape's boundary coordinates, and obtain magnitudes of the relative contributions from different

Fourier descriptor terms (f_{n}), with indices ranging from $-5 \leq n \leq 5$, which describe the shape.

Quantifying shape from complex perimeter function

In this method, the boundary of the shape is described as a complex function:

$$b_{\mathrm{m}} = x_{\mathrm{m}} + iy_{\mathrm{m}} \tag{5.2}$$

where b_{n} is the m^{th} boundary point describing the shape perimeter, and x_{m} and y_{m} the respective x and y coordinates.

The Fourier descriptors are defined as:

$$a_{\mathrm{n}} + ib_{\mathrm{n}} = \sum_{m=-M/2}^{M/2} (x_{\mathrm{m}} + iy_{\mathrm{m}}) \left(cos\frac{2\pi nm}{N} - isin\frac{2\pi nm}{N} \right) \tag{5.3}$$

where n is the harmonic (or descriptor) number, M the number of edge points, N the total number of descriptors and m the index number for edge points; descriptor magnitudes were then calculated using $f_n = (a_n^2 + b_n^2)^{1/2}$. [2] In all cases, the same number of points was used to describe all shapes. Further more, the coordinates sampled from the boundary required a fixed distance s between each point - s would of course be different for different shapes however, since some shapes would be larger than others.

The resulting values of f_n provide information on the shape. Fig.5.8 shows that simple shapes have very different spectra of f_{n} values, and broadly speaking, shapes with N sides have peaks at index values $n = N$, and $n = -(N-1)$ [57, 58]. Bowman *et al.* showed the central peaks at f_{-1} and f_1 were associated with aspect-ratio and asymmetry of the object in question. The resulting Fourier descriptor index values can also be used to re-construct the original shape; by omitting higher order terms, finer features of the shape are smoothed out, while suppressing lower terms, larger scale features are suppressed in the reconstruction.

[2] Sampling rates are governed by Nyquist frequency requirements: the maximum number of terms taken by the series must be half the boundary sample number, otherwise *aliasing* errors (inability to distinguish between different signals) are introduced.

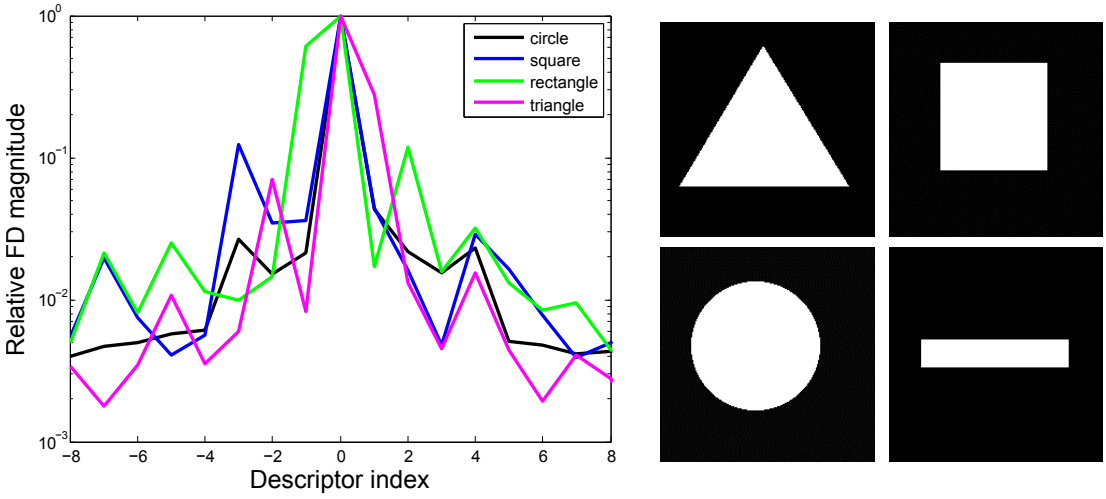

Figure 5.8 (a) Fourier descriptor spectra for idealised shapes. (b) The exact shapes analysed

Following the convention in other studies [57, 58], index values closer to zero quantified large scale features, and those further away quantified finer details.

Calculation steps

The following steps describe the steps taken to quantify the Fourier descriptors for each colony and Voronoi polygon.

1. Extract boundary coordinates from thresholded image.
2. Interpolate between each boundary point, and sample from these coordinates such that there is a fixed distance between each point.
3. Describe the closed boundary as a complex function using these sampled coordinates, ensuring an even number of points.
4. Apply a Fast Fourier Transform.
5. Delete the DC term and normalise all harmonics with respect to the f_1 term.
6. Calculate the amplitude of each term.
7. Centre the transform.

This process produced n Fourier descriptor terms, of which the median portion was used for analysis.

Results

By plotting the individual Fourier descriptor term magnitudes for a Voronoi polygon, and the subsequent colony against each other, we could explore to what extent shape was preserved in 'winners' and 'losers'. Fig.5.9 shows the Pearson's r values for each of these correlations for the Fourier descriptor terms f_{n}, $-5 \leq n \leq 5$. An r value of unity would imply a direct one-to-one relationship between Fourier magnitudes measured for each Voronoi and colony pair, and that the Voronoi shape had been preserved.

From the r values in Fig.5.9, we can see that 'loser' colonies tended to preserve less of their predicted shape than winners, or those close to $WI = 1$ (neutrals). Furthermore, for higher Fourier descriptor indices, the correlation for winners, losers and neutrals all decreased. This reflects the fact finer features of the Voronoi shapes (which are captured by the larger absolute f_n indices) are lost during the growth process, regardless of the cell success.

However, we can see from Fig.5.9 that larger scale features (smaller absolute f_n indices) of the Voronoi polygons are preserved to a greater extent in 'winner' colonies compared to 'loser' colonies. This potentially suggests that Voronoi shape (*i.e.* neighbour geometry) might aid certain patches as they compete for space at collision boundaries, an aspect of competition which is addressed later in this chapter.

5.2.5 Cell-lagtimes and expansion competition

One possible reason for the broadness of the observed WI distributions is that the cells start growing at different times - *i.e.* they have different lengths of 'lag' before growth, after being placed on the surface. Individual colonies could also show different growth rates following the lag phase. Because growth is exponential, this could have major effects on competition. In the context of the ecological scenarios discussed in §5.1.3, this relates to 'expansion competition', the race to colonise empty space.

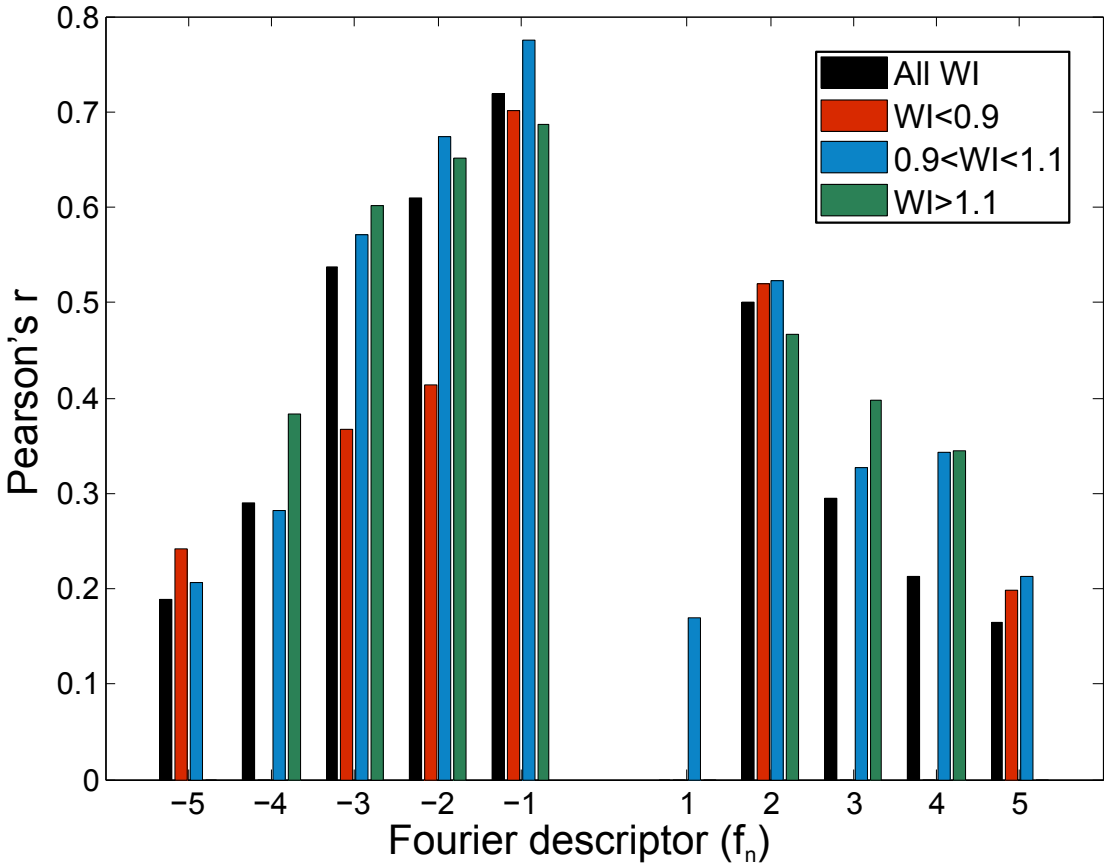

Figure 5.9 A comparison of Pearson correlation coefficients between Voronoi and colony Fourier descriptor magnitudes for a range of indices in the low density experiments (black bars). Sub sections of the data have also been analysed using WI thresholds, and the resulting correlation values shown as well (coloured bars). Only Pearson values at the $p < 0.1$ confidence level are shown here.

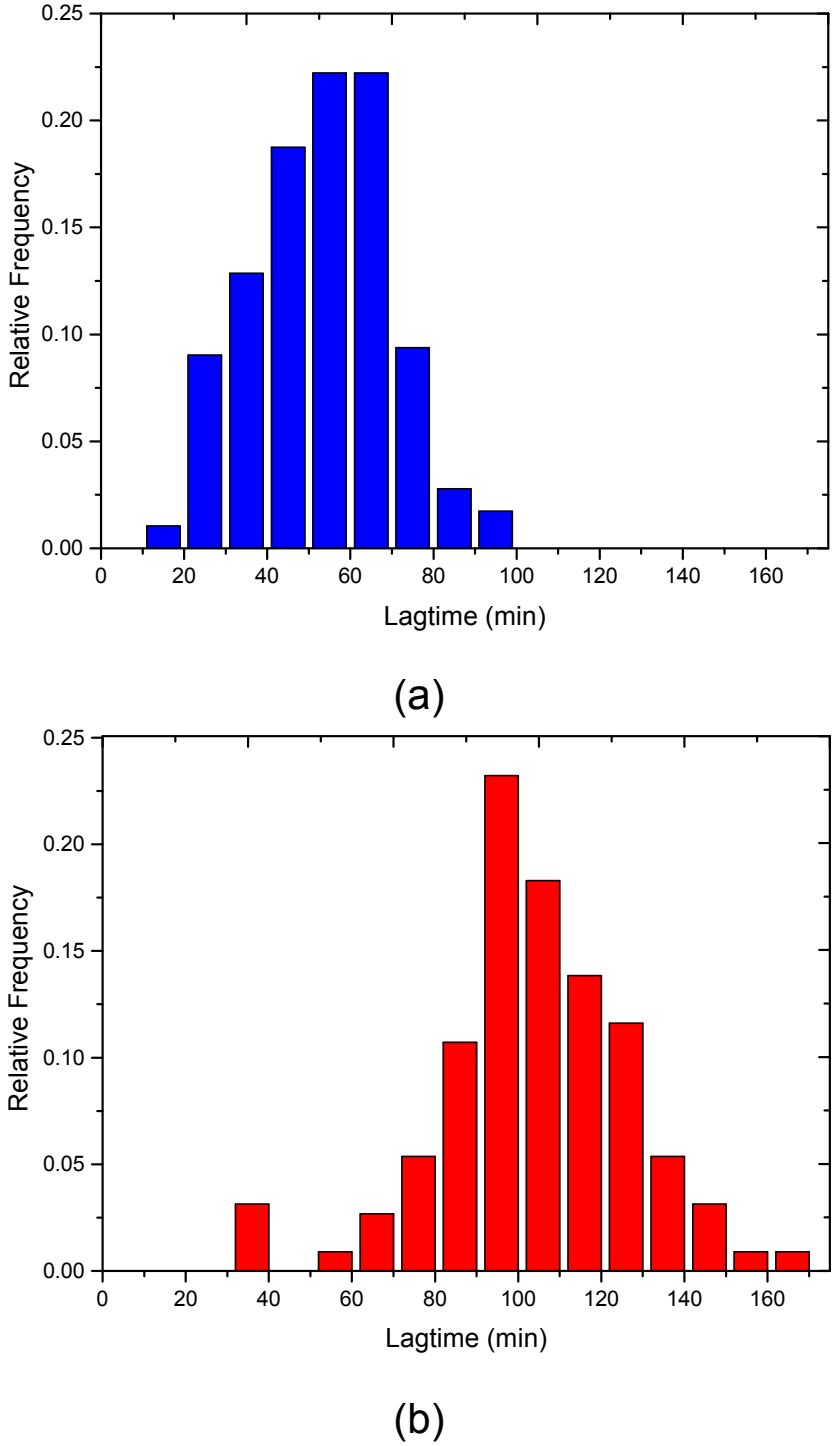

Figure 5.10 Combined histogram of lag-times (t_{lag}) for both RJA002 and RJA003, seeded on agarose when in: (a) exponential phase of growth ($\langle t_{\mathrm{lag}} \rangle$ =53 min, σ = 16 min); (b) stationary phase and subjected to a 50 °C heat-shock for 15 min ($\langle t_{\mathrm{lag}} \rangle$ =102 min, σ = 25 min).

To investigate this in more detail, we measured the distribution of individual cell lagtimes in our experiments, and tracked the growth rates of individual colonies. To do this, we used single-cell microscopy to measure the time at which single cells underwent their first division after being scattered over an agarose surface, and the rate at which the colony area grew. Colony area growth rates were also measured using time-lapse microscopy. A detailed explanation to these protocols is given in §5.6.2 (p.72).

Measuring lagtime distributions and growth rates

Measurement of the lag-times of cells taken from exponential RJA002 and RJA003 culture revealed a mean lag-time of 53(16) min (Fig.5.10(a)); strain-specific mean lag-times were 51(15) min and 54(16) min respectively, showing no significant difference between the fluorescent strains. However, for both strains, there was a broad distribution of lagtimes, so some cells growing on the agarose surface clearly had a head-start over other cells, which would give them an advantage over neighbouring cells during colonisation of the surface.

We observed much less variability in colony area expansion rates on the agarose substrate: up to a colony area of $5.3(8) \times 10^3\,\mu\text{m}^2$, colony area doubling times were constant at ($\langle g_\text{d} \rangle$ =20.00(12) min), beyond which the doubling time reduced due to agarose invasion by the colonies (this phenomenon is studied later in this thesis). However, while sub-exponential, this rate was judged by eye to be consistent between colonies measured here. Batch culture of measurements of population growth in the media (M9 glucose(0.4 %)+casamino acids (0.5 %)) showed consistency between repeats, with RJA002 $\langle g_\text{d} \rangle$ =39.6(12) min and RJA003 $\langle g_\text{d} \rangle$ =36.6(13) min.

We conclude from this that a difference in growth rates between individual colonies was unlikely to affect competitiveness, but that differences in lagtimes might play an important role in a colony's likelihood of success.

Manipulating the lagtime distribution

Our measurements of individual cell lagtimes and growth rates showed that lagtime variability was very significant. We hypothesized that this might be

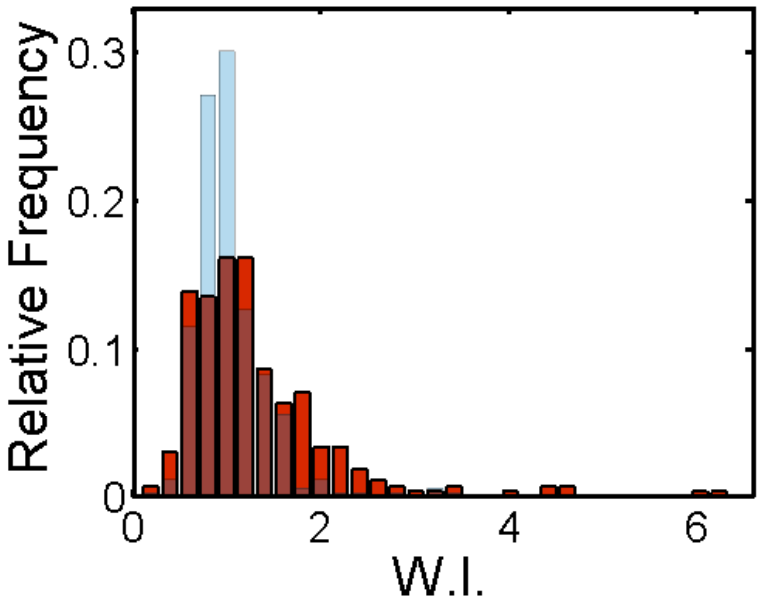

Figure 5.11 Red bars correspond to the WI distribution for sub-lethal heat-shocked cells (15 min at 50 °C). For comparison, the histogram in Fig.5.6(a) is shown as a transparent overlay. The heat-shock treatment has resulted in more outliers, but also a marked shift in the peak of the distribution. median(WI)=1.23, MAD=0.55, $c_v = 0.54$

responsible for the variability in outcomes of competition, as measured by WI distributions. To test this hypothesis, we manipulated the lagtime distribution by changing the physiological state of cells deposited on the agarose surface.

Specifically, before they were deposited on the agarose surface, we exposed the cells to a sub-lethal heatshock while they were in liquid culture; this process has been shown to both extend the mean, and width, of a cell population's lag-time distribution [60–62]. In RJA002, a 15 min heat-shock increased both the mean and width of the measured lag-time to t_{lag} =102(25) min from t_{lag} =53(16) min in the untreated case.

The effect of introducing a wider lag-time distribution on the eventual WI distribution was then checked. These experiments were performed at lower seed cell densities (med($A_{\mathrm{vor}} \approx 2 \times 10^3\,\mu\mathrm{m}^2$)), for which WI variation was relatively low for experiments seeded with exponential phase cultures. Using a 15 min heatshock had a marked effect on the distribution of the WI (Fig.5.11); we observed that the distribution width increased relative to the exponentially growing cell WI

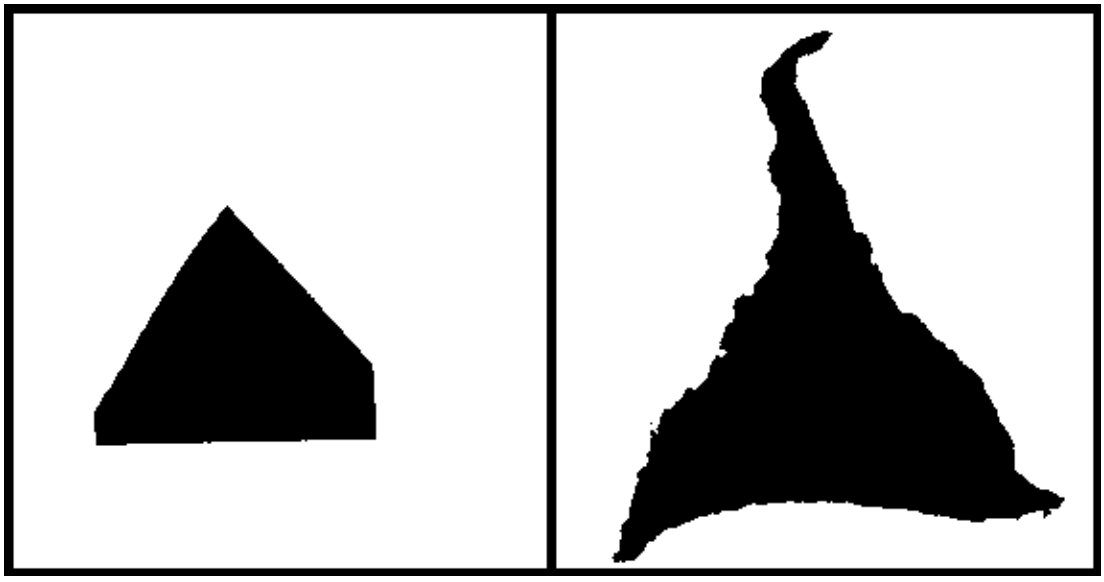

Figure 5.12 Images of a binarised Voronoi-colony pair, showing that some colonies might succeed more as a result of boundary competition, rather than expansion competition. In this case, the colony (right panel) looks broadly similar to the Voronoi polygon, except it has extended its colonisation at the tips as a result of collision with neighbouring colonies (represented by the white regions).

distribution by a factor of two ($c_{\mathrm{v}} = 0.55$).

Increasing the width of the lag-time distribution gives some cells a greater 'head-start' than their neighbours, likely allowing them to steal space that otherwise would have been colonised by a nearby competitor. This was reflected in the wider WI distribution for heat shocked cells, compared to the untreated case. Expansion competition therefore clearly plays an important role in the likelihood of success for surface competing bacterial populations.

5.2.6 Boundary competition at high cell density

Interestingly, we observe that in some cases the final colony shapes are very different from the Voronoi shapes, or possess similar gross features but differ in finer detail. This suggests that 'pushing' interactions at the colony edges have been significant. Fig.5.12 shows an example of this, where extra areas have been colonised at the 'tips' of the Voronoi polygon. Could this play a role in the outcome of competition? These effects are akin to the concept of boundary

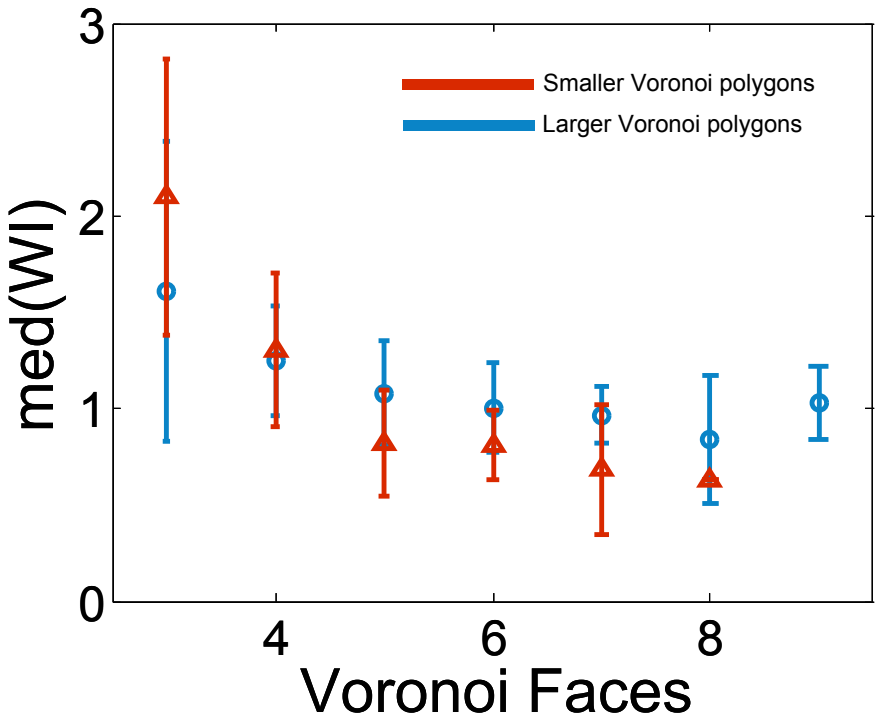

Figure 5.13 Median WI versus Voronoi face numbers for low and high Voronoi area distributions; error bar the median absolute deviation for each .

competition which were introduced in §5.1.3 (p.42). By this ecological mechanism, competing organisms attempt to gain control of space at the patch edges.

If pushing at colony boundaries is a major factor in the outcome of competition, then we would expect cells that start off with different Voronoi patches to experience different pushing interactions once they collide with neighbours and to have different fates. To test this hypothesis, we assessed whether any morphological features of the Voronoi shape were correlated with WI. We first addressed the number of Voronoi faces, *i.e.* the number of neighbours of an initial colonising cell.

Interestingly, we did see a correlation between the number of neighbours of the original cell and the WI. For both high and low densities, triangular Voronoi polygons returned, on average, the highest median WI, and the widest distribution (Fig. 5.13). This fits (assuming it still does) with the idea that bacterial growth converging at corners, where space would be more limited, might be the areas where space was won.

This analysis suggests that indeed Voronoi patch shape may play a role in the outcome of competition. However, analysis of simple descriptors like number of faces is limited in its scope. We therefore decided to look in more detail for correlations between patch shape and WI, using the Fourier descriptor methods which were introduced earlier in this chapter.

5.2.7 Does Voronoi patch shape influence success? A more detailed analysis

In this section we use Fourier descriptor analysis to describe Voronoi patch shapes in more detail, and we test whether particular features of the Voronoi spectra are correlated with WI.

Individual Fourier descriptor magnitude - WI correlations

Perhaps the most obvious way to look for correlation between the Fourier descriptor spectra for Voronoi patch shape and WI is simply to test whether individual Fourier descriptor magntitudes correlate with WI. Since there is some evidence that individual Fourier descriptor magnitudes are associated with simple geometries (*e.g.* triangles have a large value at f_{-2} [57, 58]), this might help us identify key features of Voronoi patch shape that are associated with success. To this end, Fig.5.14 and Fig.5.15 show median WI values plotted against Fourier descriptor magnitudes for a number of different Fourier descriptors for high and low cell density cases.

Where Voronoi areas were large (low density cells, Fig.5.14), there was a large amount of variation in WI across all Fourier descriptor magnitudes, suggesting there wasn't a typical Voronoi shape signature associated with cells that eventually went on to become winners. A similar picture was observed in experiments using high cell densities (smaller Voronoi polygons), even when the data were split into 'winners' and 'loser' sub-sets, implying colonies grown in higher cell densities were not any more, or less, likely to have their success outcome influenced by idealised neighbour arrangements.

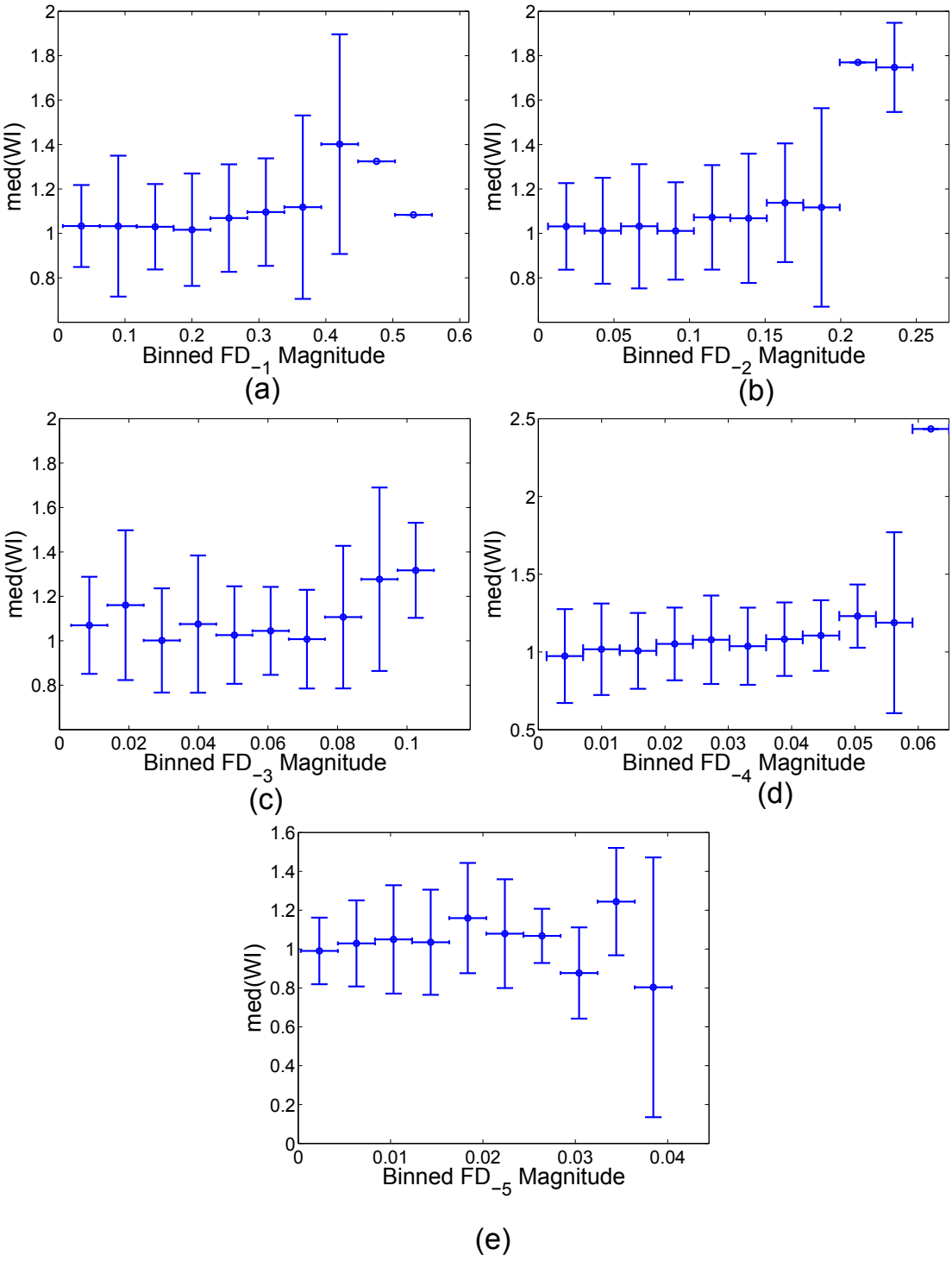

Figure 5.14 Median WI values against binned Fourier descriptor magnitudes for low density experiment. The individual plots correspond to Fourier descriptor indices (f_{n}) (a)$n = -1$ (b) $n = -2$, (c) $n = -3$, (d) $n = -4$ (e) $n = -5$.

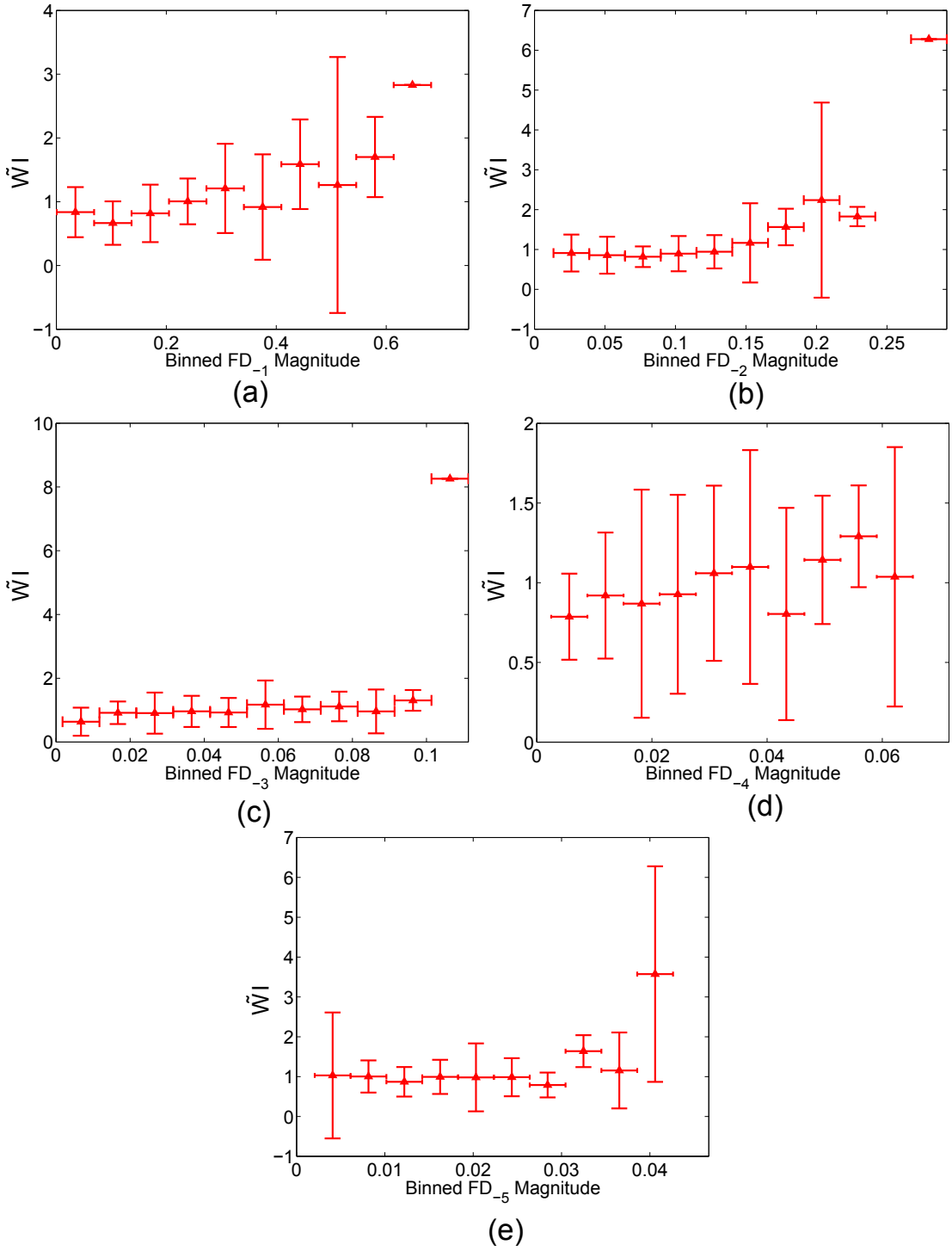

Figure 5.15 Median WI values against binned Fourier descriptor magnitudes for high density experiment. The individual plots correspond to Fourier descriptor indices (f_{n}) (a)$n = -1$ (b) $n = -2$, (c) $n = -3$, (d) $n = -4$ (e) $n = -5$.

Experiment	Fourier descriptor index							
	-3	-2	-1	1	2	3	4	5
Low density	-	-	1.78	4.68	-6.07	-	-	-
High density	11.25	14.33	7.67	-17.82	-24.42	-28.64	-28.05	-20.59*

*$p < 0.05$

Experiment	F-stat	F-stat p-value	R^2
Low density	12.68	7.14E-08	0.094
High density	16.65	2.18E-19	0.3457

Table 5.1 Predictor values for each Fourier descriptor from a linear, stepwise multilinear regression model. Each predictor has a $p < .01$, except where otherwise marked. Dashes represent rejected predictors; while Fourier descriptor values -5 to 5 were tested, in both instances, f_{-5} and f_{-4} were rejected, and are not shown here.

Multilinear Fourier descriptor analysis

Although our analysis of individual Fourier descriptor magnitudes does not show any obvious correlation with WI, shapes are described by entire Fourier descriptor spectra rather than by individual Fourier descriptor magnitudes. We therefore decided to extend our analysis by looking for correlations between the properties of complete Fourier descriptor spectra for Voronoi patches, and WI values.

To this end, multi-linear regressions were carried out on both high and low density data sets. This approach allowed us to build a model which, using a linear combination of Fourier descriptors, rather than multiple, individual regressions, could potentially predict variation in WI, based on Voronoi morphology. As this was exploratory data analysis, a stepwise approach was taken, whereby we started with a simple model using one term, before iteratively adding more terms. The quality of the fit was constantly queried as these extra terms were added to the model, with existing or new terms rejected depending on the overall fit quality. Full details of this approach are provided in the additional methods section at the end of this chapter (§5.6.3, p.74).

Incorporating all data from the experiments showed linear combinations of three Fourier descriptors could explain 9.4% of the variation observed in WI for low density environments (Tab.5.1, low density R^2 value). For high density environments, the situation was more complex: eight predictors could explain 34.6% of the variation in WI (Tab.5.1, high density R^2 value). This suggests that

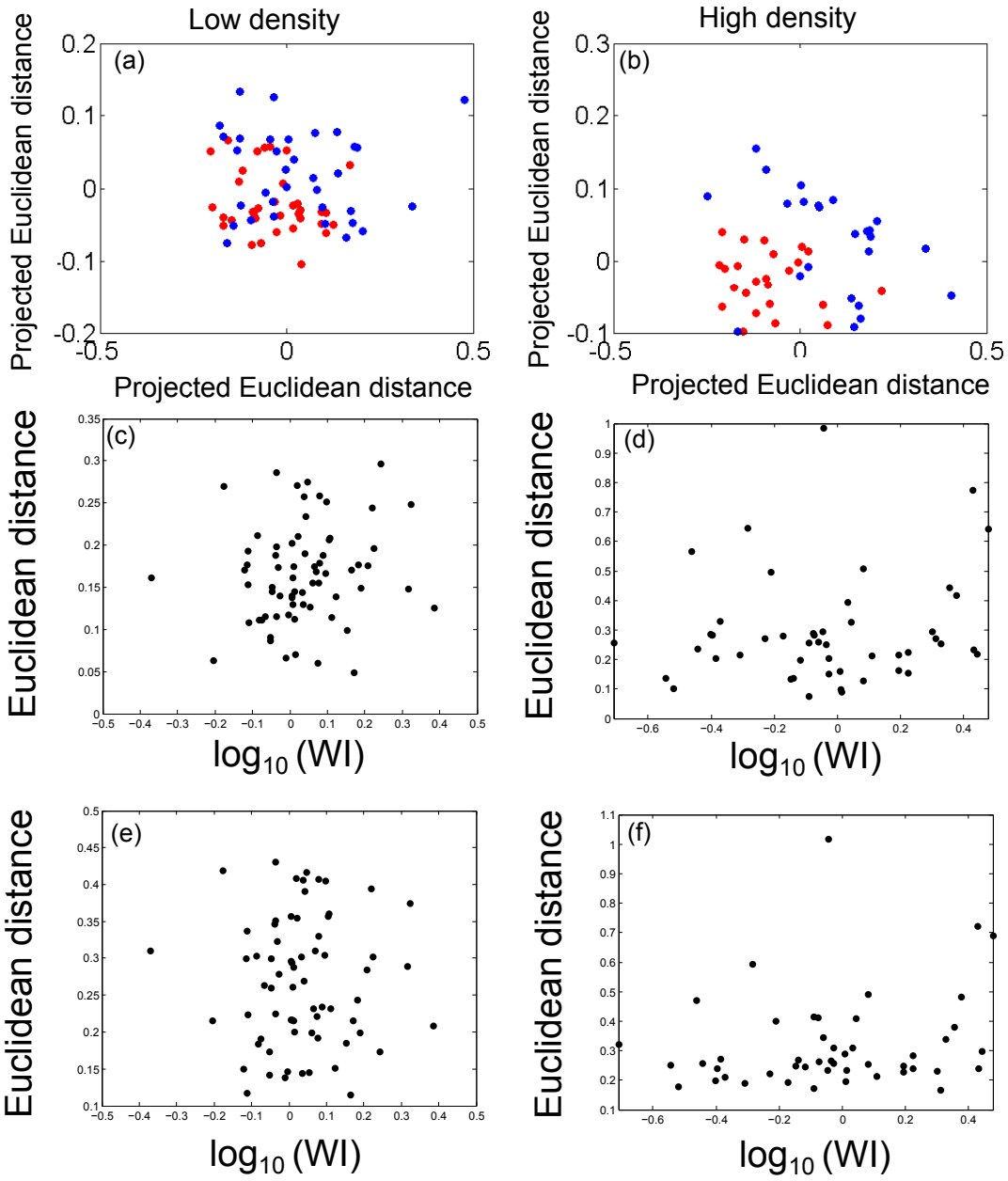

Figure 5.16 (a,b) Multidimensional scaling plots of similarities between Fourier descriptor spectra of Voronoi polygons for the top and bottom 10% of 'winners' and 'losers'. Each point represents a sample (Voronoi polygon in each plot), and their relative distances corresponds to the similarity their respective Fourier descriptor spectra have with each other. Red points correspond to $WI < 1$, and blue $WI > 1$. (a) Low density, (b) High density. (c-f) Euclidean distances between the Fourier spectra of Voronoi polygons and different shapes against $\log_{10}$(WI). Smaller Euclidean distances indicate greater similarity between each spectra and the ideal shape. (c) Low density and (d) high density Voronoi polygons compared to an equilateral triangle. (e) Low density and (f) high density Voronoi polygons compared to a square.

neighbouring cell configurations do appear to affect eventual WI values in higher density environments more than compared to lower density growth environments. However, the amount of variation captured by the model in the high density case was still small, which suggests a linear combination of Fourier descriptor terms is likely a limited predictor of potential progenitor cell success across the entire WI population.

Similarities between Fourier spectra

Inspired by the partial success of our attempt to correlate Fourier descriptor spectra with WI, we also carried out a complementary analysis, in which we tested whether there were significant differences between the Fourier descriptor spectra of Voronoi patches of cells that went on to become winners, compared to those that went on to become losers. This way we could determine if there was a common Voronoi morphology which tended to have higher, or lower, eventual WI values.

To achieve this, we used *Multidimensional Scaling Analysis* (MDS), a method which allows similarities (or dissimilarities) between samples (our Fourier spectra) to be visualised. In this method, a matrix quantifying the pairwise (dis)similarity between each sample is built, from which an 2d visual representation of these pairwise distances can be used to determine if some samples are more similar to each other than others.

In this case, pairwise Euclidean distances between each Fourier spectra were used to build a dissimilarity matrix, quantifying the difference in shape between pairs of Voronoi polygons associated with a given experiment. These distances were calculated by summing the differences between each Fourier descriptor term (f_{n}) between $n = -5$ and $n = 5$. These pairwise distances were then visualised via a 2d projection, in which dots represent samples, and the distance between two dots the dissimilarity between the samples - in other words, the further apart two points in a 2d MDS plot are, the more dissimilar the two samples are. Furthermore, we colour-coded the resulting plot according to whether the samples related to eventual winners or losers.

To compute if there were any broad differences between the spectra of Voronoi polygons of eventual winners and losers, we compiled a list of colonies which fell

within the top and bottom 10 % of the WI distribution. For this list of colonies, we computed pairwise Euclidean distances between each Fourier spectra; this provided our measure of similarity between each spectra. We also computed the similarity of each Voronoi spectra to one of two ideal shapes, namely a square and triangle.

Fig.5.16(a,b) shows the MDS plots for Voronoi polygons in both the low and high density experiments. For low seed density, we see that the points form a compact cluster, and that the red and blue points (losers and winners) are mixed up with each other. Remarkably however, for high seed density, we see less overlap between the clusters of red and blue points. This indicates that Voronoi patches of progenitor cells which eventually win form a separate cluster in Fourier descriptor space from those which eventually form loser colonies. Furthermore, the red points (losers) show more clustering compared to the blue (winners) points, suggesting there is a common 'losing' configuration, while 'winning' geometries are more diverse.

Conversely, there was not a clear relationship between the similarity of the Voronoi polygons to an ideal shape (triangle or square), and their eventual WI (Fig.5.16(c-f)).

Further work to uncover the similar feature in loser configurations would be interesting continuation of this analysis.

5.3 Discussion

In this chapter, a simple microbial system was used to study the effects of competing ecological drivers in the race to colonise space between neighbouring organisms. We used microscopy to image a population of cells which, other than their fluorescent markers, were identical to each other. We tracked which cells eventually went on to become 'winners', occupying more space than their Voronoi patches, and 'losers', occupying less space. Having identified the winners and losers, we attempted to identify those factors which were important in the competition for space. Our analysis identified both single cell lag-times, and neighbour configuration as being significant factors.

Importantly in these experiments, the absolute position of each progenitor cell was known, allowing for the complete reconstruction of the entire bacterial "landscape" in post-processing image analysis steps. A simple metric based on the ratio of colonised area to "predicted" area was used to quantify the degree of success. Predicted area was demarcated by a Voronoi tessellation based on the initial cell seeding coordinates. This provided information both on the expected colony morphology and the amount of area 'belonging' to each progenitor cell.

5.3.1 Voronoi-colony shape correlation

The Voronoi shape associated with an individual progenitor cell was governed by the configuration of neighbouring cells. If colonies grew identically and at the same rate, colony shapes would be expected to match the Voronoi prediction, and all colonies would have a $WI = 1$.

In our experiments at high initial cell density, more variation was observed between the expected, and resulting colony shapes, compared to the low density case. A possible reason for this is that at the point of collision, the colonies were still undergoing anisotropic expansion, which could lead to complicated force balances upon collision with neighbours. In contrast, in the low density experiments, we expect the colonies had approached a more circular shape, and therefore were undergoing isotropic expansion.

Interestingly, other authors have reported fractal interfaces between colliding colonies in similar experimental set-ups [20, 46, 47]. This is in contrast to our results, where we see mostly close correlation between Voronoi patches and final colony shapes. While confocal analysis might reveal more detailed features of our colony boundaries, it seems likely that the difference is due to experimental set-up; for example in our experiments, the colonies are vertically confined by a coverslip, which might influence the outcome of microcolony collisions by virtue of the vertically applied pressure.

5.3.2 Why do smaller colonies show higher WI values?

For the two cell density regimes (Fig.5.5, p.46), there was a tendency for the smallest polygons to be associated with higher WI values. This was also true of the heat-shocked population, which had a comparable global cell density to the low density experiment. One possible explanation is that the WI metric is biased to rewarding smaller colonies: A cell with a small Voronoi polygon would have to colonise less area in absolute terms to achieve the same WI as a significantly larger colony. On the other hand, cells with small Voronoi patches would likely lie next to smaller patches (and so a winning small patch would result in a loser small patch). Nevertheless, alternative measures of WI would be a useful area to explore so as to ensure patch size is fully accounted for; for example, the WI could be defined by the absolute difference between Voronoi polygon and final colony area. Alternative Voronoi metrics are another possibility: here, the Voronoi boundaries were based on Euclidean distances as they were the most straightforward. More complex ways of demarcating space between progenitor cells, such as 'Manhattan distances', might predict colonisation distributions in a better way [63].

5.3.3 Expansion competition versus boundary competition

The importance of expansion competition was investigated by manipulating the lag-time distribution within the population of cells in the lower cell density regime. A 50 % increase in the lag-time distribution width resulted in a doubling of the measured WI distribution dispersions. Intuitively, this result makes sense: by increasing the range between the first and the last cell to start growing, one would expect there to be more winners and more losers overall.

As previously mentioned, the Voronoi polygons contain information on the configuration of neighbouring cells, and hence, points where competing colonies converged, and this provides some probe of the role of boundary competition. By quantifying Voronoi polygons shapes using a Fourier analysis method, we found that in high density environments, there was greater difference between winner and loser Voronoi morphology than in the low density experiments. Furthermore, loser colonies had less difference between their spectra compared to the winners,

suggesting that there may be a common configuration of neighbouring cells associated with patches that eventually go on to become losers.

The wider distances between 'winner' Fourier spectra at high density also suggests that factors other than Voronoi morphology play a role in the progenitor cell's eventual success. It is suggested this is related to the colony growth: at smaller colony sizes, where fewer cells have invaded the agarose, colony fronts would propagate quickly compared to larger colonies. At collision interfaces, cells could potentially squeeze into the available uncolonised gaps between other impinging colony fronts.

5.4 Conclusion

A "landscape" of competing bacterial colonies was successfully imaged at the micrometre scale, which allowed the fate of individual bacterial patches descended from individual cells to be directly tracked. This setup was used to probe the relative contributions of two ecological drivers of space colonisation, namely, expansion competition, and boundary competition. Using two differently coloured fluorescent strains of *E.coli* bacteria, it was shown that both cell lag-times and local cell density play an important role in determining the eventual success of an individual bacterial patch growing on an agarose surface. Furthermore, the neighbouring configuration of cells was shown to potentially be a factor in deciding the fate of colonies, but only at higher cell densities.

5.5 Future Work

Building on this work, an interesting next step would be to attempt to remove the spread of lag-times from the population of cells by synchronising cell division times through centrifugation, for example. This would allow us to zoom in directly on the effects of cell density and Voronoi patch shape. In the following chapter, we do precisely this in a simulation context. Furthermore, while we focused on the area colonised by cells, cells were very likely to be also invading the agarose and growing in 3d, especially in the later stages of colonisation: it would be interesting to incorporate the volume of biomass of a single patch into

the final measure of success. Literature also suggests that collision boundaries [64] might fluctuate in time - it would be interesting therefore to see if colony patches deviate from their initial collision points, or whether they remain relatively fixed in longer timescale experiments.

The method described here could also be used to study more complex ecological and evolutionary phenomena, closer to those seen in the natural world. An obvious route would be to use bacterial strains which chemically interacted at the collision interfaces, or a mixture of strains, one of which would inhibit the growth of the other, to model inhibitory interactions in the wild. An exciting potential area would be to investigate the propagation of phage (viruses which infect bacteria), or plasmids, in a structured population of cells - thus, the setup established here is highly versatile, and should lead to a broad diversity of further work.

5.6 Expanded methods

In this section, I expand on the methods used for the experimental results detailed in §5.2.

5.6.1 Microbial competition protocols

In this chapter, large portions (of the order of mm^2) of the bacteria-colonised agarose landscape were imaged using a microscope. In addition, cell lag-times were measured. Here, I describe the relevant extensions and amendments to the protocols detailed in §3 and §4 necessary for these experiments. In all cases, both RJA003 (CFP - expression) and RJA002 (YFP - expression) were used.

Sample preparation

Starter cultures of both RJA002 and RJA003 were prepared separately as described in §3.2.2 (p. 17) and grown to the desired phase, all in M9 +glucose (0.4%) + CAA (0.5%). The cultures were then diluted to a normalised density, and combined at a 19 : 1 ratio using a vortex mixer. This culture was then diluted to a further experimental density that varied depending on the experiment being carried out. Thick agarose pads were prepared using the protocol described in §3.3.2 (p. 21).

Microscopy

To image large portions of agarose, either one of the 20x objectives in Tab.4.1 (p.23) were used. High precision stage movement was required, so a motorised xy stage was employed. The CCD camera was also levelled with a spirit meter to ensure stage translations correlated with the matching of adjoining camera field of views. Edges of the inoculate were first identified by a characteristic 'coffee-ring' pattern made by cells at the boundaries, and the coordinates recorded. From these, a set of coordinates describing a raster pattern for the microscope field of view were generated in MS Excel and passed to the software controlling the microscope stage. Typically, the points were described with a 5 µm overlap

between each field of view, which was accounted for in image processing steps. Fluorescence images at each coordinate were captured in both YFP and CFP wavelengths. Each field of view took approximately 10 s to capture, which included manual focus and acquistion commands, before moving onto the next coordinate. An entire slide would therefore take between 30 min and 60 min to image in full, depending on the size of the inoculate.

Following a night's incubation at 37 °C (to reduce the risk of samples drying out, slides were kept in a small tupperware box), the founder cells had colonised the agarose surface (Fig.5.3), and the imaging process was repeated. Using a reference coordinate from the previous day allowed an approximate match to the initial start coordinate, aiding matching of Voronoi - colony pairs.

Image processing and analysis

In order to define regions which were closest to founder cells than their neighbours, a Voronoi tesselation was performed with the set of points describing the centroid coordinates of all the cells either in ImageJ or Matlab. This produced a Voronoi diagram (Fig 5.17), a useful method of breaking space up that has applications in a variety of fields, from crystallography to town and regional planning [63]. Here, it provided a convenient means of identifying the zones defined as 'belonging' to a progenitor cell.

Because there were relatively few CFP cells to YFP cells, the resulting CFP colony shapes from the second day of imaging could be resolved. For Voronoi polygons generated in ImageJ, the boundary lines were thresholded out from the output image, and where overlaps with CFP cells were identified, Voronoi polygons were manually flood-filled; these were then thresholded out themselves, leaving a map of Voronoi polygons relating specifically to CFP cells. Edge cells generated unbounded Voronoi polygons (Fig.5.17(a)) and so were ignored. Similarly, cells lying in a coffee-ring region often seen at the edges of a dried bacterial were ignored, since cells did not have a random distribution of positions. For maps generated in Matlab, the same approach was taken, although because greater control was exerted over data handling, CFP Voronoi polygons could be generated straight from known CFP cell positions. Each colony image was manually thresholded to acquire a binary image using 'Otsu's Method', and

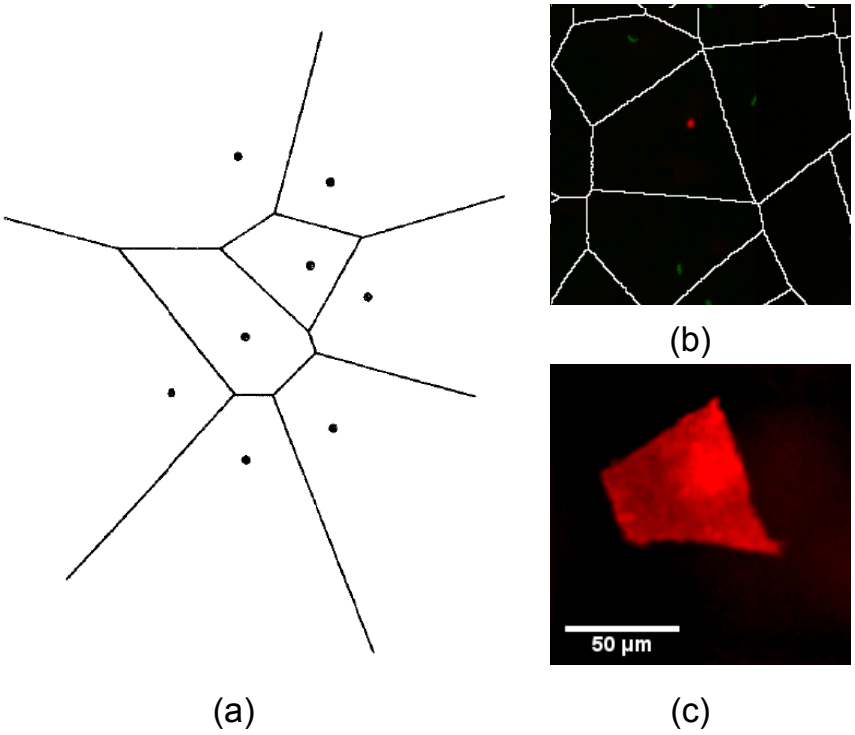

Figure 5.17 (a) Illustration of a Voronoi tessellation generated by eight points. Adapted from [65]. (b) A detail of a bacterial landscape, with fluorescent cells (red and green points) used to generate a Voronoi map (white lines). (c) The resulting shape of the colony descended from the red progenitor cell in the previous frame. Note, panels (b) and (c) are re-prints of Fig.5.4, and have been reproduced for the reader's convenience.

stitched together to form a complete image of the colonial landscape. Because the CFP and YFP images were effectively negatives of each other, it provided a convenient means of ensuring the shape was properly captured in the thresholding process.

The CFP-Voronoi polygon images were then cropped into sub-images to reduce file sizes, and then matched up to CFP colony images using scripts written in Matlab; these sought to match colonies based on the maximum amount of overlap between Voronoi and colony objects. Once matches had been made, gross morphological properties of the Voronoi polygons and colonies were extracted using Matlab functions.

5.6.2 Lag-time protocols

In order to quantify the lag-time distributions of cells used in these experiments, the following protocols were used.

Sample preparation

Starter cultures of both RJA002 and RJA003 were separately prepared as described in §3.2.2 (p.17) and grown up in M9 +glucose (0.4%) + CAA (0.5%). A mixture of the two strain cultures was then prepared by adding 500 µl of culture from each strain's liquid batch into a sterilised eppendorf, and gently vortexed for several seconds (both strains were used to test cells behaved the same way regardless of their fluorescent expression). Thin agarose pads were prepared using the protocol described in §3.3.1 (p. 20), and 1 µL of culture dropped onto the agarose pad. The pad was tipped to ensure an even distribution of culture along the length of the pad, left to dry under a petri dish and sealed with rectangular glass coverslip.

Microscopy

Samples were imaged in both the fluorescent microscopes described in §4.1 (p.23) with a phase contrast time resolution Δt_{phase} =1 min frame^{-1}, and fluorescence time resolution Δt_{fluo} =20 min frame^{-1} in both CFP and YFP excitation

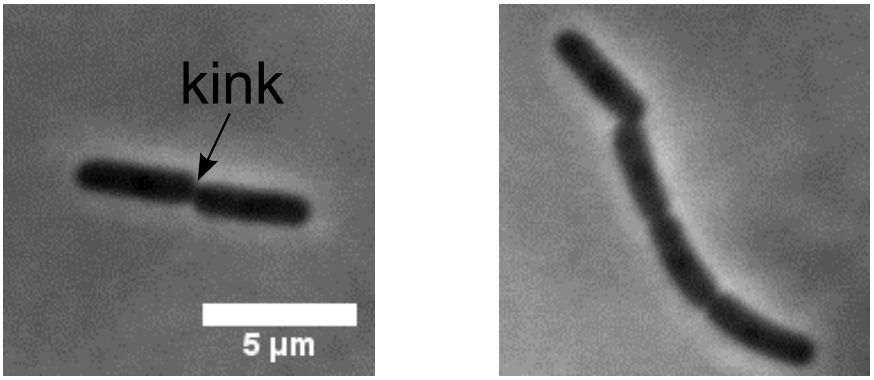

Figure 5.18 Phase contrast images of dividing cells. (a) The cells have just divided, and exhibit the kinking used to objectively assess the division state (marked with arrow). (b) Very occasionally, cells would show clear division event signatures (such as the cinching at the cell mid-point) but would not completely divide. Discretion was used in these instances to define whether a division event had occurred or not.

wavelengths; an infrequent fluorescence exposure allowed each cell strain to be segregated at the start of acquisition, and to provide occasional reminders in the resulting movies when analysing them. The general time-lapse protocol used is described in §4.2 (p. 34).

Image processing and analysis

Image stacks were created by sorting images using macros written in ImageJ, and the individual wavelengths movies merged into single RGB movies for each field of view captured. Using the 'Cell Counter' macro, the frame where a cell divided was manually determined by identifying the frame when a cell kinked after division; Fig 5.18 shows the criteria used to objectively define a division event. Division times were analysed in Origin separately for strains RJA002 and RJA003 to check strain-specific distributions. To ensure that identifying and recording the division times manually had not introduced a bias, the box-counting method described in [66] was used retrospectively on a sub-set of data to confirm agreement between manual and automated methods.

5.6.3 Multi-linear regressions

In this chapter, multi-linear regression was used to explore the possibility that multiple Fourier descriptors which described Voronoi polygons might predict a cell's chance of success. In this section, I provide more detail on this technique, and how it was applied in this chapter. All these analyses were performed in Matlab; the relevant scripts can be downloaded from `http://goo.gl/6Nuf2z`.

Multi-linear regression is an extension of simple linear regression. In simple regression (commonly known as linear regression), an outcome variable is predicted from a single predictor variable, summarised below:

$$Y_i = (\beta_0 + \beta_1 X_i) + \epsilon_i \tag{5.4}$$

where Y_i is the predicted outcome, β_0 is the intercept, β_1 the gradient and ϵ_i the residual.

Instead of using one predictor to build a model, here, multiple predictors (in this chapter, Fourier descriptors) are linearly combined with respective weightings to predict an outcome variable (in this chapter, a colony's success, or WI).

The following general equation summarises this idea. For an outcome variable, Y, the Y_i'th observed value will be described by

$$Y_i = (\beta_0 + \beta_1 X_1 + \beta_2 X_2 + ... + \beta_n X_n) + \epsilon_i \tag{5.5}$$

where β_1 is the coefficient of the first predictor (X_1), β_2 is the coefficient of the second predictor (X_2), β_n is the coefficient of the n'th predictor (X_n), and ϵ_i is the residual value. In the context of this chapter, the outcome variable is WI, and the predictors the magnitudes of the respective Fourier descriptor indices.

As we performed exploratory data analysis, we used a *stepwise method* to build our model (specifically, the '`stepwisefit`' function within Matlab. By this method, we add predictor terms to the model iteratively, first starting with the descriptor term which best captured variation in our outcome variable. In our case, this was magnitudes associated with a particular Fourier descriptor

index that best captured variation in WI. As each term was added, the fit and significance of *each* descriptor term tested using the F-statistic p value. If the p-value for a new term fell below the 0.01 significance threshold, the null hypothesis that the term had a zero coefficient if added to the model was rejected, and the term added in the model. If the p-value for an existing term fell below the 0.01 significance threshold, the null hypothesis the term had a zero coefficient was rejected [67].

The final model would then consist of a linear combination of Fourier descriptor magnitudes for specific Fourier indices that best captured the observed variation in the WI. This method allowed us to explore the possibility that combinations of Fourier indices might capture the likelihood of success, rather than individual descriptors.

Chapter 6

Simulating microbial competition

6.1 Introduction

In the previous chapter we used experiments to investigate how bacteria compete for space as they proliferate to fill a habitat. In this chapter, we attempt to reproduce and understand these factors using a simple discrete event simulation written in Matlab. Our experimental study revealed that both individual cell lag-times and neighbour geometry were significant factors in the competition for space. The aim of our simulations is to separate the roles of these two factors. This was achieved using a series of simple growth rules on a square lattice.

The results provide further insight into the observed WI distributions in the previous experimental chapter, and show that the main features of our experiments can be captured by a relatively simple model. First, lag-times are shown to be important to the eventual success of a colony, but the effects become amplified when colonies expand exponentially, as opposed to perimeter-growth. In the absence of lag-times, exponential growth also strongly affects the variation in WI measured. This expansion behaviour also becomes important at high cell densities. It is found that combining exponential growth with high density environments results in patch shapes becoming more important in determining eventual success.

The structure of the chapter is as follows. First, the simulation method is

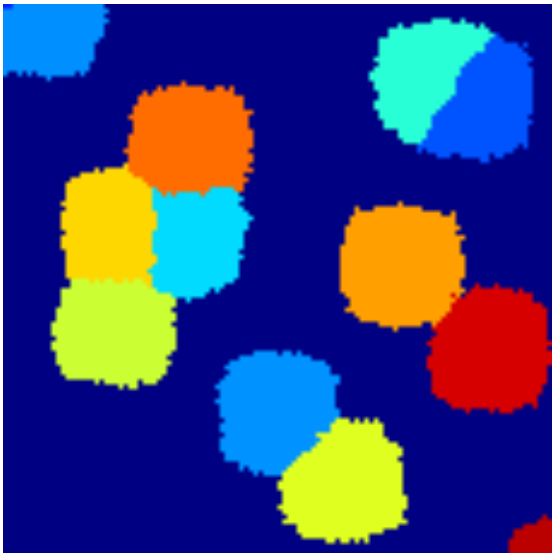

Figure 6.1 A snapshot of a example simulation showing 12 coloured 'colonies' competing for free space (dark blue pixels) on a 100x100 square lattice.

introduced. Next, the results are presented, which are split into two main themes to complement the experimental studies: The first addresses the effect of density and lag-times on WI, while the second focuses on the morphological effects of Voronoi polygons on WI probabilities. Next, I discuss how these results both relate to the experimental study, chapter conclusions, and possibilities for further study.

6.2 Simulation method

In this section, the simulation details are described. Fig.6.1 shows a snapshot of a typical simulation run, and Fig. 6.2 a summary of the growth rules. We can see that the simulation takes place on a square lattice, where each lattice site is assumed to host a single bacterial cell, or be empty. A summary of the simulation steps are shown in Fig.6.3.

6.2.1 Simulation setup

Initial configuration

First, seed-cell coordinates were generated by a random number generator, without replacement to ensure no two cells were placed in the same site. From this, a list of cells was created (henceforth referred to as the 'cell list'), each with a colony index number.

Assignment of lag-times

If lagtimes were assigned, these were sampled from the experimental lag-time distributions described in §5.2.5 (p.51); the cell-list was then sorted in ascending order by these lag-times. If no lagtime was used, then division times were assigned instead, picked from a uniform distribution (18 min - 22 min, chosen based on colony area expansion rates of cells growing on 3 % agarose, measured through time-lapse microscopy), and the cell list sorted by the division times. This section is summarised in Fig.6.3 (blue box).

Boundary conditions

If a mother cell tried to place a daughter cell beyond the boundary edge, it was allowed, but the new cell was not tracked. This way, the edges were treated as open, and did not confine growth. This is similar to the experimental set-up, where a microscope has a finite field of view which colonies at the edges can grow beyond. However, because we did not then know the true area of colonies that touched the edge of our simulation 'field of view', these colonies were not used in analysis.

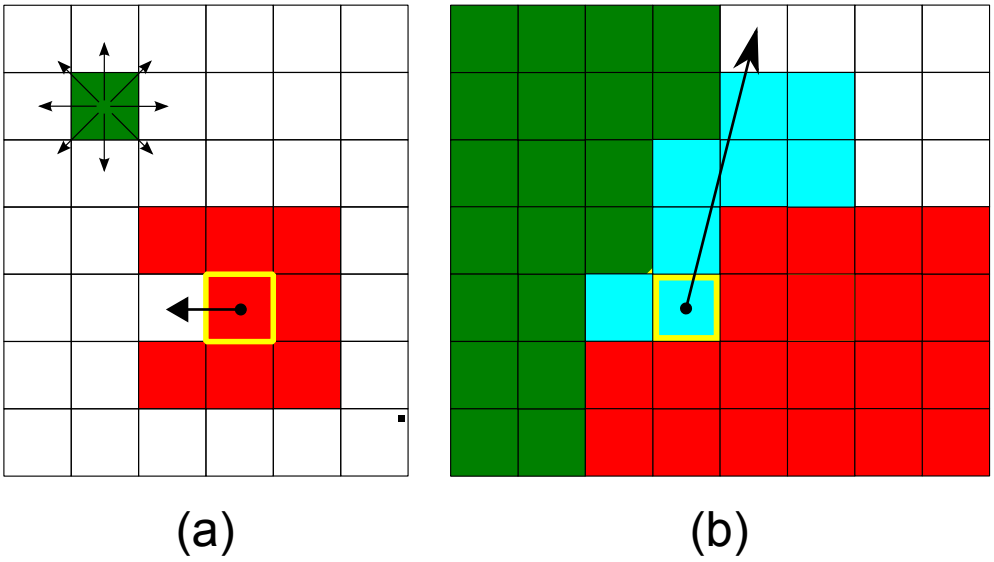

Figure 6.2 Illustration demonstrating the growth methods for simulated colonies. Cells are represented by coloured sites; white sites represent uncolonised areas. (a) An isolated single cell (green) is able to place its progeny in one of eight directions, while the highlighted red cell can only pick one. (b) In the case where a cell is locked in (highlighted cyan) by neighouring colonies (red and green), and cells from its own colony (cyan), the cell determines the distance to the colony edge, and if less than η sites, places its daughter cell at one of the available perimeter locations.

6.2.2 Growth rules

Early growth

In the early stages of a simulation, when the cell density is low, cells mostly divide into neighbouring empty sites. This is implemented in the following way.

If at least one of 8-way connected sites was empty, a new cell (daughter) carrying the same colony index number as the mother cell was placed there. If there were two or more empty lattice sites in the neighbour list, one was selected at random, and a new cell placed in it (Fig.6.2(a)). Both the mother and daughter cells were then assigned a new division time from the uniform distribution, and the simulation stepped forward to the next cell due to divide.

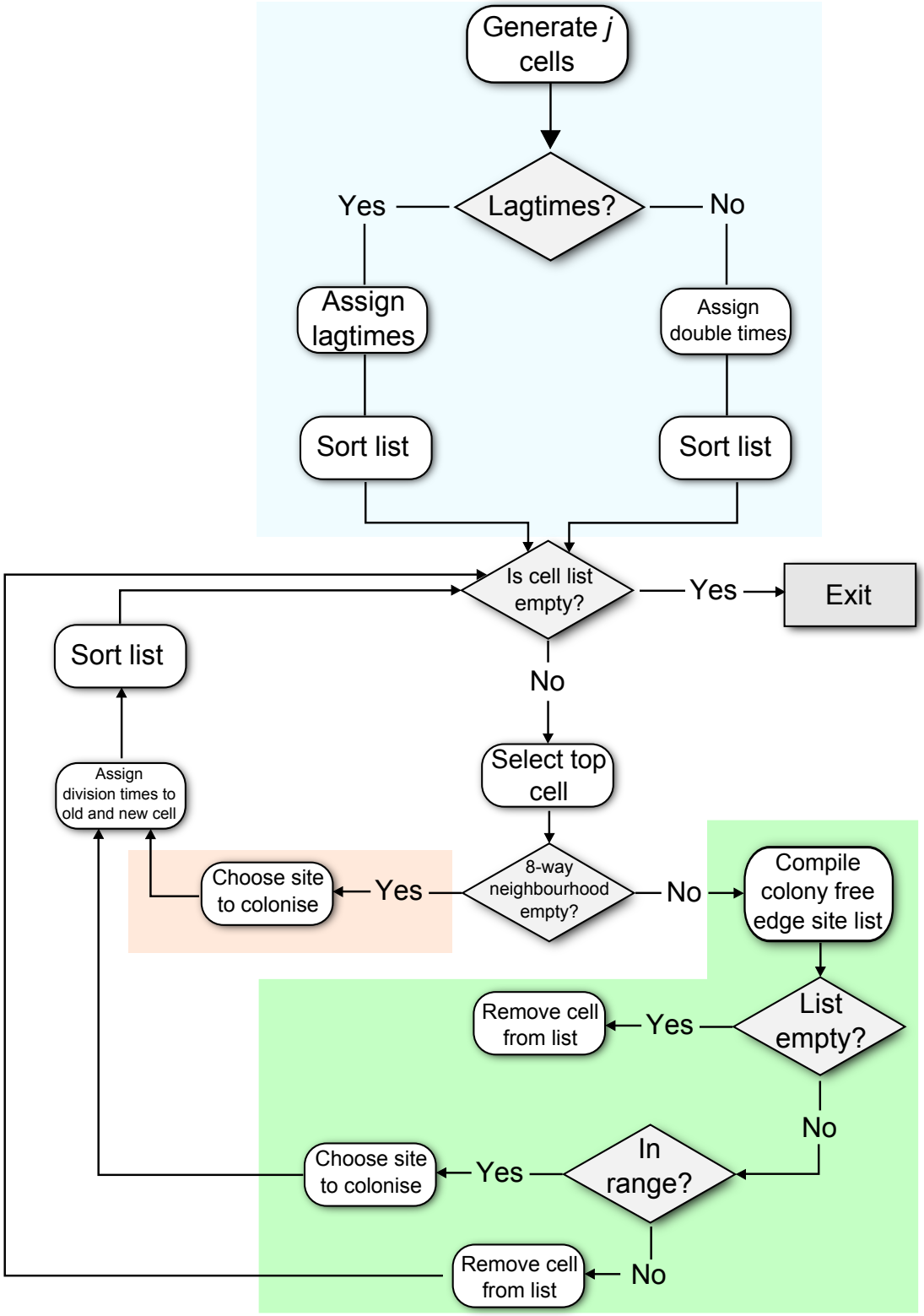

Figure 6.3 A flowchart of the main steps taken in colony propagation. Coloured boxes highlight key stages of the run: assigning cell positions and growth times (blue), initial growth dynamics (red), and colony propagation once cells become locked in their colony (green).

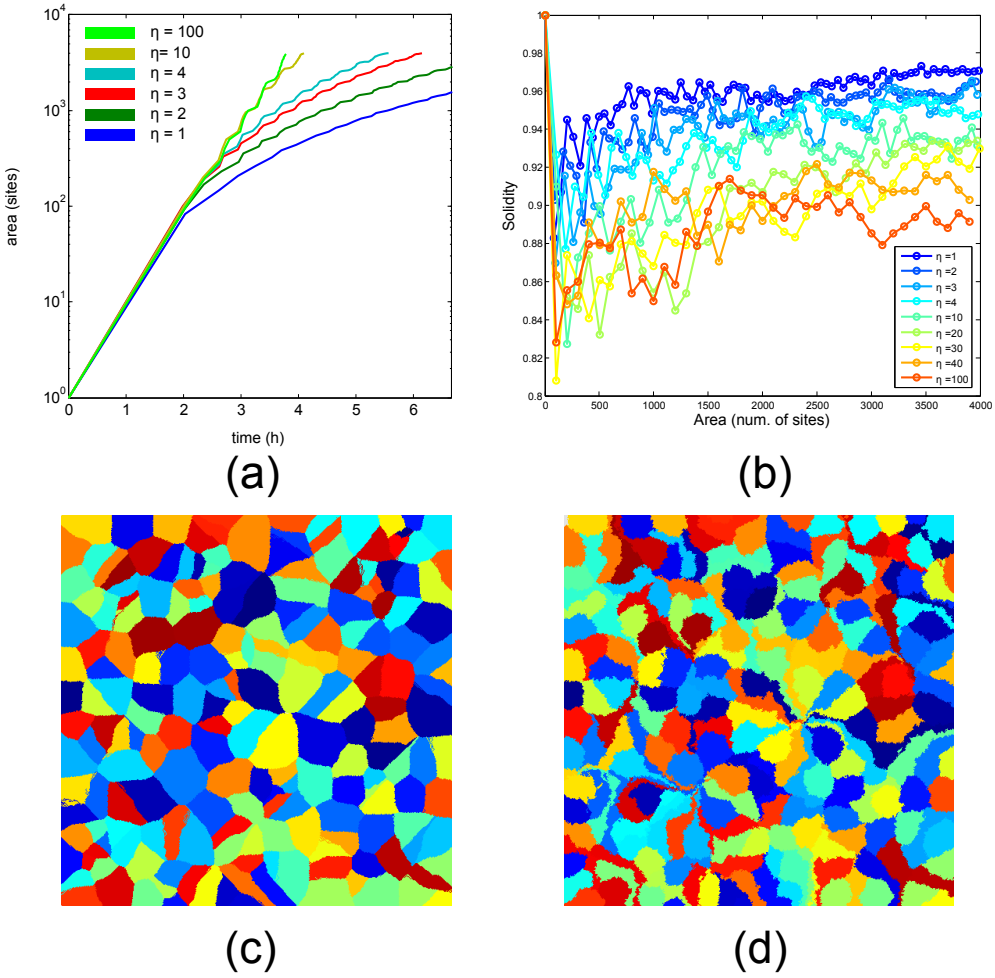

Figure 6.4 The effects of varying η, the maximum distance cells can be from the colony edge to divide, on colony area growth rates and colony morphologies. (a) Area growth curves for a single colony (no competitors) with different η values, and their (b) solidity measurements (defined as the ratio of colony area to convex hull area [59]). (c) The resulting landscape between 200 competing colonies for perimeter only growth ($\eta = 0$) and (d) exponentially growing colonies ($\eta = 500$).

Colony proliferation and collision

In the latter stages of a simulation, the chosen mother cell is often unable to divide into a neighbouring empty site, because they are full. In real life however, cells in the centre of colonies do divide, and surrounding cells are pushed aside to make room for the daughter cells. To mimic this process, we used the following protocol.

If the eight-way connected neighbours of a chosen mother cell were all occupied, a mother cell attempted to place its daughter on the edge of the colony; this is analogous to the growing mother cell's pushing forces propagating to the colony edge, resulting in the colony front advancing a small amount (Fig.6.2(b)). First, a list of all vacant neighbouring sites on the edge of the colony was compiled. From these, only sites which were less than a distance η (in dimensionless site units) from the mother cell were considered for colonisation - provided at least one candidate site existed, one was randomly picked for colonisation. If no free sites were within range, the mother cell was removed entirely from the cell list to minimise simulation times. This allowed us to implement a limit on the 'pushing power' of cell division. These steps are summarised in Fig.6.3 (green box).

We will test the effects of changing the 'pushing parameter' η in our simulations. A large η value however, corresponds to exponential growth (since most cells in the colony would be dividing), while small η values correspond to perimeter growth (*i.e.* there is an active growing ring of cells).

6.2.3 The effects of 'pushing parameter' η

Adjusting the parameter η affects both the rate colonies expanded, and their morphologies. Fig.6.4(a) shows the effect of varying η on the growth of a single, unbounded colony, without any collisions. For large values of η, the colony grew exponentially with no decay in the rate of growth. For smaller values of η, the growth rate decreased as cells near the centre of the colony were removed from the growth list. At the smallest value of η, only cells on the edge of the colony contribute to growth, and so the colony is in a perimeter-growth regime. Smaller values of η also resulted in smoother colonies: Fig.6.4(b) shows the solidity of a single colony for different values of η, where larger η resulted in rougher

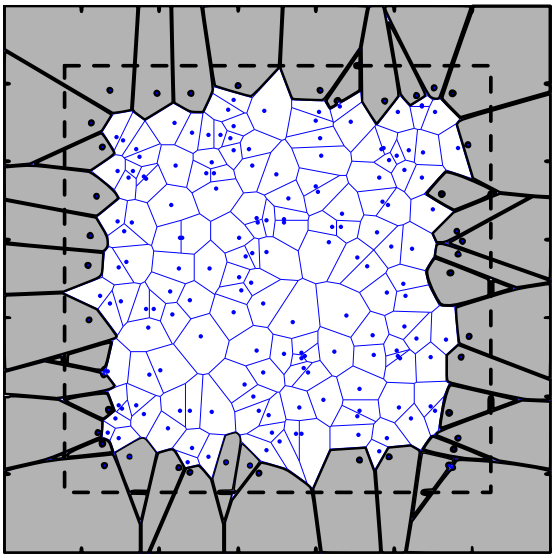

Figure 6.5 An example of a Voronoi diagram generated by cell positions (dots), and how edge polygons extended beyond the field of view. Cells near the field of view edges generated unbound Voronoi patches which had an 'infinite area' (shown as grey). These were ignored in data analysis: only the central, non-edge touching white Voronoi polygons were used. The dashed line represents the simulation field of view.

boundaries.

Fig. 6.4(c) and (d) show the effect of using $\eta = 0$ and $\eta = 500$ on the resulting colony morphologies after they have collided with each other. In both cases, the same initial configuration of 200 cells was used on a 500x500 square lattice. $\eta = 0$ resulted in regular-shaped polygons, while $\eta = 500$ produced more irregular colonies. This was a result of 'squeezing' behaviour at the collision points between colonies: for large η, when cells proliferate within the colony, their offspring cannot be placed at the collision boubdary, and instead the colony is 'squeezed', tending to expand at a fast rate in those regions of its boundary where there is empty space. This does not happen with smaller values of η. For example, when $\eta = 0$, only a small actively growing shell of cells would be growing, hence less squeezing through tight gaps.

Table.6.1 summarises the different simulation parameters tested and presented in this chapter.

Lagtime distribution	Number of seed cells	η (pushing parameter)	Repeats
None	100	0	9
		500	6
	400	0	5
		500	6
Exponential phase	100	0	10
		500	10
	400	0	10
		500	10
15 minute heatshock	100	0	10
		500	10
	400	0	5
		500	6

Table 6.1 A summary of the different simulation parameters presented in this chapter, and the number of repeats for each. η is the pushing parameter described in the main text, where $\eta = 0$ and $\eta = 500$ correspond to perimeter and exponential colony expansion respectively. Each simulation was performed on a 500×500 lattice, and each row of the table took ≈ 1 week to run and analyse.

6.2.4 Analysis

We analysed the data from our simulations in the same way as the experimental data from Chapter 5, namely Voronoi polygons, and final colony shapes. Only non-edge touching colony and Voronoi patch pairs were kept for analysis: Fig.6.5 shows that edge Voronoi patches had infinte area, and because colonies were not tracked when they grew out of the field of view, their true area was unknown. For Voronoi polygon morphology analysis, graphical patch objects had to be converted into pixel objects; doing so resulted in a small loss of shape resolution, but did not affect the resulting WI distributions.

6.3 Expansion competition: lag-time, growth regimes and density

In this section, we investigate the effects of lag-times and cell density in our simulations. In analogy with our experiments, we carry out simulations starting from both 'high' and 'low' density regimes (in a fashion similar to experiments),

where either 400 or 100 initial cell coordinates were generated in each run. This corresponds to a mean, global cell density of 1.6×10^{-3} cell site^{-1} and 4×10^{-4} cell site^{-1} respectively (compared to the experimental densities of 7.2×10^{-3} cell µm^{-2} and 1.5×10^{-4} cell µm^{-2}). We also investigate two different colony growth regimes: perimeter-only growth ($\eta = 0$) and 'maximally' exponential growing colonies ($\eta = 500$).

6.3.1 WI distributions with no lagtimes

In the experiments described in Chapter 5, we were able to vary the lag-time distribution by pre-treating the progenitor cells, but there was significant lag-time variation even for initially exponentially growing cells. The obvious question, therefore, is to what extent would variation in the outcome of competition (*i.e.* WI) be seen when the lag-time was removed altogether? We therefore carried out simulations in which all cells initiated growth simultaneously. Fig.6.6 summarises these studies.

For both high and low initial cell densities, but with perimeter-only growth, strong peaks around $WI = 1$ were measured (Fig.6.6(a,c)), although the higher density case had a slightly wider distribution. However, when we switched on exponential growth, the variation in WI increased dramatically for both the high and low cell densities. Significantly, because there was no lag-time to give any given cell a significant head start, this variation was caused by the exponential colony growth.

6.3.2 WI distributions with lag-times

Our simulations in the absence of lag-times showed that exponential growth ('squeezing') at the boundaries between colliding colonies can play a significant role in the competition for space, leading to some cells becoming winners, and others losers. How are these results changed if we do include a lag-time? This is closer to what happens in the natural environment, where environmental pressures might inhibit the growth of organisms at early stages of development; these effects have been observed experimentally in soil bacteria [61]. Furthermore, it was a feature of the experimental studies described in the previous chapter.

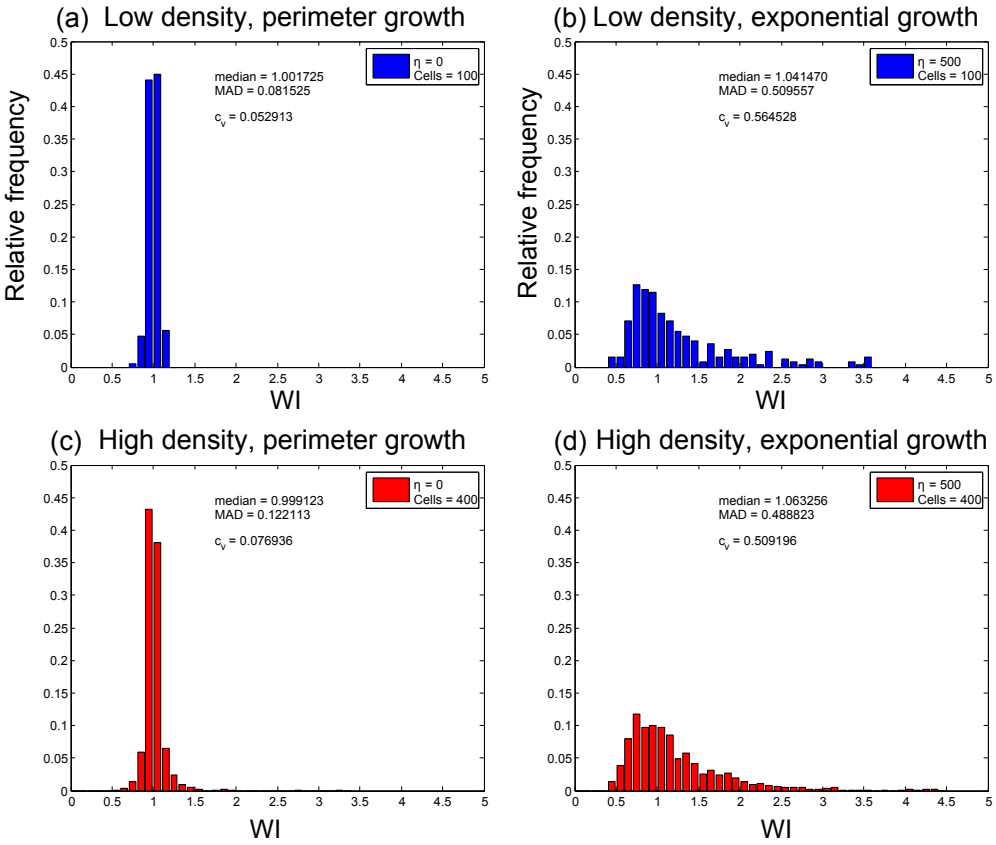

Figure 6.6 WI distributions for simulated bacterial landscapes with different numbers of initial cell densities to cover 'low' and 'high' Voronoi area distributions. Distribution statistics are shown in each panel, where MAD is the median absolute deviation, and C_{v} the log-normal coefficient of variation. (a)100 initial cells, $\eta = 0$, $N = 581$ (b)100 initial cells, $\eta = 500$, $N = 257$ (c)400 initial cells, $\eta = 0$, $N = 1950$ (d)400 initial cells, $\eta = 500$, $N = 1432$.

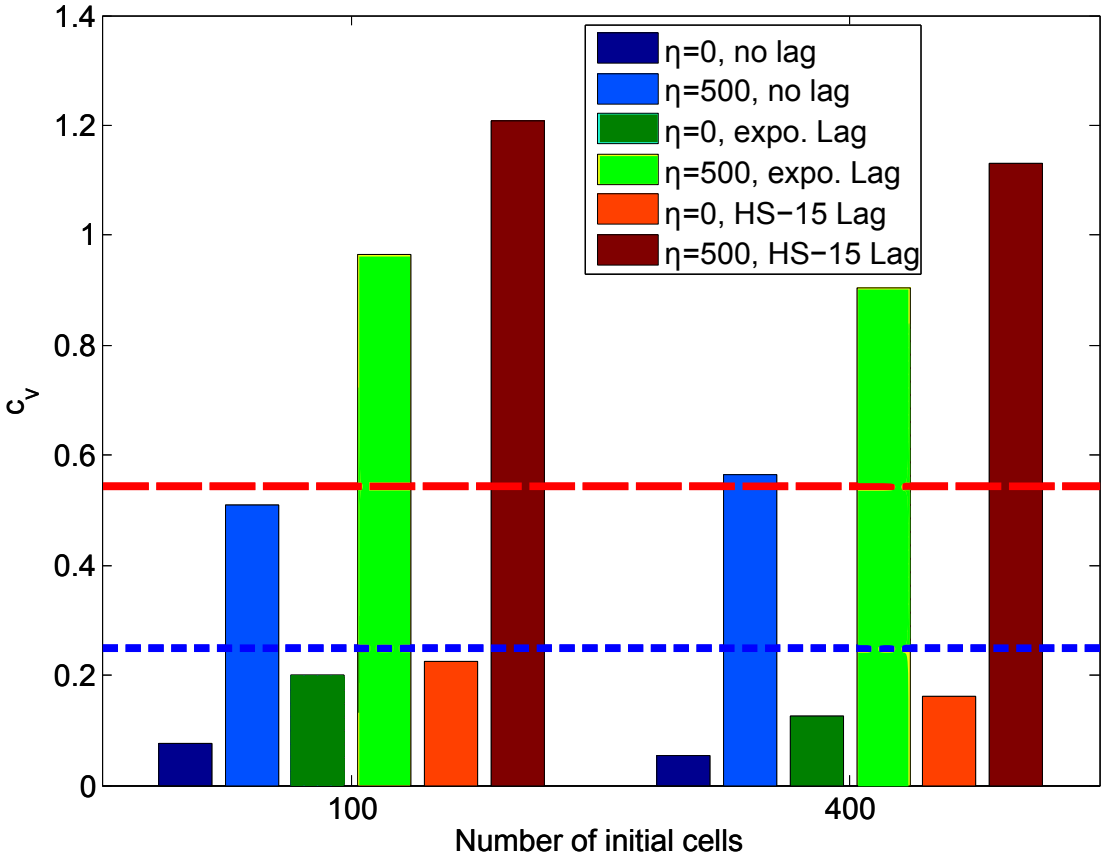

Figure 6.7 Comparison of coefficients of variation (log-normal) for WI distributions, as determined from simulations with the parameters defined in the legend. Increasing the lag-time distribution width increases the dispersion of WI values, with exponentially growing colonies more sensitive to the wider range of lag-times sampled. The lag-time distributions were sampled from the experimental ones described in the previous chapter, namely, exponentially growing cells (expo. lag), and heat-shocked stationary phase growing cells (HS-15 lag). The horizontal lines mark measured c_v values for the exponential low density (blue), and low density heat-shocked (red) experiments from Chapter 5

.

To keep our simulations as close as possible to our experiments, we replicated the experimentally measured lag-time distributions for exponential phase and heat-shocked cells in our simulations. To achieve this, we sampled lag-times for individual cells from the measured experimental distributions by generating a random number, which selected a point along the relevant cumulative lag-time distribution.

The two lag-time distributions presented in Fig.5.10 (p.53) were sampled by the progenitor cells before they commenced growth; that is, the lag-times measured for cells taken from exponentially growing cultures($\langle t_{\text{lagtime}} \rangle$ =53(16) min), and heat-shocked stationary phase cultures ($\langle t_{\text{lagtime}} \rangle$ =102(25) min). We then carried out simulations with these lag-time distributions for two separate density and growth regimes.

Fig.6.7 summarises the measured dispersion (using the log-normal coefficient of variation) in the resulting WI distributions from these runs, as well as for equivalent runs with no lag time. In all cases, wider lag-time distributions lead to broader WI distributions. Furthermore, lag-time distribution and growth strategy had a stronger effect than cell density. Lastly, WI distribution widths increased more with wider lag-time distributions when colonies grew exponentially, compared to when the lag-time distribution was widened for perimeter growth.

6.3.3 Does lag-time or colony area play a dominant role?

Combining exponential growth with wide lag-time distributions produced the largest variations in WI. However, the density did not appear to have a marked effect on the width of WI dispersions, which is in contrast to the experimental results, where increasing the cell density resulted in wider WI distributions. So, to confirm that density played a minor role in simulations, we investigated how WI varied as a function of both Voronoi area (which depended on cell density) and lag-times.

Fig.6.8 shows the relationship between cell lag-times, Voronoi patch area, and the resulting WI, for both low and high density, and for perimeter and exponential growth. In all panels of Fig.6.8, longer lag-times are associated with lower WI,

regardless of the mode of growth, and density. When exponential growth was switched on however, the inverse relationship between WI and lagtime became clearer for both densities (Fig.6.8(b,d)).

For both densities tested, there was a indication smaller Voronoi areas were associated with higher WI (Fig.6.8(a,c)). The effect was amplified when cells grew exponentially (Fig.6.8(b,d)). For example, in Fig.6.8(b), we can see that at intermediate lag-times, smaller Voronoi patches tended to win more compared to larger Voronoi patches. As discussed in the experimental chapter, the WI metric could be biased to smaller colonies, however.

From these results, it is clear that exponential growth amplifies the effects associated with lag-time, and density. However, lag-time has a clear, and more intuitive relationship with eventual success regardless of the mode of growth, while dependence of Voronoi patch size on WI could possibly be an artefact of the WI metric.

6.3.4 Summary

These results are consistent with our experimental results that lag-times are very important to the overall chances of colony success. However, the growth strategy also affected how much WI distributions changed due to wider lag-time distributions: the WI distribution widened more with exponential growth as lag-times were increased, compared to the increases seen in perimeter growth. Furthermore, even when there was no lag present, there was a remarkable amount of variation in the WI distributions when colonies expanded exponentially. Finally, there was some evidence that smaller Voronoi areas were associated with success when cells grew exponentially.

Given the clear importance of growth strategy, we next considered why exponential cells would produce such large variations in WI. As discussed, it likely involves the way exponential growing cells in our simulation would 'squeeze' at collision interfaces (§6.2.3, p.82). Could it be the case that a combination of this growth mechanism, and certain Voronoi morphologies helped some colonies outcompete others at collision points? This corresponds to the principle of boundary competition, where space is fought for at patch edges. We address this question

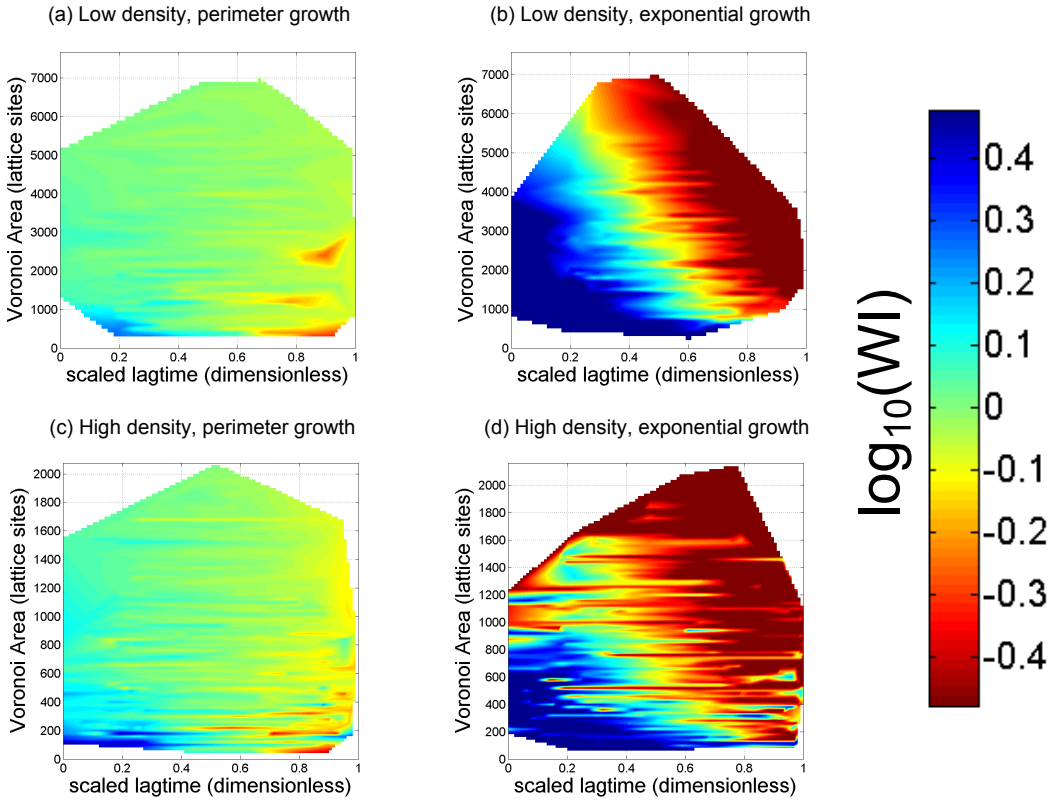

Figure 6.8 Interpolated surface plots showing the relationship between Voronoi polygon area, exponentially growing cell lag-times, and $\log_{10}$(WI) (scale shown in colour bar) for different initial seed cell numbers ($N = 100$ and $N = 400$) and growth regimes ($\eta = 0$ and $\eta = 500$). Scaled lagtimes are normalised to the maximum lagtime for that particular lagtime distribution. Winner colonies have $\log_{10}(\text{WI}) > 1$, and loser colonies $\log_{10}(\text{WI}) < 1$. (a) N=100, $\eta = 0$, (b) N=100, $\eta = 500$, (c) N=400, $\eta = 0$, (d) N=400, $\eta = 500$.

in the next section.

6.4 Boundary effects: Voronoi polygon morphologies

The manner of colony growth appeared to have the greatest effect on the resulting WI distribution, In the previous chapter, we hypothesised that boundary effects might arise because of squeezing at collision interfaces. We used numbers of neighbours and Fourier descriptor analysis to characterise Voronoi shapes, and found some evidence that 'winners' and 'losers' had distinct patch shapes. Here, we repeat this analysis for simulation data, where we have the advantage that we can turn off lag-times and control the amount of squeezing at colony boundaries. Despite simulation results indicating there wasn't a large difference between low and high density environments, we still included both global densities in our shape analysis so we could compare with experiments.

6.4.1 Does the number of neighbours affect WI?

We first checked if the number of neighbours, which determined the number of Voronoi polygon faces, affected the chances of a cell becoming a 'winner' or 'loser' colony. This is analogous to Fig.5.13 (Chapter 5, p.57).

Fig.6.9 shows the median WI measured for different number of Voronoi polygon sides for both low and high density simulations, and perimeter and exponential growth. For perimeter growing colonies (Fig.6.9(a,c)), there was no variation in the median WI for different Voronoi faces. This was perhaps expected, since previous results showed the WI distribution for perimeter growing colonies had only a small amount of dispersion.

A similar picture was seen in exponentially growing colonies - there was no trend in WI as a function of Voronoi faces (Fig.6.9(b,d)). However, examination of the error bars (defined as the median absolute deviation (MAD) for that Voronoi face number's WI distribution) showed there was more variation in the WI for each Voronoi face compared to the perimeter growth simulations, for both low and

high cell density.

To compare the WI distribution widths associated with each Voronoi face number, the ratios between each density's WI distribution width ($\sigma_{\mathrm{MAD}}(S)$) was calculated, for each S-sided polygons.

For Voronoi faces $S > 3$, the MAD ratio between high and low density simulations was on average $\sigma_{\mathrm{MAD}} = 1.0(2)$. However, for three-sided Voronoi patches, $\sigma_{\mathrm{MAD}}(3) = 3$.

In simple terms, three-sided Voronoi polygons, in high density environments, have the largest amount of variation in eventual colony success. It does not mean that 3-sided polygons are necessarily correlated with success, however, but rather they are associated with much of the variation seen in high cell density, exponentially growing simulations. What is interesting, is that the greater variation was seen in high cell environments, showing colonies growing in close-quarters, when combined with exponential growth, may be more sensitive to a 3-sided Voronoi patch shape. This provided evidence that Voronoi patch shapes may play a role in a progenitor cell's eventual success in certain environments.

6.4.2 Predicting WI based on morphology

In tandem with experimental analysis, we then check if a multi-linear regression model could be built, using the measured Fourier descriptor index magnitudes of Voronoi polygons to predict the variation in WI. Experimental results showed that more of the variation in WI could be captured in high density environments. In this case, we were able to test two global cell densities, but also control the growth mechanism.

To recap, the model is built iteratively, with Fourier descriptors only kept if they had a particular p-value. Tab.6.2 summarises the coefficients obtained using this approach when we built the model using 10 Fourier descriptors ($f_{\mathrm{n}}, -5 \leq n \leq 5$).

Tab.6.2 summarises the coefficients for each Fourier descriptor term in the final models. We can see that in the case of low density environments, fewer terms have been included in the model compared to higher density simulations. Moreover, for both densities, exponential growth resulted in more terms in the model, which

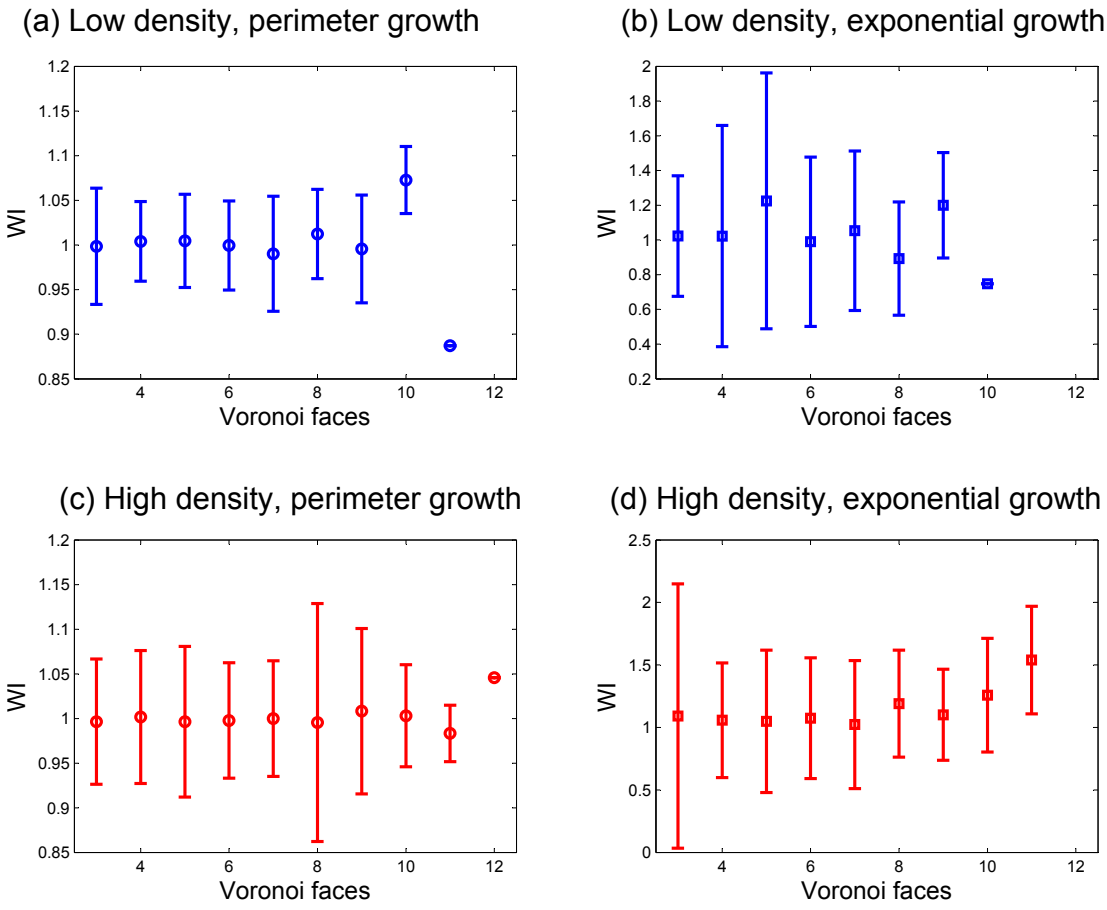

Figure 6.9 Median WI versus Voronoi faces for simulations run with no lag-time present. Error bars are the median absolute deviation.N = number of cells in the simulation. (a) N=100, $\eta = 0$, (b) N=100, $\eta = 500$, (c) N=400, $\eta = 0$, (d) N=400, $\eta = 500$

Simulation	Fourier descriptor index									
	-5	-4	-3	-2	-1	1	2	3	4	5
Low density, perimeter growth	1.12	-	-	-	0.58	-	-2.19	-	-	-
Low density, exponential growth	-	-	-	6.57	10.70	-	-32.42	-	-	-
High density, perimeter growth	1.46	1.66	-	0.47	0.58	-	-2.02	-	-	-
High density, exponential growth	19.48	13.54	8.52	6.31	2.24	-3.26	-	-	-9.51	-

Simulation	F-stat	F-stat p-value	R^2
Low density, perimeter growth	17.32	<0.01	0.076
Low density, exponential growth	17.26	<0.01	0.12
High density, perimeter growth	19.35	<0.01	0.04
High density, exponential growth	74.10	<0.01	0.25

Experiment	F-stat	F-stat p-value	R^2
Low density (experiment)	12.68	7.14E-08	0.094
High density (experiment)	16.65	2.18E-19	0.3457

Table 6.2 Coefficient values for each Fourier descriptor (our predictors) from a stepwise multilinear regression model. Each predictor has a $p < .01$, except where otherwise marked. Dashes represent rejected predictors; while Fourier descriptor values -5 to 5 were tested. Experimental R^2 values from the previous chapter (Tab.5.1,p.61) for high and low density experiments have also been re-printed here for comparison.

captured more of the variability in WI (as shown by the R^2 values). High density simulations, with exponential expansion, used the most Fourier predictor terms to capture the WI variability.

How do we interpret this? Firstly, the R^2 values for each simulation parameter combination were low, suggesting that a multi-linear model is likely to be a limited predictor of success, as we also found in the experimental models. However, comparisons between the models shows that for high cell density, with exponential growth, the most variation was captured, by using the highest number of predictors. This suggests that it is in this environment where Voronoi shape becomes most important in affecting the chances of colony success.

6.4.3 Similarities between Voronoi polygon Fourier spectra

In our experiments, we observed a clear clustering between Voronoi patch shapes of eventual winners and eventual losers, when we carried out a multidimensional

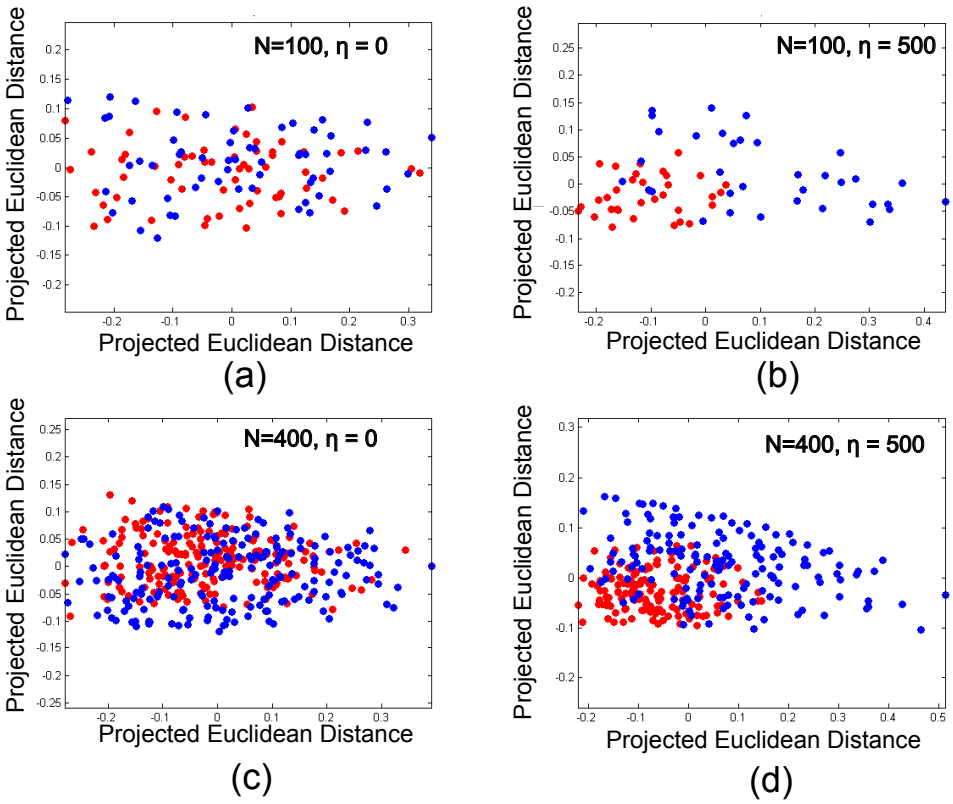

Figure 6.10 Multidimensional scaling plots of Euclidean distances betweeen Fourier spectra of the top and bottom 10 % of WI Vorono-colony pairs from simulations with the following parameters: (a) N=100, $\eta = 0$, (b) N=100, $\eta = 500$, (c) N=400, $\eta = 0$, (d) N=400, $\eta = 500$. In all panels, ●: $WI < 1$ and ●: $WI > 1$.

scaling analysis (Fig.5.16, p.62). This analysis is repeated for our simulation data.

For the two global cell densities tested, perimeter-only growth resulted in no clear distinction between the spectra of winners and loser colony Voronoi polygons (Fig.6.10(a,b)). However, for exponential growth ($\eta = 500$), where cells would squeeze along collision interfaces, there was a shift in the clustering behaviours that was consistent across both densities: loser colonies appeared to have consistent spectra, while winners had a broader range, but distinct from loser colony morphology. This is consistent with the experimental results described in the previous chapter for Voronoi polygons in high density environments.

6.5 Discussion

In this chapter, a simple simulation was used to explore the relative contributions of expansion competition and boundary competition described in the previous chapter. We focused on two global cell densities and two growth scenarios, and carried out simulations with and without a distribution of lagtimes.

6.5.1 Removing lag-times

Perimeter growing colonies match their Vornoi polygons

When the lag-time was removed altogether from the simulations in the lower of the global cell densities tested, and only cells permitted to grow from the edges of the colony, the final WI distribution was closest to a peak centred around WI= 1 than in any other parameter combination. Consequently, colonies growing in this manner will match their Voronoi patch the best, and confirms that the Voronoi model predicts colony area for when when all colonies grow identically.

However, there was still some variability in WI distributions, with some colonies out performing others. The origin of this is likely due to differences in doubling times between individual cells, and so some colonies will have had a slight growth advantage over others.

Exponential growth causes WI variability

The WI distribution widths between different cell densities with the same growth method were comparable with each other, suggesting global density on its own did not play a large role in the outcome of patch success. Changing the growth strategy so the colony grew exponentially resulted in a large increase in the width of the WI distribution for both cell densities.

This result was the first indication that for the simulations, the growth mechanism of colonies was an important contributor to the chances of colonies being either 'winners' or 'losers'. Within the context of the experimental results, that higher densities produced wider WI distributions is significant, since it shows that

density alone is not enough to explain the variability, and that in the high density environments, the variability in WI was due to the colonies still undergoing exponential expansion. For the low density experiments, colonies would be larger at the point of collision, and not undergoing exponential expansion.

6.5.2 Lag-times are more important than density

We also tested the competitive outcome when colonies sampled a lag-time from the experimentally obtained distributions in the previous chapter. We found a negative trend between cell lag-times, and the resulting WI: longer lag-times were associated with smaller WI. However, this trend was clearer when colonies expanded exponentially, again showing the importance of this growth mechanism in determining WI variability. The smaller contribution of cell density was also apparent here, where the variation in WI distributions between different density simulations was very similar for the same lag-time distributions.

6.5.3 Voronoi morphology

How important is the neighbour geometry in determining the outcome of competition? To recap, it seems likely that certain morphologies would lead to particular collision interface geometries, which might affect the resulting propagation, whereby cells would "squeeze" into the area being colonised. The Fourier descriptor method, which allows an objective measure of perimeter geometry, provided some insight into this question. The experimental results implied that in fact *loser* colonies possessed more similar shapes than winners, while there was a comparatively wider degree of 'winner' Voronoi morphology; this explains why a measure of 'geometry quality' was not forthcoming when attempting to build a multilinear model which would incorporate the descriptor terms to predict the likelihood of success.

Significantly, in the simulations, there was more clustering between outlying winners and losers when colonies were allowed to grow exponentially regardless of cell density. This result can help explain the clustering seen in high density experiments: colonies are still expanding exponentially at the point of collision in the high density experiments. For larger colonies (in low density experiments),

the expansion rate of the colonies is lower, leading to less 'squeezing' at collision points.

These results show the importance of boundary interactions in general in the natural environment, particularly when competing organisms are in close proximity. For bacteria, this squeezing behaviour arises from the manner of its growth - in other organisms, it might not manifest in the same way (such as contiguous plant growth), however. In these experiments and simulations, we also did not include lottery competition, which could offset the advantages of fast initial growth.

6.6 Conclusion

A simple discrete event simulation was used to capture the properties of a growing population of competing bacterial cells, as investigated by the experiments in Chapter 5. We found that the increase in WI variability was caused by the mode of colony expansion, where exponentially expanding colonies led to more variability in WI measurements. Global densities of the scattered population did not affect the likelihood of success, but when combined with exponential growth, Voronoi morphology became more important in determining cell success. We propose that the squeezing effects which accompanied the exponential growth are what caused these effects. Short lag-times were also shown to give colonies an advantage, in agreement with experiments.

In the context of the results presented in Chapter 5, this suggests that in the high density experiments, the wider WI distributions were partly a result of the colonies expanding exponentially, or at least, at a faster rate than the colonies in the low density experiments.

Clearly, the type of growth a surface growing population undergoes is important in deciding the extent to which it will proliferate. In the case of bacteria, which initially expand at an exponential rate, this can lead to important boundary interactions, particularly at high cell densities, where neighbourly geometries become important because of the squeezing effects.

6.7 Future work

These simulations modelled bacteria in the simplest possible way, and still managed to capture key features of the experiments in the previous chapter. A possible extension to this work could be to investigate how colonies fare in environments where neighbouring colonies possess different growth strategies altogether; a mixture of exponential and perimeter growth, for example. Furthermore, here we studied two extremes of colony growth. It would be useful to study how the WI distributions change as the squeezing parameter η is varied at intermediate values, and at what point Voronoi morphology becomes important.

Finally, while there are benefits to using a simple set of growth rules, it would still be interesting to introduce interactions between the growing colonies, similar to the suggestions made in the previous chapter, such as inhibition of growth in neighbouring colonies.

Chapter 7

Confined microcolony growth

7.1 Introduction

In the natural environment, bacteria often inhabit small crevices or niches such as interstices between soil granules, the surfaces of marine snow particles in the ocean [68], or even crevices between epithelial cells [69]. In these situations, growth of the bacterial population is geometrically confined. Given their ubiquity, it is important to understand how confined geometries affect the properties of growing bacterial populations.

In this chapter, we use a micro-patterning technique to create agarose-based microstuctures, which allow confined growth of micro-colonies in well controlled geometries. We do this using a novel method described by Moffitt *et al.* [70], whereby molten agarose is cast around a PDMS mould, resulting in structurally stable agarose micro-channels, whose widths can start from 3 µm. Using this method, we investigate three aspects of confined microcolony growth. First, we address how the physical structure of the colony, in terms of the positions, velocities, orientations and cellular density of the constituent cells is affected by confinement. Second, we investigate the genetic structure of the colony in terms of relatedness between cells. Third, the age structure of the colony, in terms of the migration of 'old poles' is investigated.

We conclude that narrower micro-channels induce longer range nematic-like

ordering of cells at smaller population sizes, which likely facilitates the high cell velocities driven by cell expansion. Furthermore, despite micro-channels restricting cell movement along channel minor axes, regions of locally more closely related cells were sometimes measured at lower colony populations compared to an unconfined colony. It is speculated that the high cell velocities mitigate confinement, allowing 'mixing' between genetically distant neighbours. Moreover, older poles are often driven to the colony edges in confined growing colonies, while in unconfined colonies, the oldest pole was internalised.

7.1.1 Physical structure of the confined colony

In the first part of this chapter, we study the effect of varying the level of geometric confinement on the structural properties of the growing micro-colony.

The structural properties of the colony are determined by cell-cell physical interactions, as well as interactions between the cells and the confining surfaces. At high cell densities, these factors become important for the colony's overall function, since sub-optimal cell arrangements can impede incoming nutrients and outgoing waste products to the colony core.

Previous studies have shown that for cells grown in PDMS quasi-2d channels, a net flow field of cells along the long axis of the chamber was established due to cells proliferating and pushing against one another as they expanded: Cells were found to rapidly reorient themselves along the flow direction until imperfect nematic ordering was reached[14]. This work demonstrated that cells growing in a confined space could experience structural rearrangements thanks to expansion flow: the combination of cells replicating in the centre of the colony and pushing against each other due to steric interactions. Studies employing more complex growth geometries also showed that close packing of cells quickly resulted in cell alignment directed towards growth-chamber exits, but that cell alignment tended to be governed by the chamber wall shape. Further, local order was found to extend over many cell lengths [13], although *buckling instabilities* within the colony arising from high-pressure regions were found to prevent a perfectly ordered nematic state (Fig. 7.1(a)) [15]. While the cell orientation was believed to facilitate cell escape, others showed cells nearer trap exits often stagnated which impeded cell escape. This arose due to higher concentrations of nutrients

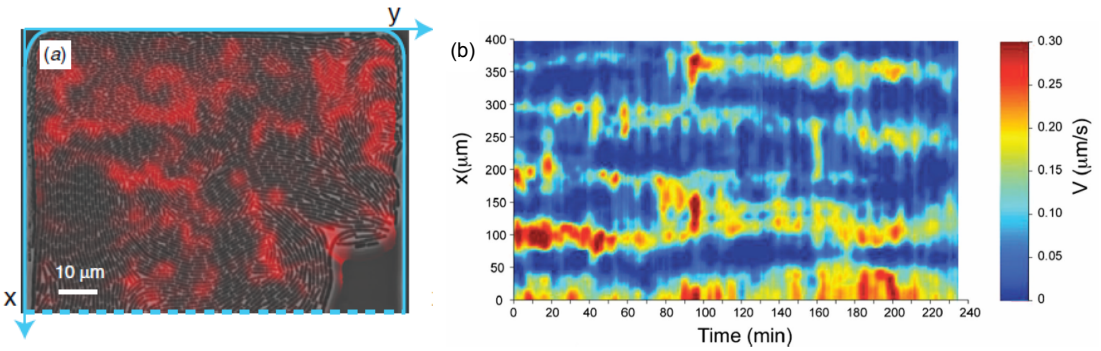

Figure 7.1 Plots adapted from [15] and [16]. (a) A phase contrast image of a colony growing in a PDMS corral, with overlays showing regions of disorder. (b) A kymograph showing the evolution of cell streaming patterns at a cell trap exit; red regions correspond to faster moving cells flowing around slower cells stagnating at the trap exits.

leading to larger cells: cell escape was therefore an interplay between cell size and orientation (Fig.7.1(b)) [16]. Frictional forces were also found to play a part in these streaming patterns, and have also been shown to play a significant part in the transition from to 3d colony development [71].

These previous studies all used growth chambers made from PDMS. In contrast, in this chapter we confine colony growth using agarose. As agarose is comparatively softer, it will exert a smaller force on the cells. Moreover, the channel depths used are 2 µm, which means cells will not experience a frictional force from the glass coverslip. While previous studies have investigated cell structure in open-ended channels at a fixed width, here we use a range of quasi-2d channels, each with different aspect ratios [14, 70].

7.1.2 Relatedness and cooperation

Later in this chapter we will also track a different aspect of colony structure: the genetic structure. By this, we mean the generational gap (or *genetic distance*) between any two cells in the colony, at a particular point in time. Fig.7.2 provides an illustrative example of this concept. Genetic distances are potentially very important in explaining how apparently cooperative behaviours can be maintained in populations. Cooperative behaviours, in which one individual apparently sacrifices its own fitness for the good of the "community", has been observed in a range of organisms including bacteria, but has long posed a problem

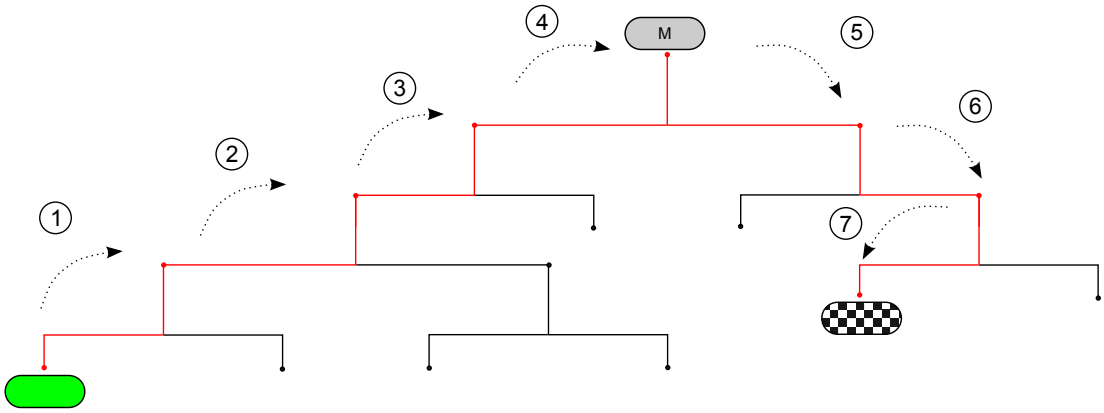

Figure 7.2 An illustration of how genetic distances between cells are calculated. In this example, we wish to know the genetic distance between the green cell and the chequered cell. The genetic distance is quantified by counting the number of 'steps' taken when moving along the colony genealogical tree between cells. Here, the target cell is comparatively distant with $D = 7$, since we have to count all the way back to the original mother cell, labelled 'M'.

for evolutionary biology. For example, altruism between individual organisms has been observed in a variety of organisms, including bacteria [72]. However, the phenomenon has long posed a problem for evolutionary biology. This problem arises because evolutionary theory suggests that non-cooperative 'cheats' should have higher fitness and eventually take over the populations [73, 74].

A potential solution to this problem is the concept of kin selection [75], which states that cooperating with closely related individuals is evolutionary stable, since the recipient of the cooperative behvaiour shares genetic material with the cooperator [76]. In bacteria, these ideas have been proposed as potential explanations for the production of metabolically costly, but beneficial to surrounding cells, iron scavenging molecules in the bacterium *Pseudomonas aeruginosa* [73, 77].

The concept of kin selection is closely interlinked with spatial structure within a population, since relatives are often likely to be found close by. In particular, because bacteria reproduce via binary fission, descendant cells (daughters) in microcolonies will initially be in close proximity to each other, in contrast to liquid culture, where cells will be well mixed. A local abundance of close relatives has interesting implications for kin selection since it implies that the benefits of cooperative behaviour can be distributed non-selectively, without the risk of

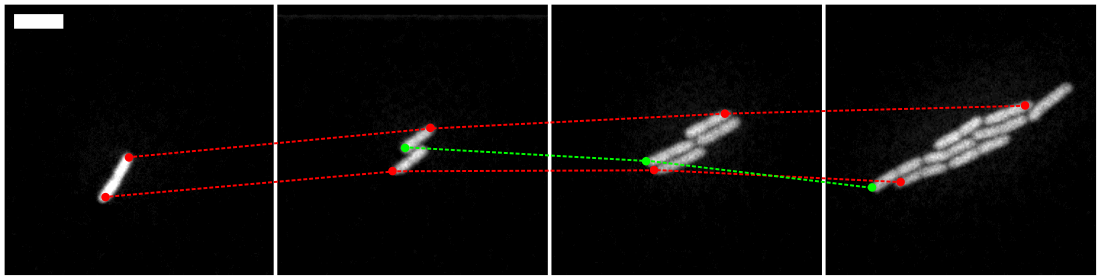

Figure 7.3 Snapshots of a growing microcolony at different times. The original poles from the mother cell are tracked between frames by the red line. These are deemed the eldest of the poles in the resulting microcolony. The green line marks the progression of a younger pole from its birth in the second frame. Scalebar = 5 µm.

inadvertently aiding a non-closely related cell. Spatial structure therefore, within the wider context of cooperation and altruism, is a very important aspect in communities which have limited dispersal of individuals. Effects on the spatial structure of a growing cell population due to confinement might be expected to have important implications for the maintenance of cooperative traits within that population.

7.1.3 Ageing in colonies

Finally, in this chapter we will also investigate the age structure of the confined colonies. A key feature of growth in *E. coli* is that it undergoes morphological symmetric division, with each mother cell splitting into two daughter cells of equal size. The two new cells in the past have assumed to be brand new [78]. This would imply that a bacterial cell lineage is 'functionally immortal', replicating forever at the same growth rate in a steady state environment [78–80].

However, it has recently been pointed out that the relatively small rate of cell wall turnover means that mother-pole material is conserved in the daughter poles [81, 82]. Thus, because a physical part of the mother has been conserved in the daughter cell, we can can consider a given cell pole as being younger or older based on the number of generations is has existed (Fig.7.3). The question is then whether this marker of age correlates with ageing-like behaviour.

Experiments tracking the growth rate of cells carrying an old pole have shown that over many generations, they start slowing their growth rate, a feature of

ageing [79]. This slowing rate was directly attributed to asymmetric divisions of protein aggregate within the cell upon division, leaving one side of the cell accumulating more damage than the other [82]. Furthermore, cells carrying new poles experienced a metabolic boost in the form of an increase in biomass yield and growth rate [83]. Alternatively, the old pole age has been shown not to affect growth rate reduction, but instead contributes to the cell death probability [84], possibly as a result of some accumulation of disadvantageous chemical. Nevertheless, this highlights the importance of a cell's elder pole age within a colony, even if the exact ramifications of old poles are still being understood: cell movement is comparatively restricted compared to well-mixed populations, so any age-related effects will be localised to particular points within the colony.

7.2 Method for constructing patterned agarose structures

In this section I describe how our experiments were set up. In all parts of the chapter, we compare results for colonies grown in agarose channels to those for cells grown unconfined on a flat agarose surface (referred to as *unconfined* colonies). The strain RJA002 was used in all experiments, and cells grown in M9 + glucose (0.4%); this media was also used as the base for the agarose surfaces. YFP fluorescence exposure times were chosen to limit cell photo-bleaching, and the time-step in all experiments was Δt=4 min.

The following sections detail the protocol, adapted from [70], used to create the agarose structures. DNase and RNase free, electrophoresis tested low melting point agarose, supplied by Fisher Scientific (product code:10377033, $T_{gel} = 25\pm 5\,^{\circ}\mathrm{C}$, $T_{melt} \leq 65\,^{\circ}\mathrm{C}$) was used in all microchannel experiments.

Briefly, the agarose channels were created by casting molten agarose around a PDMS mould. Once the agarose had solidified, it was peeled away from the mould, leaving small grooves 2 µm deep in which bacterial cells could grow in (summarised in Fig.7.4). The agarose walls spatially restricted cell movement, and by using moulds with different channel aspect ratios, the degree of cell confinement could be controlled. In the next section, I explain the protocol used to create the channels in more detail.

Designed dimensions (L × B × D)	Final dimensions (L × B × D)	Used?
1 µm × 200 µm× 2 µm	<2 µm × 200 µm× 2 µm	no
2 µm × 200 µm× 2 µm	2.7 µm × 200 µm× 2 µm	yes
4 µm × 200 µm× 2 µm	5 µm × 200 µm× 2 µm	yes
8 µm × 200 µm× 2 µm	10 µm × 200 µm× 2 µm	yes

Table 7.1 The agarose microchannel dimensions designed in autoCAD, and final dimensions as measured by phase contrast microscopy.

7.2.1 PDMS masks

Channels were designed in AutoCAD (Autodesk, Inc.) with the dimensions listed in Tab.7.1. From this, an SU-8 photoresist was built by the Zagnoni lab at Strathclyde University. The mould consists of a Silicon wafer, onto which an SU-8 path was etched. The wafer was cleaned thoroughly by subjecting it to multiple exposures to pressurised Nitrogen, and then placed in glass petri dish. To prepare the PDMS, a base elastomer and curing agent (Sylgard®184, *Dow Corning*, ratio 10 : 1) were stirred thouroughly with a fork for at least 5 min, and placed in a dessicator connected to a pump for de-gassing. After 30 min, the PDMS was poured over the Si wafer, and de-gassed for a further ≈60 min, until the number of bubbles rising to the surface was small, and limited to the edges of the petri dish. Depending on the amount of bubbles in the PDMS prior to casting, this step could vary in duration, but repeated vacuum-pressure cycles sped the overall process up without affecting the overall structure quality.

Once the number of bubbles rising to the surface had diminished, the PDMS was cured at 80 °C for 1 h, and cut from the petri dish with a scalpel. Ethanol was used to rinse the PDMS-Si interface, which helped separate them. The PDMS channels were inspected using phase contrast microscopy (Fig.C.1, p.181), which showed the narrowest channels were consistently malformed. However, repeating the protocol several times eventually yielded satisfactory channel quality for the second smallest channel and upwards (Tab. 7.1).

7.2.2 Agarose channels

The PDMS block was first cut to size and placed face-up in a 60 mm diameter glass petri dish for storage. Before use, it was cleaned using Scotch tape (3M™

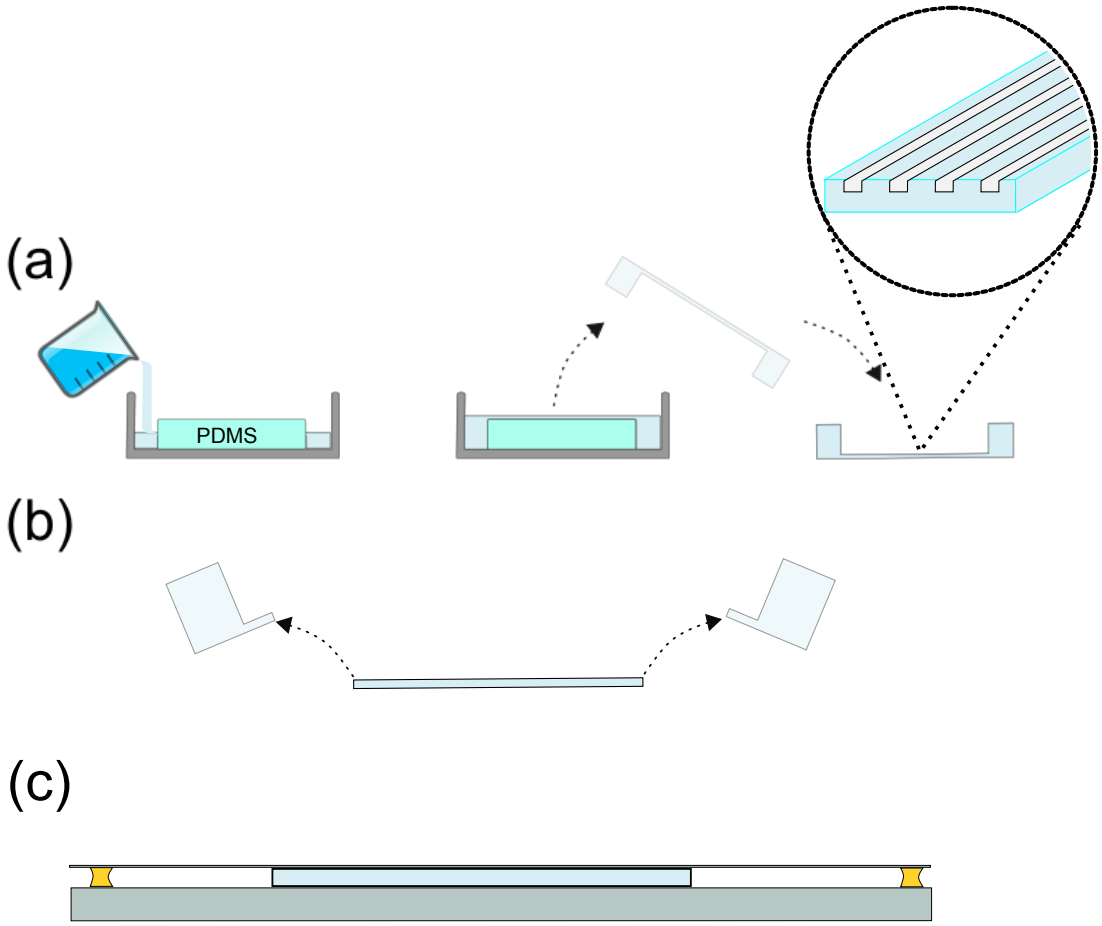

Figure 7.4 Cartoon of agarose casting process while building agarose microchannels. (a) First, the molten agarose is poured around the PDMS mould and left to solidify. Once removed, the agarose is patterned with microchannels (inset). It is then: (b) cut to shape and (c) inoculated and sealed with a glass coverslip.

Vinyl Tape 471.) to lift large contaminants, and then subjected to a series of pressurised Nitrogen bursts to ensure all small contaminants were removed.

0.5 g low melting point agarose was weighed out into a sterile 50 ml falcon tube, and 10 ml media added. A sterile pipette tip was used to break up any large clumps of agarose. The falcon tube was placed in a 80 °C water bath for an hour, by which time the agarose had melted. The molten agarose was mixed gently, and left for a further hour, gently mixed again, and poured into the petri dish holding the PDMS structure, until the block was fully submerged (Fig. 7.4(a)) It was found a depth of 5 mm was sufficient to account for the agarose contracting while cooling, but still leave an appropriately deep layer of agarose over the channels; if too shallow, the final slab was flimsy, while if too deep, the final sample was

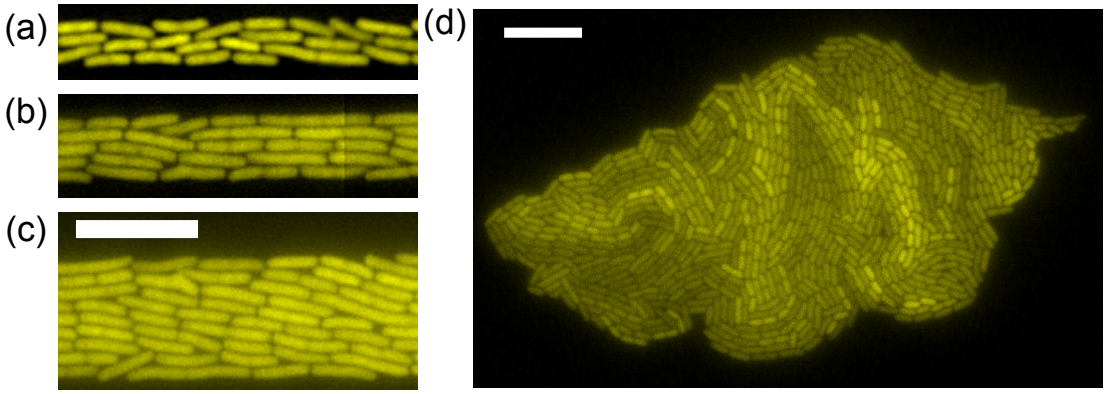

Figure 7.5 Fluorescent images of colonies growing in (a) 2.7 µm, (b) 5 µm, (c) 10 µm channels. (d) Fluorescent image of a normal, surface growing microcolony. Scale bar =10 µm.

hard to make airtight. The agarose casting step was performed in a 30 °C room at 40 % humidity, and the agarose left to solidify over the course of an hour.

Next, impurities and contaminants were removed from a glass coverslip by subjecting it to plasma treatment; this also served to increase the glass surface hydrophilicity, leading to improved adhesion between the coverslip and agarose microstructures. Within 5 min of plasma treatment (to best take advantage of the coverslip's clean state) the now patterned agarose block was coaxed from the petri dish using a scalpel, cut to shape and placed on a microscope slide ready for inoculation (Fig. 7.4(b)). Once the inoculate had dried, a coverslip was placed over the agarose, and the edges sealed with VALAP (Fig. 7.4(c)). Any spare agarose pads were kept submerged in aqueous media in an airtight container at 4 °C for up a to a week. Using high percentage agarose meant the channels were structurally stable, and could be handled with a degree of robustness. Following agarose-imprinting, PDMS intermediates were washed in a 90 °C de-ionised water bath and stored in airtight containers between experiments.

Agarose channels were shown to hold cells up to the limit of the channel length (200 µm). Initial imprinting attempts resulted in cells bursting from channels and escaping into adjacent channels. However, while repeated use of the PDMS mould is believed to improve their wettability [70] (and therefore the imprinting process), the coverslip plasma treatment was likely the key factor in these experiments. Fig.7.5 shows the effect of different channel widths used in these experiments on colony widths compared to a normal growing colony. The primary gross morphological difference between colony types was therefore aspect ratios as a

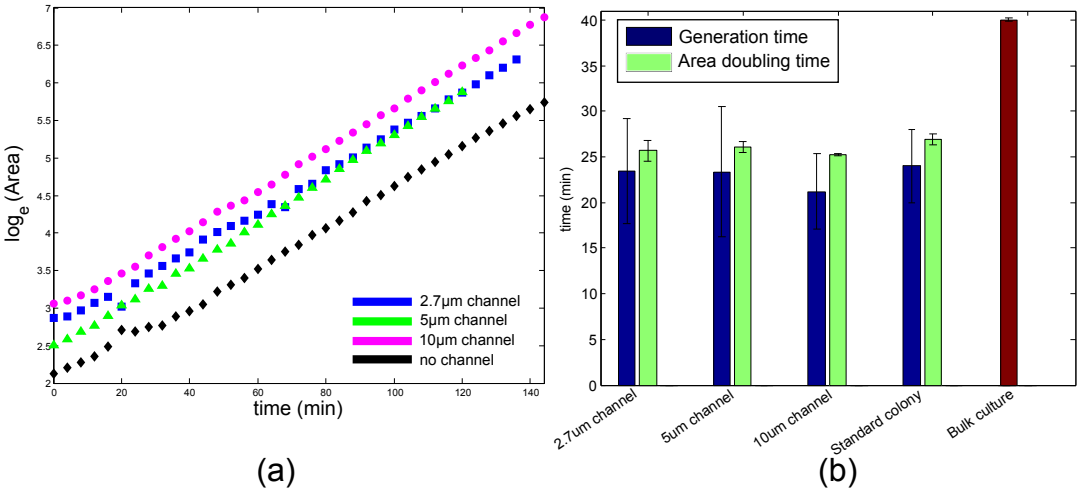

Figure 7.6 (a) Colony area versus time for microchannel growing colonies and normal surface growing colonies. (b) Comparison of growth rate metrics for the different colony types. Generations times (blue) are the length of time a single cell lineage existed. Doubling times (green) are calculated from linear least square fits made to area growth data in (a). Also shown are population doubling times from liquid bulk culture (red).

function of cell population.

7.3 Charactering the physical structure of confined microcolonies

In this section, I compare the results from studies comparing structural and morphological features of microchannel grown colonies, compared to those of an unconfined colony.

7.3.1 Microchannel growth

We first tested whether there were significant differences in the rate of growth of colonies grown in microchannels compared to the unconfined colony. Such differences might have been expected [85], since, even though the nutrient and temperature environment were the same in all experiments, the agarose concentrations for unconfined and confined colonies were very different (2 %

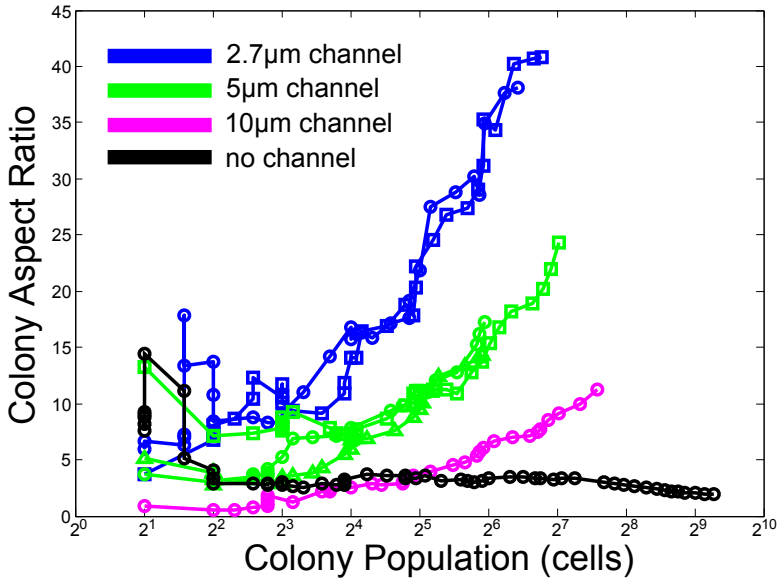

Figure 7.7 Aspect ratios of colonies grown in different microchannels, as a function of their colony population.

compared to 5 %). To analyse the rate of growth, the time-lapse movies were thresholded in ImageJ, and the colony area measured in time.

Representative area growth measurements for each experiment type are shown in Fig 7.6(a). From these, linear least square fits were used to calculate estimated colony doubling times (g_d), which were very similar (Fig.7.6(b)). To check consistency with alternative data sources, mean generation times were checked from the individual lineage data of each cell. These times (Fig.7.6(b)) were consistent with colony area doubling times, although the 4 min timestep contributed to a larger uncertainty. For comparison, the doubling time extracted from liquid media optical density measurements for RJA002 is also shown, demonstrating how area and population measurements don't necessarily match those of light scattering measurements. However, we can conclude the nature of geometrical confinement has no impact on the overall population growth rate.

7.3.2 Microchannel colony morphology

In spatially restricting the growth of colonies in microchannels of varying widths, the morphologies of the colonies were expected to be affected.

Fig.7.7 shows the aspect ratio of the growing microcolony as a function of its

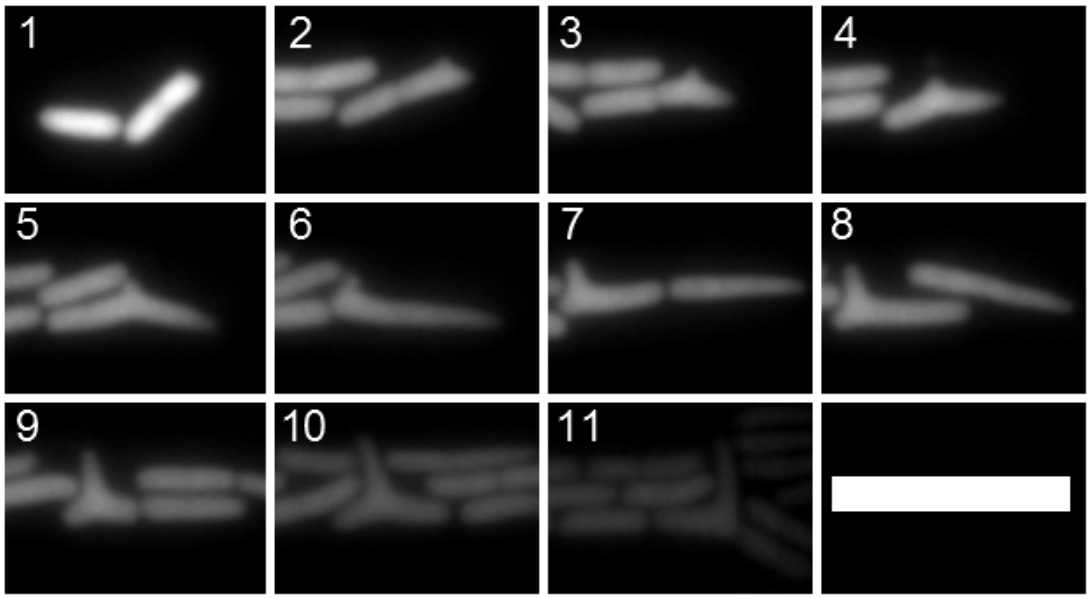

Figure 7.8 Snapshots in time of a growing microcolony in a 2.7 µm channel, tracking a single cell exhibiting anomalous morphological features. The frame 1 shows a pair of normally shaped cells, before a spur develops just short of the cell pole. The spur gradually ends up at the mid-point of the cell (frame 3) before growing. Frames have been picked at non-regular intervals of colony lifetime, but are in order of panel number. Scale bar= 10 µm.

area. While early stage microcolony development (before channel walls affected the colony shape) could be very similar between channels, the colony aspect ratios differed significantly between population sizes larger than about 32 cells (2^5) (Fig. 7.7). Therefore, any comparisons between colonies were made for population sizes greater than this threshold. Fig.7.7 also shows that as the colony populations increased, narrow channels resulted in longer, but thinner, colonies, compared to wider channels and unconstrained growth.

7.3.3 Cell morphology

As shown earlier, geometrical confinement did not affect either the growth rate of colonies or cell generation times. However, non-standard cell shapes were observed in ≈8 % of microchannel experiments; Fig.7.8 shows an example of these cells. The spur which appears near the end of the cell in Fig.7.8 was observed to 'drift' to the cell midpoint due to asymmetric cell elongation. Cell growth from the spur soon resulted in a large protrusion which persisted despite further

cell division, resulting in a striking Y shaped cell. These cells were not observed in unconfined colonies, but occurred in of channel experiments. Onset of spurs could occur at any point of the colony's development.

Erroneous cell shapes, such as filamentation, can often hint at sick cells, but in the case of the 'budding' in *E. coli* cells as seen in Fig.7.8, previous work has suggested the driving process can be abortive attempts of separation, split polar caps, or *de novo* generation of pole caps [81, 86]. While damage to the peptidoglycan cell envelope has been shown to result in bulging of the cell wall at the cell midpoint [87], the initial spurs observed here appear near the pole cap. Such types of abnormal growth are believed to originate from mis-localized inert patches of peptidoglycan which typically support the cell shape at poles[81, 86]. Furthermore, the resulting extra pole functions biochemically as a normal pole [88]. The triggering factor is still not understood however, so it is unclear what factor in these experiments caused some cells to change their shapes. It would be interesting to investigate this in future work. However, since the frequency of these events was uncommon, and since cell growth rates were unaffected by the channels, the occasional appearance of these misshapen cells was not considered a cause for concern.

7.3.4 Cell orientational order

Previous studies of *E. coli* microcolonies have often observed orientational ordering of the cells [13, 14, 16]. Orientation ordering within a colony may provide a way to aid the passage of nutrients and waste to and from the interior of colonies, and may also provide a way to relieve mechanical stresses originating from cell growth in a confined environment [13]. The latter idea might suggest that orientational ordering might be significantly different in confined colonies compared to unconfined ones.

Here we tracked the average cell orientation and its variation among cells in the population, as a function of the size of the population. Fig.7.9 shows the effect of confinement at different channel widths on cell orientation with respect to the long-channel axis. Generally speaking, the wider the channel, the more variation in cell angles were observed as a function of colony population. Variations reduced once cells became packed by the channel walls however. The two smallest width

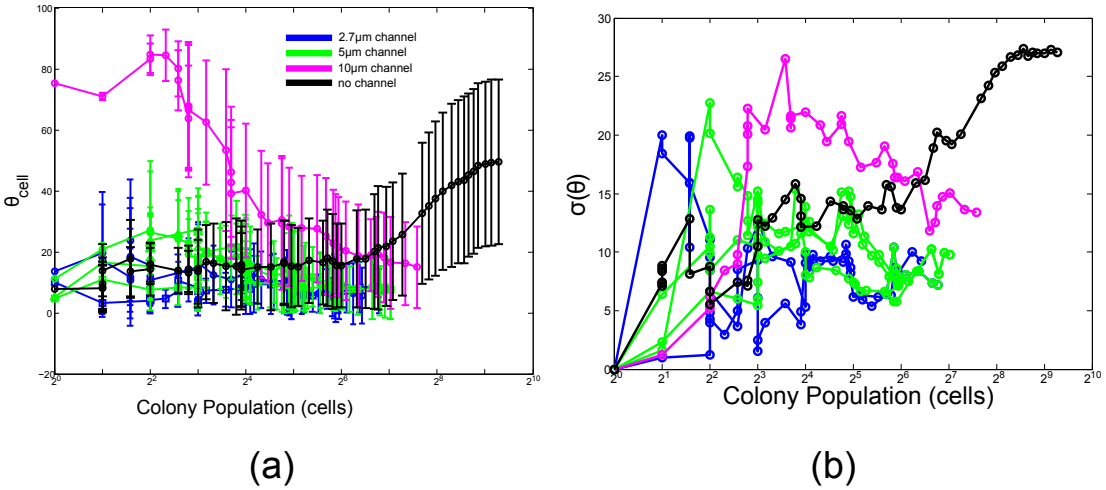

Figure 7.9 (a) Variation in the mean cell angle to the horizontal (θ_{cell}) in each colony type, errorbar standard deviation. (b) Standard deviation of cell angles (i.e., the error bars in (a)) as a function of colony population.

channels also showed closer agreement with each other in the variation of cell angles as the colony grew, suggesting the channel walls greatly restricted possible cell orientations. For an unconstrained colony, the variation plateaued after 8 generations, suggesting that the colony was large enough at this point for cells to equally sample particular angles.

The local orientation was probed by defining an orientational order parameter as [89]:

$$\eta(r) = \langle \sum_{i=1}^{N} |cos\theta_{i,j}| \, / N \rangle \tag{7.1}$$

where N was the number of cells found in a shell of width r, and $\theta_{i,j}$ the angle between cells i and j. $\eta(r)$ therefore describes the average distance over which cell orientations are correlated with each other: $\eta(r) = 1$ for the case where two cells a distance r are on average perfectly aligned, while $\eta(r) = 0$ when the cells are orthogonal.

Fig.7.10 shows the function $\eta(r)$ in channels of different widths, at different stages in colony growth. Cells growing in the 2.7 µm and 5 µm wide channels collided with the channel walls early in their growth, and so exhibited high orientational order ($\eta(r) > 0.9$) across the length of the channel for even low colony sizes -

each panel of Fig 7.10 shows the curves for these channels at high values for all values of r. Comparatively, the 10 µm channel initially showed less local order, and even less than the unconfined colony (Fig.7.10(a), $N = 61$ cells), until the effect of restriction from the channel walls were felt at ≈ 100 cells, whereupon cells showed more evidence of orientational order at small distances; Fig.7.10(c,d) shows this transition.

These results show that the greater the degree of confinement, the longer range the orientational ordering there is in the colonies between the cells. Narrower channels also had longer range order at smaller colony population sizes. Furthermore, results from the 10 µm channel show that order could increase for a colony that had been free to grow unresticted for a period before colliding with the channel walls.

7.3.5 Density and cell size

For colonies growing in enclosed environments, cell density is expected to increase rapidly as space quickly becomes scarce. This may impair the transport of nutrients and waste products. In our experiments however, cells were free to escape mechanical pressure from one of two exits, which might be expected to reduce the overall pressure, and lower the cell density. We therefore probed the effect of our particular channel design on the resulting cell density, and compared it to a normal growing colony.

Fig 7.11(a) shows the colonies' average cell density as a function of colony population, calculated as the total colony area (including cell-cell interstices) divided by total population: $\rho_{\text{cell}} = N/A_{\text{colony}}$. No apparent difference was detected between micro channel colony experiments, although a standard growing colony had marginally higher densities than all microchannel growing cells beyond a colony population of 16 cells by 0.06 cell μm^{-2}. This is equivalent to an extra cell every extra 17 μm^2 of total colony area.

Examination of maximum density measurements within each colony type (Fig.7.11(b)) showed indistinguishable results for all channel widths, although maximal cell density did increase with population growth in all experiments. This suggested the difference in cell densities seen between channel grown colonies and standard

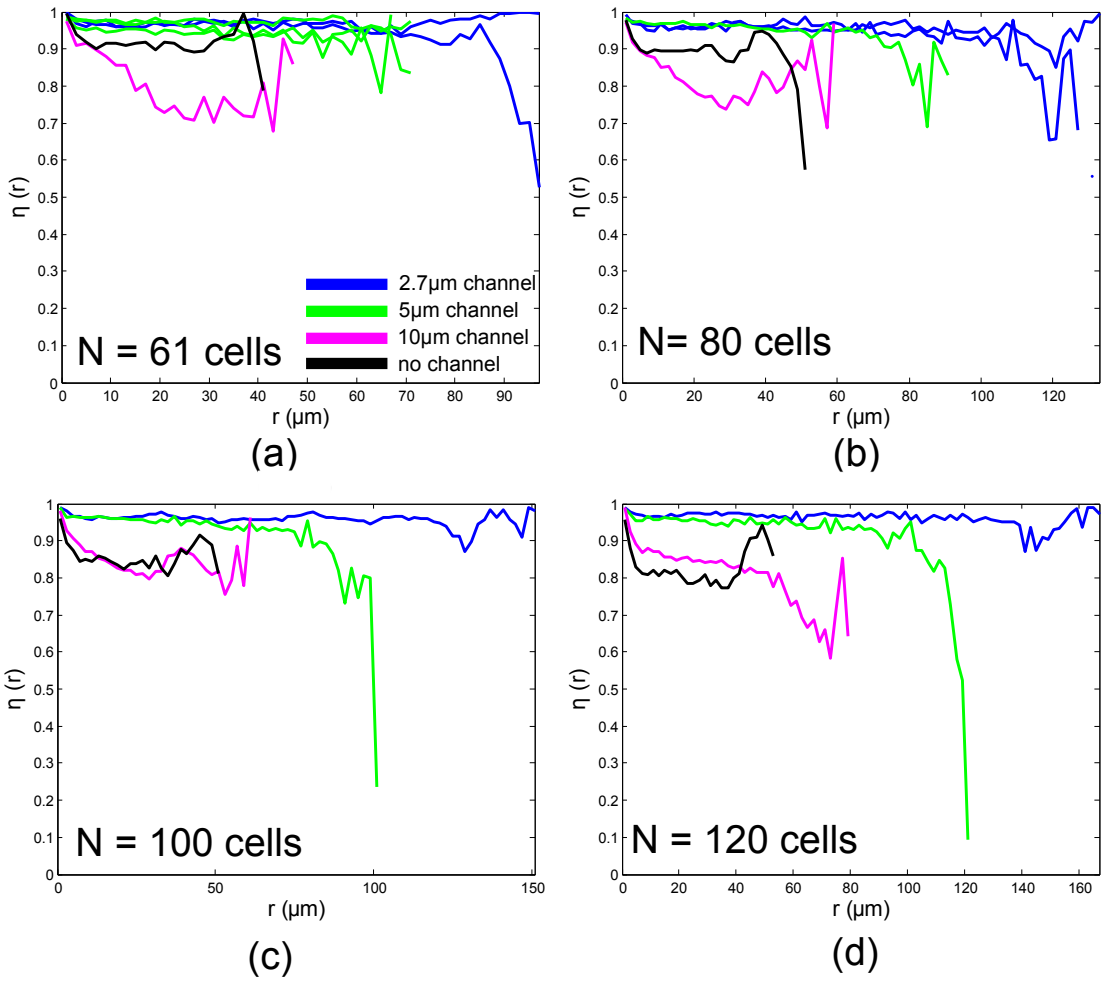

Figure 7.10 Variation in orientation order parameter for cells growing in channels and normal growing colonies at different colony populations. The different channel widths means variations in colony lengths, hence variations in the distance over which the parameter has been calculated. η measured for each colony at the following colony population: (a) 60 cells, (b) 80 cells, (c) 100 cells, (d) 120 cells.

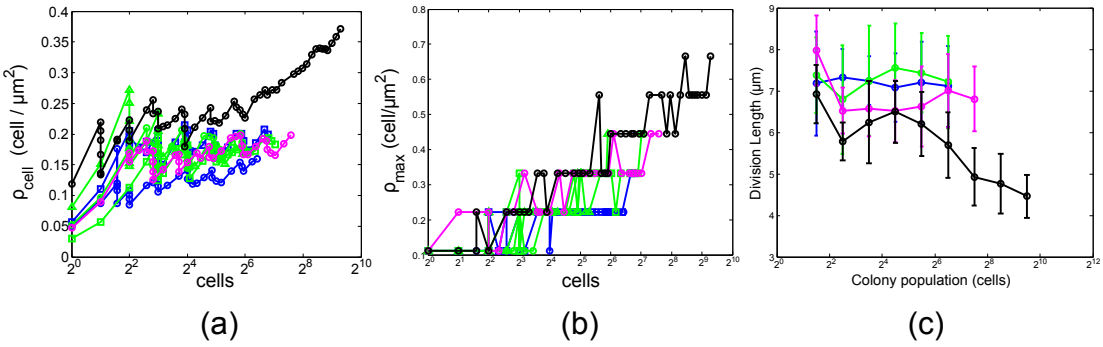

Figure 7.11 (a) Global colony cell density versus population. (b) Maximum measured colony cell density versus population. Bin area =9 μm^2. (c) Mean cell length at division versus colony population.

is potentially driven by a difference in average cell size. Fig. 7.11(c) shows the mean length of cells at the point of division as tracked during population growth in the channels and in the unconfined colony. In most cases, the standard colony cell length is lower than that of the microchannels, which would translate to more cells being found in a unit area. The standard colony also shows an extended trend towards smaller division lengths as the colony becomes larger, which is possible a result of a depletion of nutrients [90].

The channel structure might offer an explanation for this difference: cells growing in the channels inhabited a 2 μm deep gutter, and so the colony front did not have to push through agarose, whereas the standard growing colony did. In the latter case, the agarose would exert a radial force, serving to compress the cells more than channel-growing colonies. This would result in fewer or smaller gaps between cells, even if the cells were considered incompressible; indeed, comparison of typical colony snapshots in Fig.7.5 shows that microchannel growing cells appear have larger interstices between cells.

7.3.6 Cell velocities

Given the confined growth environment, it was expected cells would experience larger mutual pushing forces inside the microchannels than would be expected in a freely growing colony. Because the channel ends are open, these pushing forces should be manifest as higher cell velocities in the confined growing microcolonies. Moreover we would expect that in the channels, the average cell velocity in the lengthwise direction will increase as the channel width decreases, because cells

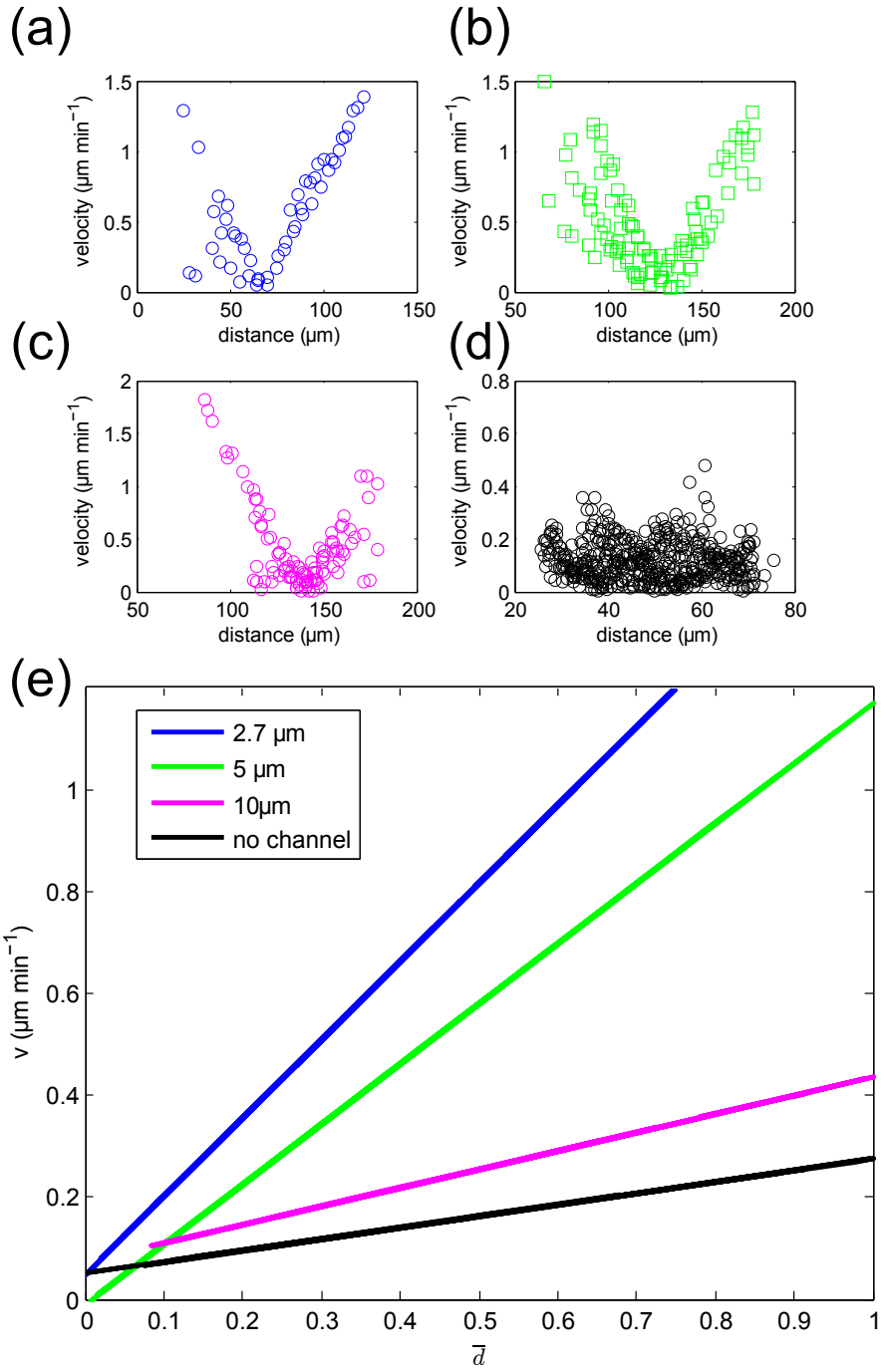

Figure 7.12 Instantaneous cell velocities for cells growing inside and without microchannels as a function of distance to a fixed point, or normalised distance to the zero velocity coordinate ($\bar{d}$), showing clear zero velocity points for the microchannel growing cells,and steeper velocity profiles for smaller channel widths. $\bar{d}$ for the unconfined colony is measured with respect to the colony's centre of mass. All data are for colonies with $\approx$ 61 cells. Channel widths:(a)2.7 μm (b)5 μm (c)10 μm (d)no channel. (e) Linear least square fits of instantaneous velocities of cells with respect to the zero velocity coordinates identified in (a)-(d).

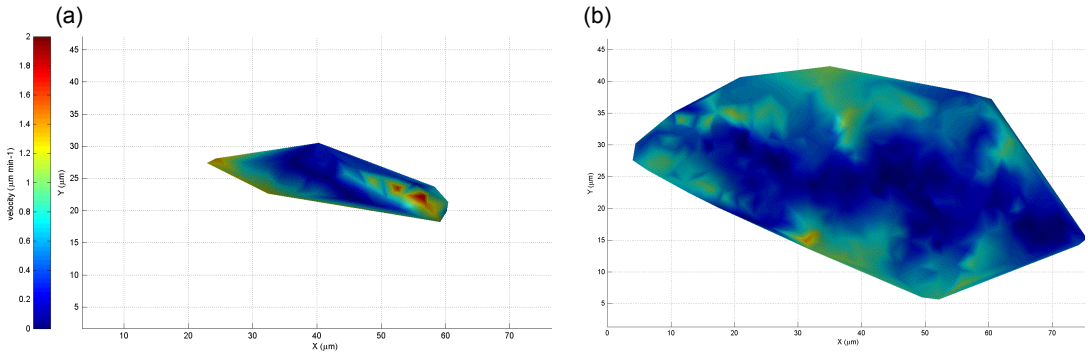

Figure 7.13 Surface maps of instantaneous cell velocities for a microcolony with (a) 61 cells and (b) 624 cells. Higher velocities are observed for smaller colony sizes, likely driven by high colony aspect ratios. Larger low velocity regions developed at higher population levels, although the highest velocities were still found at the edge of the colony.

would fill available space within the channels quicker.

Fig 7.12 (a-d) show instantaneous cell velocity profiles as a function of the coordinate along the channel length, for both microchannel colonies and unconfined colony (N≈ 61), measured with respect to the image origin coordinate. These were measured by computing the displacement of single cells between two frames near the end of the time-lapse movie. For colonies confined in microchannels, there is a clear minimum in the velocity profiles, which might suggest velocities are a result of cell pushing, rather than active motility. The zero velocity point was fixed spatially as the colony developed. Additionally, 'laning' between stacks of cells were sometimes observed in microchannels (Fig.7.12(b)), as evidenced by the fact that the data points fall onto multiple different straight lines.

From the coordinates identified in Fig.7.12(a-d), instantaneous cell velocities at N=61 cells were measured as a function of the distance to the zero velocity coordinate. Fig 7.12(e) shows the linear least square fits to these data. The steepness of the velocity profiles scaled approximately with the width of the channel, with cells growing in narrower channels being displaced faster than in wider channels.

The importance of confinement for a clear, radial velocity profile is seen when

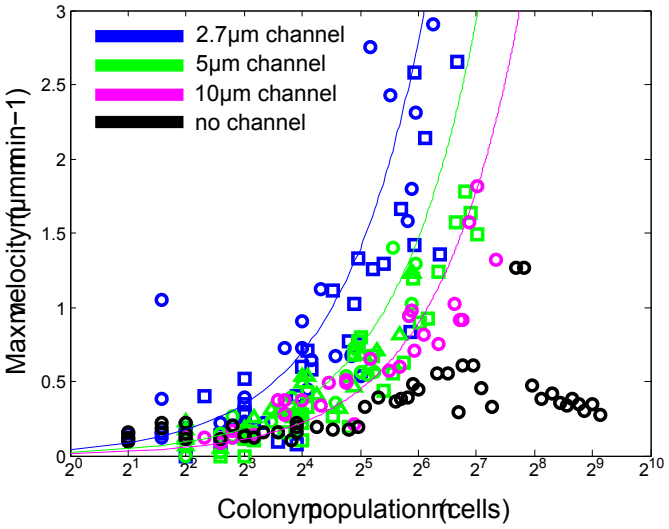

Figure 7.14 Maximum cell velocities in colonies grown in and out of microchannels versus colony population. The maximum cell velocity is defined as the fastest travelling cell between each frame of the time-lapse movie. The lines are expected maximum velocities when treating the colony growth as a line of cells, and the markers experimental data; matching markers correspond to the same colony. Narrower channels result in higher velocities, and the relative decrease in velocity broader channels is attributed to the fact there are more cells side by side in the y-direction.

comparing channel grown colonies to the unconfined colony. An unconfined colony has no clear zero velocity point measured in Fig. 7.12(d), making a linear correlation along a semi-major axis less meaningful. However, closer examination of individual cell velocities showed qualitatively similar velocity profiles compared to the channel grown colonies; Fig 7.13(a), $N = 61$ cells shows that cells at the edges of the colony still possessed the highest velocities, however, although larger areas of the colony were moving slowly compared to the microchannel colonies. Furthermore, the fast moving cells were found lying along the colony's semi-major axis, similarly to cells in microchannels.

Examining a velocity map in the same colony at a higher cell population (Fig.7.13(b), N= 624 cells) showed the colony had grown more in the direction of the faster growing cells, but also that the extent of the low velocity region had grown. Higher velocities were found at more perimeter locations too, suggesting the colony was approaching a more isotropic expansion behaviour. Therefore, without the channel walls to direct growth in a particular directions, an unconfined colony will quickly lose its preferred growth axis as cells begin to

proliferate more in 2d. Interestingly, maximum velocities ($v_{\max}$) in the normal colony peaked, while in the microchannels, $v_{\max}$ increased linearly with population size.

One hypothesis is that the cell velocity profile is entirely due to cell proliferation within the colony, which pushes cells outward. In this case, we would expect cell velocity to correlate with cell elongation rates and population, and be tempered by the number of bacteria which could be stacked across the width of the channel. To test this, the following equation was used to model colony velocities at the edge of colonies growing in microchannels: :

$$v_{\max}(N) = N\frac{\langle \Delta L \rangle}{N_{\mathrm{w}} g_{\mathrm{d}}} \tag{7.2}$$

where N is the colony population, $\langle \Delta L \rangle$ the mean cell length increase between birth and division across the colony, N_{w} the maximum number of cells stacked within the channel, and g_{d} the colony's doubling time. Fig.7.14 (solid lines) shows there was good agreement between the experimental data and model. This suggests cell velocities were caused by cell growth, rather than motility. For cells in the standard growing colony, the situation was more complex, since cells were found to grow preferentially along one axis in early stages of growth, similarly to channel growing cells, before the aspect ratio of the colony reduced as cells propagated further in both dimensions.

These results show that channels produced comparatively fast moving cells compared to an unconfined colony, which was able to spread more in 2d, despite having a high aspect ratio early in its growth. Cells were also able to move quickly by virtue of their elongation alone, which sometimes resulted in 'laning' between rows of cells, introducing the possibility that more mixing might occur between cells in these types of confinment (open ended channels) compared to a unconfined colony.

7.3.7 Summary

In this section, the effects of confinement on growing microcolonies of *E. coli* were investigated. The growth rate of cells was not affected by the comparatively stiff

agarose used to construct the microchannels compared to the softer agarose used for a 'normal' growing colony. While erroneous cell morphologies were observed in channels, these events were rare. Cells were also shown to be well confined by the channel walls, with a marked effect of geometrical confinement on the resulting colony aspect ratio at small population sizes. For growth in channels, the cell density in growing colonies was found to be invariant to channel width, although an unconfined colony was generally denser, likely because of radial forces reducing gaps between cells and smaller cell lengths, possibly arising from nutrient depletion. Channel width was shown to have a strong effect on the velocity gradient measured from the centre of the colony to the open edge, with cell displacements arising from cell expansion, rather than cell motility. Furthermore, the range of nematic-like ordering measured in channels was found to extend across the entire length of the colony, regardless of population size, for 2.7 µm and 5 µm channels. The 10 µm channel showed nematic-like ordering over a spatial range similar to the unconfined colony until the cells collided with the channel walls, resulting in an increase in both the range and degree of order measured.

These results highlight some of the differences we would expect to see in colonies growing in confined geometries compared to unconfined, surface growing colonies. The implications are that in confined geometries, we might expect the spatial arrangement of cells to their neighbours to be more dynamic in time, given their high velocities at the channel edges. Also, as others have indicated [13, 14], high degrees of orientational order could facilitate passage of nutrients into the colony. Here we have seen this phenomenon occur at much lower cell numbers, and across a variety of confinement aspect ratios, suggesting even highly constrained environments don't prohibit viable colony development.

7.4 Genetic structure in confined colonies

In this section, the results investigating the effect of confinement on the spatial distribution of genetic distances (D) between neighbouring cells are presented. By genetic distances, we mean the generational gap between any two cells in the colony, quantified by counting the number of steps required to navigate between them on the colony family tree (Fig.7.16, p.123). Genetic distances are important within the context of cooperative behaviours in populations, since they essentially

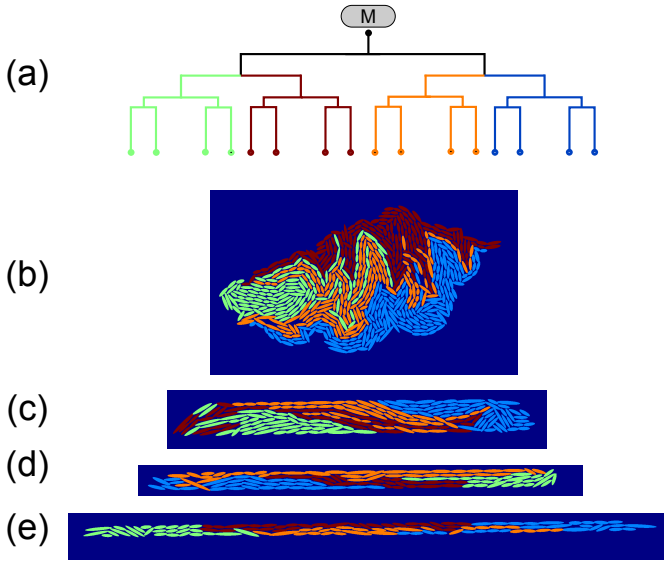

Figure 7.15 Representative cell masks in colonies growing in different microchannels, coloured by their common ancestor. Cells from time-lapse movies are represented by ellipses, and coloured in relation to one of 4 common cell ancestors. (a) Genealogical tree showing how the four common ancestors in the following panels are related to each other. (b) Normal colony. (c)10 µm, (d) 5 µm, (e)2.7 µm width channels.

determine to what extent another individual is 'kin', which has potential knock-on effects on the maintenance of cooperative traits within that population.

7.4.1 Common ancestor interfaces

First, to gain an understanding of the degree to which cells mixed (or didn't) in growing confined microcolonies, genetic sub-domains were identified within colonies, based on their link to one of four common ancestors, as illustrated in Fig.7.15(a). Elliptical cell masks were generated based on centre of mass coordinates, angles and lengths, and coloured by the lineage of one of four common ancestors (Fig 7.15).

Regardless of the confinement (or lack thereof), there were clearly distinct domains of related cells, showing that growing colonies were in general not genetically mixed: in contrast, their ancestors stayed in close proximity to each other. This is in comparison to liquid batch culture, or possibly even cells swarming over a low concentration agarose surface, where a high degree of mixing

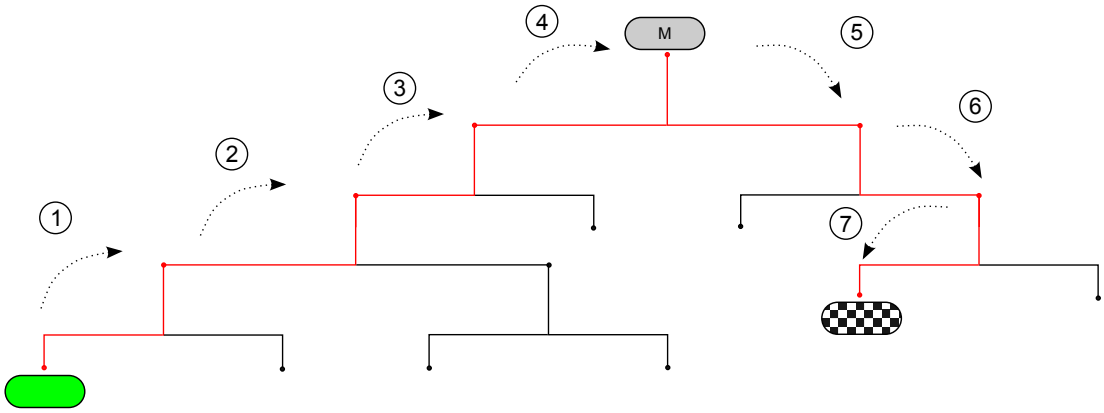

Figure 7.16 Reprint of Fig.7.2 for convenience. An illustration of how genetic distances between cells are calculated. In this example, we wish to know the genetic distance between the green cell and the chequered cell. The genetic distance is quantified by counting the number of 'steps' taken when moving along the colony genealogical tree between cells. Here, the target cell is comparatively distant with $D = 7$, since we have to count all the way back to the original mother cell, labelled 'M'.

between different domains of the 'family tree' might be expected. Interestingly, in all the examples shown in Fig7.15(b-e), not all domains were compact, with relatively large interfaces between domains arising from stretched regions, which appear to leave some cells isolated, likely contributing to local regions of mixing. In the case of the channels, these domains ran along the length of the channel, which is perhaps not surprising given that cells principally move along the channel axis. However, in the case of the normal growing colony, the stretched domain (Fig7.15(b), orange ellipses) was aligned along the semi-major axis of the colony, suggesting cell flow had affected the internal structure of the familial domains. Generally however, it was clear to the eye that there were discrete regions comprising of more than a few cells for each ancestor-type, suggesting a lack of genetic mixing within the colony.

7.4.2 Calculating genetic distances

As explained in §4.3.2, cell tracking software 'Schnitzcells' allowed each cell lineage to be linked to its immediate ancestor ('mother'). By linking the lineages of a cell to any other cell, complete genealogical trees of the growing microcolonies were generated (such as shown in Fig.4.7(c) p.36). This allowed the generational

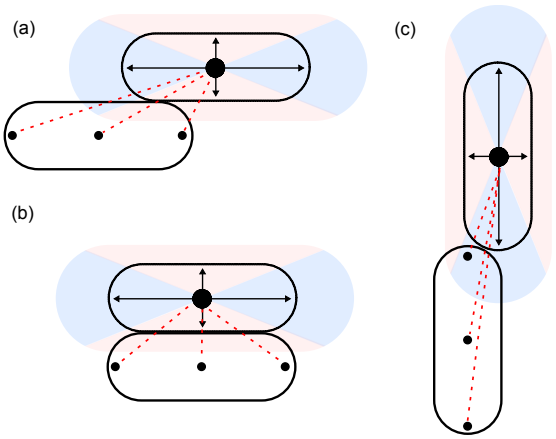

Figure 7.17 To classify a neighbour as either longitudinal or latitudinal, a 20° or 150° projection was made from each cell pole and flank coordinate respectively (blue and red regions). If two out three test coordinates (centre of mass and two poles, marked with black dots) in the neighbour candidate cell fell within one of the cone types, the cell was appropriately classified. The following neighbour types shown are: (a) Neither neighbour type (b) longitudinal (c) latitudinal

gap, or '*genetic distance*' (D), between any two cells in the colony to be quantified. Fig 7.16 summarises how D was calculated. The minimum possible distance between any two cells is $D_{min} = 2$, since two steps are required through the genealogical tree in order to reach a sister cell: one to reach the most recent common ancestor (MRCA, in this case, the mother cell), and a second to step down to the target cell. The more distant the MRCA, as shown in Fig.7.16, the more steps are required to navigate from the source cell to the target cell, with the largest returned values of D arising from tracks which traverse to the original mother cell from which the entire colony has descended from.

Neighbours were identified by first generating elliptical pixel masks based on cell centre of mass coordinates, length and angles in Matlab. They were then dilated by extending the semi-major and semi-minor axis by a factor of 1.3, thus increasing the area of each mask by a factor of 1.69. If pixel overlaps between two dilated cell masks were identified, then the cell-pair were labelled as mutual neighbours. To account for the fact that relatedness probabilities might have an inhomogeneous spatial distribution around a given cell, cells were additionally classified as either 'longitudinal', or 'latitudinal', *i.e.* in front and behind, or to the left and right (Fig.7.17). To classify each neighbour type, cones

were projected from the mask extremities (two poles, and two flanks) and three reference coordinates relating to the neighbouring cell tested for which cones they lay in. If two out of three test coordinates were found to lie in the same cone, the cell was classified appropriately (Fig.7.17). This method succeeded in classifying most cells, although a small proportion were not counted due to a small angular region between longitudinal and latitudinal zones which was not defined. However, this buffer provided a clearer distinction between the two neighbour classes.

Each and every lineage had to be manually confirmed, which owing to the exponential manner of growth, meant lineages rapidly increased as the colony grew. In total, the data from 7 colonies are presented in the chapter, but collectively comprise 2577 individual cell lineages.

7.4.3 Genetic distance distributions

Fig.7.15 suggests that there are likely to be regions within the colony of high and low genetic relatedness, based on the fact there were often extended interfaces between different genetic sub-domains. However, it is not clear from Fig.7.15 whether the extent of genetic mixing changes with geometrical confinement. Therefore, we computed the distributions of genetic relatedness for different channel widths at similar colony populations to check if spatial confinement did indeed affect the distribution of neighbour-to-neighbour genetic distances. Fig 7.18 shows the relative frequency of neighbour genetic distances for all colony types studied, at $N = 61 \pm 2$ cells, the maximum population which allowed all colony data to be pooled. These values were calculated using the counting method described previously in §7.4.2 (p.123). For comparison, a 'null model' is also shown, where the distributions for the same colonies have been jumbled up to simulate a well-mixed scenario, which show that spatial structure does indeed produce different genetic distance distributions.

In all cases, there was a strong contribution from sister ($D = 2$) cells, which was expected given sister pairs would be close to each other following their respective births, in all experiments. However, slightly different distributions for larger D were measured between colonies: the 2.7 µm grown colonies and standard growing colony had the highest counts of largest genetic distances

($D > 10$), while the 5 µm and 10 µm had lower overall, but increasing respectively, relative frequencies. Intuitively, a monotonic increase in the relative frequency of more distant neighbours was expected as channel widths were increased (thus decreasing the degree of confinement), allowing cells more freedom to move around and encounter genetically distant neighbours. However, this wasn't the case implying that in situations where genetically distant regions are close to each other early on in the colony's growth, it becomes hard in small channels to reverse this positioning, effectively 'locking in' the genealogically distant cells into close proximity.

7.4.4 Genetic distance dynamics in growing colonies

In the previous section, we investigated the distribution of neighbour genetic distances at a fixed colony size, from which small differences between colony types were seen, but the exact role of channel width was unclear. To determine how patterns of relatedness changed with time during the development of the colonies, we plotted, as a function of colony size, the probability of a neighbour having a certain genetic distance $p(D = d)$ for each individual colony, starting first with the simplest case of sister cells ($D = 2$), before moving onto more distant cells ($D > 2$).

Sister cell displacements

Figure 7.19(a) shows the probability of a neighbouring cell being a sister ($p(D = 2)$) as a function of colony population for all colony types. This probability tended to $p(D = 2) \approx 0.2$ as the colony grew. This is consistent with the average number of neighbours a cell had (≈ 5)at the corresponding colony population (Fig.7.19(a), inset); of these neighbours, we would expect one to be the sister cell. Similar results were seen for the different degrees of geometric confinement, but the smallest channels (width$\leq$5 µm) had a marginally higher probability, likely arising from channels restricting cell movement and preventing cells moving laterally.

To check the extent related cells stayed close to each other, we also analysed the distances between sister cells at the point one of the pair divided, in the channel

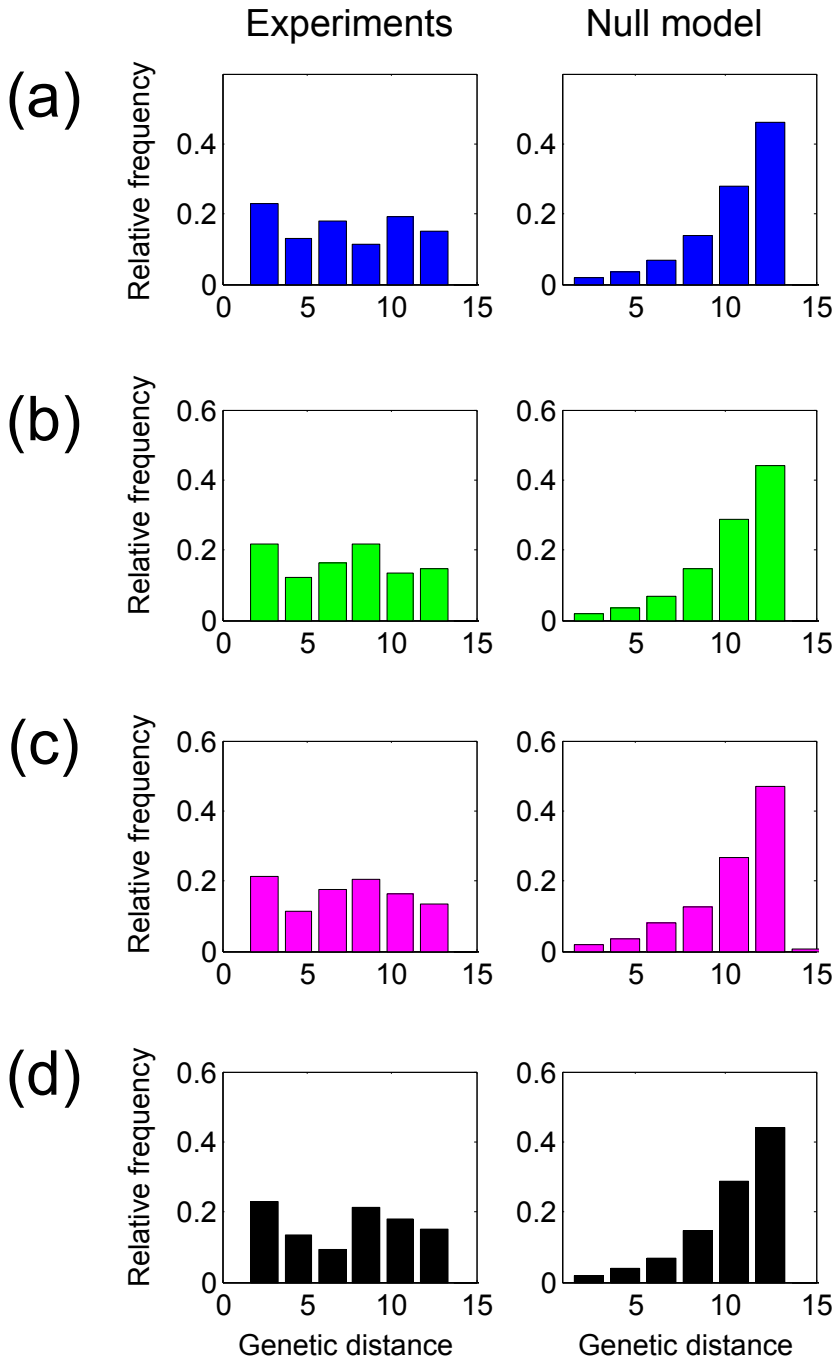

Figure 7.18 Histograms of genetic distances to nearest neighbours in microchannels and normal growing colony at $N = 61$ cells in both experiments, and where data has been jumbled to simulate a well-mixed (*i.e.* unstructured) case. Channel widths (w): (a) 2.7 µm (b) 5 µm (c) 10 µm (d) unconfined colony.

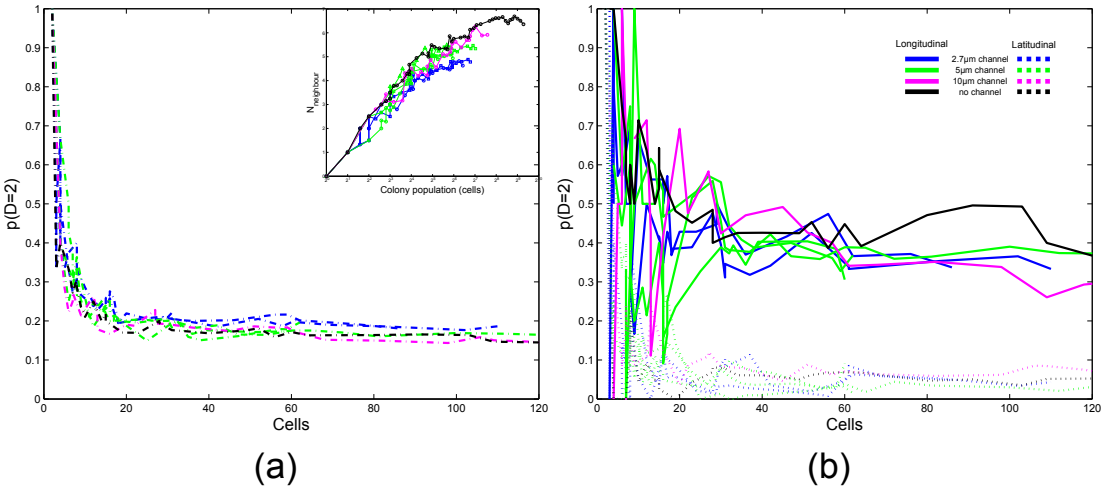

Figure 7.19 (a) Variation in the probability that a neighbour cell is your closest relative ($(D = 2)$, *i.e.*'sister'). Inset: the mean number of neighbours as a function of population. (b) Variation in the probability that cells longitudinally or latitudinally have $D = 2$.

grown colonies and unconfined colony. For the unconfined colony, this analysis showed on average, sister pairs stayed closer together (Fig.7.20) compared to sister cells in colonies what were confined in channels; the dominant contribution to the larger microchannel distances being larger differences in x -axis positions, with y-axis gaps limited by the channel width (data not shown). The high radial cell velocities measured previously in the chapter are the probable cause of this increased distance, since the sister cell closer to the channel exit would move further in a given unit time than the other sister cell.

Moreover, over the course of a colony's lifetime, sister cells tended to stay longitudinal to each other more often before dividing again in smaller channels (Fig.7.21)), while in 10 µm channels the distribution was more even. In contrast, in a normal growing colony, while still possessing a broad distribution of relative sister locations, sister cells had a slightly higher chance of being found side by side over the course of a colony's lifetime.

Dividing cells in channel grown colonies are therefore more likely to be kept in their longitudinal configuration following division, and be found further apart by the next division event. This likelihood decreases as the width of the channel is increased, and reverses for cells in unconfined colonies: in this case, sister cells are marginally more likely to be found latitudinal to each other. Given smaller microchannels have less lateral room to move around in, this is not surprising.

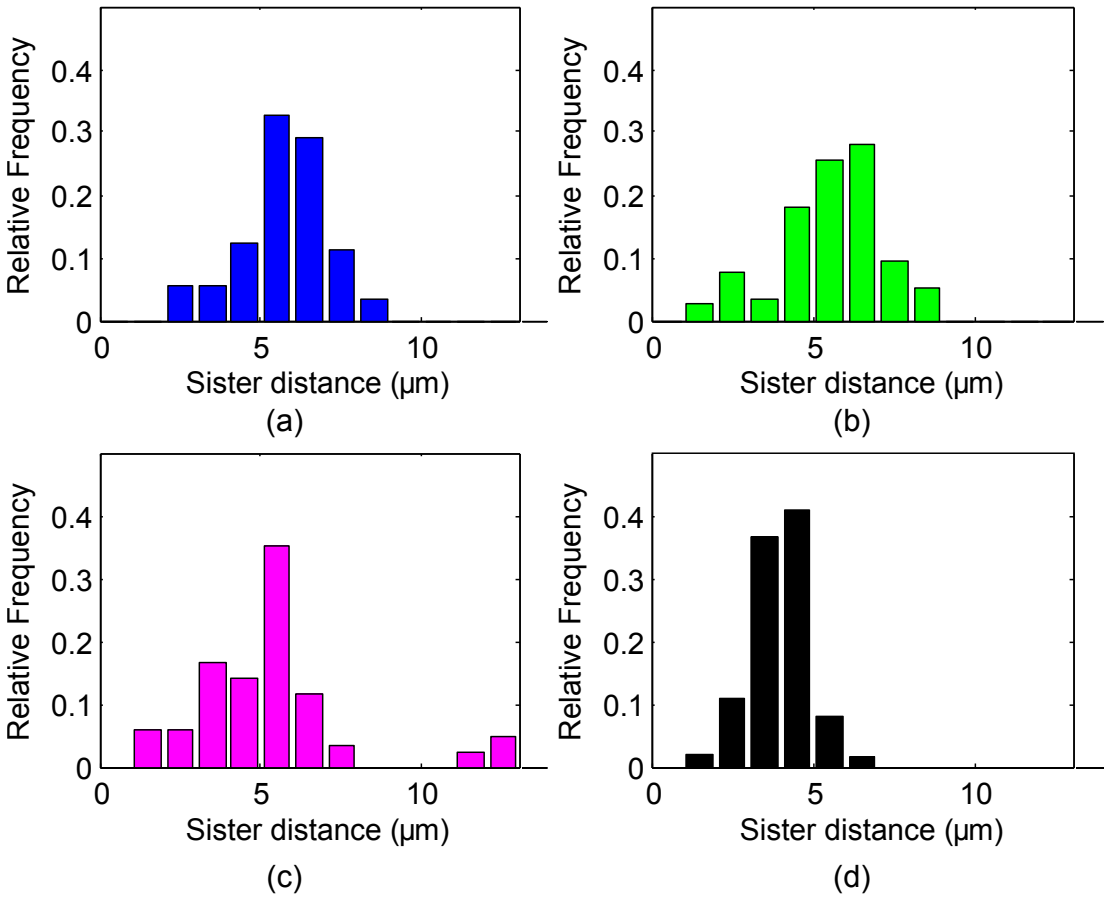

Figure 7.20 Distributions of the distance between two sister cells immediately prior to one of them dividing (and thus terminating their lineage). (a)w =2.7 µm (b) w =5 µm (c)w =10 µm, ; (d) normal colony.

However, sister cells were also found to be further apart from each other in channel grown colonies compared to the unconfined colony, probably as a result of the radial cell velocities measured earlier in the chapter.

Spatial decomposition of neighbour genetic distances.

Based on the differences in daughter-daughter positions in channel grown colonies and unconfined colonies across their entire lifetimes, we looked at the development of neighbour relation probability as a function of colony size by defining neighbour cells as either *longitudinal* or *latitudinal* (defined as shown in Fig.7.17, p.124).

We first checked the probability of sister cells ($p(D = 2)$) being each neighbour class: data confirmed that sister cells in channel grown colonies were most likely

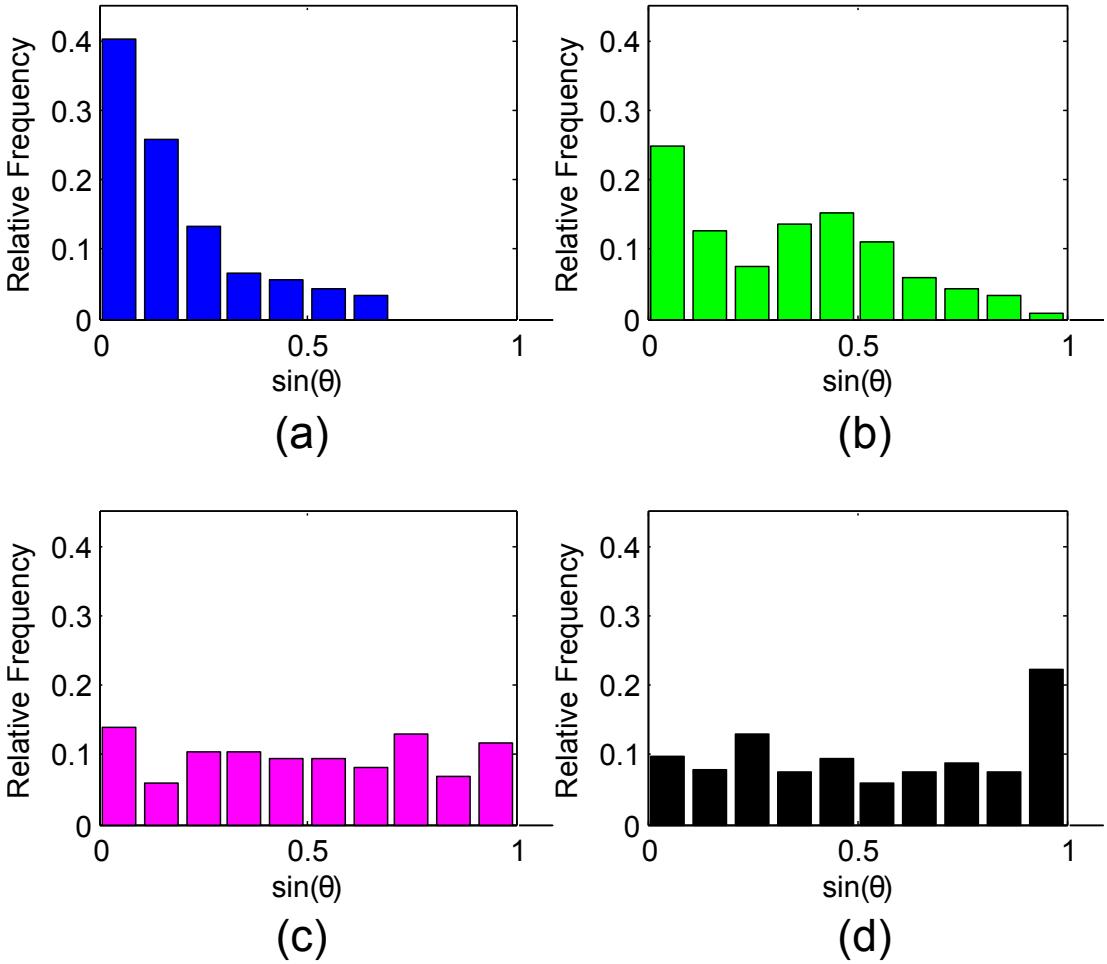

Figure 7.21 $\sin\theta_{s1-s2}$ distributions of the relative angular direction between two sister cells immediately prior to one of them dividing (and thus terminating their lineage). $\sin\theta = 0$ implies longitudinal cells, and $\sin\theta = 1$ latitudinal cells. (a)w =2.7 µm (b) w =5 µm (c)w =10 µm, ; (d) normal colony.

to be found longitudinal to a given cell over the lifetime of the colony. Fig.7.19(b) shows that at lower populations, $p(D = 2) = 0.5$ before dropping to between 0.3 and 0.4 for longitudinal. Comparatively, for latitudinal cells $p(D = 2) < 0.1$ from $N = 20$ cells. This is consistent with the cell division process, where cells undergo binary fission from the cell midpoint, and the results presented in the previous section on sister-sister positions. The two cells would naturally be expected to be found lying along the longitudinal axis. However, cells have been shown to kink relative to each other soon after division , before sliding alongside one another [9, 11]. In the context of the measures presented here, this would correspond with the non-zero latitudinal probabilities

We next addressed the likelihood of neighbour cells in both neighbour classes being more genetically distant ($D > 2$). Peaks in $p(D)$ for higher values of D (more genealogically distant) were typically seen at the earliest population level which would support that value of D (Fig.7.23). For example, for $D = d$, a minimum population of $2^{d/2}$ cells is required before it could be supported, since a smaller population would not have a family tree large enough. It would also be at that colony size where any given cell was most likely to have a neighbour with that particular D value.

Moreover, neighbouring cells with $D > 2$ were found more often latitudinally than longitudinally (Fig.7.24), indicating regions of higher genetic distances might be found along internal colony interfaces which were orientationally aligned; this finding correlates well with relative orientation of cells seen at the interfaces in Fig7.15(b-e) (p.122).

We could independently check this by a closer examination of spatial distributions of cell to cell genetic distances. We therefore plotted the mean genetic distance measured at each cell coordinate at different colony sizes across all experiments. Some examples of these are shown in Fig.7.22. These showed continuous regions of longer genetic distances between neighbouring cells (Fig.7.22) at similar population levels. These areas increased in size as the colony constraints relaxed (*e.g.* comparing Fig.7.22(a) with Fig.7.22(d)), and their growth (Fig.7.25) corresponded well with interfaces of regions which were descended from one of four common ancestors (Fig.7.15, p.122). Furthermore, as a parallel to the null model described in §7.4.3, jumbling the cells to simulate a well mixed scenario has the effect of producing maps in all cases which are homogeneously unrelated

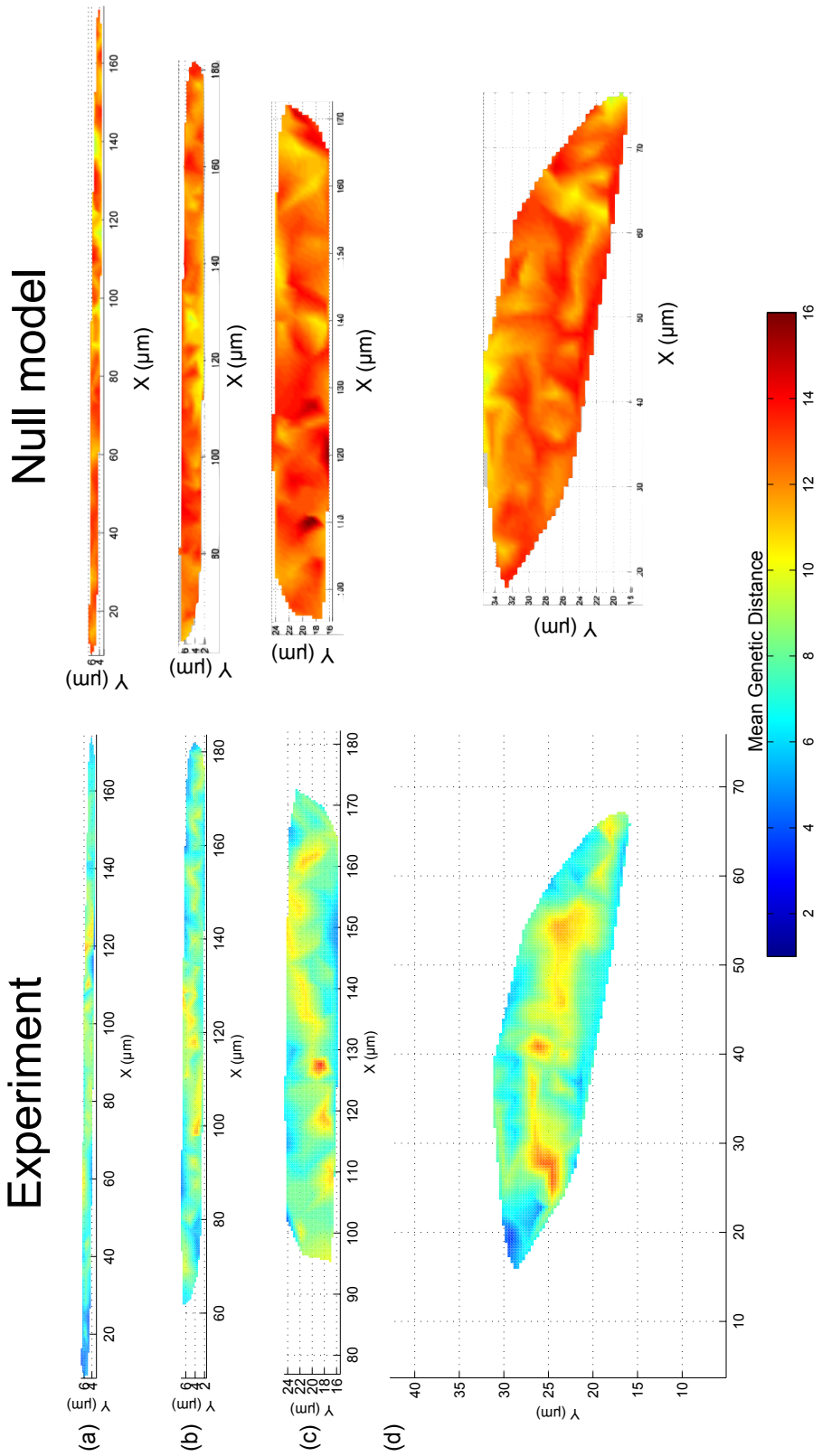

Figure 7.22 Maps showing the mean genetic distances of cells to their neighbours in colonies (N_{cell} = 120) grown in and out of microchannels, and when the data are 'jumbled' (null model) to simulate a well-mixed scenario (using the same spatial coordinates). (a)w =2.7 µm (b) w =5 µm (c)w =10 µm, ; (d) normal colony.

(high genetic distance) across the colonies.

7.4.5 Summary

In this section, we investigated the effect of colony confinement on spatial distribution of genetic distances. Despite their confining geometries, microchannels did not necessarily prohibit regions of high genetic distances between neighbours. However, there were small differences in genetic structure between confined and unconfined colonies. In particular, smaller channels prevented dividing cells from sliding alongside each other, with the net effect that sister cells were most often found longitudinally, rather than latitudinally. Comparatively, a normal growing colony had a higher incidence of latitudinal sister cells over its lifetime, although at higher colony populations, sister cells were more confined to longitudinal arrangements, possibly because of the high cell density restricting movement.

The implications of these results are that despite colonies growing in a confined geometry, cells which were genetically distant (relative to the cell population as a whole) could still lie in close proximity to one another. In terms of cooperativity, this would mean cells growing in crevices or niches, which had escape exits, could not necessarily rely on the characteristic property of a growing colony always having local neighbours which were related. However, there were still discrete regions where cells where relatively related to each other, which may hint to patches of cooperativity in confined multicellular structures.

7.5 Age distribution of old poles in confined colonies

Here, the results of tracking the positions of old poles within confined colonies are presented. As discussed in the introduction, when a cell divides, the daughter cells will each carry an older pole, and a new pole. There is increasing evidence that cells accrue damage through their old pole, which results in ageing-like behaviour, such as a reduced growth rate. For a structured population such as a microcolony, this has implications since old poles would not necessarily be well mixed in the population, leading to discrete regions in the colony where age-related effects

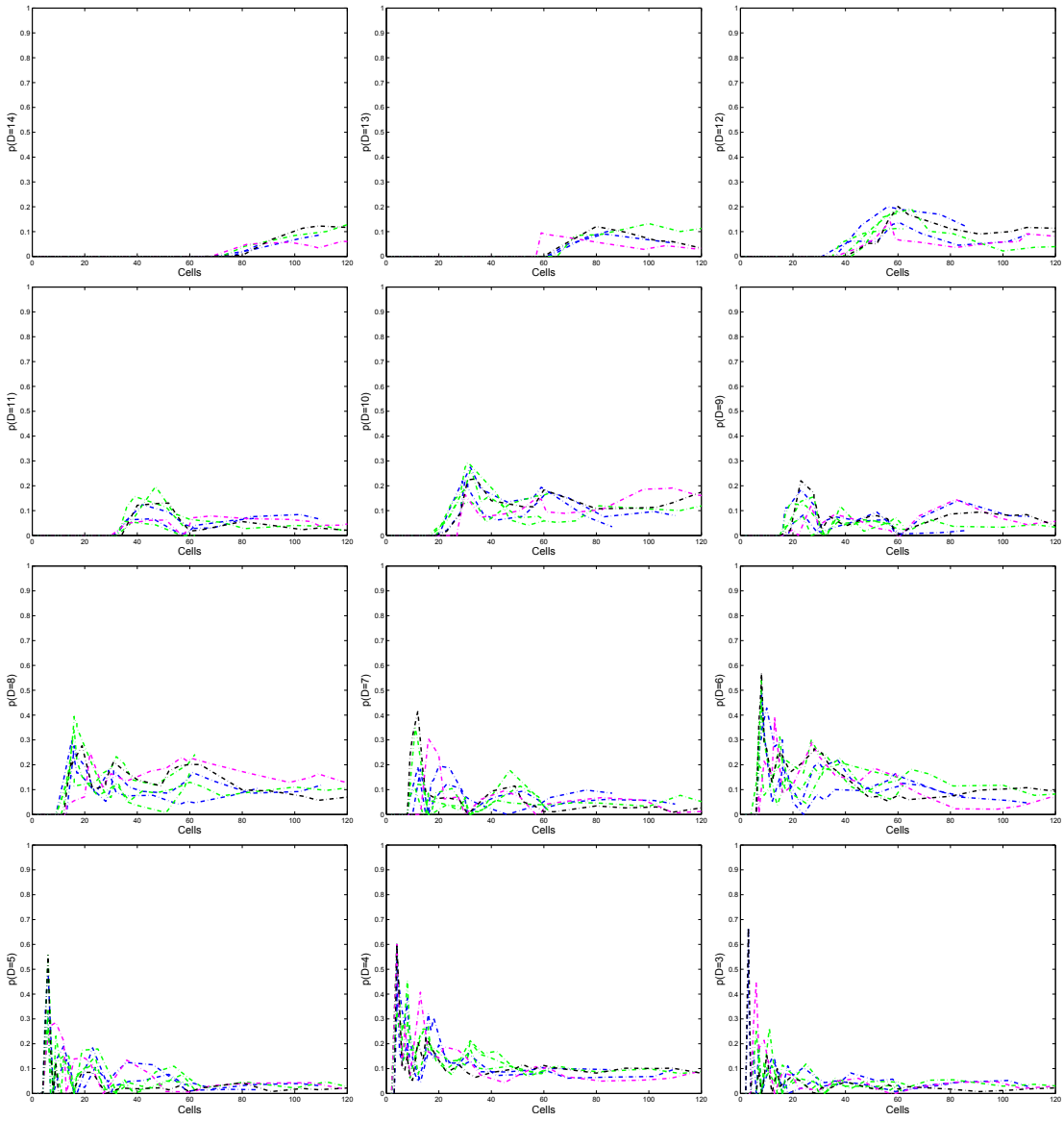

Figure 7.23 P(D=d) as a function of colony population, for $3 \leq d \leq 12$.

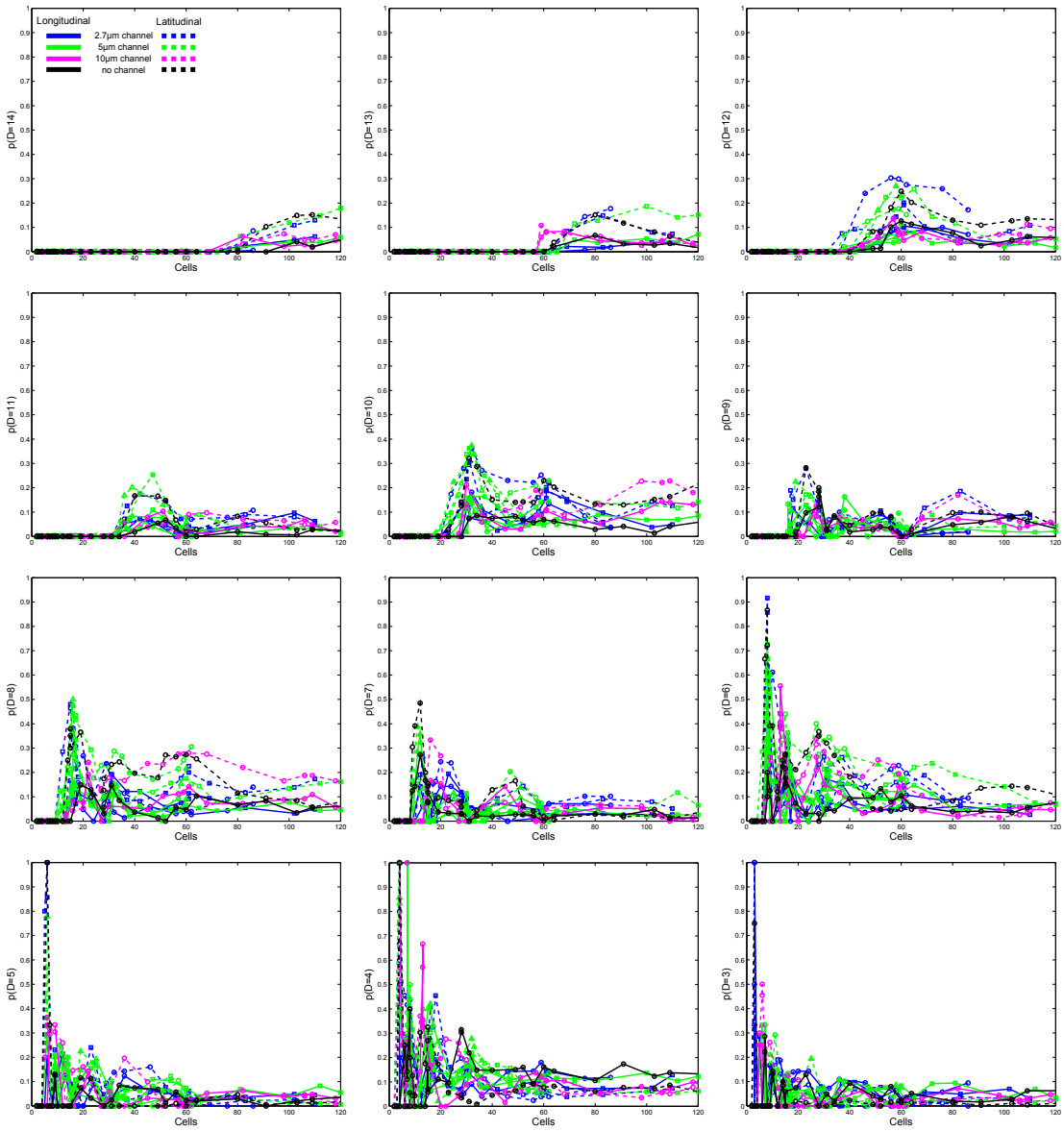

Figure 7.24 P(D=d) as a function of colony population, for longitudinal and latitudinal cells. $3 \leq d \leq 12$.

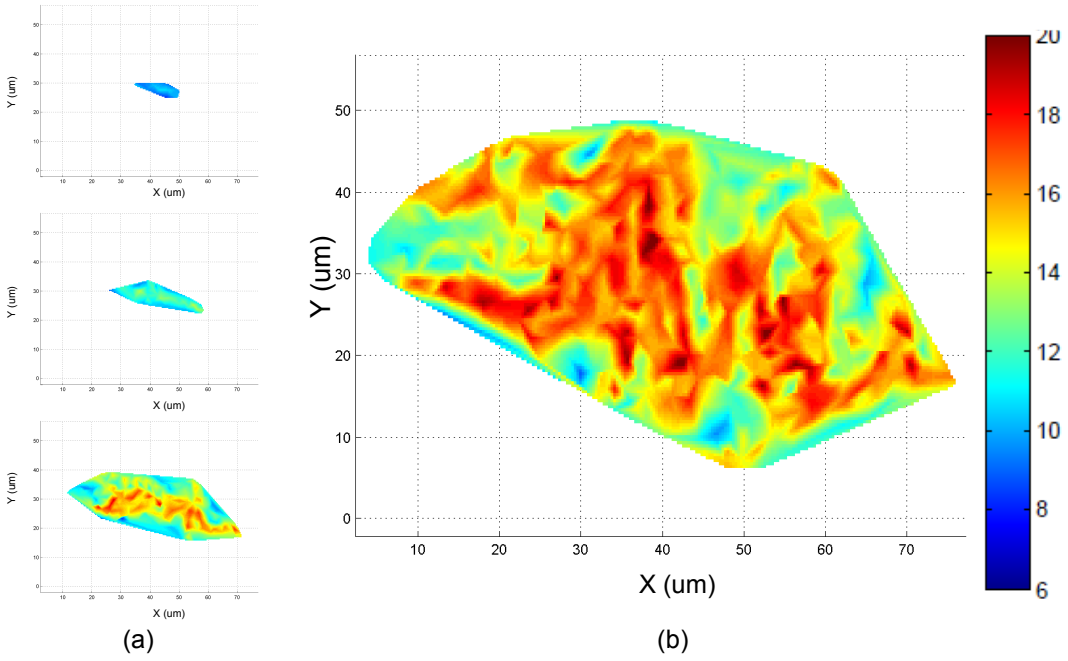

Figure 7.25 (a) Interpolated maps of mean neighbour genetic distances of a normal growing colony at various points of colony development, and (b) an interpolated map at $N = 624$ cells.

might occur.

7.5.1 Quantifying pole ages

First, the metric used to quantify pole age (T_p) is outlined. Each colony is descended from a single, progenitor cell; we assume at this point the ages of both poles are the same, and nominally assign a pole age $T_p = 1$ to each. Following the first division event, the old-pole ages are increased by one (Fig.7.26, black regions), and the two new poles (Fig.7.26, white regions) have their age counters set to $T_p = 1$. Thus, every cell beyond the original mother cell will carry an elder pole, and brand new pole; for the sake of simplicity, the age of a cell is therefore governed by the elder pole age.

Image analysis routines written in Matlab ensured old poles were correctly tracked between frames by minimising the relative distance between poles in different frames.

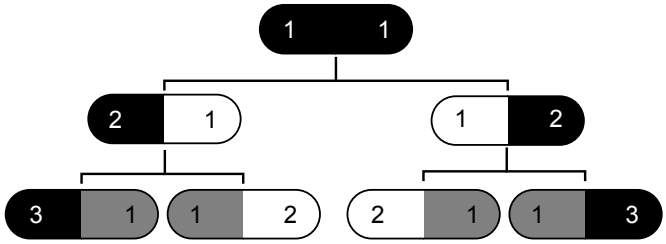

Figure 7.26 Illustration demonstrating how pole age is quantified using a genealogy tree. The original progenitor cell (black) is nominally assigned a pole age $T_p = 1$ at each pole. After division, the two daughter cells each carry a brand new pole ($T_p = 1$), and a slightly aged pole carried from the previous generation ($T_p = 2$). We therefore defer to the elder of the two poles and state $T_p = 2$ for the entire cell.

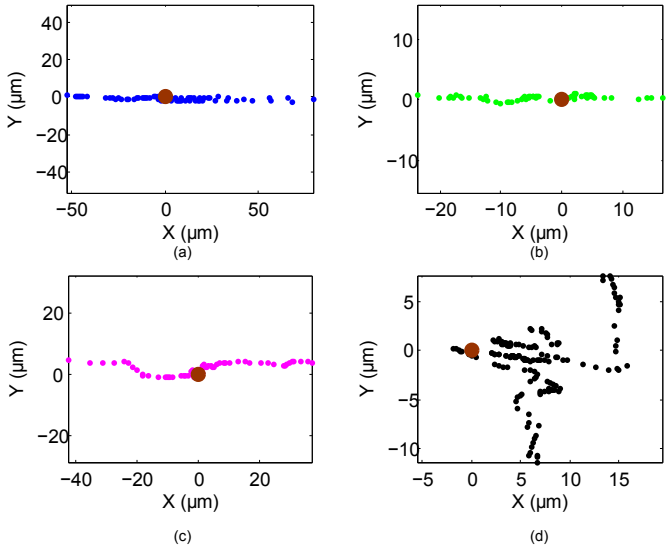

Figure 7.27 Trace plots showing the progression of the oldest pole positions within different microchannels. Cells all started at the origin, marked by brown circle. The timestep between each dot was 3 min. Channel widths were: (a)2.7 µm (b) 5 µm and (c) 10 µm (d) unconfined colony.

7.5.2 Old pole positions

By definition, old poles were all at the colony edge with a colony population $N = 1$. In the smallest microchannel (2.7 µm), oldest poles persisted at this relative position, and tracked the colony edge as the colony front expanded. The oldest poles also diverged, moving to opposing sides of the channel (Fig.7.27). This colony-front tracking behaviour was not always observed in channels, however. While old poles continued to move to the opposing open ends of the channels, they didn't necessarily track the outer edge of the colony (Fig.7.28(b)). Nevertheless, where old poles didn't track the colony edge, they were still found to move away from the colony centre of mass.

For the unconfined colony, the behaviour of the old pole was very different. Fig.7.28(d) shows that old poles were confined to the internal portions of the colony (Fig.7.28(d)), and showed evidence of stagnating at a fixed distance from the centre of mass. We speculate that, since the unconfined colony does not show an outward radial velocity profile, the cells did not have the same pressure driving them to the colony edge, resulting in a smaller distance between the original two pole at similar colony populations.

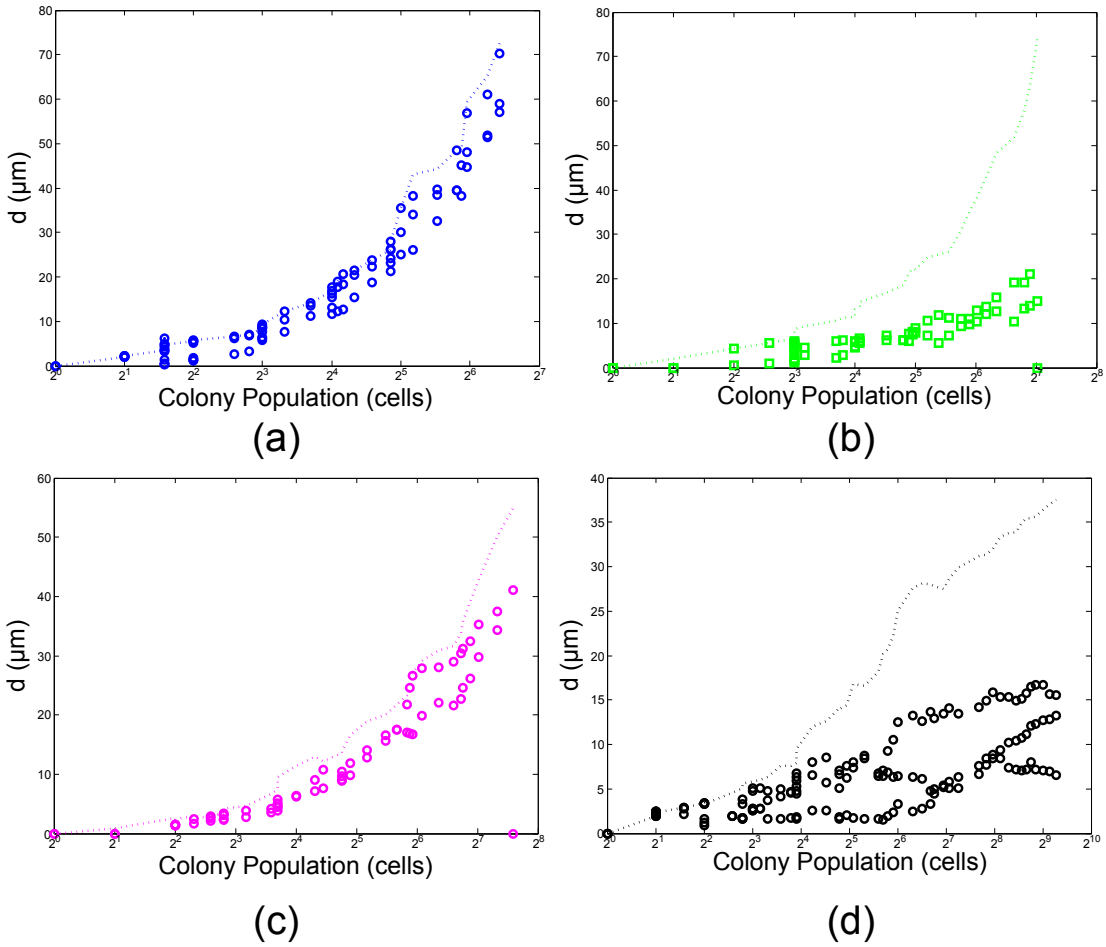

Figure 7.28 Distances of cells carrying the older poles from the colony centre of mass. Dashed lines represent the distance of the edge of the colony. (a)2.7 µm (b) 5 µm and (c) 10 µm width channels; (d) standard colony.

7.6 Discussion

In this project, we used high resolution fluoresence microscopy to capture time-lapse movies of growing microcolonies of *E. coli* in confined environments. Agarose microstructures were used to provide as equal a comparison between confined and unconfined colonies as is possible. In doing so, we also successfully reproduced the main features of the protocol described by Moffitt *et al.* [70], albeit a more straightforward version since no media flow was present. From the resulting movies of colony growth, we were able to investigate the effect of spatial restriction on colony and cell morphology, as well as cell organisation in the colony. Furthermore, using cell-tracking software, we explored how patterns of genetic relatedness between cells were affected by confinement, and tracked the location of old cell poles within the growing confined and unconfined colonies.

Importantly, we found that the cell growth rates, measured both as cell doubling times, and colony area growth rate were unaffected by the geometrical confinement in our experimental setup. From this, we can infer the higher percentage agarose used for the microchannels didn't inhibit nutrient flow at the cell populations observed here, validating a primary motivation for using this method. Maintaining a fixed growth rate between experiments is important because it indicated the cells were growing under as similar conditions as was possible, other than the growth geometry.

Cell velocities were markedly higher within microchannels compared to an unconfined colony, and the fact we observed velocity profiles that scaled inversely with channel width was consistent with a model in which cell displacement was caused just by cell expansion and the resulting mutual pushing. In the natural environment, this is significant since it could provide a mechanism by which cells can rapidly colonise interstices without having to resort to other cell transport methods. The high velocities were likely part-facilitated by a high degree of orientation order within the colonies. For narrower channels, higher degrees of order were measured, and over a larger distance, and smaller colony population. This is in comparison to a standard colony, where order was found to decay to lower orders at smaller distances as the colony grew. Others have shown that cell flow can induce orientation order in growing colonies ([13, 14], and so we are likely seeing a similar phenomenon here.

Analysis of genetic distance distributions showed that on the whole, sister cells stayed remarkably close to one another. Microchannels restricted the degree of y-axis movement, and so the narrower the channel, the more often daughter-daughter cell pairs were to remain longitudinal to each other. However, daughter-daughter pairs in channel grown colonies were generally further apart compared to the unconfined colony. This is likely a result of the steep velocity profiles measured in confined colonies (regardless of their width) pushing one of the daughter cells to the exit faster than the other cell.

We also observed local regions of lower relatedness (higher genetic distance) within colonies. These regions coincided with interfaces between distinct common ancestor regions. The central regions of the colony, regardless of the microchannel constraints, tended to have more interfaces in a smaller area, leading to these regions having a larger average genetic distance compared to other colony regions. Thus, it is not necessarily true that cells will always be surrounded by neighbours who are closely related, within the limitations of the population sizes described here. While there are indeed highly related areas of the colony (particularly towards the edges of the colony in the micro channel experiments), these are a result of cells inhabiting the same early branches of the genealogical tree. Inevitably however, cells will collide with cells from different branches, and where this occurs, the colony will have a high degree of unrelatedness. Indeed, the marginally higher probability of finding neighbour cells with larger genetic distances in narrow microchannel colonies is likely driven by a combination of steep velocity profiles along the channel axis, and cells sliding alongside each other ('laning').

This could have possible implications for cooperative behaviours within confined geometries. While we have shown there are interfaces of relatively high genetic differences at small populations, these could persist and become even more distant as the colony developed. Potentially, this could lead to particular domains of cooperativity within multicellular assemblages, of which their size, location and persistence depends on the level of confinement.

Motivated by growing evidence that old poles might act as a marker for ageing behaviour in bacteria, old pole positions were also tracked. In two out of three of the microchannel types, cells tracked the colony edge closely (2.7 µm and 10 µm channels). It is speculated that because channels (regardless of their width)

cause edge cells to travel faster than internal cells, oldest poles will persist at being at the edge, since they, by definition, will be at colony edge when the population is $N = 1$ cell. A normal growing colony would not be expected to have the same radial velocity profile at the populations described here, and so oldest poles would instead be more likely to be internalised within the colony, despite being at the 'edge' at the colony's start point. Thus, colony confinement may have implications for the spatial distribution of occurrences of age-related cell behaviours within growing cell populations: within confined environments, the old pole may be evacuated from the colony quicker than a unconfined colony. An example of where this could be significant is in filamentous cells, a common stress-response in growing colonies. It has been proposed by others [13] than *E. coli* has an evolutionary defined aspect ratio which facilitates cell escape - in the context of narrow or confined geometries, filamentous cells would increase the chances of blocking cell escape, and impeding nutrient flow into the colony.

7.7 Conclusions

Confinement of growing colonies had a marked effect on their structural properties, in particular, cell velocity gradients, driven by cell expansion, and orientational order, driven by cell flow towards the open exits. It is likely the persistence of orientational order also aids maintaining the high velocities of cells, allowing cells to easily pass each other by, and reducing the chances of channel blockages. Therefore, paradoxically, the increased confinement results in greater movement of cells, albeit along one axis, while in a unconfined growing colony, cells have more freedom to move in 2d at small populations, before they become restricted by neighbouring cells, but without a cell-expansion pressure to push cells at higher velocities. This becomes significant in terms of the spatial distribution of genetic distances, since genetically distant cells are able to slide alongside each other, contributing to areas of slightly higher local genetic distances in greater confinement, compared to a normal growing colony. This interplay between velocity and restriction is also the cause of colony-edge tracking old poles, which were found at colony edges in channels, while in standard growing colonies, they were internalised. Our work is the first to directly measure single-cell relatedness structure within colonies growing in

different confinement geometries with that of unconfined growth, and may have implications for predicting the locations of cooperative cell behaviours within these colonies, in addition to age related mutations.

7.8 Future Work

The primary limiting feature of these experiments was the time taken to segment many cells over many movies, to ensure that each cell's lineage had been correctly linked. Increasing movie processing throughput would therefore be a sensible place to start in order to gather data on more colonies. Cell tracking was generally fine for standard colonies with a 4 min timestep, but could struggle with cells at the edge of channel growing microcolonies. Therefore, alternative means of tracking cells should be considered: two suggestions would be to correlate the level of fluorescence expressed by cells between frames, or to use very high quality phase contrast images to increase the time resolution so intermediate points of cell displacements could be tracked. Because continuous regions of high genetic distances were observed to lie along internal interfaces within colony, it would also be interesting to study the behaviour of cooperative strains along these regions in small colonies. For example, one could envisage testing whether cells are truly 'aware' if they are in regions of the colony which are less related to them, and if so, at what genetic distance they cease cooperating. This could be accomplished using fluorescent reporter strains tracking cooperative traits, like siderophore production [91].

Chapter 8

Microcolony growth in three dimensions

8.1 Introduction

In this chapter, I present a study of the transition to three dimensional growth in surface growing colonies of *E. coli* (Fig.8.1). 3d multicellular bacterial structures, such as biofilms, are ubiquitous in the natural environment [28, 92], but a transition from 2d to 3d growth occurs in many biological situations, from skin tumours [93] to organ development [94]. Our study therefore has relevance to growth of multicellular structures more generally.

Returning to the bacterial world, the transition from surface attachment and 2d growth to formation of 3d biofilms has received much attention. Biofilms are spatially structured aggregates of cells which are held together by a matrix of extracellular polymeric substance (EPS), which helps protect the cells within from a plethora of external challenges, such as toxins [95], chlorination [96] and antibiotics [97–99]. Furthermore, the complex population structure may improve the efficiency of horizontal gene transfer within the colony, aiding survival strategies in harsh environments [100]. Consequently, biofilms can be hard to eliminate in clinical [92] and industrial environments [101], proving costly in both human and monetary terms - for example, biofilm fouling of US Navy ship hulls is estimated to decrease fuel efficiency by as much as 20.4 %, an additional fuel

cost of $2.3M per ship, per year [101]. Intervening in the early stages of bacterial 3d growth could provide a way to avoid the establishment of a persistent biofilm. Understanding the early stages of 3d colony development is necessary if we are to develop effective ways to do this.

The transition from surface 2d growth to 3d growth can occur as a result of individual cell responses to nutrient and waste concentrations, coordinated action via quorum sensing, or via purely mechanical, but still collective processes [71, 102]. In established macroscopic colonies, some bacteria can even use community-level stress responses to trigger cell death, causing structural instabilities at the base of the colony, eventually leading to complex 3d colony topography [103].

In the experimental system investigated in this chapter, a colony growth starts from a single cell which is located on the agarose surface, and confined by a glass coverslip. This growth environment is typical in single-cell studies of bacteria [36], but it is also similar to real-world environments. For example, biofilms growing on catheters develop sandwiched between the relatively hard catheter surface, and soft tissue [92]. This system therefore provides a useful and well controlled model with which to study 3d structure development in general.

Our study builds on previous work which has investigated the early stages of 2d microcolony growth, starting from individual cells. In particular, important work in this area has shown growth [9, 28], cell-cell alignment [8] and cell-surface interactions [11] can all play important roles.

The interplay identified in this early work between expansion forces arising from cell growth and compression forces from friction and agarose 'pressure' persists in larger, but still microscopic, colonies and is directly responsible for the eventual transition of 2d to 3d growth in agarose surface growing *E. coli*. A recent combined experimental and theoretical study suggests that once net retraction forces (cumulatively comprising of the cell-substrate friction, and agarose edge compression forces) exceed vertical compression forces, cells will move into the agarose bulk, rather than remain in its colony growth plane and push cells out of the way. Furthermore, the critical invasion area has been shown to possess a complex relationship with the structural properties of the substrate, in particular the area at which a colony undergoes the transition to 3d growth was shown to depend non-monotonically on the agarose concentration [71].

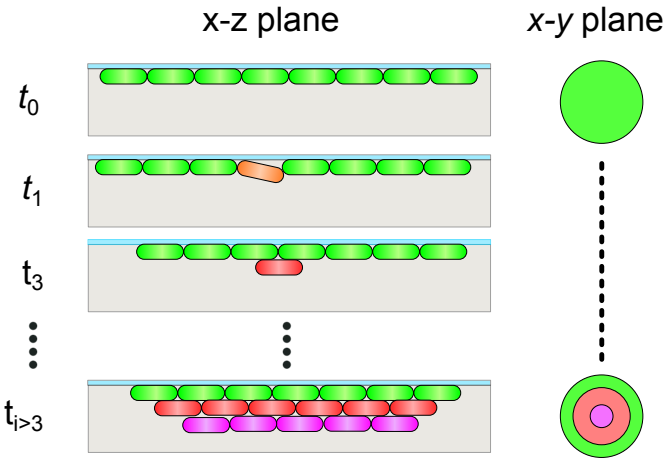

Figure 8.1 Idealised illustration of a cell buckling into an agarose surface, as from two viewing perspectives. Grey regions represent agarose, which the cells are embedded in by the glass coverslip. Initially, the colony grows as a monolayer. Eventually, a cell escapes deeper into the agarose as a result of cumulative inward directed forces exceeding vertical compression forces exerted by the agarose, and establishes a new growth plane. This continues, leading to multiple growth layers, which manifest as approximately concentric discs in phase contrast microscopy, each with a different intensity.

Work studying the early stages of 3d colony development has also shown that the bacteria form well defined 'layers' within the agarose bulk, much like a wedding-cake, but also that the balance of forces at the edge of the colony front is important in the continued proliferation of these layers [102]. Our work addresses the growth and structure of the bulk layers in more detail.

Building on this work, in this chapter we perform observational studies of the development of additional layers of cells after the initial agarose invasion event, using phase-contrast microscopy to create time-lapse movies of the colony's development from a few surface confined cells to 3d growth. We show that colony growth initially progresses in the agarose surface plane, until a transition to 3d growth occurs, whereby individual cells move from the primary layer into the agarose bulk, creating a secondary plane of growth (Fig.8.1). Eventually, cells also move further into the agarose bulk, creating additional 'layers', although the distinction between distinct, tiered planes becomes less clear. The 2d proliferation of the primary layer is reduced by the loss of cells into secondary layers, and a ring of monolayer cells with fixed width develops at the colony periphery at longer times. These features are shown to be dependent on the concentration of agarose

used, but also the cellular growth rate, suggesting that friction continues to play an important role in the development of the colony even during 3d growth.

8.2 Methods

In this section, I detail the particular methods used here which supplement the main ones described in Chapter 3 and 4. In all experiments, the strain RJA002 (YFP) was grown on agarose pads.

8.2.1 Sample preparation

High melting point agarose (Invitrogen, $T_{\text{gel}} = 36 \pm 1.5°\text{C}$, lot:113086, BP:165 − 25), supplemented with liquid media was used in all experiments. Agarose pads were prepared using Geneframes, as described in §3.3.1 (p.20), and cut to shape so three separate slabs of agarose were on each slide. The inoculate was diluted from exponentially growing culture to $OD_{600} = 0.005$ so well-developed colonies ($A_{\max} = 4 \times 10^4\,\mu\text{m}^2$) did not collide with other neighbouring colonies over a 5 h to 8 h imaging period. This ensured nutrient limitation through resource competition was minimised and colonies had consistent growth rates across the pad. M9 + glucose (0.4 %), with the addition of casamino acids (0.5 %) where specified, were used in all liquid media and supplemented agarose. All time-lapse movies were captured within an incubator set to 37 °C.

8.2.2 Microscopy set-up

For 2d colony tracking, time-lapse movies were captured on the Nikon E800 using MicroManager for multidimensional acquisition, Retiga CCD camera and a 20x Ph1 objective. All movies were captured with timestep Δt =3 min .

For 3d colony imaging, fluorescence confocal microscopy was performed, with excitation light provided by a 488 nm diode laser, with either a 63x or 40x oil objective depending on the size of the colony with a 0.2 µm z-step. Huygens Software (Scientific Volume Imaging) was used for deconvolution of some colony

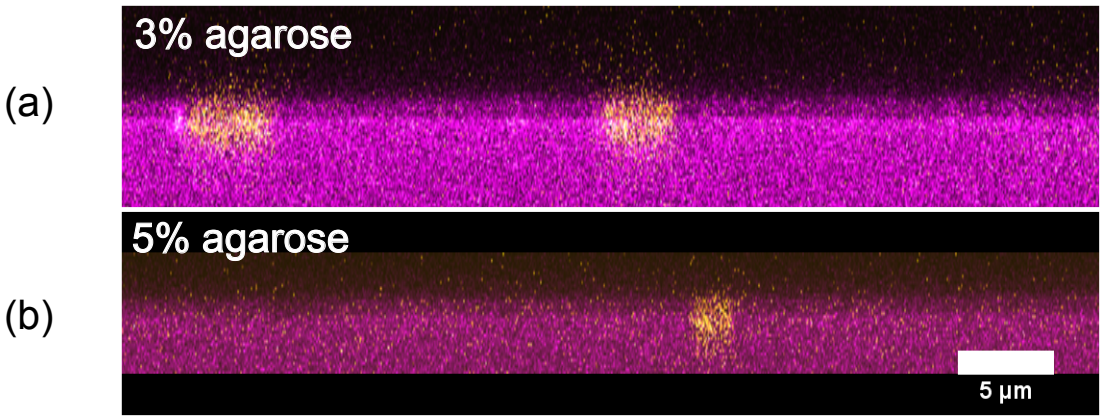

Figure 8.2 $x - z$ slice through a confocal stack showing RJA002 cells (yellow) embedded in rhodamine-B stained agarose (pink) at (a) 3 % and (b) 5 % concentration and confined by a glass coverlsip (not shown). The sharp interface between the rhodamine-B and black region is where the glass coverslip meets the agarose. In both instances, the cells are shown to be at least partially embedded in the agarose, even in stiff, high concentration agarose layers.

confocal images; point spread functions were obtained using 200 nm TetraSpek fluorescent beads (lot 91B5).

8.2.3 Image analysis

All image analysis was performed either in ImageJ or Matlab. For a summary of the macro used to obtain quantitative data on colony morphology, including a download link, see Appendix B (p.177).

8.3 Results

8.3.1 Transition from 2d to 3d growth

To gain an overview of how the transition from 2d to 3d growth happens in our experiments, we first analyse phase contrast images of growing colonies as the transition happens. All colonies start from a single bacterial cell. Even though we begin simply by placing the starter cells on the agarose pad, confocal microscopy shows that at the start of colony growth, the initial cell is pushed into the agarose

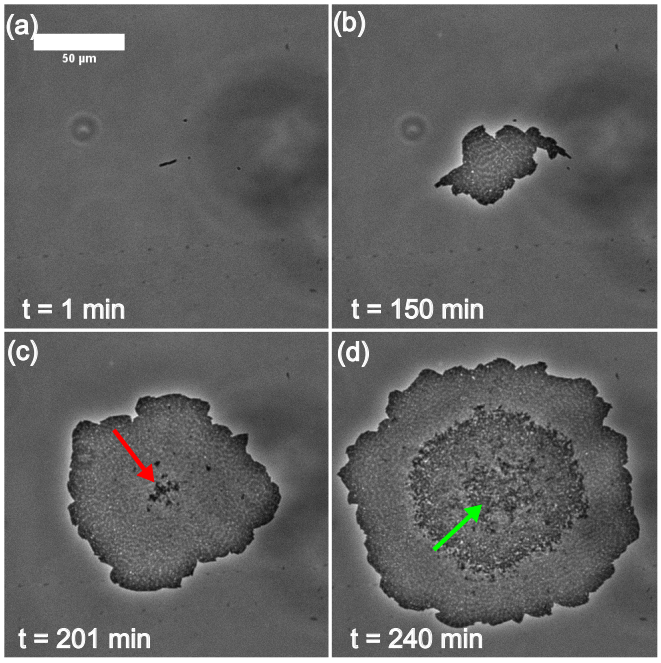

Figure 8.3 A montage of phase-contrast micrographs showing the development of an *E. coli* colony starting from a single cell, growing on 3 % agarose. (a-b) At $t = 1$ min and $t = 150$ min, the colony is undergoing 2d planar growth. At t =201 min (c), cells start to move into the agarose bulk, which manifests as a dark spot near the centre of the colony (shown by the red arrow). By t =240 min (d), the dark spot has increased in size, creating a secondary layer to the original primary layer. A tertiary layer is also visible (green arrow) in the centre of the colony, but this was not always visible in phase-contrast images.

by the glass coverslip pressing down on the agarose. Fig.8.2 shows how a cell is at embedded in the agarose, even at very high agarose concentrations (Fig.8.2(b)). The cell undergoes binary fission at regular intervals, quickly creating a small micro-colony, whose area grows exponentially (Fig.8.3(a,b)). At some point in the colony's development, dark spots in the colony appear in our phase contrast images (Fig.8.3(c)), which signify the transition to 3d growth; these dark regions are cells which have moved into the agarose, forming a new growth plane. The colony continues to grow, and in some instances, even darker regions can develop within the centre of the colony, signifying even deeper invasion of the agarose (Fig.8.3(d)). Because these regions were concentric, it also hinted that the 3d colony might have a tiered structure.

As mentioned in the introduction, previous work [71] has shown that the colony

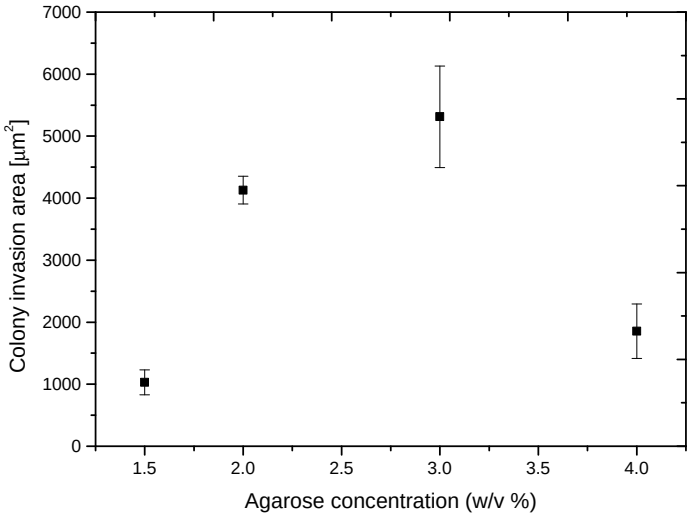

Figure 8.4 Colony buckle area as a function of agarose concentration, showing the non-monotonic relationship with agarose concentration. Colony areas were measured by thresholding the phase contrast images, and buckle times identified by the appearance of dark spots in the colony. These results are in good agreement with the data originally published by Grant *et al.* [71].

area where cells invade the agarose has a complex, non-monotonic relationship with the agarose concentration. We first checked if similar results were seen in our system, and indeed, this was the case (Fig.8.4). Varying the agarose concentration we found that the colony area at which agarose invasion occured peaked at an agarose concentration of 3 %. Motivated by this result, later in the chapter we will investigate the effect of agarose concentration on the development of the bulk layer as a whole.

8.3.2 Growth of a second layer of cells after agarose invasion

Prior to agarose invasion, the areas of the microcolonies in our experiments were observed to grow exponentially as we would expect for exponentially growing cells confined to a single plane. However, shortly after agarose invasion, the expansion rate of the primary layer slows, resulting in a characteristic 'kink' in the curves of colony area versus time (Fig.8.5(a)). This phenomenon can be rationalised as follows: upon invasion of the agarose, some newborn cells in the first layer move

into the second layer, so that fewer cells contribute to the mutual pushing which drives the colony front outwards. Comparing the time-point where invasions were observed in our microscopy experiments and where the colony expansion rate slows shows that the kink in the colony expansion rate sometimes happens later (≈20 min). This delay is likely because the initial invasion comprises a small fraction of the colony population as a whole, which would initially have only a very small effect on the colony expansion rate. For this reason, dark spots in the time-lapse images were used as invasion marker in all these experiments, rather than the kinks in the colony expansion curve.

In our microscopy experiments, following the first appearance of invading cells, a new layer of cells is established rapidly, resulting in a striking 'bloom' of cells contributing to the propagation of a secondary layer front, as shown in Fig.8.3(c,d). The rapid increase in the area of the secondary layer initially follows an exponential growth rate; as measured from the gradient of the secondary area growth curve between secondary and tertiary layer arrows on 3 % colonies in Fig.8.5(a), $\langle g_d \rangle$ =5(2) min. This rate is well in excess of the colony doubling times (Fig.8.5(a)), population doubling times measured in batch culture, and maximally measured growth rates of *E. coli* [104]. For example, for colonies grown on 3 % agarose, the mean area doubling time (g_d) was measured as $\langle g_d \rangle$ =20.00(12) min prior to agarose invasion, while in batch culture, the strain's doubling time was measured to be $\langle g_d \rangle$ =40.9(17) min in the exponential phase.

Interestingly, the expansion rate of the secondary layer decreased to match that of the primary layer very soon after a third layer (as shown in Fig.8.3(d)) appeared, and the primary layer growth rate appreciably slows during the rapid secondary layer expansion period. It is interesting to speculate that if the third-layer area could be measured, it would follow a similar shape to the secondary layer growth curve, albeit shifted along the t axis. Image contrast in the phase contrast images shown here however was not clear enough for these data to be obtained via image thresholding. However, the extremely fast expansion of the secondary layer implies that it cannot be caused by cell proliferation in the secondary layer alone, but rather must be due to a flow of cells from the primary to secondary layer. The observed reduction in area growth rate of the primary layer after the onset of the secondary layer (Fig.8.5(a)) would also support this interpretation, since fewer cells would be contributing to the colony front's expansion after invasion.

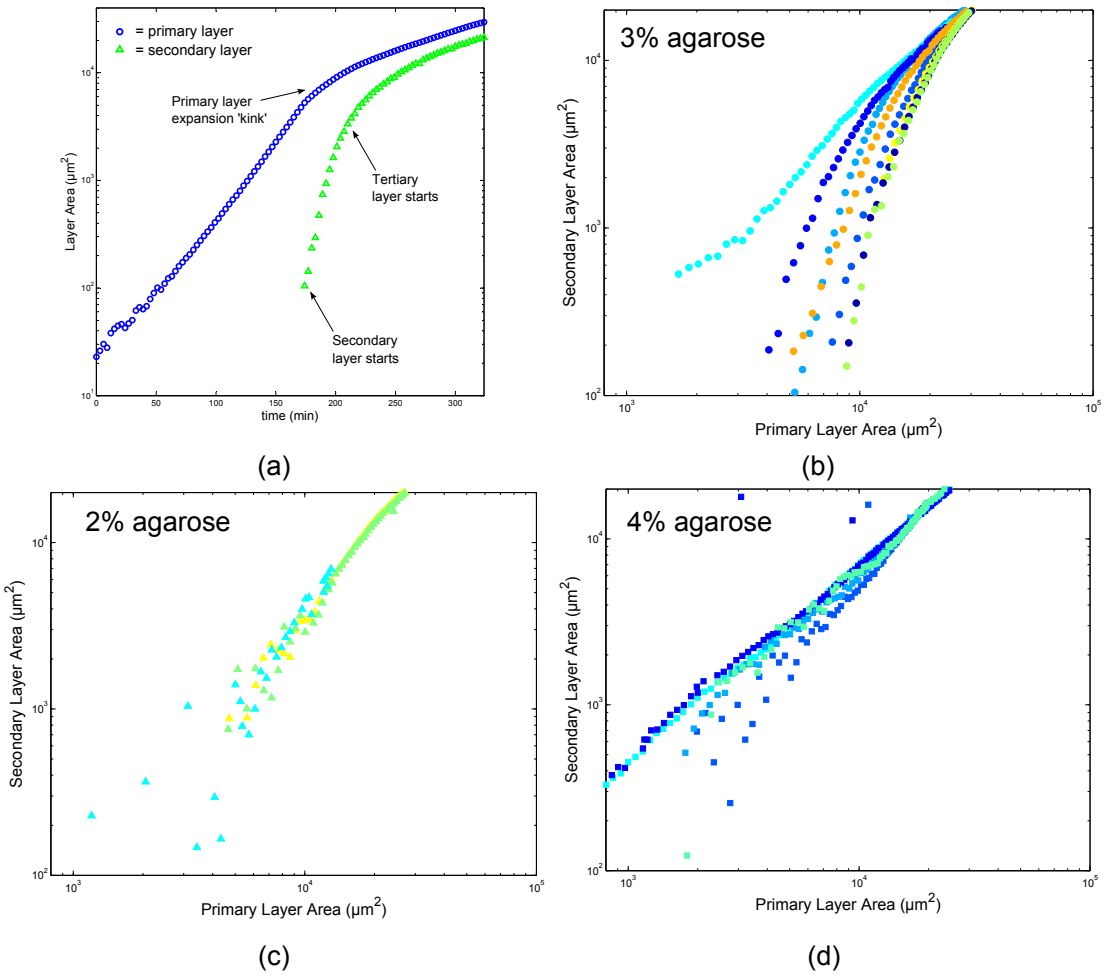

Figure 8.5 (a) A representative plot showing the colony area as a function of time for a growing colony on 3 % agarose, showing the growth dynamics for both the primary layer, and the secondary layer following agarose invasion. The rapid expansion of the secondary layer at early times could vary widely for colonies growing on the same concentration of agarose (except 3 %), and is difficult to measure with the frame intervals used here. For 3 % agarose however, an effective doubling time for the initial growth of the inner layer was g_d =5(2) min, which is far in excess of the pre-invasion colony area expansion rate. (b) Growth of secondary layer areas as a function of the primary layer area for colonies growing on 3 % agarose, (c) 2 % and (d) 4 % agarose. Different colours represent individual colonies.

Visual inspection of colonies grown on 1.5 %, 2 % and 4 % agarose showed a similar sequence of secondary layer developmental stages. However, because these colonies invaded the agarose comparatively earlier compared to colonies on 3 % agarose, secondary layers were comparatively smaller during their rapid expansion, and quantitative data were harder to extract from images. However, what was clear was that the earlier the secondary layer appeared, the sooner its expansion rate slowed to match that of the primary layer.

To investigate the difference in expansion rate between primary and secondary layers, we can plot the secondary layer area as a function of the primary layer area. For colonies growing on 3 % agarose, there was a clear transition between two different expansion rates (Fig.8.5(b)). For 2 % and 4 % agarose, which both had smaller colony areas at invasion than 3 % agarose, there was not as much of a distinction between the expansion rates of the secondary layer at early and late times (Fig.8.5(c,d)).

Taken together, these results suggest the rapid expansion of the secondary layer is driven by a large influx of cells from the primary layer, rather than by proliferation of the original invading cells. Where the tertiary layer could be seen (3 % growing colonies only), its appearence coincided with the secondary layer's expansion rate reduction. As such, this suggest cells invade past the secondary layer, resulting in the secondary layer's expansion rate reduction in a similar fashion to the primary layer.

8.3.3 Expansion dynamics of the primary and secondary layers

Our initial observations, reported in the previous section show that soon after the initial invasion event, a secondary layer grew rapidly before slowing down to match the rate of the primary layer. This observation is intriguing and seems to merit more detailed study.

Examination of the resulting time-lapse movies reveals two striking features of the secondary layer expansion: First, that the layer rapidly approaches a circular shape, and second, that once the initial very rapid expansion period has finished, the secondary layer front expands at a fixed distance d behind the primary layer;

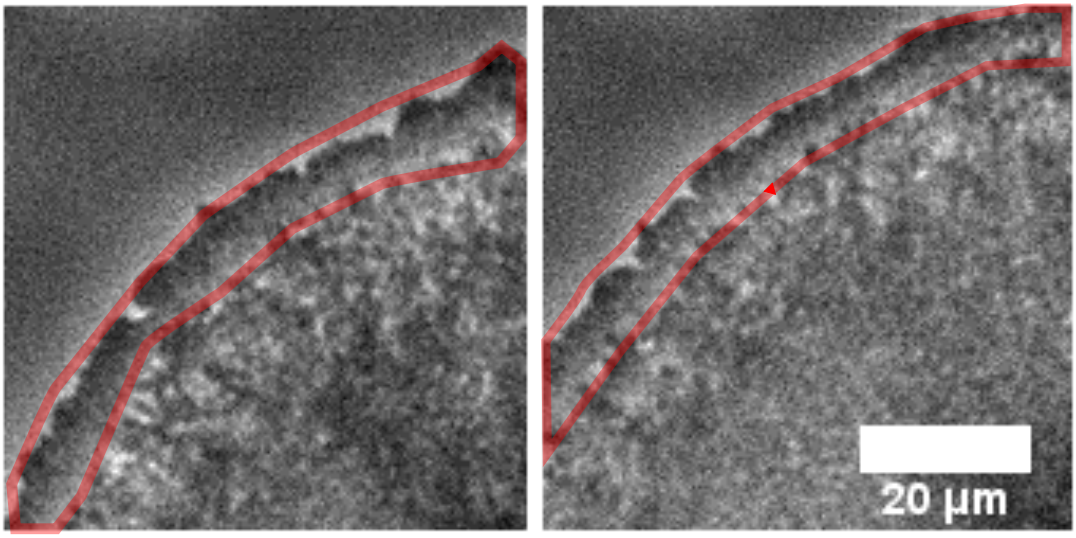

Figure 8.6 Phase-contrast micrographs showing the fixed width difference between layer fronts for a colony growing on 4 % agarose. Δt =42 min between each frame. The region between the two colony fronts is outlined by the red lines, and shows that, to the naked eye, little appreciable difference in its width despite the time difference, and initial secondary layer growth rates.

Fig.8.6 is an example of such a 'ring' for a colony growing on 4 % agarose. To quantify this apparently striking phenomenon, we defined the width as $d = \langle r_\mathrm{p} \rangle - \langle r_\mathrm{s} \rangle$, where $\langle r_\mathrm{p} \rangle$ and $\langle r_\mathrm{p} \rangle$ are the mean distance of both the primary and secondary layer perimeters (r_p and r_s) to the colony centre of mass, the coordinates of which are calculated as $\mathbf{s}_\mathrm{com} = (\langle\ \mathbf{x}_\mathrm{i} \rangle, \langle\ \mathbf{y}_\mathrm{i} \rangle)$, where $(\mathbf{x}_\mathrm{i}, \mathbf{y}_\mathrm{i})$ were the list of $i = 1, 2, \ldots, N$ primary layer pixel coordinates

Fig.8.7(a) summarises the time evolution of the distance d between the primary and secondary layer fronts. For all agarose concentrations, we observed qualitatively similar results: an initial decrease in the distance d as the secondary layer underwent its rapid expansion, followed by d stabilising to a broadly fixed value at larger primary layer areas ($A > 3 \times 10^4$ µm^2, Fig.8.7(b)) which continued until the end of the observation period (6 h to 8 h). Interestingly this 'steady' distance between the expanding primary and secondary layers showed a non-monotonic dependency on agarose concentration which, strikingly, matched the trend measured in colony areas at the point of invasion discussed previously [71] (Fig.8.4, p.150). While such an observation might have been expected, it provides more evidence of the importance of the substrate's physical properties

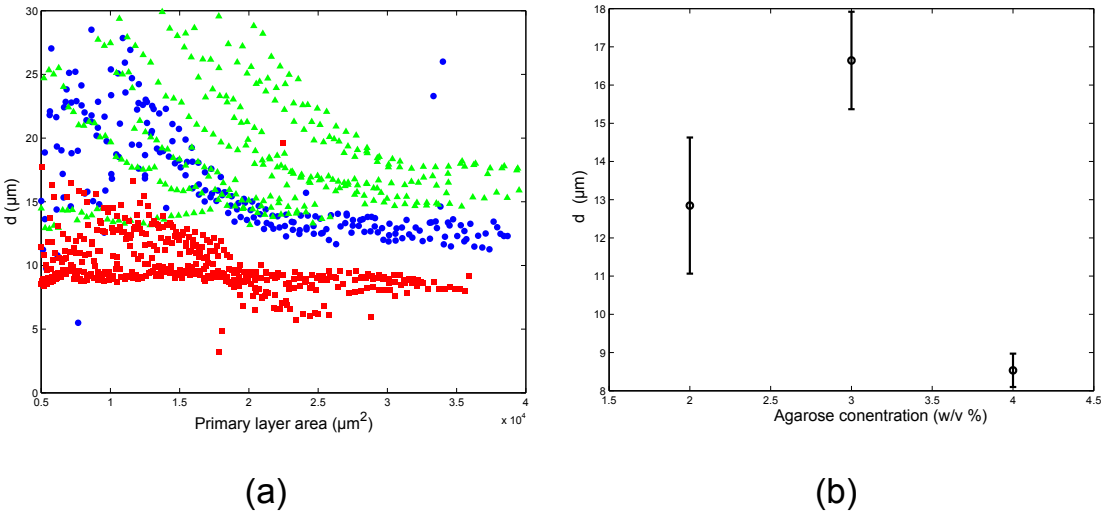

Figure 8.7 (a) Evolution of the distance d between the primary and secondary layer fronts for different agarose concentrations, as a function of the primary layer area. (b) The mean d at large colony areas ($A > 3 \times 10^4$ µm^2).

on the dynamics and morphology of 3d colony development beyond the initial invasion event.

Where it was possible to be seen in the microscope images, the onset of the tertiary layer followed a similar developmental pattern, whereby a fast expansion was followed by a rapid reduction in the rate of propagation, before a fixed distance between it and secondary layer (and by extension, the primary layer) was established. Fig.8.8 illustrates this phenomenon: each layer is marked by a different coloured line to guide the eye. It should be noted that it was only possible to see these structures in phase contrast for colonies grown on 3 % agarose, a factor likely linked to the colony size at the point of colony invasion and the phenomenon of 'zone-of-action effect' [34], whereby the central portions of an object being imaged start to approach the background intensity, thus allowing more contrast for the secondary layer when it appeared. Moreover, the distinction between the second and third layers was less clear than the second and first. A fourth layer could not be seen, but as discussed later, is presumed to develop.

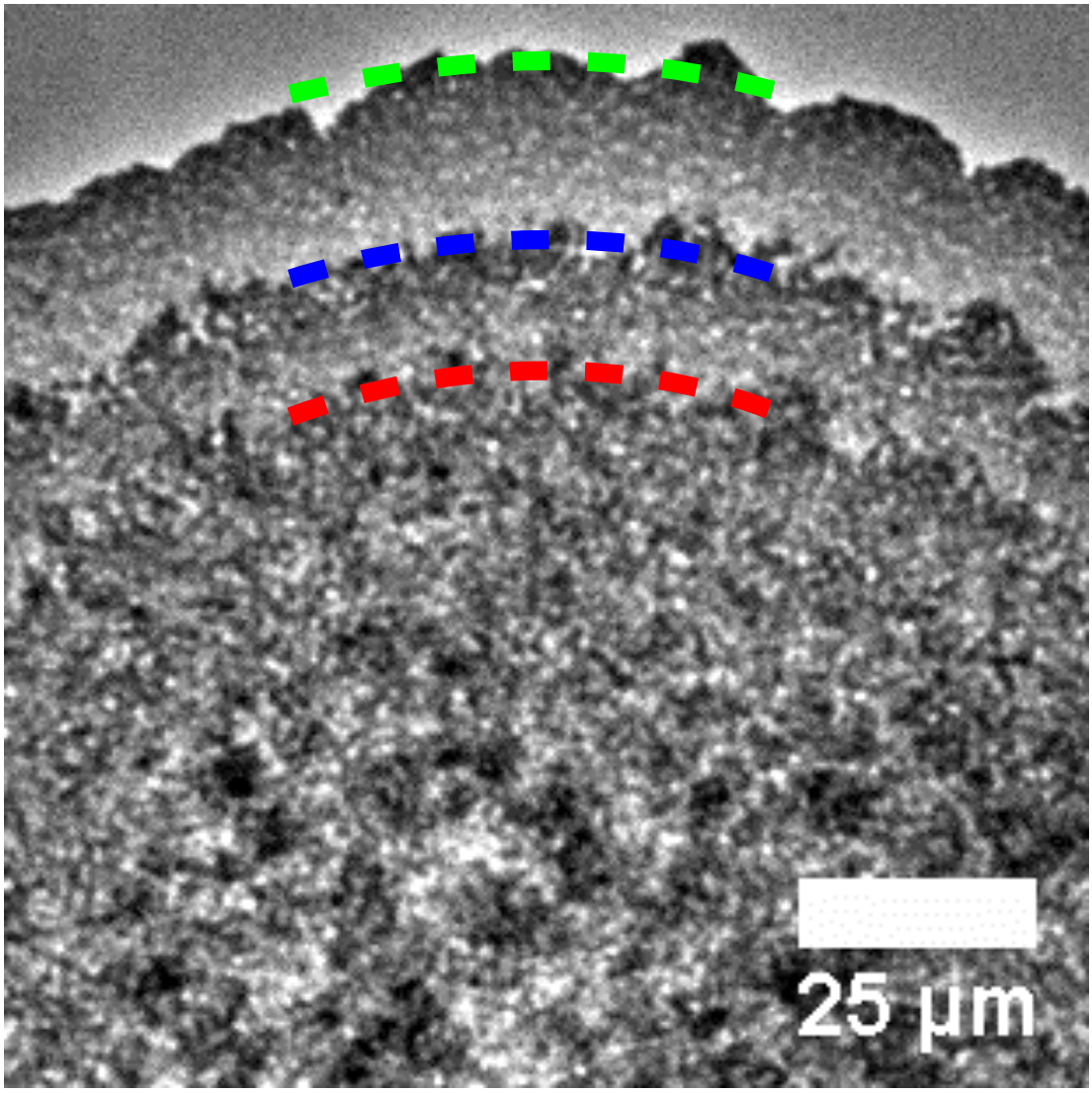

Figure 8.8 Phase contrast micrograph detail of a colony growing on 3 % agarose with lines showing the layer fronts, highlighting the apparently tiered structure of the microcolony, and similar fixed distance behaviour between tertiary and secondary layers as seen between secondary and primary layers. Green corresponds to the primary layer, blue the secondary layer, and red the tertiary layer. The deeper the layers, the harder it is to resolve the interfaces between them.

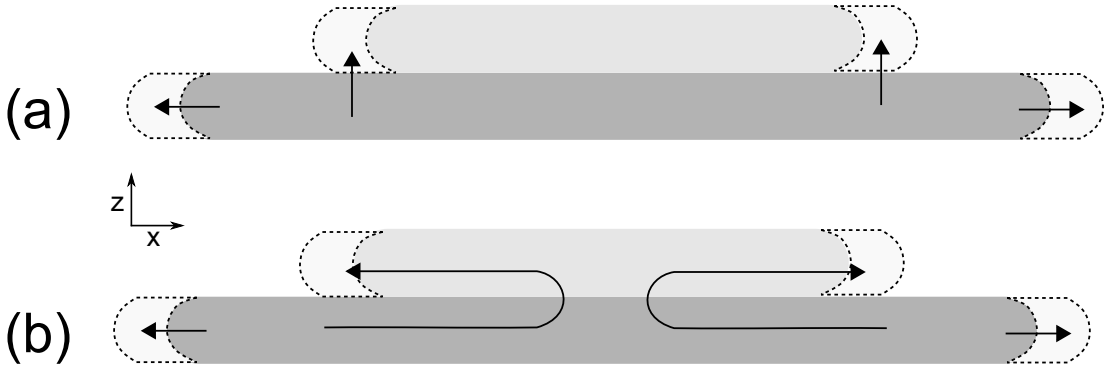

Figure 8.9 Illustration of the two proposed ways cells can migrate from the primary to the secondary layer. In both cases, cells near the primary layer edge contribute to the layer's propagation. The secondary layer front propagates by (a) cells leaving the primary layer at the secondary layer front contact point or (b) through cells flowing through the centre at the original invasion coordinate.

8.3.4 Invasion occurs at multiple locations

What drives the expansion of the secondary layer? It is clear that cells from the primary layer must be migrating into the secondary layer at least in the initial stages. Do these 'migrant' cells all come from the centre of the primary layer, where the initial buckling event happens, or can they also enter the second layer at the periphery, ahead of the secondary layer front (Fig.8.9)? Our microscopy experiments show in fact, both phenomena were likely to be occurring

Soon after the secondary colony front underwent rapid expansion, portions of the primary layer which were close to the secondary layer front could be seen 'flowing' towards the colony centre. This suggested cell movement towards the colony centre, but as the microscope objective resolution was insufficient to confirm if this was indeed the case, single-cell tracking on small colonies was performed. This would confirm if cell velocity vectors did indeed pointed towards the agarose invasion coordinate after a secondary layer had formed. Fig.8.10(b) shows that shortly after the first appearance of cells invading the agarose, some cells within the colony shifted towards the invasion coordinate. These measurements suggest that indeed there is potentially a 'fountain' of cells flowing inwards in the primary layer and moving into the secondary layer once they reach the colony centre.

In our microscopy we can also clearly resolve individual invasion events as dark spots in our phase contrast images, and we consistently see that these events

continue to happen long after the second layer has formed (Fig.8.10(c)), in those parts of the advancing primary layer front. These regions would sometimes grow a small amount independently of the central invasion region, but usually merged with the expanding secondary layer front as it advanced. Furthermore, the secondary layer often preferentially expanded in the direction of isolated invasion regions, suggesting it was easier for the layer front to advance towards areas where invasions had already occurred. Fig.8.10(c) shows two examples of this phenomenon in the same colony, where the secondary layer front can be seen 'reaching' to isolated invasion events in the monolayer ring.

This might indicate that the secondary layer front's advancement is limited by elastic forces from the surrounding agarose; cells which have already invaded the agarose ahead of the advancing secondary layer front might be expected to reduce these forces, accelerating expansion in a particular direction.

8.3.5 3d structure of colonies

Our observation of explicit 'third-level' invasion events in 3 % agarose (and the implied deeper invasion events from secondary layer growth curves in the remaining agarose concentrations) provided motivation to study the 3d profile of the colonies. The phase-contrast images suggested a tiered 'wedding-cake' structure might be expected (and proposed by others [102]), but confocal studies were required to confirm if this was the case. In particular, we are interested in whether the colony is really ordered in layers of cells as our dynamical observations would suggest, or whether cells are instead 'jumbled' inside the growing colony. Colonies were therefore left to grow for 6 h to 8 h on different agarose concentrations to allow sufficient colony development, and imaged using confocal microscopy.

Fig.8.11(a) shows that, in fact, cells did not lie in the plane parallel to the agarose surface as the imaging plane was moved deeper into the imaged colonies; *i.e.* the 'wedding cake' structure does not persist in the colony. This suggests that cells did not simply move into a new growth plane and realign, but actually possessed a complex organisation structure. Indeed, even cells in the primary layer were found to be lying outwith their growth plane, particularly close to the centre of the colony. This dis-order increased as the colony was imaged further into the

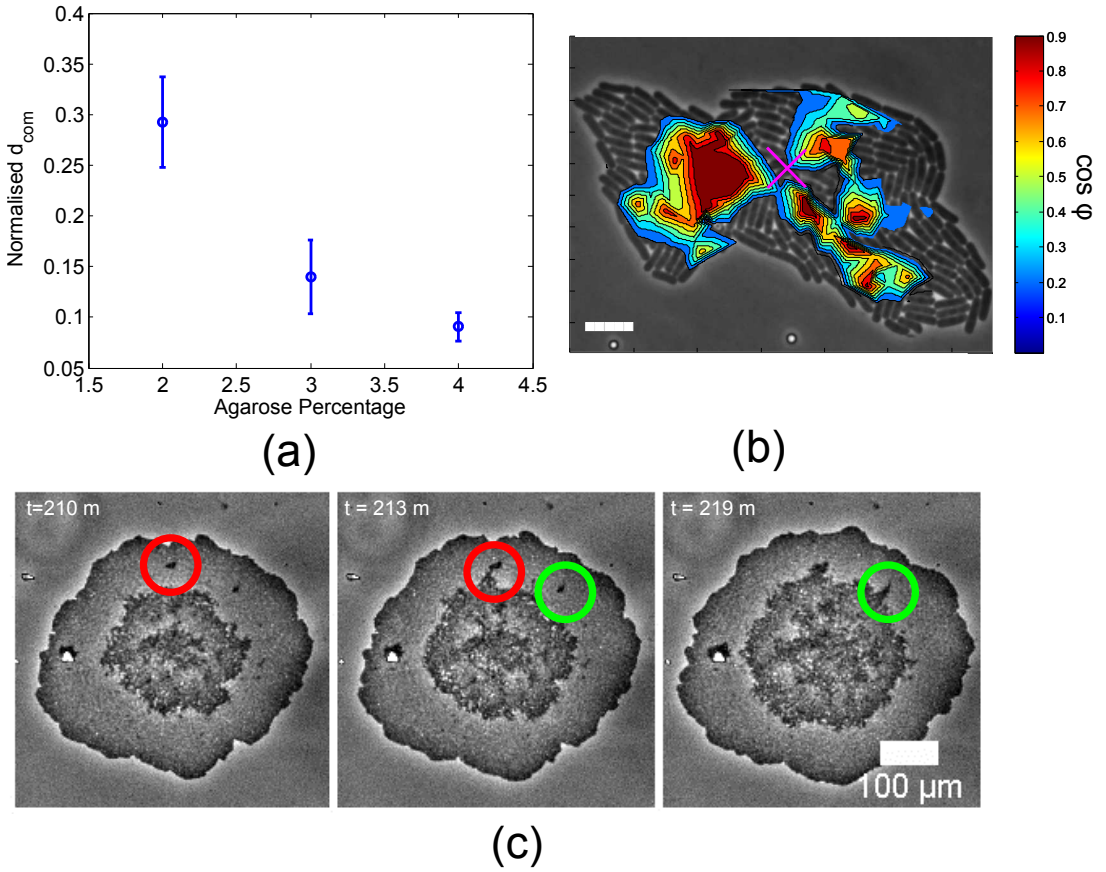

Figure 8.10 (a)Normalised distances of the initial invasion regions to the colony centre of mass as a function of agarose concentration. (b) Interpolated, normalised, velocity map showing the movement of individual cells in a small colony soon after agarose invasion. Regions of cell movement towards the invasion coordinate (marked by 'X') are shown by red; cells moving away from the invasion coordinate have not been coloured for clarity. ϕ is the angle between a cell's velocity vector, and the directional vector pointing towards the invasion coordinate. Scale bar = 5 µm. (c) Micrographs taken in close succession (see timestamps) showing that invasion events often occurred in regions of the primary layer that were beyond the secondary layer interface. In these examples, circles mark the paired invasion events or interest, and the merging with the secondary layer as it propagates. Colony grown on 3 % agarose.

agarose bulk.

We also observed a complex relationship between the lateral area and the depth of a colony. Fig.8.11(b) shows that for both 3 % and 4 % agarose, colonies which proliferated more in the $x - y$ plane (had larger areas) tended to have deeper z-profiles. However, colonies on 2 % agarose did not follow this pattern, instead plateauing in height despite the primary layer area increasing. This had a striking effect on the colony profiles: Fig.8.11(c) shows $x - z$ projections from confocal microscopy of colonies grown on different agarose concentrations. Those grown on 2 % were more spread out, while those on 3 % and 4 % agarose had greater curvature.

This behaviour possibly reflects the radial compression forces exerted by the agarose on the colonies, whereby a smaller agarose concentration (*i.e.* a softer surrounding medium) makes it easier for colonies to proliferate in the original growth plane, than to invade deeper into the agarose. A noticeable feature was that despite the same incubation times, and cell inoculation densities, there was considerable variation in the size of colonies on different agarose concentrations, even when considering the time-delay between imaging each sample. We therefore checked what effect the agarose concentration had on the area growth rates of the colonies, since as discussed in the following section, this could play an important role in the development of 3d structure.

8.3.6 Agarose invasion area dependency on cell growth rate

Our experiment, and previous work by others [71], suggest that the shape and expansion rate of the growing colony should be determined by a balance of outward forces due to cell growth and inward forces due to agarose elasticity, and friction between the cells and glass and agarose surfaces. This picture would suggest that the cell growth rate would have an important effect as a faster growing colony would exert a greater outward expansion force than a similarly sized, but slower growing, colony. Furthermore, in the event the agarose had dynamic frictional properties, the friction experienced by cells would be greater.

Therefore, a more detailed study of the colony expansion rates was carried out. Fig.8.13(a) shows that for the three lower agarose concentrations tested, colonies

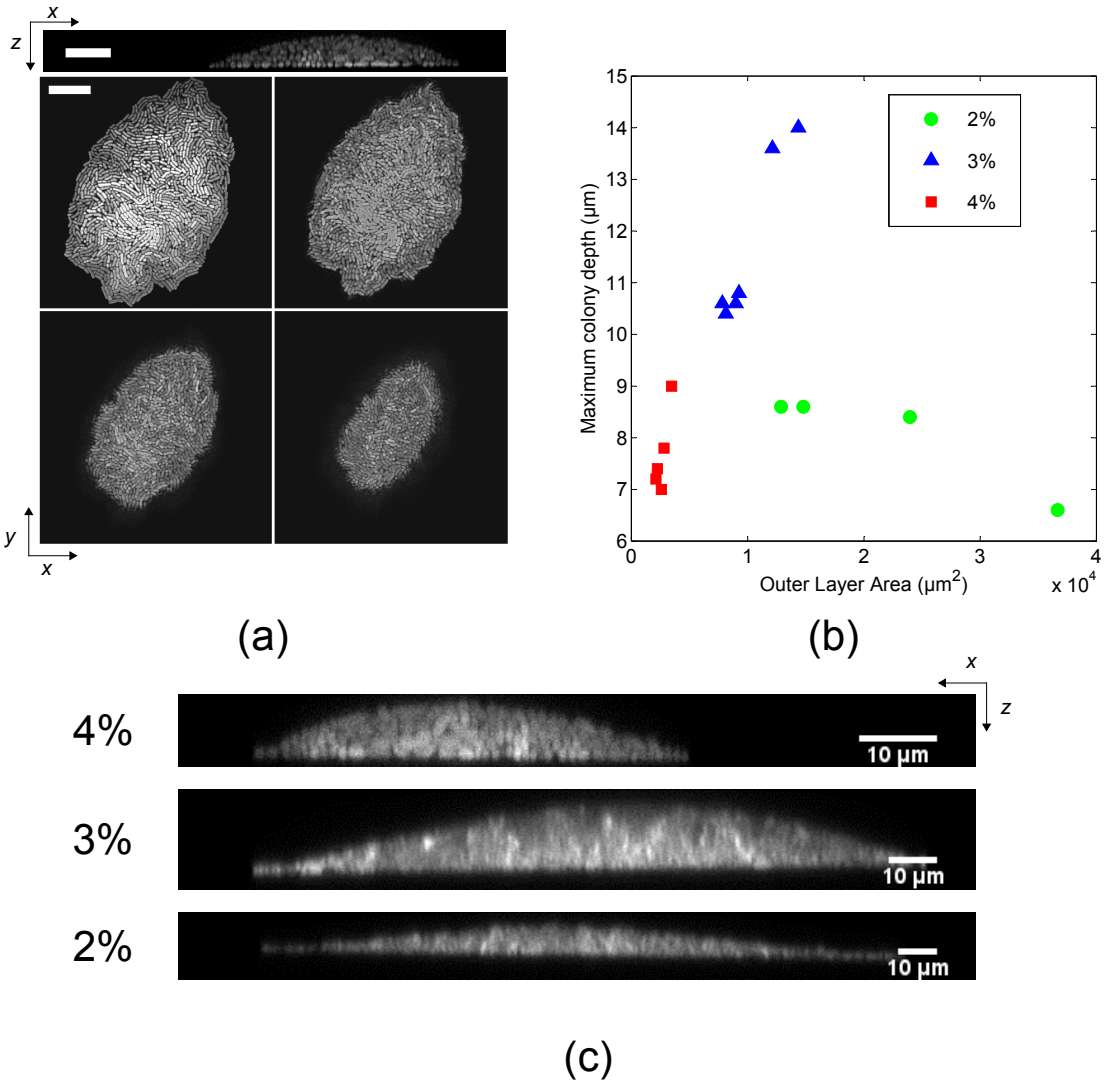

Figure 8.11 (a)Deconvolved z-stack slices of a colony grown on 4 % agarose, scale bar = 10 µm, acquired using confocal fluorescence microscopy. The top panel shows the $x-z$ profile and the non-tiered structure of the colony. (b) Comparison of colony penetration depths into the agarose bulk against the area of the primary layer for different agarose concentrations. (c) $x-z$ profiles of colonies grown on different agarose concentrations showing the different profiles despite having similar primary layer areas.

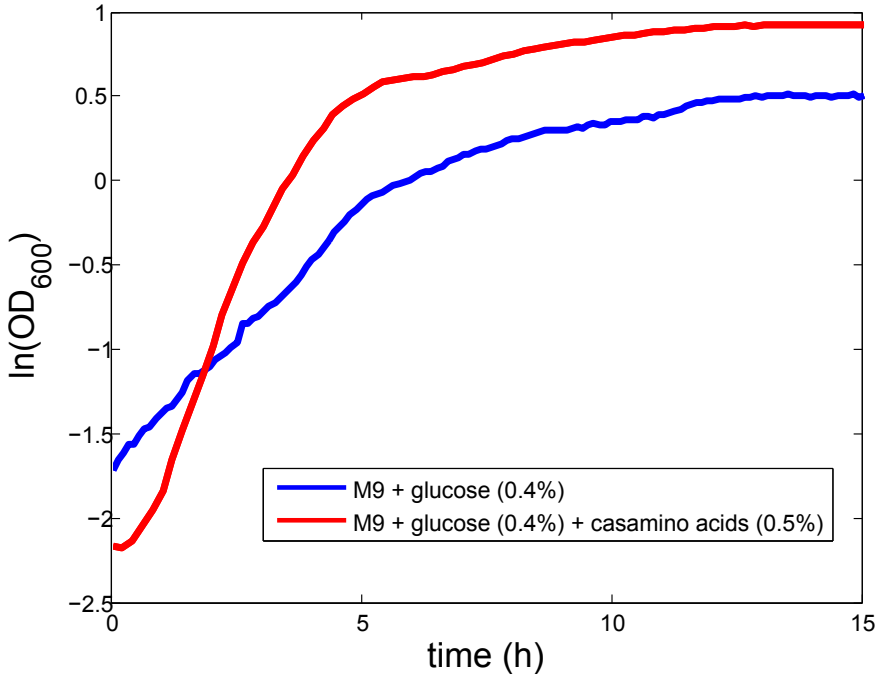

Figure 8.12 Growth curves for RJA002 growing in M9-glucose (0.4 %) (blue line,$\langle g_{\mathrm{d}} \rangle$ =84.2(17) min), with added casamino acids (0.5 %,) (red line, $\langle g_{\mathrm{d}} \rangle$ =40.9(17) min). Doubling times were measured by fitting a straight line to the exponential phase of the curves ($0 < t < 5$).

had an area doubling rate of $\langle g_{\mathrm{d}} \rangle \approx$20 min, while those on 4 % had both a lower mean doubling time of $\langle g_{\mathrm{d}} \rangle$ = 27 min, and wider distribution of area doubling times. Indeed, work by others has shown that an *E. coli* cell's expansion rate can be limited by the compressive force exerted by the agarose, which is proportional to the agarose concentration, rather than by nutrient diffusion limitations [85]. Thus, the reduced colony area expansion rates at high agarose concentrations may have been due external forces. However, the effect of slower growing colonies on 3d colony development was still unclear.

Therefore, to check if slower growth rates did affect 3d colony development, greater control over the growth rate was exerted by performing a series of experiments using a different growth medium: M9-glucose (0.4 %), not supplemented by casamino acids.

Using the new media recipe resulted in longer-pre invasion colony area doubling times for all agarose concentrations tested, as expected, since the growth rate in planktonic phase is also slower on this medium (Fig. 8.12, mean exponential phase doubling times: $\langle g_{\mathrm{d}} \rangle$ =84.2(17) min and $\langle g_{\mathrm{d}} \rangle$ =40.9(17) min). The effect on the

pre-invasion colony area doubling times are summarised in Fig.8.13(a): as agarose concentration was increased, small increases in the colony doubling times were measured, with the greatest increase seen for 4 % grown colonies. Crucially, the factor increase in the colony doubling times between comparable data points was the same (on average, 2.60(12) times greater), showing a consistent reaction across agarose concentrations compared to the faster growing colonies. This suggests the lower colony area growth rates at 4 % agarose arise from the compression forces exerted by the agarose.

During this process, it became clear the invasion point was different than previously observed, however. Analysis of the colony areas at the point of invasion showed colonies shifted to 3d growth at comparably smaller colonies compared to the results presented earlier in this chapter; whereas the range of colony invasion areas for faster growing colonies was 1000 µm^2 to 5000 µm^2 (Fig.8.13(b)), here it was in the 150 µm^2 to 350 µm^2 range (Fig.8.13(d)). Furthermore, a different pattern in colony invasion areas was measured, with colonies growing on 2 % agarose invading agarose at similar colony sizes compared to 3 % agarose. The slowest growing colonies (4 % agarose) also invaded the agarose at the smallest areas overall.

It is clear, therefore, that colony area expansion rates affected bulk layer development. Investigating the effect of a wider range of cell growth rates on the invasion area would be a very interesting route to further untangle the role of colony growth rates.

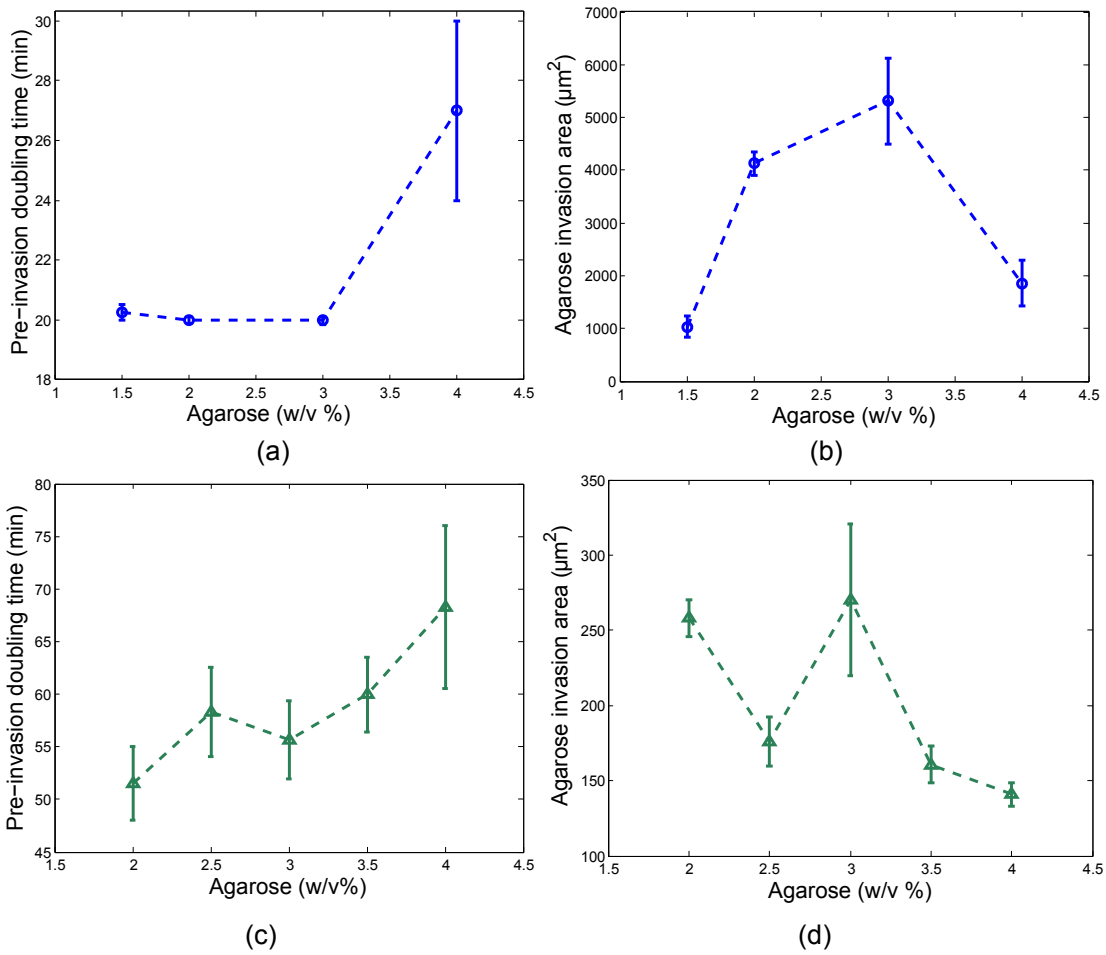

Figure 8.13 (a) Colony area doubling times on M9-glucose (0.4 %) + CAA (0.5 %) for different agarose concentrations, and (b) the resulting colony invasion areas. (c) Colony area doubling times on M9-glucose (0.4 %) for different agarose concentrations, and (d) the resulting colony invasion areas. Note that panel (b) is a reprint of Fig. 8.4.

8.4 Discussion

In this chapter, phase-contrast and confocal microscopy was used to observe the growth of a colony from a single cell, to its transition from 2d growth to 3d growth and beyond to gain insights into the developmental processes of a 3d microcolony. Crucially, the cells were confined by a glass coverslip, and so were prevented from growing into free space, resulting in the cells invading the agarose, producing a series of 'fronts'. In single cell studies of gene regulation [29**?**], this invasion is usually regarded as a problem since it signals the end of a viable imaging period, but it also reflects the real life developmental stages of bacterial colonies in some natural environments, such as bacterial growth between catheter implants and soft-tissue. Using phase-contrast imaging techniques in 2d allowed longer term observations and higher time resolutions than might have been possible using purely confocal and fluorescence studies, which can be limited by photo-bleaching. This provided information on the developmental behaviour of bulk layers in the colony to a higher degree of time-resolution otherwise possible.

8.4.1 Transition from 2d to 3d

Previous work by Grant *et al.* [71] has suggested that the invasion of cells into the agarose bulk is a purely mechanical phenomenon, and that the area at which colonies invade the agarose likely depends on the frictional properties of the substrate, which itself is controlled by the agarose concentration. Here, we reproduced the key result that a non-monotonic relationship between agarose concentration and colony area at the point of invasion exists, with a peak at an intermediate agarose concentration. It should be noted the peak was observed at a different agarose concentration (2.5 % compared to 3 % here), but this could have been due to only integer concentration values being tested. However, the areas at which colony invasions were measured were in rough agreement with Grant *et al.*, with the range of areas lying between $1 \times 10^4\,\mu m^2$ and $5 \times 10^4\,\mu m^2$ for the agarose concentrations tested. Further consistency with Grant *et al.* was shown in that colonies first invaded the agarose near the centre of colony, regardless of the agarose concentration tested, although a correlation with increasing agarose concentration was measured in these experiments, but with only three data points,

it is hard to say if this relationship truly exists. However, we can conclude that the buckling phenomenon observed in these experiments was in broadly in good agreement with the results reported by Grant *et al.*.

Interestingly, reducing the growth rate of the colony by changing the growth medium resulted in significantly smaller colonies when the agarose invasion occurred. Such a result is not expected, and highlights the problem's complexity. First, consider expansion forces: the transition point for colonies is governed fundamentally by the balance of inward and outward pushing forces [71, 102]: once the inward forces, arising from the frictional forces between cell and substrate, and edge compression force of the agarose, exceed those exerted by the vertical compression force, the cells move into a new growth layer. The gross outward force generated by the colony arises purely from the cell-cell pushing resulting from their elongation; the faster the cells lengthen per unit time, the larger the expansion force, leading to a greater compression at the centre of the colony, and earlier buckling. In turn, this would imply faster growing colonies would invade the agarose at smaller areas, which is in disagreement with the experimental results.

The second point concerns the frictional contribution. In order to reduce the growth rate, casamino acids were removed from the growth medium, resulting in a ≈ 2.6 factor reduction in the colony area growth rate pre-agarose invasion. It is unknown if the agarose has velocity-dependent frictional properties, which could also affect the balance of forces: faster growing cells would experience more friction if the agarose had dynamic friction coefficients, and so for faster growing cells, an earlier invasion area might be expected. Moreover, it has been shown in other *E. coli* strains, a reduction in the growth rate of cells is associated with a lower rate of fimbrial production [105] - fimbria are cell appendages which help adhesion to surfaces, and so it would be expected that cells would experience smaller frictional forces if a growth-dependent link had occurred here, resulting in larger buckling areas, too.

Finally, it is also important to note that the dependence of colony area at invasion on agarose concentration seen in the faster growing colonies was not preserved in the slower growing colonies. The characteristic curve identified by Grant *et al.* was believed to arise from an unknown, but necessarily complex relationship between agarose concentration and its elastic properties, which directly affected

the agarose friction coefficient. An environment which limits growth rates might therefore also affect the relative contribution of friction, since fewer cells would mean smaller cumulative frictional forces on the colony. Moreover the speed at which the cells move along the surface could also affect the magnitude of the frictional forces. Even at fixed agarose concentration, the area at invasion might be sensitive to small differences in the growth rate. Indeed, the lowest and highest invasion areas occurred at 2 % and 4 % respectively, which also had the lowest and highest initial growth rates - these agarose concentrations are also predicted to have the highest friction coefficients [71]. The peak observed at 3 % may reflect the fact that despite having an intermediate colony area growth rate compared to other agarose concentraions, it has the lowest frictional coefficient.

It is also known that slower growing cells are on average both shorter, and thinner than faster growing cells [106, 107]. This could potentially explain some of the difference in invasion areas seen between colonies with different area expansion rates: for similar cell population levels, colonies consisting of slower growing cells would be smaller than those colonies formed by faster growing cells. Could the colony cell population at the point of invasion be similar, despite having different areas? Based on typical cell sizes reported by others at particular growth rates [106], a factor of 2.4 difference in cell doubling times resulted in an approximate two-fold reduction in average cell area. This can not entirely account for the order of magnitude difference in colony invasion areas observed between fast and slow growing colonies. Furthermore, complete characterisation of the cell sizes in the growth environments tested here would be required to confirm to what extent cell size accounts for the difference in invasion areas in different growth environments.

In summary, reducing the growth rate of the colony to $\langle g_{\mathrm{d}} \rangle$ =84.2(17) min from $\langle g_{\mathrm{d}} \rangle$ =40.9(17) min results in colony buckling at areas that are smaller by almost an order of magnitude. While the exact cause of this is unknown, it is likely to be physical in nature, and arising from the relative contributions of friction, and the expansion forces exerted from within the colony.

8.4.2 Secondary layer dynamics

Although phase contrast is inherently a 2d imaging method, we were able to image the secondary layer was visible in time-lapse movies as a dark central region. Observations of these movies showed that these dark regions grew rapidly after first appearing, which coincided with a rapid reduction in the rate of expansion of the primary layer. Eventually, the secondary layer's expansion slowed to an extent that its radial expansion grew linearly in time at the same rate as the primary layer, resulting in concentric expanding fronts separated by a fixed distance d. Such a phenomenon has recently also been observed by others [102].

That the initial area growth rate of the secondary layer was in excess of the colony area growth rate prior to agarose invasion, and that the primary expansion slowed after invasion, implies the growth of the secondary layer was driven by a loss of cells from the primary layer (possibly in addition to cell proliferation within the layer itself). Furthermore, the secondary layer almost always grew radially from the initial buckle points, rather than from additional, discrete, invasion regions appearing at different points in the colony, suggesting its continued expansion was mechanical in nature since we expect the compression stress to be greatest at the centre of the primary layer [71].

Colonies grown on 3 % agarose had the greatest difference between initial and longer term secondary growth rates, compared to the other agarose concentrations tested. This is likely a product of the colonies simply being larger than the other agarose concentrations at the point of invasion. Internal pressures would be expected to be greater within larger colonies, suggesting that more cells might be pushed into the secondary layer. However, that additional invasion events were sometimes seen beyond the secondary layer growth front, which then preferentially 'grew' towards each other, suggests the agarose may be structurally affected locally by invasion events, making it easier for more cells to move into the bulk close to where the invasion event has happened.

The fixed distance between primary and secondary layer fronts was a consistent feature seen in colony development regardless of the agarose concentration, and indicated the radii of the two layers were growing linearly in time. Linear radial growth for colonies growing *on* agarose (rather than being pushed in by a glass coverslip), has been attributed to depleted nutrients, oxygen starvation and non-

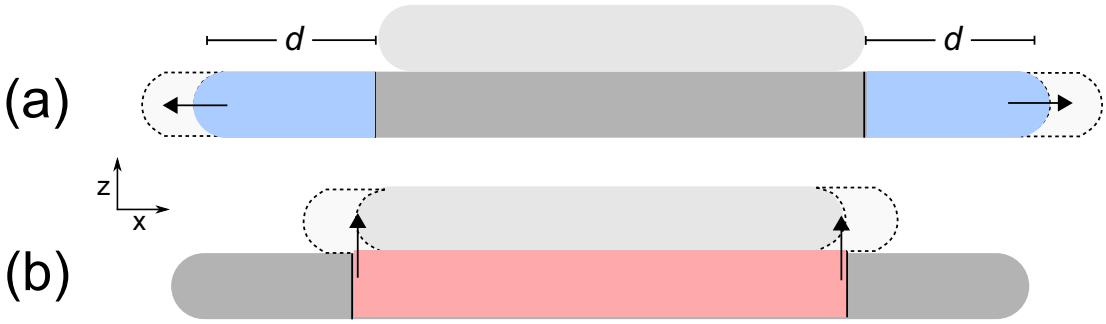

Figure 8.14 Illustration showing of how the distance d between primary and secondary layer fronts could potentially appear. (a) Cells in the monolayer region (blue) are able to push neighbouring cells when growing, which causes the colony front to expand. (b) Cells in the primary layer area beneath the secondary layer (red) are unable to push the cells in the monolayer region (gray) out because or cumulative frictional forces.

optimal temperatures [108]. However, the colony sizes in my experiments were at least an order of magnitude smaller in scale, such that nutrient or oxygen depletion was not expected to play a role [108], suggesting another mechanism was at play.

Others have suggested the fixed distance d reflects the maximum number of cells which a cell in the primary layer can 'push' as a result of its elongation [102]: only cells within a distance d of the colony edge can advance the colony front. If the cell lay in the mono-layer region, they could push cells radially outwards, thus propagating the primary layer colony front. Otherwise, if the cell was further than a distance d from the colony edge within the primary layer, it would have to move into the secondary layer. Fig.8.14 summarises this idea.

The dependence of d on agarose concentration would support this, if we assume the frictional coefficient of agarose has a non-monotonic dependence on concentration [71]. A larger substrate frictional coefficient would mean that a cell in the primary layer would be unable to push as many cells outwards to accommodate cell growth and division, and if this route is blocked by too many cells, it would instead find it easier to move into the secondary layer, thus propagating the secondary layer colony front.

While this reasoning cumulatively implies buckling events would occur at the secondary-primary layer interface, cells were still seen to invade in the monolayer region (Fig.8.10). It is speculated this could be because of inhomogeneities on

the agarose surface, leading to greater inward forces than normal, thus pushing the colonies into the bulk. That these regions did not proliferate independently of the central multilayer region suggests that the internal pressure at these points was insufficient to push more cells into the bulk, supporting our hypothesis that the first buckling event relieves pressure within the primary layer.

8.5 Conclusion

Bacteria growing sandwiched between a glass coverslip and an agarose surface will proliferate in 2d, until radial pressures exerted on the colony cause cells near the centre of the colony to invade the agarose and form a new growth layer. This new layer grows well in excess of the cell growth rate as a result of a high flux of cells entering from the original monoloayer, which is likely driven by the monolayer's internal pressure. Once the secondary layer reaches a critical size, cells will then start to invade deeper into the agarose, creating additional layers. A characteristic fixed-width monolayer ring soon develops, arising from the primary and secondary layers growing radially at the same rate. This distance likely depends on the frictional properties of the agarose, with smaller frictional forces resulting in larger ring widths. Colonies were also shown to invade agarose at smaller colonies when the colony growth rate was reduced which potentially also shows the importance of the interplay between expansion and inward forces acting on the colony as it develops in 3d.

8.6 Future work

In this chapter, I characterised in detail the morhology and dynamics of *E. coli* colonies as they invade an agarose substrate. This study raised multiple question meriting further study. First, a detailed characterisation of the microscopic structural properties of the agarose as a function of its concentration would provide more insight into the scale of forces acting on the colony as it develops in 3d. This is particularly important since it is unknown if macroscopic agarose properties translate to small scales. Combining these experimental results with theory and simulations would also be a vital next step in understanding the forces

exerted by the agarose.

Similarly, tuning the surface properties of the bacterial cells (such as using flagellaless cells) would be an obvious extension to properly resolve the importance of friction in the development of secondary layers. Furthermore, use of tracer particles embedded in the agarose, or traction force microscopy could potentially yield insights into the forces exerted by the colony, as has been conducted for eukaryote cells [109]. Doing so would also help reveal to what extent bacteria compress or break the agarose as they move through it. 3d cell tracking would also be a useful option, since it would allow a robust quantification of the transfer rate of cells between layers.

Finally, I have addressed the issue of colony growth where cells start attached to a surface. The logical extension to this would be to study the effect of agarose in bacterial suspensions. This environment is arguably simpler to model, since the forces acting on the colony would be isotropic, and is similar to the way bacteria can proliferate in foodstuffs.

Chapter 9

Conclusions

This thesis experimentally investigates different properties of surface growth of *Escherichia coli*, using microscopy to track the development of microcolonies on agarose surfaces.

In Chapter 5, we used a system in which differently labelled populations of *E. coli* were allowed to compete for space on the agarose surface, similar to [21, 64]. Using this, we investigated the importance of spatial structure and growth strategies between competing organisms. We found that expansion competition, manifest as cell lag-times, played an important role in the eventual distribution of 'winners' and 'losers', whereby increasing the range of times cells start growing leads to a larger variety of eventual success. Boundary interactions were also found to be partially responsible for colony success, but only at higher initial seed cell densities. We speculated this might have been due to squeezing behaviour at collision interfaces. We also demonstrated the experimental feasibility of tracking the fates of many competing colonies; this is important, because relatively few laboratory experimental system exist which allow the testing of ecological theory of spatially structured environments.

In Chapter 6 we captured the main features found in the experiments in Chapter 5 by using a simple simulation. This allowed us to eliminate lag-times altogether to better study the role of growth behaviour on the eventual distribution of 'winners' and 'losers'. We found that a significant amount of variation in the eventual success of colonies could occur simply by virtue of exponential expansion, which

resulted in squeezing behaviour at collision interfaces. This is in comparison to perimeter-growth, which resulted in fewer winners and losers. Initial cell densities played a much smaller role in determining eventual success, indicating that in our high density experiments, the colonies were exponentially growing at the point of collision. Furthermore, there was evidence that for exponentially growing colonies at high cell densities, the morphology of available space could impact the chances of success. Again, this was attributed to boundary interactions at colony collision interfaces.

Collectively, it would be interesting to apply the experimental side of this competition project to more complex ecological and evolutionary phenomena, and continue to compare to simulations. The recent interest in spatially orientated ecological theory [74, 110] makes this system ideal for controlled experiments. One suggestion is to study the propagation of cell death induced by viral warfare between competing colonies.

In Chapter 7, motivated by the fact bacterial colonies often grow in small cavities, we investigated the effect of confinement on both the colony's physical and genealogical structure. In agreement with work by others [13, 14, 70], we found that confinement resulted in a high degree of cell orientational order, but also that the narrower the channels, the further the orientational order extended. Confined growth also resulted in a steep velocity profile pointed from the colony interior to the edges. These effects likely contributed to the resulting distributions of neighbourly 'relatedness' in the confined colonies. In the narrowest channel, cells had more neighbours which were genetically distant, compared to the intermediate and widest channels, despite the greater spatial restrictions. More distantly related relatives were found to the side of cells, than at the poles. Similarly, confined geometries affected the spatial positions of 'old poles', which are increasingly believed to induce age-related effects on bacterial function. These results demonstrate that particularly confined geometries might still facilitate 'mixing' between cells when there are escape points to promote cell flow.

An interesting route to take from here would be to see if cooperative behaviours are indeed affected by the different growth geometries, particularly at the small colony sizes studied here. Using fluorescent reporter strains would indicate at what regions cells were participating in cooperative behaviours (such as

production of public goods, like siderophores).

In the final project presented in Chapter 8, I investigated the transition of 2d colony growth to 3d. Specifically, I addressed the growth of secondary layers when colonies, which are sandwiched between a glass coverslip and the agarose surface, invade the agarose bulk. This builds on the work of others [71, 102]. Growth of secondary layers grew at rates which were in excess of colony and cell growth rates, which also coincided with a reduction in the expansion rates of the primary layer. From this, we concluded there was a flux of cells leaving the primary layer and entering the secondary after the main invasion event occurred. A monolayer ring of cells encircling the perimeter of the primary layer has a width that depended on the agarose concentration - we speculate that frictional forces, which depends on the agarose concentration, are responsible for the different widths. Also, colony growth rates were associated with smaller agarose invasion areas than faster growing colonies, which highlights the complex interplay between the forces exerted by, and on, the agarose. Finally, colony structure was not as idealised as others have suggested [102], where we found that cells in secondary and tertiary layers were disordered.

The biggest unanswered question from this project were the size of the forces being exerted by the agarose at the micrometre scale, and so this is probably the best place to explore further work. While the macroscopic properties of agarose have been characterised, it is unknown how they scale to micrometre levels. Combining simulations with experiments would be a useful step in understanding these forces in greater detail.

Appendix A

Schnitzcells workflow

Schnitzcells provided an extensive suite of segmentation, tracking and correction routines to quantitatively analyse time-lapse movies of growing microcolonies. The software was written by the Elowitz lab at Caltech, and is free to download from their website [36]. However, extra functions were written in Matlab for this thesis to re-sort data, and to quantify other parameters required for this thesis. Here, the general workflow following segmentation and tracking is presented, along with a description of what each function did.

The final Schnitzcells output file is a structure array with N elements, where N is total number of lineages in the colony. Contained within each element are data on the individual lineage in question, such as cell length, width, angle, in addition to pointers to parent and daughter lineages; in keeping with the nomenclature of Schnitzcells, each lineage is referred to as a 'schnitz'. Tab.A.1 summarises some of the key functions used in this thesis. For a complete guide of how they were implemented, see `http://goo.gl/aq1j0H`, and for all the Schnitzcells supplementary functions used in this thesis, see `http://goo.gl/VqJu0p`.

Function name	Description
schnitzdescendants	Returns a vector holding all the schnitz indices which descend from a given schnitz. For example, passing the original mother schnitz would return a list of each and every lineage.
PoleCoords_DPL	Calculates the coordinates of each cell pole in the time-lapse movie, based on the cell length and angle as measured by Schnitzcells.
DaughterPoles_DPL	Determines which of the daughters inherits which pole from the mother, as well as tracking these poles during each schnitz.
selected_schnitz_data_DPL	Reorders the lineage data into chronological order, rather than by the arbitrary schnitz index
OldPoleTrackingTest_DPL	Writes markers onto the time-lapse movie showing the position of the elder poles. Used for checking old poles have been correctly tracked.
CoMSchnitzcells_DPL	Calculate the colony centre of mass at each point in the movie.
SchnitzcellsRates_DPL	Calculate rates of change in cell features, such as position and length.
movierelatedness_DPL	Determine the average genetic distance of each cell to its neighbours
cell2cellrelatedness_DPL	Similar to above, but rather than calculate a mean, a record of each cell's neighbour genetic distance distribution is recorded.

Table A.1 Summary of key functions written to exploit Schnitzcells datasets.

Appendix B

Isolating secondary layers in growing colonies

B.1 Tracking layer dynamics

Quantitative data on the 2d projection of both the primary layer and secondary layer were acquired from the phase contrast movies by threshholding. The former were achieved using standard background removal tools and thresholding functions in ImageJ. Secondary layers were obtained automatically through the following image analysis steps, which are also presented in Fig.B.1. The macro can be downloaded from `http://goo.gl/VbHzwF`.. A Laplacian filter was applied to obtain the edges of the primary and secondary layer edges, and local thresholding performed. The outer layer was then removed by subtracting a dilated, inverted thresholded version of the outer layer itself from this image, and bright outliers removed. The remaining object was a 'blob' of pixels corresponding to the inner region. To ensure a continuous perimeter, the image was inverted, then watershed, inverted again, and flood filled. To remove spurious watershed lines, a copy of this image was inverted, flood-filled, the outline detected, and subtracted from the original, leaving a thresholded image of the inner, buckled layer.

The resulting binary image broadly follows the inner layer, but from the overlay (Figure B.1,panel 8), it's clear the boundary deviates from the true perimeter slightly. Therefore, inner layer morphological features obtained via this process

will have a higher uncertainty than the outer layer. Sometimes, the binarised perimeter can significantly bow or bulge from the true perimeter, although for features such as mean radius, these would be averaged out.

Colony features were measured using MATLAB's `regionprops` function. The mean radius (r_{mean}) of colony layers was calculated by averaging the Euclidean distance of each perimeter pixel to the layer's centre of mass. Radius of gyration was then calculated using

$$R_{gyr} = \sqrt{\frac{1}{N}\sum_{k=1}^{N} r_k^2} \tag{B.1}$$

where N is the number of perimeter pixels, and r_k the distance of the k^{th} perimeter pixel to the colony centre of mass.

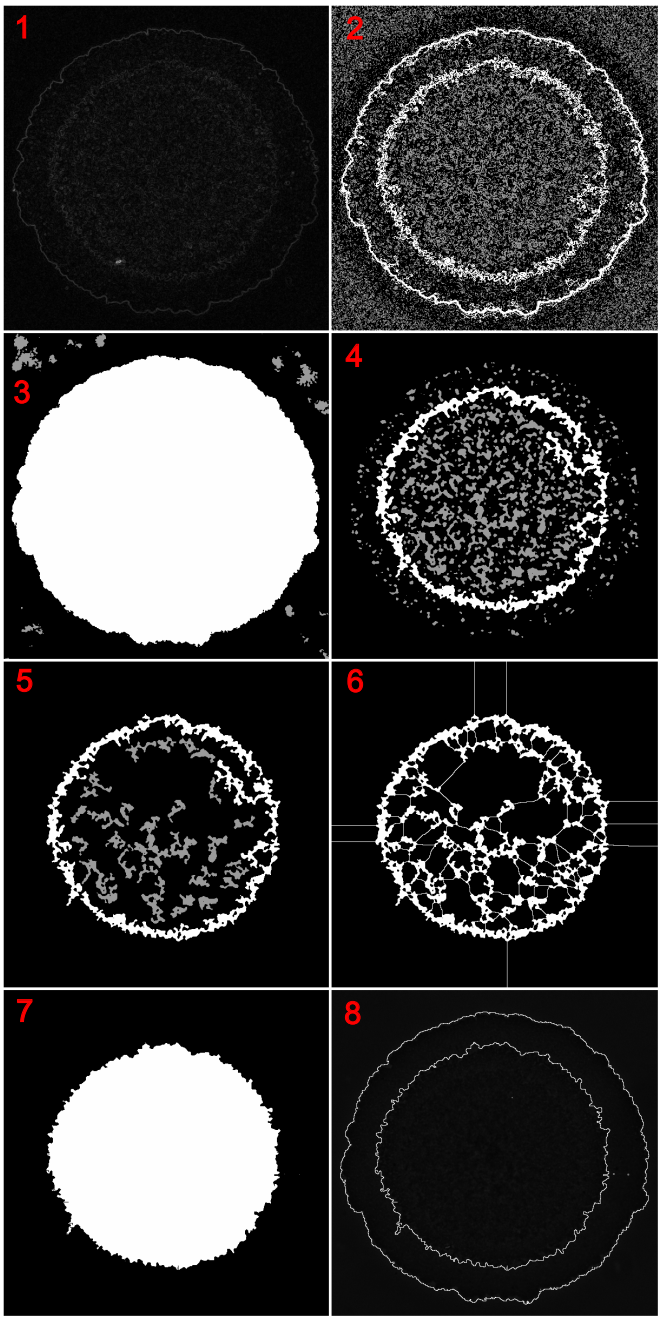

Figure B.1 Montage of image processing steps; numbers refer to points in main text. Options for enhancing contrast and controlling native ImageJ function parameters (such as selecting local thresholding algorithms and outlier removal radii) are kept in the macro so there is flexibility when dealing with images of varying quality. Some features have been highlighted in the panels $2, 4$ and 5 to guide the eye.

Appendix C

Supplementary information to microchannel colonies

C.1 Malformed channels

We originally attempted to reproduce the sub-micron wide channels described by Moffitt *et al.* [70]. However, attempts to synthesise the PDMS moulds at this scale were not successful, as shown in Fig. C.1. Generally, the larger the channel width, the higher quality the mould. Repeated attempts at PDMS synthesis evetually yielded 2.7 µm wide channels, the smallest width achieved. 5 µm and 10 µm channels were generally produced without problems, although occasionally malformations would be present at the channel ends.

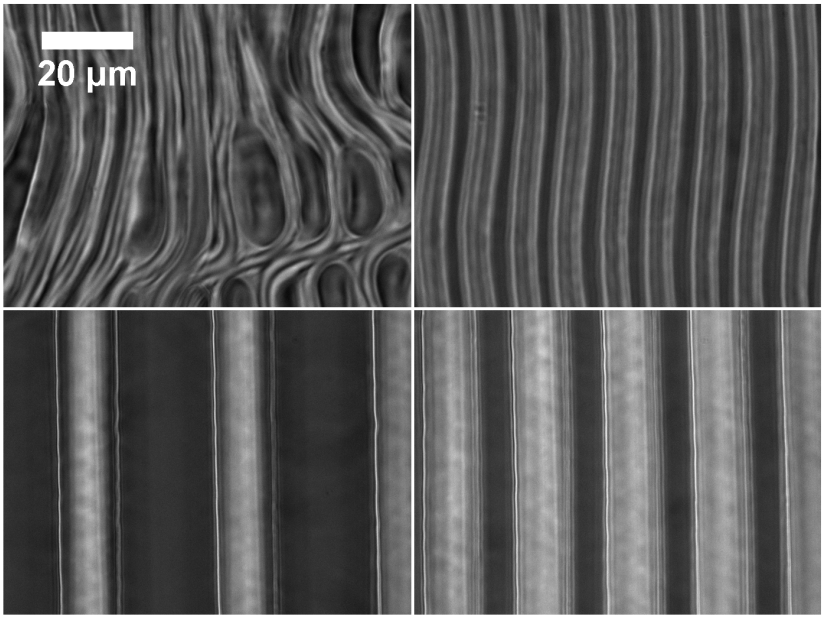

Figure C.1 A montage of phase contrast images of the PDMS mould used to create the patterned agarose micro structures. The first panel was an attempt to create sub-micron sized channels; however, they were never properly rendered. Similarly, agarose channels approaching micron widths (second panel) tended to exhbit deformities which only after many repeats were suitable PDMS mould constructed. The largest channels (bottom row) consistently produced straight mould walls.

Bibliography

[1] Whitman, W, Coleman, D. C, & Wiebe, W. J. (1998) Prokaryotes: The unseen majority. *Proceedings of the National Academy of Sciences* **95**, 6578–6583.

[2] Costerton, J. W, Lewandowski, Z, Caldwell, D. E, Korber, D. R, & Lappinscott, H. M. (1995) Microbial Biofilms. *Annual Review of Microbiology* **49**, 711–745.

[3] Zobell, C. (1943) The effect of solid surfaces upon bacterial activity. *Journal of Bacteriology* **46**, 39–56.

[4] Tuson, H & Weibel, D. (2013) Bacteria – surface interactions. *Soft Matter* **9**, 4368–4380.

[5] Busscher, H. J, Norde, W, Sharma, P. K, & van der Mei, H. C. (2010) Interfacial re-arrangement in initial microbial adhesion to surfaces. *Current Opinion in Colloid & Interface Science* **15**, 510–517.

[6] Chao, Y & Zhang, T. (2011) Probing roles of lipopolysaccharide, type 1 fimbria, and colanic acid in the attachment of Escherichia coli strains on inert surfaces. *Langmuir* **27**, 11545–11553.

[7] Krasteva, P, Fong, J, & Shikuma, N. (2010) Vibrio cholerae VpsT regulates matrix production and motility by directly sensing cyclic di-GMP. *Science* **327**, 866–868.

[8] Donachie, W. D & Begg, K. J. (1970) Growth of the Bacterial Cell. *Nature* **227**, 1220–1224.

[9] Shapiro, J. A & Hsu, C. (1989) Escherichia coli K-12 Cell-Cell Interactions Seen by Time-Lapse Video. *Journal of Bacteriology* **171**, 5963–5974.

[10] Shapiro, J. (1992) Pattern and control in bacterial colony development. *Science Progress* **76**, 1–36.

[11] Su, P. T, Yen, P. W, Wang, S. H, Lin, C. H, Chiou, A, & Syu, W. J. (2010) Factors Affecting Daughter Cells' Arrangement during the Early Bacterial Divisions. *PLOS ONE* **5**, e9147.

[12] Park, S, Wolanin, P. M, Yuzbashyan, E. A, Lin, H, Darnton, N. C, Stock, J. B, Silberzan, P, & Austin, R. (2003) Influence of topology on bacterial social interaction. *Proceedings of the National Academy of Sciences* **100**, 13910–5.

[13] Cho, H. J, Jonsson, H, Campbell, K, Melke, P, Williams, J. W, Jedynak, B, Stevens, A. M, Groisman, A, & Levchenko, A. (2007) Self-organization in high-density bacterial colonies: Efficient crowd control. *PLOS Biology* **5**, 2614–2623.

[14] Volfson, D, Cookson, S, Hasty, J, & Tsimring, L. S. (2008) Biomechanical ordering of dense cell populations. *Proceedings of the National Academy of Sciences* **105**, 15346–15351.

[15] Boyer, D, Mather, W, Mondragon-Palomino, O, Orozco-Fuentes, S, Danino, T, Hasty, J, & Tsimring, L. S. (2011) Buckling instability in ordered bacterial colonies. *Physical Biology* **8**, 026008.

[16] Mather, W, Mondragon-Palomino, O, Danino, T, Hasty, J, & Tsimring, L. S. (2010) Streaming instability in growing cell populations. *Physical Review Letters* **104**, 208101.

[17] Shapiro, J. A. (1988) Bacteria as Multicellular Organisms. *Scientific American* **258**, 82–89.

[18] Ingham, C. J & Jacob, E. B. (2008) Swarming and complex pattern formation in *Paenibacillus vortex* studied by imaging and tracking cells. *BMC Microbiology* **8**, 36.

[19] Shapiro, J. A. (1995) The significances of bacterial colony patterns. *BioEssays* **17**, 597–607.

[20] Rudge, T. J, Federici, F, Steiner, P. J, Kan, A, & Haseloff, J. (2013) Cell Polarity-Driven Instability Generates Self-Organized, Fractal Patterning of Cell Layers. *ACS Synthetic Biology* **2**, 705–714.

[21] Hallatschek, O, Hersen, P, Ramanathan, S, & Nelson, D. R. (2007) Genetic drift at expanding frontiers promotes gene segregation. *Proceedings of the National Academy of Sciences* **104**, 19926–30.

[22] Stoodley, P, Sauer, K, Davies, D. G, & Costerton, J. W. (2002) Biofilms as complex differentiated communities. *Annual Review of Microbiology* **56**, 187–209.

[23] Tolker-Nielson, T & Molin, S. (2000) Spatial Organization of Microbial Biofilm Communities. *Microbial Ecology* **40**, 75–84.

[24] McLoon, A. L, Kolodkin-Gal, I, Rubinstein, S. M, Kolter, R, & Losick, R. (2011) Spatial regulation of histidine kinases governing biofilm formation in *Bacillus subtilis*. *Journal of Bacteriology* **193**, 679–85.

[25] Branda, S, Gonzlez-Pastor, J, Ben-Yehuda, S, Losick, R, & Kolter, R. (2001) Fruiting body formation by *Bacillus subtilis*. *Proceedings of the National Academy of Sciences* **98**, 11621–6.

[26] Bassler, B. L. (2002) Small talk: Cell-to-cell communication in bacteria. *Cell* **109**, 421–4.

[27] Davies, D. G, Parsek, M. R, Pearson, J. P, Iglewski, B. H, Costerton, J. W, & Greenberg, E. P. (1998) The involvement of cell-to-cell signals in the development of a bacterial biofilm. *Science* **280**, 295–8.

[28] Shapiro, J. A. (1998) Thinking about bacterial populations as multicellular organisms. *Annual Review of Microbiology* **52**, 81–104.

[29] Elowitz, M. B, Levine, A. J, Siggia, E. D, & Swain, P. S. (2002) Stochastic gene expression in a single cell. *Science* **297**, 1183–6.

[30] Luria, S. E & Burrous, J. W. (1957) Hybridization between *Escherichia coli* and *Shigella*. *Journal of Bacteriology* **74**, 461–76.

[31] Black, J. G. (2012) *Microbiology: Principles and Explorations*. (Wiley).

[32] Bradley, M. D, Beach, M, Jason de Koning, A. P, Pratt, T. S, & Osuna, R. (2007) Effects of fis on *Escherichia coli* gene expression during different growth stages. *Microbiology* **1153**, 2922–2940.

[33] (2007) Valap. *Cold Spring Harbor Protocols* **2007**, pdb.rec10885.

[34] Nikon. (2000) http://www.microscopyu.com.

[35] Murphy, D. B & Davidson, M. W. (2001) *Fundamentals of light microscopy and electronic imaging*. (Wiley), p. 368.

[36] Young, J. W, Locke, J. C. W, Altinok, A, Rosenfeld, N, Bacarian, T, Swain, P. S, Mjolsness, E, & Elowitz, M. B. (2011) Measuring single-cell gene expression dynamics in bacteria using fluorescence time-lapse microscopy. *Nature Protocol* **7**, 80–88.

[37] Tilman, D. (1994) Competition and biodiversity in spatially structured habitats. *Ecology* **75**, 2–16.

[38] Turner, M. G. (2005) Landscape ecology in North America: past, present, and future. *Ecology* **86**, 1967–1974.

[39] Jules, E, Kauffman, M, Ritts, W, & Carroll, A. (2002) Spread of an invasive pathogen over a variable landscape: a nonnative root rot on Port Orford cedar. *Ecology* **83**, 3167–3181.

[40] Reichenbach, T, Mobilia, M, & Frey, E. (2007) Mobility promotes and jeopardises biodiversity in rock-paper-scissors games. *Nature* **448**, 1046–1049.

[41] Malchow, H, Petrovskii, S. V, & Venturino, E. (2008) *Spatiotemporal patterns in ecology and epidemiology.* (Chapman & Hall / CRC, Boca Raton, FL.).

[42] Ben-Jacob, E, Cohen, I, & Levine, H. (2000) Cooperative self-organization of microorganisms. *Advances in Physics* **49**, 395–554.

[43] Momeni, B, Chen, C, Hillesland, K. L, Waite, A, & Shou, W. (2011) Using artificial systems to explore the ecology and evolution of symbioses. *Cellular and Molecular Life Sciences* **68**, 1353–68.

[44] Zhang, Q, Lambert, G, Liao, D, Kim, H, Robin, K, Tung, C. K, Pourmand, N, & Austin, R. H. (2011) Acceleration of emergence of bacterial antibiotic resistance in connected microenvironments. *Science* **333**, 1764–7.

[45] Kerr, B, Neuhauser, C, Bohannan, B. J, & Dean, A. M. (2006) Local migration promotes competitive restraint in a host-pathogen 'tragedy of the commons'. *Nature* **442**, 75–78.

[46] Hallatsheck, O & Nelson, D. R. (2009) Life at the Front of an Expanding Population. *Evolution* **64**, 193–206.

[47] Hallatschek, O. (2011) The noisy edge of traveling waves. *Proceedings of the National Academy of Sciences* **108**, 1783–1787.

[48] Armstrong, R. A. (2002) The effect of rock surface aspect on growth, size structure and competition in the lichen *Rhizocarpon geographicum*. *Environmental and Experimental Botany* **48**, 187–194.

[49] Steneck, R, Hacker, S, & Dethier, M. (1991) Mechanisms of competitive dominance between crustose coralline algae: an herbivore-mediated competitive reversal. *Ecology* **72**, 938–950.

[50] McLetchie, D. N, Garcìa-Ramos, G, & Crowley, P. H. (2002) Local sex-ratio dynamics: a model for the dioecious liverwort *Marchantia inflexa*. *Evolutionary Ecology* **15**, 231–254.

[51] Stoll, P & Bergius, E. (2005) Pattern and process: competition causes regular spacing of individuals within plant populations. *Journal of Ecology* **93**, 395–403.

[52] Crowley, P. H, Davis, H. M, Ensminger, A. L, Fuselier, L. C, Jackson, J. K, & McLetchie, D. N. (2004) A general model of local competition for space. *Ecology Letters* **8**, 176–188.

[53] Crowley P. H. McLetchie, D. N. (2002) Trade-offs and spatial life-history strategies in classical metapopulations. *American Naturalist* **159**, 190–208.

[54] Williams, G. C. (1966) Natural selection, the costs of reproduction, and a refinement of Lack's principle. *American Naturalist* **100**.

[55] Kisdi, E & Geritz, S. A. H. (2003) On the Coexistence of Perennial Plants by the Competition – Colonization Trade Off. *American Naturalist* **161**, 350–354.

[56] Yodzis, P. (1978) *Competition for Space and the Structure of Ecological Communities*. (Springer-Verlag Berlin Heidelberg).

[57] Bowman, Elisabeth T., Saga, K, & Drummond, T. W. (2001) Particle shape characterisation using Fourier descriptor analysis. *Geotechnique* **51**, 545–554.

[58] Rice, K. P, Saunders, A. E, & Stoykovich, M. P. (2012) Classifying the Shape of Colloidal Nanocrystals by Complex Fourier Descriptor Analysis. *Crystal Growth & Design* **12**, 825–831.

[59] Gonzalez, R. C & Woods, R. E. (1992) *Digital Image Processing*. (Addison-Wesley Publishing Company).

[60] Métris, A, George, S. M, Mackey, B. M, & Baranyi, J. (2008) Modeling the variability of single-cell lag times for *Listeria innocua* populations after sublethal and lethal heat treatments. *Applied and Environmental Microbiology* **74**, 6949–55.

[61] Ernebjerg, M & Kishony, R. (2012) Distinct growth strategies of soil bacteria as revealed by large-scale colony tracking. *Applied and Environmental Microbiology* **78**, 1345–52.

[62] Niven, G. W, Morton, J. S, Fuks, T, & Mackey, B. M. (2008) Influence of environmental stress on distributions of times to first division in Escherichia coli populations, as determined by digital-image analysis of individual cells. *Applied and Environmental Microbiology* **74**, 3757–63.

[63] Atsuyuki Okabe, Barry Boots , Kokichi Sugihara, S. N. C. (2002) *Spatial Tessellations: Concepts and Applications of Voronoi Diagrams* ed. Wiley-Blackwell. 2nd edition.

[64] Rudge, T. J & Steiner, P. J. (2012) Computational modeling of synthetic microbial biofilms. *ACS Synthetic Biology* **1**.

[65] Aurenhammer, F. (1991) Voronoi diagrams—a survey of a fundamental geometric data structure. *ACM Computing Surveys* **23**, 345–405.

[66] Niven, G. W, Fuks, T, Morton, J. S, Rua, S. A. C. G, & Mackey, B. M. (2006) A novel method for measuring lag times in division of individual bacterial cells using image analysis. *Journal of Microbiological Methods* **65**, 311–7.

[67] Draper, N. R & Smith., H. (1998) *Applied Regression Analysis.* (Wiley-Interscience, Hoboken, NJ), pp. 307–312.

[68] Davey, M. E & O'Toole, G. (2000) Microbial biofilms: from ecology to molecular genetics. *Microbiology and Molecular Biology Reviews* **64**, 847–67.

[69] Anderson, G. G, Dodson, K. W, Hooton, T. M, & Hultgren, S. J. (2004) Intracellular bacterial communities of uropathogenic *Escherichia coli* in urinary tract pathogenesis. *Trends in Microbiology* **12**, 424–30.

[70] Moffitt, J, Lee, J, & Cluzel, P. (2012) The single-cell chemostat: an agarose-based, microfluidic device for high-throughput, single-cell studies of bacteria and bacterial communities. *Lab on a Chip* **12**, 1487–94.

[71] Grant, M. A. A, Waclaw, B, Allen, R. J, & Cicuta, P. (2014) The role of mechanical forces in the planar-to-bulk transition in growing Escherichia coli microcolonies. *Interface* **11**, 20140400.

[72] Rainey, P & Rainey, K. (2003) Evolution of cooperation and conflict in experimental bacterial populations. *Nature* **425**, 72–74.

[73] Griffin, A. S, West, S. A, & Buckling, A. (2004) Cooperation and competition in pathogenic bacteria. *Nature* **430**, 2–5.

[74] Brown, S. P, West, S. A, Diggle, S. P, & Griffin, A. S. (2009) Social evolution in micro-organisms and a Trojan horse approach to medical intervention strategies. *Philosophical Transactions B* **364**, 3157–68.

[75] Smith, J. (1964) Group selection and kin selection. *Nature* **201**, 1145–1147.

[76] Hamilton, W. D. (1964) The genetical evolution of social behaviour. I. *Journal of Theoretical Biology* **7**, 1–16.

[77] Ross-Gillespie, A, Gardner, A, West, S. A, & Griffin, A. S. (2007) Frequency dependence and cooperation: theory and a test with bacteria. *American Naturalist* **170**, 331–42.

[78] Ackermann, M, Stearns, S. C, & Jenal, U. (2003) Senescence in a bacterium with asymmetric division. *Science* **300**, 1920.

[79] Stewart, E. J, Madden, R, Paul, G, & Taddei, F. (2005) Aging and death in an organism that reproduces by morphologically symmetric division. *PLOS Biology* **3**, e45.

[80] Nyström, T. (2002) Aging in bacteria. *Current Opinion in Microbiology* **5**, 596–601.

[81] Pedro, M. A. D, Young, K. D, Höltje, J. V, & Schwarz, H. (2003) Branching of *Escherichia coli* Cells Arises from Multiple Sites of Inert Peptidoglycan Branching of Escherichia coli Cells Arises from Multiple Sites of Inert Peptidoglycan. *Journal of Bacteriology* **185**, 1147–1152.

[82] Lindner, A & Madden, R. (2008) Asymmetric segregation of protein aggregates is associated with cellular aging and rejuvenation. *Proceedings of the National Academy of Sciences* **105**, 3076–81.

[83] Stewart, P. S & Franklin, M. J. (2008) Physiological heterogeneity in biofilms. *Nature Reviews Microbiology* **6**, 199–210.

[84] Wang, P, Robert, L, Pelletier, J, Dang, W. L, Taddei, F, Wright, A, & Jun, S. (2010) Robust growth of *Escherichia coli*. *Current Biology* **20**, 1099–103.

[85] Tuson, H. H, Auer, G. K, Renner, L. D, Hasebe, M, Tropini, C, Salick, M, Crone, W. C, Gopinathan, A, Huang, K. C, & Weibel, D. B. (2012) Measuring the stiffness of bacterial cells from growth rates in hydrogels of tunable elasticity. *Molecular Microbiology* **84**, 874–91.

[86] Cabeen, M. T & Jacobs-Wagner, C. (2005) Bacterial cell shape. *Nature Reviews Microbiology* **3**, 601–10.

[87] Huang, K. C, Mukhopadhyay, R, Wen, B, Gitai, Z, & Wingreen, N. S. (2008) Cell shape and cell-wall organization in Gram-negative bacteria. *Proceedings of the National Academy of Sciences* **105**, 19282–7.

[88] Nilsen, T, Ghosh, A. S, Goldberg, M. B, & Young, K. D. (2004) Branching sites and morphological abnormalities behave as ectopic poles in shape-defective Escherichia coli. *Molecular Microbiology* **52**, 1045–54.

[89] Morikawa, R, Miyakawa, T, Tamakoshi, M, & Takasu, M. (2013) Simulation study of bacterial colonies formed by the twitching motility: The effect of slingshot-like motions of bacteria on the colony edge. *AIP Conference Proceedings* **590**, 590–593.

[90] Long, Z, Olliver, A, & Brambilla, E. (2014) Measuring bacterial adaptation dynamics at the single-cell level using a microfluidic chemostat and time-lapse fluorescence microscopy. *Analyst* **139**, 5254–5262.

[91] West, S. A & Buckling, A. (2003) Cooperation, virulence and siderophore production in bacterial parasites. *Proceedings B* **270**, 37–44.

[92] Donlan, R. M. (2002) Biofilms: Microbial life on surfaces. *Emerging Infectious Diseases* **8**, 881–890.

[93] Liotta, L & Kohn, E. (2001) The microenvironment of the tumour – host interface. *Nature* **411**, 380–384.

[94] Harris, W. A. (1997) Pax-6: Where to be conserved is not conservative. *Proceedings of the National Academy of Sciences* **94**, 2098–2100.

[95] Flemming, H. (2002) Biofouling in water systems–cases, causes and countermeasures. *Applied Microbiology and Biotechnology* **59**, 629–40.

[96] Scher, K, Romling, U, & Yaron, S. (2005) Effect of heat, acidification, and chlorination on *Salmonella enterica* serovar Typhimurium cells in a biofilm formed at the air-liquid interface. *Applied and Environmental Microbiology.*

[97] Borriello, G, Werner, E, & Roe, F. (2004) Oxygen limitation contributes to antibiotic tolerance of *Pseudomonas aeruginosa* in biofilms. *Antimicrobial Agents and Chemotherapy* **48**, 2659–2664.

[98] Ito, A, Taniuchi, A, May, T, Kawata, K, & Okabe, S. (2009) Increased antibiotic resistance of *Escherichia coli* in mature biofilms. *Applied and Environmental Microbiology* **75**, 4093–100.

[99] Garcia-Medina, R & Dunne, W. (2005) *Pseudomonas aeruginosa* acquires biofilm-like properties within airway epithelial cells. *Infection and Immunity* **73**, 8298–8305.

[100] Molin, S & Tolker-Nielsen, T. (2003) Gene transfer occurs with enhanced efficiency in biofilms and induces enhanced stabilisation of the biofilm structure. *Current Opinion in Biotechnology* **14**, 255–261.

[101] Schultz, M. P, Bendick, J. A, Holm, E. R, & Hertel, W. M. (2011) Economic impact of biofouling on a naval surface ship. *Biofouling* **27**, 87–98.

[102] Su, P. T, Liao, C. T, Roan, J. R, Wang, S. H, Chiou, A, & Syu, W. J. (2012) Bacterial colony from two-dimensional division to three-dimensional development. *PLOS ONE* **7**, e48098.

[103] Asally, M, Kittisopikul, M, Rué, P, Du, Y, Hu, Z, Çaatay, T, Robinson, A. B, Lu, H, Garcia-Ojalvo, J, & Süel, G. M. (2012) Localized cell death focuses mechanical forces during 3D patterning in a biofilm. *Proceedings of the National Academy of Sciences* **109**, 18891–6.

[104] Marr, A. (1991) Growth rate of *Escherichia coli*. *Microbiological Reviews* **55**, 316–33.

[105] van der Woude, M & Arts, P. (1990) Growth-rate-dependent synthesis of K99 fimbrial subunits is regulated at the level of transcription. *Journal of General Microbiology* **136**, 897–903.

[106] Pierucci, O. (1978) Dimensions of *Escherichia coli* at various growth rates: Model for envelope growth. *Journal of Bacteriology* **135**, 559–574.

[107] Donachie, W, Begg, K. J, & Vicente, M. (1976) Cell length, cell growth and cell division. *Nature* **264**, 328–333.

[108] Pirt, S. (1967) A kinetic study of the mode of growth of surface colonies of bacteria and fungi. *Journal of General Microbiology* **47**, 181–197.

[109] Mertz, A. F, Banerjee, S, Che, Y, German, G. K, Xu, Y, Hyland, C, Marchetti, M. C, Horsley, V, & Dufresne, E. R. (2012) Scaling of Traction Forces with the Size of Cohesive Cell Colonies. *Physical Review Letters* **108**, 198101.

[110] Brown, S. P, Fredrik Inglis, R, & Taddei, F. (2009) Evolutionary ecology of microbial wars: within-host competition and (incidental) virulence. *Evolutionary Applications* **2**, 32–39.